

DISS. ETH NO.

Microwave photonics in superconducting circuits

A thesis submitted to attain the degree of
DOCTOR OF SCIENCES of ETH ZURICH
(Dr. sc. ETH Zurich)

presented by
Marek Pechal
MSc ETH Physics, ETH Zurich
born on 16.04.1987
citizen of the Czech Republic

accepted on the recommendation of
Prof. Dr. Andreas Wallraff, examiner
Prof. Dr. Jonathan Home, co-examiner
Prof. Dr. Konrad Lehnert, co-examiner

2016

*There is much pleasure
to be gained
from useless knowledge.*

Bertrand Russell

Abstract

This thesis presents the main results of my work in the Quantum Device group, dealing mainly with the generation and manipulation of microwave photons in superconducting circuits and their use for quantum information processing. Photons, whether confined in a resonant cavity or propagating in an open transmission line, can be used as mediators of interaction and carriers of quantum information among spatially separated quantum bits.

The first experimental chapter of this work describes a proof-of-principle experiment in which we used the cyclic evolution of a single discrete mode of a 3d cavity to realize a two-qubit phase gate. This type of quantum gate can be easily generalized to more than two qubits but in our case was found to be limited by the current coherence properties of the used samples. Therefore, we did not deem it suitable as a replacement for other well established implementations of multi-qubit gates.

The subsequent chapters present experiments on the generation of single microwave photons with a controllable temporal shape and the possibility of their efficient reabsorption by a quantum system. We demonstrate a photon shaping scheme which, in contrast with other recently realized protocols that require fast flux control of the sample, is fully controlled by microwave signals. We show that the scheme can be used to generate photons with a time-reversal symmetric shape and in some instances may be useful as a tool for cooling the system towards its ground state. Furthermore, we present an experiment performed as an extension of the photon shaping work, aimed at reabsorption of the shaped photons. Here we establish the exchange of a single energy quantum with an efficiency of approximately 40% which is limited mainly by dephasing processes in the used qubits.

Finally, to extend the quantum photonics toolbox at our disposal, we developed a switching device capable of routing microwave signals on a superconducting chip. The presented device is essentially free of dissipation, has a sufficiently large bandwidth and high linearity for most circuit QED applications, and can be toggled on a very fast time-scale of several nanoseconds.

Zusammenfassung

Diese Doktorarbeit präsentiert die wichtigsten Ergebnisse meiner Arbeit in der Quantum Device Gruppe, hauptsächlich betreffend die Erzeugung und Manipulation von Mikrowellenphotonen in supraleitenden Schaltkreisen und deren Verwendung für die Verarbeitung von Quanteninformation. Photonen, ob in einer Resonanzkavität lokalisiert oder in einer offenen Transmissionsleitung ausbreitend, können als Vermittler der Interaktion zwischen räumlich getrennten Quantenbits und als Träger von Quanteninformation verwendet werden.

Das erste experimentelle Kapitel dieser Arbeit beschreibt ein proof-of-principle Experiment, in dem wir die zyklische Entwicklung eines einzelnen diskreten Modes eines 3D-Hohlraums verwenden, um ein 2-Qubit-Phasengatter zu realisieren. Diese Art von Quantengattern kann einfach auf mehr als zwei Qubits erweitert werden, aber in unserem Fall wurde es durch die aktuellen Kohärenzeigenschaften der verwendeten Proben limitiert. Daher betrachten wir es nicht als Ersatz für andere gut etablierte Implementierungen von Multi-Qubit-Gattern.

Die nachfolgenden Kapiteln präsentieren Experimente mit der Erzeugung von einzelnen Mikrowellenphotonen mit einer steuerbaren Wellenform und die Möglichkeit für deren effiziente Reabsorption durch ein Quantensystem. Wir stellen einen Photonformungsprozess dar, das im Gegensatz zu anderen kürzlich realisierten Protokolle, die eine schnelle Flusssteuerung der Probe erfordern, vollständig durch Mikrowellensignalen gesteuert wird. Wir zeigen, dass das Schema zur Erzeugung von Photonen mit einer Zeit-symmetrischen Form verwendet werden kann, und in einigen Fällen für die Kühlung des Systems in den Grundzustand nützlich ist. Ferner stellen wir ein Experiment vor als eine Ausdehnung der Photonformung, mit dem Ziel, die Reabsorption der geformten Photonen zu realisieren. Hier wird der Austausch eines einzigen Energiequants mit einem Wirkungsgrad von etwa 40% demonstriert, der hauptsächlich durch Dekohärenzprozesse in den verwendeten Qubits limitiert ist.

Schliesslich, um die "Quanten Photonics Werkzeugkiste", die uns zur Verfügung steht, zu erweitern, haben wir ein Schalterelement entwickelt, die Mikrowellensignale auf einem supraleitenden Chip steuern kann. Das dargestellte Element ist im Wesentlichen frei von Energieverlust, hat eine Bandbreite und Linearität hoch genug für die meisten circuit-QED Anwendungen, und kann auf einer sehr schnellen Zeitskala von einigen Nanosekunden umgeschaltet werden.

Contents

Abstract	iii
Zusammenfassung	v
Contents	vii
Introduction	1
1 Basics of Circuit Quantum Electrodynamics with Transmons	5
1.1 Coplanar waveguides	7
1.2 Transmission-line resonators	9
1.3 Josephson junction	13
1.4 Transmon qubit	15
1.5 Jaynes-Cummings coupling	22
1.6 Dispersive approximation	26
2 Measurement setup and techniques	29
2.1 Cryogenic setup	29
2.2 Sample and its control lines	31
2.3 Room-temperature electronics	34
2.4 Characterization measurements	36
2.5 Transmon state read-out and tomography	46
2.6 Microwave field measurements and state tomography	55
Experiments	67
3 Multi-qubit gates induced by steered resonator field	67
3.1 Geometric phase	67
3.2 Geometric phase in a harmonic oscillator	69
3.3 Non-adiabatic protocol	72
4 Generation of shaped microwave photons and active qubit cooling	77
4.1 Photon shaping	78
4.2 Qubit cooling	89

5	Reabsorption of single microwave photons	91
6	On-chip microwave switch	99
6.1	Basic characterization of the switch	101
6.2	Single photon source	115
6.3	Routing of single photons	118
7	Outlook	123
Appendices		129
A	Designing a qubit	129
A.1	Calculating qubit parameters analytically	129
A.2	Black-box quantization	131
A.3	Qubit as a single-photon source: Analysis of direct drive leakage . . .	135
B	Dissipation in electrical circuits	141
B.1	Classical analysis	141
B.2	Quantum description of dissipation	146
B.3	Example - qubit coupled to a transmission line	153
B.4	Example - Purcell effect	153
C	A shortcut to circuit quantization	157
C.1	Example – LC oscillator	160
C.2	Example – two coupled LC oscillators	161
C.3	Derived quantities	162
D	Optimizing a second order transition	165
D.1	Method 1: Optimizing final state fidelity	165
D.2	Method 2: Optimizing time-averaged fidelity	169
E	Photon shaping and reabsorption theory	171
E.1	Photon shaping	171
E.2	Photon reabsorption	174
E.3	Photon reabsorption simulations	176
F	Derivation of CPW properties	179
F.1	Propagating modes	179
F.2	Capacitance, inductance, impedance	183
G	Qubit spectroscopy with a weak probe	193
G.1	Weak resonator drive	194
G.2	Weak qubit drive	197
H	Theoretical considerations on dispersive read-out	205
H.1	Extraction of state populations from time traces	205

H.2 Resonator response in dispersive readout	208
I Switch controlled by a single impedance: a no-go statement	215
I.1 Dependence of S -matrix on lumped control impedances	215
I.2 Impossibility of switching with a single control element	218
J Microwave $\pi/2$ hybrid	221
K Modification of a RADIALL switch for cryogenic operation	223
Bibliography	233
List of publications	245
Curriculum vitae	247
Acknowledgements	249

Introduction

It is no wonder that light, being such an omnipresent phenomenon and an indispensable part of our perception of the world, has been the subject of much attention since the advent of modern science (Al-Khalili, 2015). To explain its refraction in optically dense materials, sir Isaac Newton and other proponents of the corpuscular theory imagined it as a stream of minuscule particles (Newton, 1730). With the observation of interference effects (Young, 1804), this picture was abandoned in favour of a theory of light as waves which, when combined, can add up or cancel out depending on their relative phase, much like ripples on a pool of water. The new theory could explain the properties of light much better and when James Clerk Maxwell finally anchored it in mathematical rigour (Maxwell, 1865), killing the two metaphorical birds of optics and electromagnetism with one stone, it seemed that light was to remain a wave forever.

In a desperate bid to eradicate divergences from his theory of black-body radiation, Max Planck later suggested that despite its wave-like nature, the energy of electromagnetic radiation can only come in particle-like packets which he dubbed “quanta” (Planck, 1901). His assumption was soon supported by Albert Einstein’s observation that exactly the same kind of energy quantization is needed to explain the photoelectric effect (Einstein, 1905). As if these hints at the inadequacy in our understanding of light were not enough, nearly two decades later, the now famous experiment by Arthur Compton (Compton, 1923) left no doubt that X-rays colliding with electrons scatter as though they were particles rather than well-behaved waves obeying Maxwell’s equations. The resulting confusion was understandable.

As we now know, the question which of the two pictures of light is correct is answered by the theory of quantum mechanics in the famously puzzling revelation: Both of them are. Which of the two aspects we observe in the end is determined by the way in which the light was generated as well as by the details of the observation act itself. The particle-like quanta, or “photons”, observed by Compton can be seen as superpositions of many monochromatic waves with different frequencies which together form a localized wave-packet. Equivalently, the point-like photons can exist in a superposition state of different locations, forming a de-localized wave.

Even after being imported into the quantum world, the theory of electromagnetic field in vacuum remains rather simple. The linearity of the underlying Maxwell’s equations ensures that free photons do not interact with each other. Put a few of them in a mirror-lined box and no matter how long you wait, the result will be disappointingly plain – each of the photons bounces around as if the others were not there.

Fortunately for everyone who likes their physics exciting and complicated, there is always something for the light to interact with. Perhaps somewhat surprisingly, even in a space devoid of all matter. Quantum electrodynamics (Dyson, 1949), the poster-child of mid-20th century theoretical physics, added electrons and positrons into the story and predicted that photons have a small but non-zero chance to give birth to extremely short-lived pairs of virtual particle-antiparticle pairs. This very small material content of the electromagnetic field makes it in principle possible even for photons in free space to interact with each other (Heisenberg & Euler, 1936) – a tantalizingly interesting phenomenon whose signatures are however so subtle that it remains unobserved to this day (d’Enterría & da Silveira, 2013). Despite their origins in an elegant yet fully linear and therefore easily tractable theory, photons turned out to be far from boring, even when left on their own.

Their coupling to charged matter is what brings the fun into the game. In the relatively young field of cavity quantum electrodynamics (CQED) (Haroche & Kleppner, 1989; Mabuchi & Doherty, 2002), electromagnetic radiation is confined in resonant cavities whose small mode volume significantly boosts the field amplitude of single photons, allowing them to interact strongly with atoms located in the cavity. This strong coupling gives rise to a plethora of intriguing quantum-mechanical effects.

For instance, single photons have been shown to come into and out of existence periodically in a process known as vacuum Rabi oscillations when an excited atom swaps its energy with an empty cavity (Brune *et al.*, 1996). They were observed to form peculiar quantum states called polaritons where, in a true spirit of quantum-mechanical strangeness, the single quantum of energy is located in the electromagnetic field and in the atom at the same time (Thompson *et al.*, 1992). Classical light, a stream of uncorrelated photons traveling independently of each other, was sent through a CQED system acting as a turnstile, turning it into a non-classical state of light – an orderly procession of photons arriving one at a time (Birnbaum *et al.*, 2005) – a phenomenon known as “anti-bunching”. The opposite behaviour, the so-called “bunching”, can be observed when two photons arrive at a beam-splitter at the same time and, owing to their bosonic nature, always end up on the same side of it (Hong *et al.*, 1987).

These are just a few of many fascinating phenomena arising from matter-light interactions. Their study has helped further our understanding of quantum theory on a fundamental level but has also led to a progress in the rapidly growing areas of applied physics which aim to harness the strange laws of quantum mechanics for technological applications.

In his visionary speech on simulating physics with computers (Feynman, 1982), Richard Feynman posited that physical systems in which quantum mechanics plays an important role cannot be efficiently simulated by classical computers. The reason for this is the exponential scaling of the number of variables needed to describe a quantum state of a system with its size. Luckily, nature offers us a solution to this problem: Quantum systems can efficiently simulate other quantum systems. Therefore, a properly designed “quantum computer”, operating on non-classical data stored as states of quantum two-level systems – the so-called quantum bits or “qubits”, could be used to solve problems in computational physics which are impossible to tackle

with traditional computers. In fact, the types of problems this applies to are not restricted to simulation of physical systems. As shown by David Deutsch (Deutsch, 1985), solutions to a wide range of computational problems could benefit from “quantum speed-up” even though the exact characterization of this class of problems turns out to be a non-trivial task (Bernstein & Vazirani, 1997). Since the conception of the quantum computation paradigm, many concrete examples of quantum algorithms offering faster solutions to practical computational problems have been devised (Shor, 1994; Harrow *et al.*, 2009).

Apart from its potential to enable novel ways of computation, quantum mechanics has also been recognized to have interesting applications in the field of cryptography – the art of secure communication. The impossibility of copying quantum information (Wootters & Zurek, 1982) and the irreversibility of the measurement process mean that by encoding the secret message in an appropriate way (Bennett & Brassard, 1984), the adversary can be prevented from eavesdropping on the conversation without making his or her presence known. Nowadays, even though still far from wide-spread, the principles of quantum cryptography are already being used in some commercial communication systems.

Yet another area which is expected to profit from application of quantum-mechanical systems is the field of metrology. Here, quantum entanglement can be exploited to perform measurements with unprecedented precision. For example, the most accurate measurements of the acceleration of gravity to-date were made using quantum superposition states of laser-cooled atoms (Peters *et al.*, 2001). The experiment LIGO, which has recently resulted in the ground-breaking observation of gravitational waves, the last prediction of Einstein’s general relativity to be confirmed, uses non-classical states of light to improve its detection sensitivity (Andersen, 2013).

These examples illustrate the exciting progress in development of engineered quantum systems over the past few decades. Phenomena which were long accessible only in Gedankenexperiments, are now slowly popping up as tangible experimental results. Many of the quantum devices being developed rely on transmission of quantum information over a distance, be it for purposes of computation, communication or metrology. Just like in classical communication which has been dominated by electromagnetic waves since the days of Tesla and Marconi, photons turn out to be very suitable as quantum information carriers (Kimble, 2008), owing to their relatively weak interactions¹ with the environment through which they propagate. Virtual (Majer *et al.*, 2007) or real photons (Hagley *et al.*, 1997), confined in a resonant cavity or propagating through space (Ritter *et al.*, 2012), can be used to ferry quantum states between quantum bits. Certain quantum computation architectures such as linear optical quantum computing (Knill *et al.*, 2001) dispense with stationary qubits altogether and use photons for information storage, transfer *and* processing.

In the Quantum Device lab where the work presented in this thesis was done, photons are ubiquitous too. We work with superconducting circuits – artificial atoms whose transition energies lie in the microwave rather than the visible domain of the electromagnetic spectrum. Instead of lasers, we use microwave generators. Instead of

¹Compared with means of transmitting information based on massive particles such as carrier pigeons.

optical fibers, coaxial cables, and instead of photon counters, nearly quantum-limited linear amplifiers. Both optical and microwave photonics present researchers with their own specific pitfalls and advantages. For example, the lower frequencies of microwave radiation means that signals at the single-photon level can only be studied at very low temperatures. On the other hand, the same reason makes fabrication of wavelength- or sub-wavelength-sized structures significantly easier in microwave systems. In spite of the differences between the two frequency domains, the types of processes and phenomena which can be studied with microwave “light” are essentially identical to those described by quantum optics in the visible spectrum.

Over the course of my PhD studies in the lab, I have worked on several experiments which, even though not directly related to each other, all have to do with microwave photons, their manipulation and use to couple quantum bits together. I started with an experiment following up on the topic of my master’s thesis (Pechal *et al.*, 2012) – geometric phases of a microwave field confined in a resonator – and generalizing it to use the quantum-mechanical phase accumulated by the photon field to realize a two-qubit operation. I have then moved on to study (Zeytinoglu *et al.*, 2015) and later experimentally test the possibility to generate single microwave photons with a controllable temporal profile (Pechal *et al.*, 2014). The ultimate goal of this exercise was to enable efficient reabsorption of the emitted photon by a qubit and thus to realize a quantum state exchange between two distant qubits. We have prepared an experimental setup and performed proof-of-principle measurements which show that a photon can be emitted, transmitted through a few tens of centimetres of a coaxial cable and then reabsorbed by a qubit. However, the efficiency of this process still needs to be improved to make it useful for applications such as entanglement over distance. Potential future experiments with propagating microwave fields will greatly benefit from the development of devices enabling routing and manipulation of microwaves on a chip. Some of such devices used in our lab are for example on-chip microwave beam-splitters or parametric amplifiers. To extend our microwave toolbox, I have also pursued project to design and test an on-chip switch based on interference effects.

While the primary aim of a thesis is to present the obtained experimental results, the process in which these are gained is not at all straightforward, involves a lot of dead-ends and learning from one’s mistakes. On the way, one collects a set of technical and theoretical knowledge, insights, tricks and time-saving hacks. In retrospect, I realize how much effort it would have saved me, had I known these in advance. I will consider it a great success if this thesis, apart from summarizing my work in the lab, also happens to save some future struggling PhD students a bit of time and headache by explaining the dispersive approximation, qubit state tomography or some other confusing concept. This is why I have decided to present some of the more general parts and mathematical derivations in more detail than they might seem to merit (as they have been explained elsewhere – one merely needs to piece together equations from papers X and Y and fill in the gaps with a sleepless night of algebra).

Chapter 1

Basics of Circuit Quantum Electrodynamics with Transmons

The field of circuit quantum electrodynamics (cQED) (Blais *et al.*, 2004) can be considered a younger sibling of cavity QED (Haroche & Kleppner, 1989). Whereas the latter studies light-matter interaction with real atoms in resonant optical or microwave cavities, the former replaces these elements with essentially equivalent electrical circuits. The role of cavities is played by microwave-frequency resonators and the analogues of atoms are special superconducting circuits which mimic their anharmonic structure. These correspondences between the different components of cavity and circuit QED are illustrated in Fig. 1.1.

One of the main appeals of circuit QED systems is that they can be easily engineered to achieve the desired values of parameters such as the number of qubits and resonators, their frequencies or the strength and topology of their couplings. They are also expected to be easily scalable even though the problem of controlling the considerable number of components in a large-scale quantum circuit remains an unsolved challenge. On the other hand, they so far lack the excellent reproducibility and stability of parameters provided naturally by real atoms.

The first experiments reporting successful coherent manipulation of superconducting qubits emerged at the turn of the millennium (Nakamura *et al.*, 1999; Vion *et al.*, 2002; Martinis *et al.*, 2002). A few years later, an experiment by Wallraff *et al.* (2004) demonstrated that these qubits can be strongly coupled to microwave photons in a resonator. Since then, circuit QED has proved to be a promising platform for quantum computing, producing an impressive range of results over its less than two decades of existence. These range from early demonstrations of two-qubit resonator-mediated gates (Majer *et al.*, 2007) to sophisticated experiments on quantum teleportation (Steffen *et al.*, 2013) or proof-of-principle error-correcting protocols with up to 9 qubits (Kelly *et al.*, 2015). In addition to these quantum-computing applications, circuit QED systems have recently been used to implement rudimentary quantum simulations (Salathé *et al.*, 2015; Barends *et al.*, 2015). They also enable a variety of more fundamental experiments in quantum optics with microwave photons (Bozyigit *et al.*, 2011; Lang *et al.*, 2011, 2013; Eichler *et al.*, 2012b). Recent experiments with

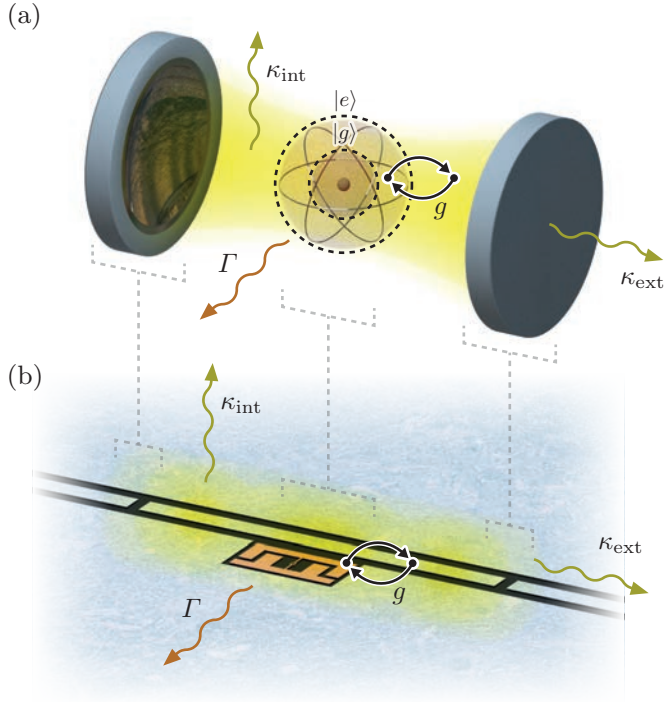


Figure 1.1: (a) Artistic representation of an optical cavity QED system – a Fabry-Perot cavity containing an atom whose two states $|g\rangle$ and $|e\rangle$ define a qubit. (b) Equivalent system in circuit QED – a superconducting qubit (artificial atom) embedded in a coplanar waveguide resonator. The corresponding elements in both architectures are indicated by the dashed connecting lines. The yellow wavy arrows represent photon losses from the resonator while the orange one shows losses of the atom due to other dissipation channels than the resonator. The black arrows indicate resonant energy exchange between the atom and the resonator caused by the Jaynes-Cummings coupling g .

qubits in one-dimensional open space (van Loo *et al.*, 2013; Liu & Houck, 2016) have started harnessing the potential of engineered quantum systems to explore the rich physics of collective phenomena mediated by a continuum of photon modes.

To observe quantum phenomena in electrical circuits, resistive losses need to be reduced to a minimum. In circuit QED system, this is achieved by fabricating the circuits out of a superconducting material such as niobium or aluminium. Superconductivity (Tinkham, 1996) is a phenomenon exhibited by certain materials which completely lose their dc electrical resistance at low temperatures.

This is caused by attractive interactions between free electrons in the material, an effect understood to be caused by electron-phonon coupling in some materials but still not well explained in others. The attraction causes electrons to form so-called *Cooper pairs*. These bosonic composite particles condense to a common ground state. A finite energy gap separating the ground state from the rest of the energy spectrum prevents low energy excitations such as electron scattering, making current conduction in the material lossless.

Circuit QED systems are typically on-chip structures fabricated from a superconducting metal such as niobium or aluminium on a non-conductive substrate, for example sapphire (crystalline Al_2O_3) or silicon.

1.1 Coplanar waveguides

In most circuit QED systems, the propagation channel for microwave photons on a chip is the so-called *coplanar waveguide* (CPW) – an element functionally equivalent to single-mode fibres in optical systems or to coaxial cables in radiofrequency devices. The latter analogy is particularly illustrative since a coplanar waveguide can be imagined as an “unwrapped” coaxial cable as shown in Fig. 1.2

The waveguide is an essentially two-dimensional structure placed on top of a dielectric substrate. It consists of a *ground-plane*, divided into two halves by a slit, and a *center conductor* – a strip in between the two half-planes. A short finite section of a CPW without the substrate is shown in Fig. 1.2(b) and its cross-section in Fig. 1.2(d).

The form of the electromagnetic wave propagating along this structure with a certain frequency ω can be found by solving Maxwell’s equations, as discussed in more detail in app. F. The shape of the electric and magnetic field lines considered in typical CPW applications is shown schematically in Fig. 1.2(d). It is usually assumed that the field is essentially identical to that of the corresponding electro- or magnetostatic problem. This so-called TEM mode (Pozar, 2011), where both the electric and the magnetic field are perpendicular to the direction of propagation, is indeed a good approximation which becomes exact in two situations: (a) when the dielectric constant is the same in both regions separated by the CPW plane or (b) in the limit of vanishingly small signal frequency $\omega \rightarrow 0$.

We should note that the description given above is only valid if it is possible to neglect the *kinetic inductance* of the waveguide. This is a component of inductance which originates from the kinetic energy of the charge carriers instead of the magnetic field’s energy. A simple calculation reveals that the kinetic inductance L_k of a conductor scales linearly with its length l and inversely with its cross-section area A and

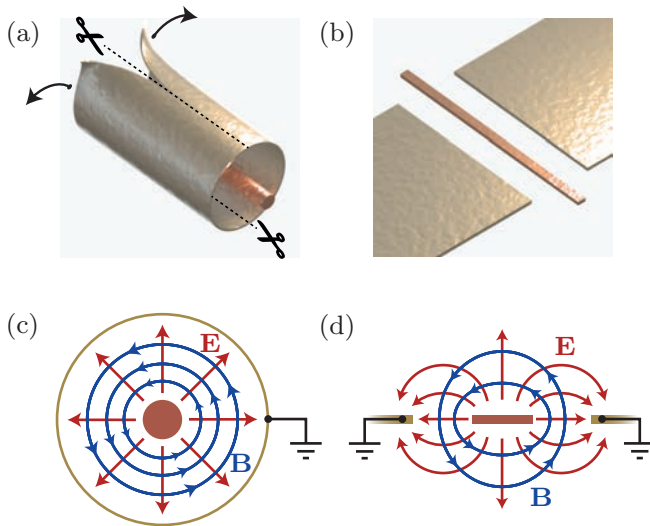


Figure 1.2: (a) Schematic drawing of a coaxial cable, showing how unwrapping the grounded outer conductor into two half-planes results in (b) a coplanar waveguide. (c,d) Shape of the electric (in red) and magnetic (in blue) field lines in the cross sections of the two guiding structures from (a,b).

density of charge carriers. In a superconductor where the charge carriers are Cooper pairs, it can be written in the form $L_k = \mu_0 \lambda^2 l / A$, where μ_0 is the permeability of vacuum and λ the *penetration depth* in the superconducting material (Tinkham, 1996). As typical values of geometric inductance L_g per unit length of a waveguide are on the order of μ_0 , the relative size of the two contributions is approximately $L_k / L_g \sim \lambda^2 / A$. In our waveguides, the cross-section of the center conductor is close to $1.5 \mu\text{m}^2$ while the penetration depth in niobium at the relevant temperatures is approximately 50 nm (Maxfield & McLean, 1965), making the kinetic inductance in this case for all practical purposes negligible.

Effectively, the waveguide can be modeled as a generic dispersionless transmission line – a two-port device where the voltages and currents at the two ends of the line, defined as shown in Fig. 1.3(a), are related by

$$V_2 = -iZ_0 I_1 \sin \frac{\omega x}{c} + V_1 \cos \frac{\omega x}{c}, \quad (1.1a)$$

$$I_2 = -\frac{i}{Z_0} V_1 \sin \frac{\omega x}{c} + I_1 \cos \frac{\omega x}{c}. \quad (1.1b)$$

Here c is the propagation speed in the line, x its length, Z_0 the characteristic impedance and ω the frequency of the propagating signal.

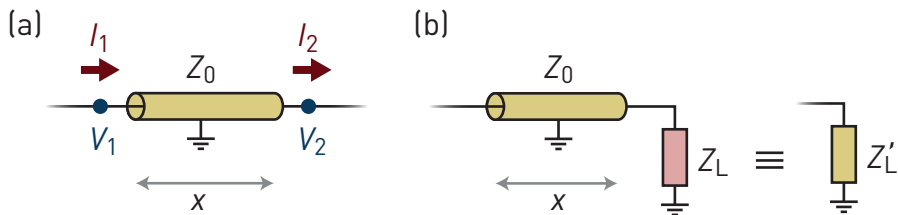


Figure 1.3: (a) Voltages and currents at the two ends of a transmission line section. (b) Transformation of a load impedance by a transmission line. The circuit consisting of the line and the load Z_L is equivalent to a lumped impedance Z'_L given by eq. (1.2).

When analyzing circuits containing transmission lines, it is sometimes convenient to view the line as an element which transforms the impedance of a load connected to one of its ends and presents a different impedance at its other end (Pozar, 2011). If a load with an impedance Z_L is connected to the line as shown in Fig. 1.3(b), this imposes the boundary condition $V_2 = Z_L I_2$. Using eq. (1.1), one can then express $Z'_L \equiv V_1/I_1$ which is the effective impedance seen at the other end of the line.

$$Z'_L = Z_0 \frac{Z_L + iZ_0 \tan \frac{\omega x}{c}}{Z_0 + iZ_L \tan \frac{\omega x}{c}}. \quad (1.2)$$

1.2 Transmission-line resonators

Coplanar waveguides are used not only for transmission of signals on circuit QED chips but also as building blocks to construct other useful microwave components. These range from filters (Reed *et al.*, 2010) and microwave beamsplitters (Bozyigit *et al.*, 2011) to parametric amplifiers (Castellanos-Beltran & Lehnert, 2007; Gao *et al.*, 2011; Eichler *et al.*, 2011). But perhaps the simplest and yet most commonly used element constructed using coplanar waveguides is the *transmission line resonator* (Göppl *et al.*, 2008).

A finite section of a transmission line supports a discrete set of resonant modes because the boundary conditions at its ends constrain the possible values of the wave number. In this aspect, the transmission line resonator is equivalent to a Fabry-Perot resonator in optics, as illustrated in Fig. 1.1.

The two most easily realized types of boundary conditions at the end of a transmission line are *open* and *short*. As the names suggest, in the first case the line is simply left open, leading to the boundary condition $I = 0$, while in the second case it is connected to the ground plane, resulting in $V = 0$. By combining the two boundary conditions, one can realize two types of resonators: The first is the so-called $\lambda/2$ resonator which has boundary conditions of the same type at both ends and therefore supports frequencies for which the length of the resonator is an integer multiple of the half-wavelength $\lambda/2$. The second type is the $\lambda/4$ resonator with unequal boundary

conditions at its ends. This type can accommodate modes for which the resonator length is a half-integer multiple of $\lambda/2$.

In real circuit QED settings, the resonators never possess perfectly reflective boundary conditions but are instead coupled to a dissipative environment. Most commonly, this environment is a semi-infinite $50\ \Omega$ transmission line used to probe the resonator. The environmental coupling makes the eigenmodes of the resonator lossy and shifts their frequencies with respect to those obtained for perfect boundary conditions. An analysis of the relaxation and frequency shift induced by coupling to an environment in the case of a $\lambda/2$ resonator is presented in sec. B.1, with the results given in eq. (B.2).

A transmission line resonator is usually connected to one or two external lines. In the first case, it can be probed only in reflection. Assuming that the probe frequency ω_d is close to one of the resonator mode frequencies ω_r , we can neglect the off-resonant modes and treat the single relevant mode separately. The evolution equation of its field α in a reference frame rotating at the frequency of the drive signal α_{in} is then¹

$$\frac{d}{dt}\alpha = -i\delta\alpha - \frac{\kappa}{2}\alpha - \sqrt{\kappa_{\text{in}}}\alpha_{\text{in}}, \quad (1.3)$$

where δ is the detuning $\omega_r - \omega_d$ between the resonator and the drive and κ_{in} is the relaxation rate of the resonator into the coupled line, which can be calculated using eq. (B.2b). κ is the total relaxation rate given by the sum of κ_{in} and the non-radiative relaxation rate κ' due to all other dissipation processes.

This equation can be easily solved in the steady state and the reflected signal α_{out} expressed as $\alpha_{\text{in}} + \sqrt{\kappa_{\text{in}}}\alpha$. The reflection coefficient of the resonator $r \equiv \alpha_{\text{out}}/\alpha_{\text{in}}$ is then

$$r = \frac{2i\delta + \kappa' - \kappa_{\text{in}}}{2i\delta + \kappa' + \kappa_{\text{in}}}. \quad (1.4)$$

The dependence of this reflection coefficient on the detuning δ is illustrated in Fig. 1.4(a,b) for several different values of κ' . We can see that if the resonator is overcoupled, that is, $\kappa' \ll \kappa_{\text{in}}$, the non-radiative losses can be neglected and the resonator fully reflects all the incoming power as expected. As κ' increases, r starts to exhibit a dip at $\delta = 0$. The minimum of this dip reaches zero for $\kappa' = \kappa_{\text{in}}$ when the resonator is said to be *critically coupled*. Further increase of κ' reduces the depth of the dip.

¹ This equation can be derived for example as the Heisenberg equation of motion for a driven damped harmonic oscillator within the input-output formalism (Walls & Milburn, 2008), reduced to classical (coherent) states. Obviously, as we are dealing with a classical system at this point, such a quantum-mechanical detour is not strictly necessary. An alternative path to this equation leads from the circuit model of the system, as shown for example in Fig. B.2(a). One can find the response functions of the circuit which link the incoming, outgoing and intra-resonator voltages in frequency space, then expand them around the resonance frequency of the relevant mode and write the corresponding time-domain equations. Finally, one could also start by writing a generic driven damped harmonic oscillator equation of motion $\dot{\alpha} = -i\delta\alpha - \kappa\alpha/2 + c\alpha_{\text{in}}$ and using an Ansatz of the form $\alpha_{\text{out}} = \alpha_{\text{in}} + k\alpha$. For a resonator without non-radiative losses, the coefficients κ , c and k can then be linked using the law of energy conservation.

As non-radiative losses in the resonator are usually undesirable, it is most often designed to be overcoupled. Since in this case the magnitude of the reflection coefficient is independent of detuning, the measurement setup needs to be capable of measuring the phase of the reflected signal in order to observe the resonance as shown in Fig. 1.4(b).

If the resonator is coupled to two external lines, one of them usually serves as the input and the other one as the output line. The evolution of the intra-resonator field is again governed by eq. (1.3) but this time the total relaxation rate is $\kappa = \kappa_{\text{in}} + \kappa_{\text{out}} + \kappa'$. The transmitted field can be expressed as $\alpha_{\text{out}} = \sqrt{\kappa_{\text{out}}}\alpha$ and the resulting steady-state transmission coefficient $t \equiv \alpha_{\text{out}}/\alpha_{\text{in}}$ is

$$t = -\frac{2\sqrt{\kappa_{\text{in}}\kappa_{\text{out}}}}{2i\delta + \kappa_{\text{in}} + \kappa_{\text{out}} + \kappa'}. \quad (1.5)$$

In contrast to a resonator with a single input/output line, the resonance of a resonator probed in transmission can be found by amplitude measurements only. As we can see in Fig. 1.4(c), the absolute value of the transmission coefficient exhibits a Lorentzian peak for any value of κ' . However, if the resonator is undercoupled, that is, $\kappa' \gg \kappa_{\text{in}} + \kappa_{\text{out}}$, the transmission on resonance is reduced. Therefore, it is typically preferable to operate the resonator in the overcoupled regime.

In this case, the resonator shows full transmission on resonance if the couplings to the input and output line are identical. For other ratios between κ_{in} and κ_{out} , the transmission is reduced, as shown in Fig. 1.4(e). The form of eq. (1.5) also implies that as long as $\kappa_{\text{in}} + \kappa_{\text{out}}$ remains constant, the ratio between κ_{in} and κ_{out} only affects the overall scaling of t while, as illustrated in Fig. 1.4(f), the phase of the transmitted signal remains unaffected.

At first glance, it may seem that one should design the resonator with symmetric coupling to both lines in order to maximize the transmission coefficient. However, it is important to note that in most cases t is not the quantity we wish to maximize. To illustrate this, imagine that t is reduced by a factor of 10. We can then simply increase the amplitude of the probe signal by the same factor to keep the amplitude of the measured signal unchanged. The increased input signal amplitude per se typically does not have any adverse effect on the system. The intra-resonator field α is, on the other hand, a quantity whose increase can bring about undesirable non-linear effects. If we wish to maximize the amplitude of the measured signal for a fixed α , we need to consider the ratio $\alpha_{\text{out}}/\alpha = \sqrt{\kappa_{\text{out}}}$ rather than $\alpha_{\text{out}}/\alpha_{\text{in}}$. If the total radiative relaxation rate of the resonator $\kappa_{\text{in}} + \kappa_{\text{out}}$ is given, the output signal amplitude is maximized for a fixed intra-resonator field simply if $\kappa_{\text{out}} \gg \kappa_{\text{in}}$. Therefore, unless there is a specific reason to keep not only α but also α_{in} low, a strongly asymmetric configuration with a weakly coupled input and a strongly coupled output is preferable.

We should note that this rule needs to be applied with caution. The transmission coefficient decreases with increasing asymmetry between the couplings. If it becomes too low, other parasitic transmission channels between the input and the output line, such as through free space around the chip, can become important and start introducing unwanted interference effects in the measured signal.

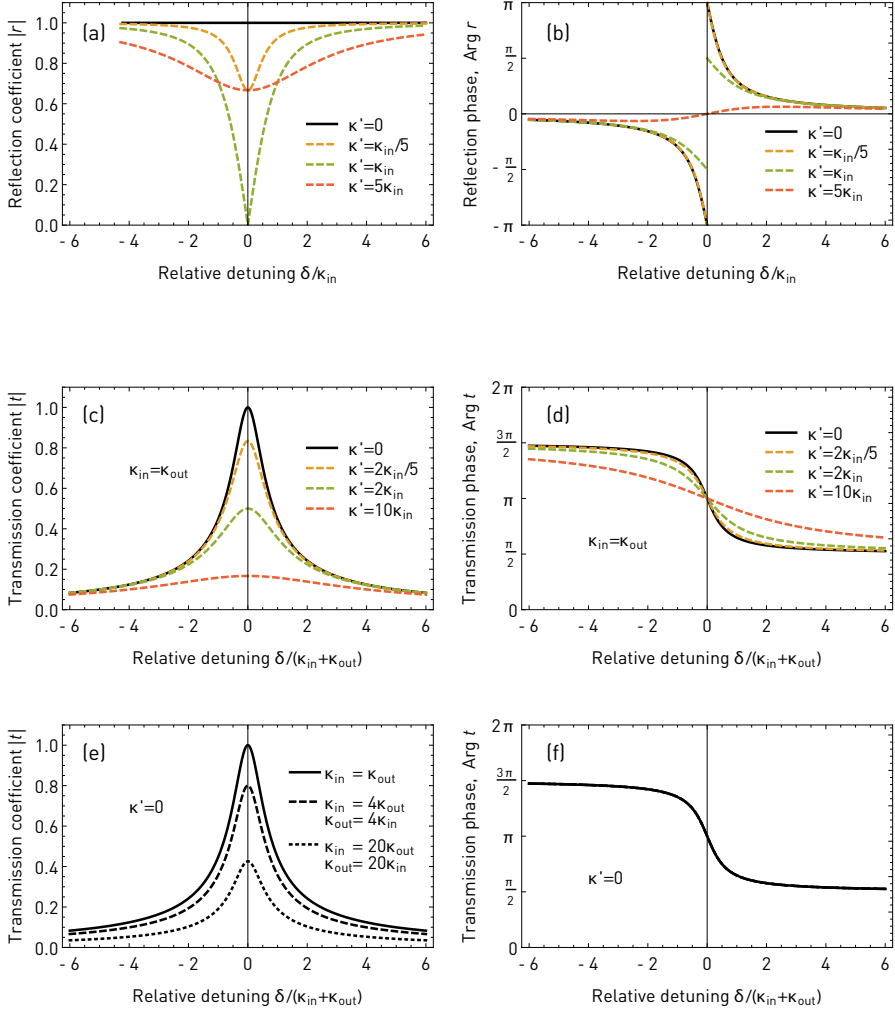


Figure 1.4: (a) Absolute value and (b) phase of the reflection coefficient of a transmission-line resonator coupled to a single external line as a function of detuning between the probe signal and the resonance frequency. The spectrum is plotted for several different values of the non-radiative relaxation rate κ' . The solid black line corresponds to the overcoupled resonator where κ' can be neglected because $\kappa' \ll \kappa_{in}$. (c,d) Plots analogous to (a,b) for a resonator connected to two external lines with equal couplings $\kappa_{in} = \kappa_{out}$. (e,f) The transmission coefficient spectrum for $\kappa' = 0$ and different ratios between κ_{in} and κ_{out} .

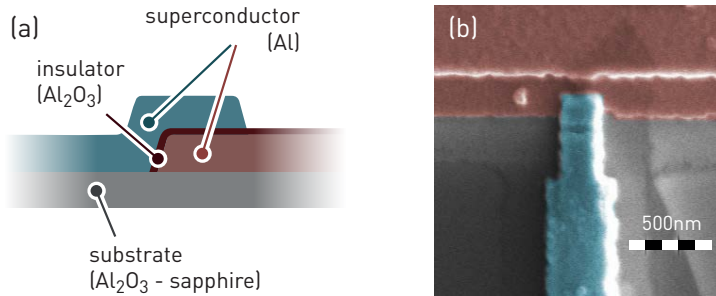


Figure 1.5: (a) Schematic picture of a longitudinal cross-section through a typical S-I-S Josephson junction used in our devices. (b) False-color scanning electron microscope image of a Josephson junction (courtesy of Arkady Fedorov). The two superconducting regions seen from the top are shown in red and blue, the substrate in grey.

1.3 Josephson junction

Even though transmission-line resonators are useful building blocks in circuit QED, they are not by themselves enough to make circuits interesting as quantum systems. A circuit consisting of only linear components, driven by classical microwave sources, will always be described by a coherent state and as such will behave purely classically under the linear measurement process used in circuit QED experiments.

To undergo non-trivial quantum evolution, the system needs to include non-linear elements. One such non-linear component which can be realized in superconducting circuit is the so-called *Josephson junction* (Josephson, 1974; Tinkham, 1996). This is a structure in which two superconducting regions are separated by a “weak link” – for example an insulating barrier thin enough to allow quantum tunneling of Cooper pairs from one side to another. In our circuit QED devices, this is realized as shown in Fig. 1.5. Two layers of metal – in our case aluminium – are deposited on the substrate with a small overlap area. The bottom layer is controllably oxidized after deposition to form insulating oxide on the surface which then serves as the insulating barrier between the layers.

Small Josephson junctions can be modeled as lumped elements whose behavior in a circuit is described by the so-called *Josephson relations* (Tinkham, 1996). The charge carriers in the superconductor – the Cooper pairs – form a condensate which is described by a single position-dependent wavefunction. The current I through the junction is related to the difference δ between the phases of the wavefunction in the two superconducting regions:

$$I = I_c \sin \delta, \quad (1.6a)$$

where I_c is the *critical current* – a constant characterizing the junction. The phase difference changes in time at a rate proportional to the potential difference V between

the two superconductors:

$$\frac{d}{dt}\delta = \frac{2eV}{\hbar}, \quad (1.6b)$$

where e is the electron charge.

If the current flowing through the junction is small in comparison with the critical current, the first relation can be linearized in δ . Then, in combination with the second one, it yields $dI/dt = 2eI_cV/\hbar$. Therefore, in the linear regime, the Josephson junction can be approximated by an inductor with inductance

$$L_J = \frac{\hbar}{2eI_c}.$$

In many experimental settings, it is highly desirable to be able to tune the value of a junction's critical current I_c . While this is not directly possible with a single junction as described so far, one can construct an element which effectively behaves as a tunable Josephson junction – the so-called *superconducting quantum interference device* (commonly known as a SQUID).

It consists of a pair of junctions connected in parallel, as illustrated in Fig. 1.6(b). External magnetic flux Φ is then applied through the loop formed by the two junctions. Let us assume that the phase difference between the connection points of the two arms of the loop is equal to δ . To see how the phase drops δ_1 and δ_2 across the two junctions depend on δ and Φ , let us split the loop into four segments, indicated in Fig. 1.6(b) as C_1 , C_2 , C_3 and C_4 . The phase drop across the SQUID loop can then be written as

$$\delta = \delta_1 + \int_{C_1+C_3} \nabla\varphi \cdot d\mathbf{r} = \delta_2 + \int_{C_2+C_4} \nabla\varphi \cdot d\mathbf{r}.$$

In a superconductor, the gradient of the wavefunction's phase can be related to the current density \mathbf{j} and the magnetic vector potential \mathbf{A} by the *Ginzburg-Landau equation* (Tinkham, 1996) $\nabla\varphi - 2e\mathbf{A}/\hbar = m\mathbf{j}/2\hbar e\rho$, where e is the elementary charge, m the mass of a Cooper pair and ρ the density of Cooper pairs in the superconductor. In most realistic circuit QED scenarios, the typical current densities and the relevant length scales are so small that the right-hand side of the equation can be safely approximated by zero. This means that the line integrals of $\nabla\varphi$ can be expressed in terms of line integrals of \mathbf{A} .

In choosing the vector potential \mathbf{A} corresponding to a given magnetic field \mathbf{B} , we have some amount of freedom, described by the *gauge symmetry* of electromagnetism. Line integrals of \mathbf{A} then generally depend on the choice of gauge, unless the curve over which they are performed is closed. We can therefore, without loss of generality, choose a gauge in which $\int_{C_1+C_3} \mathbf{A} \cdot d\mathbf{r} + \int_{C_2+C_4} \mathbf{A} \cdot d\mathbf{r} = \Delta$ where Δ is a given constant. Since the junctions are small, we can neglect the gaps which they create between C_1, C_3 and C_2, C_4 . Then the combined curve $C_1 + C_3 - C_4 - C_2$ is closed and the corresponding loop integral of \mathbf{A} is equal to the flux Φ threading the loop. This, together with the gauge condition we chose, implies that $\int_{C_1+C_3} \mathbf{A} \cdot d\mathbf{r} = (\Delta + \Phi)/2$ and $\int_{C_2+C_4} \mathbf{A} \cdot d\mathbf{r} = (\Delta - \Phi)/2$. Hence, we get the following relation between the phase drops and the magnetic flux:

$$\delta = \delta_1 + \frac{e}{\hbar}(\Delta + \Phi) = \delta_2 + \frac{e}{\hbar}(\Delta - \Phi).$$

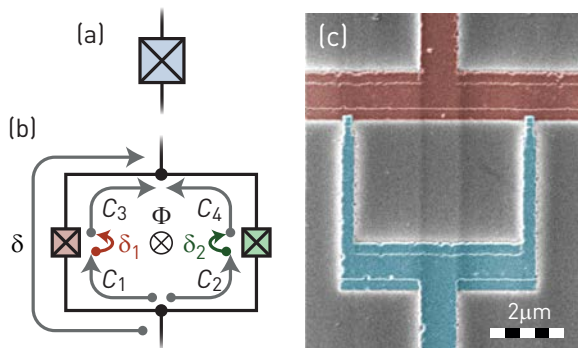


Figure 1.6: (a) The commonly used circuit diagram symbol for a Josephson junction. (b) Diagram of a SQUID loop threaded by a magnetic flux Φ . The loop is decomposed into four segments C_1 , C_2 , C_3 and C_4 . (c) False-color scanning electron microscope image of a SQUID loop (courtesy of Arkady Fedorov).

According to eq. (1.6a), the total current I flowing through the SQUID is given by $I_{c1} \sin \delta_1 + I_{c2} \sin \delta_2$, where I_{c1} and I_{c2} are the critical currents of the two junctions. After expressing δ_1 and δ_2 in terms of δ , Δ and Φ , we make use of the gauge degree of freedom and choose Δ such that $\tan e\Delta/\hbar = \frac{I_2+I_1}{I_2-I_1} \tan e\Phi/\hbar$. This particular choice makes I proportional to $\sin \delta$, following the form of eq. (1.6a). The pre-factor I_c of the $\sin \delta$ term can then be calculated using trigonometric identities:

$$I_c = \sqrt{(I_{c1} + I_{c2})^2 \cos^2 \frac{\pi\Phi}{\Phi_0} + (I_{c1} - I_{c2})^2 \sin^2 \frac{\pi\Phi}{\Phi_0}}, \quad (1.7)$$

where $\Phi_0 \equiv \pi\hbar/e$ is the magnetic flux quantum.

The SQUID loop is indeed equivalent to a single Josephson junction whose critical current I_c can be tuned by the applied magnetic flux Φ . If the flux is equal to an integer multiple of the flux quantum Φ_0 , the critical current is maximal at $I_c = I_{c1} + I_{c2}$. For a half-integer multiple of Φ_0 , it reaches the minimal value $I_c = |I_{c1} - I_{c2}|$.

A special case, which reasonably approximates many real devices, is that of a symmetric SQUID loop with $I_{c2} = I_{c1}$. Then eq. (1.7) reduces to the simple form

$$I_c = 2I_{c1} \left| \cos \frac{e\Phi}{\hbar} \right|. \quad (1.8)$$

1.4 Transmon qubit

Josephson junctions can be used to build a variety of different non-linear devices. Many of them, motivated by quantum computing applications, are used as quantum bits. In this context, the non-linear circuit is operated in such a way that only two

of its many eigenstates are relevant. These states are typically the two lowest-lying energy levels and are commonly referred to as *computational states*. Transitions out of the two-dimensional computational subspace are to first order neglected.

Superconducting qubits have been commonly classified into three broad families, as discussed for example by Clarke & Wilhelm (2008): *flux qubits*, *phase qubits* and *charge qubits*. Roughly speaking, the names refer to the degree of freedom in terms of which the qubit can be most naturally described. In recent years, other types of qubits have emerged which are not easily assigned to one of the three categories – for example the *fluxonium qubit* (Manucharyan *et al.*, 2009) or the $0-\pi$ *qubit* (Brooks *et al.*, 2013).

One of the most widely used types of superconducting qubits is currently the so-called *transmon qubit* – a member of the charge qubit family, proposed by Koch *et al.* (2007) and presently employed by many research groups around the world, including ours. It offers improved resilience against charge noise in comparison with typical charge qubits and, thanks to ongoing development in fabrication techniques (Oh *et al.*, 2006; Quintana *et al.*, 2014) and improving understanding of the various decoherence mechanisms (O’Connell *et al.*, 2008; Gao *et al.*, 2008a,b), state-of-the-art devices now often reach long relaxation times on the order of tens of microseconds (Barends *et al.*, 2013; Chang *et al.*, 2013).

A typical charge qubit, implemented as the so-called *Cooper-pair box*, was first shown to exhibit quantum-mechanical behavior by Nakamura *et al.* (1999). It consists of two superconducting regions connected by a Josephson junction which allows tunneling of Cooper pairs between the two conducting islands. The equivalent circuit diagram is shown in Fig. 1.7(a). Classically, the state of the system is fully described by the number n of excess Cooper pairs on one of the islands and the phase difference δ between the two superconductors. The energy of the system consists of the electrostatic component $E_{\text{el}} = (2en)^2/2C$, where C is the mutual capacitance between the two electrodes, and the potential energy associated with the Josephson junction. The energy of the junction can be calculated as the integral $\int IV dt$ which, after substitution for I and V from eq. (1.6), yields $E_{\text{jct}} = -E_J \cos \delta$, where $E_J = \hbar I_C/2e$ is the *Josephson energy* of the junction.

The Cooper pair box will typically experience external electric fields which may be applied intentionally or may be present due to nearby charge inhomogeneities. The added field contributes a term linear in n to the electrostatic energy, which then becomes, up to an irrelevant constant shift, $E_{\text{el}} = 4E_C(n - n_g)^2$. Here $E_C \equiv e^2/2C$ is the so-called *charging energy* of the system and n_g is an offset proportional to the external field.

Before proceeding to quantize the charge qubit, we should point out that its representation as the simple circuit shown in Fig. 1.7(a) is somewhat simplified. In real-life applications, the charge qubit shares the space on the chip with other superconducting elements which have non-zero mutual capacitances to the qubit islands. A proper model of a realistic charge qubit may rather look like the circuit shown in Fig. 1.7(b). It contains a ground plane and a control line, both of which are capacitively coupled to the qubit. However, despite the presence of the additional elements, the electrostatic energy of the system remains a quadratic function of n and can still be written in the

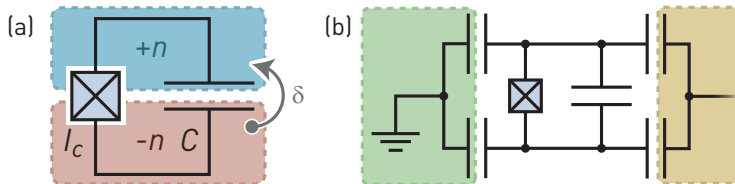


Figure 1.7: (a) Circuit diagram of a simple charge qubit consisting of a capacitance C and a Josephson junction with a critical current I_c , separating the two islands of the qubit which are indicated by the dashed boxes. The charge imbalance given by the number n of excess Cooper pairs and the phase difference δ between the two islands characterize the state of the charge qubit. (b) More realistic diagram of a charge qubit, including the ground plane (in green) and a control line (in yellow), capacitively coupled to the qubit.

form $E_C(n - n_g)^2$, where the charging energy is now a function of all the capacitances in the circuit and n_g is a linear function of the voltage applied to the control line. A detailed derivation of this result can be found in sec. A.1.

The Hamiltonian of the system is given by the sum of E_{el} and E_{jct} , that is,

$$H = 4E_C(n - n_g)^2 - E_J \cos \delta. \quad (1.9)$$

The two variables n and δ which we chose to parametrize the state of the system are, up to scaling by a constant factor $\hbar^{1/2}$, canonically conjugate variables. This can be seen from the fact that the Hamilton equations of motion for n and δ take the canonical form $dn/dt = -\hbar^{-1}\partial H/\partial\delta$ and $d\delta/dt = \hbar^{-1}\partial H/\partial n$.

To quantize the system, we therefore simply replace the variables n , δ by operators \hat{n} , $\hat{\delta}$ and impose the canonical commutation relation

$$[\hat{\delta}, \hat{n}] = i.$$

The quantum state $|\psi\rangle$ of the Cooper-pair box can be described by a wavefunction in the δ -representation, that is, $\psi(\delta) \equiv \langle \delta | \psi \rangle$, where $|\delta\rangle$ is an eigenstate of the operator $\hat{\delta}$, corresponding to the eigenvalue δ . In this representation, the operator \hat{n} is given by $-i d/d\delta$ and the time-independent Schrödinger equation takes the form

$$\left(4E_C (d/d\delta - n_g)^2 - E_J \cos \delta \right) \psi(\delta) = E \psi(\delta).$$

The variable δ is cyclic – states with phase drops δ and $\delta + 2\pi$ are identical. The wavefunction therefore needs to be 2π -periodic. If we introduce substitutions $z \equiv \delta/2$ and $y(z) \equiv e^{-in_g\delta}\psi(\delta)$, the Schrödinger equation becomes

$$\left(\frac{d^2}{dz^2} - \frac{E_J}{E_C} \cos(2z) - \frac{E}{E_C} \right) y(z) = 0. \quad (1.10)$$

This is the canonical form of *Mathieu's differential equation* (Abramowitz & Stegun, 1972) $y'' + (a - 2q \cos 2z)y = 0$ with coefficients $a = -E/E_C$ and $q = E_J/2E_C$. Its solutions can be found in terms of the *Mathieu functions* when a is one of countably many *characteristic values* corresponding to given n_g and q .

For numerical calculations, it may be more convenient to solve the time-independent Schrödinger equation in the n -representation. Here the state $|\psi\rangle$ is expressed in the eigenbasis of \hat{n} , consisting of eigenvectors $|n\rangle$, corresponding to the eigenvalues $n \in \mathbb{Z}$. The operator $\hat{\delta}$, being canonically conjugate with \hat{n} , is the generator of translations in n , that is, $\exp(i\hat{\delta})|n\rangle = |n+1\rangle$. This implies that $\cos \hat{\delta}|n\rangle = (|n+1\rangle + |n-1\rangle)/2$. Hence, the matrix form of the Hamiltonian in the eigenbasis of \hat{n} is

$$\mathbf{H} = \begin{pmatrix} \dots & n = -1 & n = 0 & n = 1 & n = 2 & \dots \\ \ddots & \ddots & \ddots & \ddots & \ddots & \ddots \\ \ddots & 4E_C(n_g + 1)^2 & -E_J/2 & 0 & 0 & \ddots \\ \ddots & -E_J/2 & 4E_C n_g^2 & -E_J/2 & 0 & \ddots \\ \ddots & 0 & -E_J/2 & 4E_C(n_g - 1)^2 & -E_J/2 & \ddots \\ \ddots & 0 & 0 & -E_J/2 & 4E_C(n_g - 2)^2 & \ddots \\ \ddots & \ddots & \ddots & \ddots & \ddots & \ddots \end{pmatrix} \begin{matrix} \vdots \\ n = -1 \\ n = 0 \\ n = 1 \\ n = 2 \\ \vdots \end{matrix}.$$

After imposing a cut-off $|n| \leq n_{\max}$ and thus reducing the dimensions of the matrix to $(2n_{\max} + 1) \times (2n_{\max} + 1)$, it can be easily diagonalized using one of the common linear algebra algorithms.

In the Cooper-pair box variant of the charge qubit, the charging energy and the Josephson energy are comparable and the eigenenergies of the system vary significantly with the offset charge n_g . This is shown for the special case $E_J = E_C$ in Fig. 1.8(a). The offset charge is adjusted by means of a dc electrode near the qubit to a half-integer value. Then the lowest two energy eigenstates are given approximately by the antisymmetric and symmetric equal superposition of two eigenstates of \hat{n} , as illustrated in Fig. 1.8(c). They are also well separated in energy from the higher states and can therefore easily serve as the two computational states of a qubit.

The dependence of the eigenenergies on the offset charge, however, makes the Cooper-pair box susceptible to dephasing due to environmental charge noise. For this reason, it has been largely replaced by a new type of charge qubit – the transmon (Koch *et al.*, 2007) which operates in the regime $E_J \gg E_C$. In this limit, the dependence of the eigenenergies on the offset charge is strongly suppressed, which can be seen in Fig. 1.8(b).

To quantify this statement, we define the *relative dispersion* of a transition between a pair of energy eigenstates as $(E_{\max} - E_{\min})/E_{\text{mean}}$, where E_{\max} and E_{\min} are, respectively, the maximum and minimum energy separation between the two eigenenergies over all values of n_g and E_{mean} is their arithmetic mean. The relative

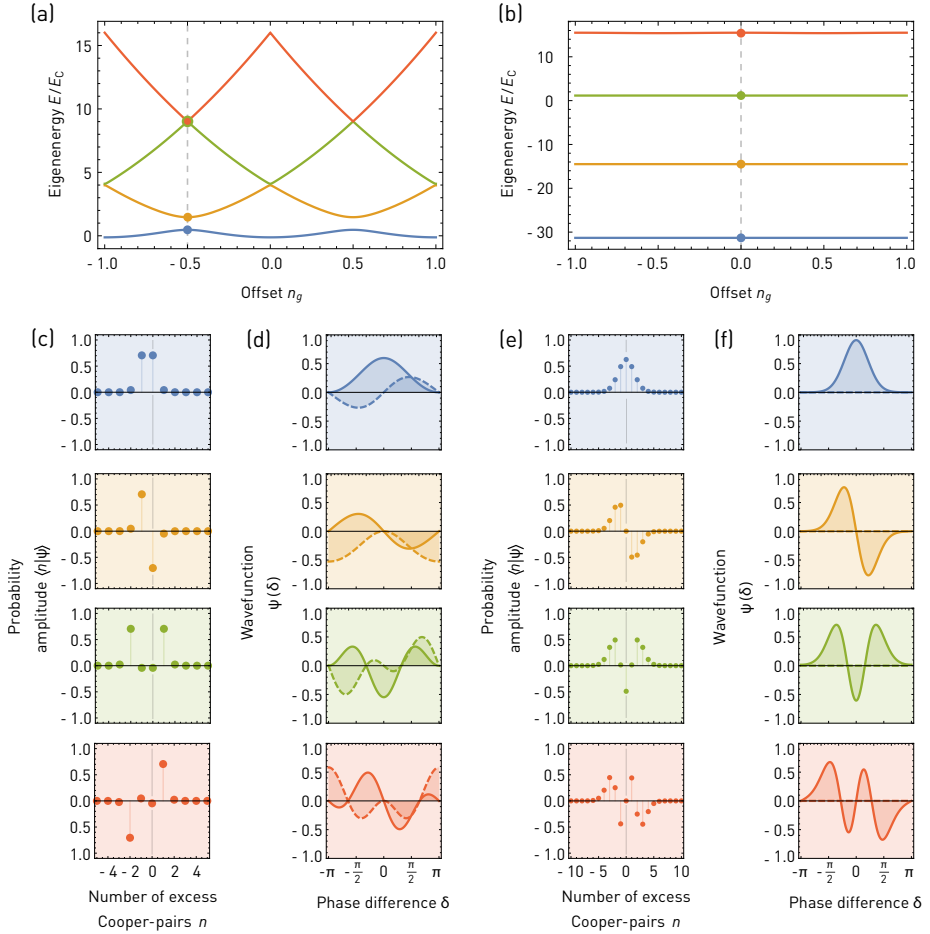


Figure 1.8: (a) First four eigenenergies of the charge qubit in the Cooper-pair-box regime at $E_J/E_C = 1$ as a function the offset charge n_g . (b) Equivalent plot in the transmon regime at $E_J/E_C = 40$. Representation of the four eigenstates at selected values of n_g (indicated in (a,b) by the dashed lines) are shown in the eigenbasis of (c,e) \hat{n} and (d,f) $\hat{\delta}$. The probability amplitudes $\langle n | \psi \rangle$ are purely real. The wavefunctions $\psi(\delta)$ are in general complex and their real and imaginary parts are shown by the solid and the dashed line, respectively.

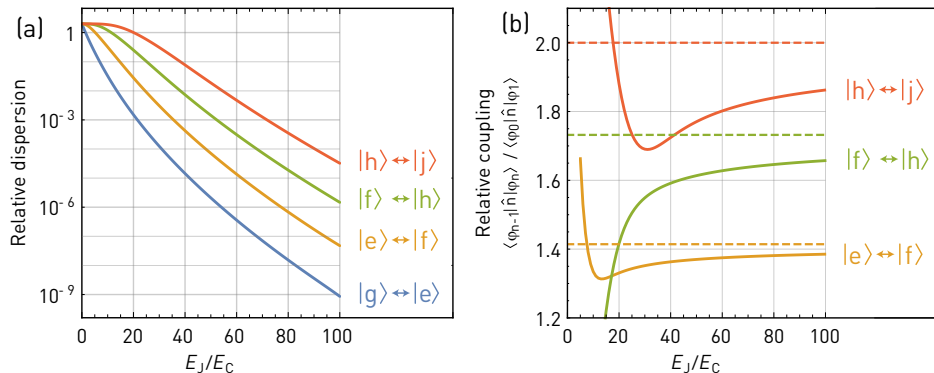


Figure 1.9: (a) Relative charge dispersion of transitions between the lowest five eigenstates of a charge qubit as a function of E_J/E_C . The states are labeled in order of increasing eigenenergy as $|g\rangle, |e\rangle, |f\rangle, |h\rangle, |j\rangle, \dots$ (b) Relative coupling between the consecutive states given by the operator \hat{n} , defined as $\langle \varphi_{n-1} | \hat{n} | \varphi_n \rangle / \langle \varphi_0 | \hat{n} | \varphi_1 \rangle$. The dashed lines show the asymptotic values $\sqrt{2}$, $\sqrt{3}$ and 2, expected for $E_J/E_C \rightarrow \infty$.

dispersion of the transitions between the five lowest-lying energy eigenstates is plotted in Fig. 1.9(a) as a function of the ratio E_J/E_C . The figure demonstrates the result derived by Koch *et al.* (2007): The dispersion decreases exponentially with increasing $\sqrt{E_J/E_C}$ and higher transitions suffer from stronger dispersion than lower ones.

As we can see from a comparison between Fig. 1.8(c,d) and Fig. 1.8(e,f), the eigenstates of a Cooper-pair box are very localized in \hat{n} and spread-out in $\hat{\delta}$. On the other hand, transmon qubit eigenstates have a considerable uncertainty in both \hat{n} and $\hat{\delta}$ and a careful reader may notice a similarity between their wavefunctions and those of a harmonic oscillator.

To understand why this is the case, consider that the Schrödinger equation (1.10) is equivalent to that of a particle in a one-dimensional cosine potential. The depth of the potential well scales with E_J/E_C and we can therefore expect that as this ratio increases, the particle will be more and more localized near the potential minimum at $\delta = 0$. Therefore, in the limit $E_J/E_C \rightarrow \infty$, we can approximate the potential by expanding it to second order in δ around the minimum.

This approximation is equivalent to treating the circuit as a harmonic oscillator – something we are justified to do if the Josephson junction has a large critical current and can be therefore described as a linear inductor. To find the eigenstates and eigenenergies of the system, we expand its Hamiltonian given by eq. (1.9) into a power series in $\hat{\delta}$ and write it as $\hat{H} = \hat{H}_0 + \hat{V}$, where

$$\hat{H}_0 = 4E_C(\hat{n} - n_g)^2 + \frac{1}{2}E_J\hat{\delta}^2 - E_J,$$

$$\hat{V} = -E_J \left(\frac{1}{4!}\hat{\delta}^4 - \frac{1}{6!}\hat{\delta}^6 + \frac{1}{8!}\hat{\delta}^8 - \dots \right).$$

We will treat \hat{V} , which contains all higher than quadratic terms in $\hat{\delta}$, as a perturbation to the quadratic bare Hamiltonian \hat{H}_0 . To diagonalize \hat{H}_0 , we employ the standard ladder operators \hat{c}^\dagger, \hat{c} (Sakurai & Napolitano, 2010) which are in this specific case defined by

$$\hat{n} - n_g = i \left(\frac{E_J}{32E_C} \right)^{1/4} (\hat{c}^\dagger - \hat{c}), \quad (1.11a)$$

$$\hat{\delta} = \left(\frac{2E_C}{E_J} \right)^{1/4} (\hat{c}^\dagger + \hat{c}). \quad (1.11b)$$

It can then be shown that \hat{c} and \hat{c}^\dagger satisfy the canonical commutation relation $[\hat{c}, \hat{c}^\dagger] = 1$ and the bare Hamiltonian takes the form $\hat{H}_0 = \sqrt{8E_J E_C} (\hat{c}^\dagger \hat{c} + 1/2) - E_J$. The transmon qubit is therefore to zeroth order approximated as a harmonic oscillator with a frequency $\omega_q \equiv \sqrt{8E_J E_C}/\hbar$ and its eigenstates are the standard Fock states, created by the ladder operators defined in eq. (1.11).

To evaluate how the transmon deviates from a purely harmonic oscillator, we can use perturbation theory to express the corrections to the eigenenergies and eigenstates, order by order in \hat{V} . For simplicity, here we will restrict ourselves to first order in \hat{V} and we will only retain the $\hat{\delta}^4$ term in the perturbation.

The perturbed eigenstate $|\varphi_n\rangle$, corresponding to the bare Fock state $|n\rangle$, and its eigenenergy E_n are approximated by (Sakurai & Napolitano, 2010)

$$|\varphi_n\rangle = |n\rangle + \sum_{m \neq n} \frac{\langle m | \hat{V} | n \rangle}{\hbar\omega_q(n-m)} |m\rangle,$$

$$E_n = \hbar\omega_q n + \langle n | \hat{V} | n \rangle.$$

Note that to keep the expression for E_n simple, we have dropped the physically irrelevant overall energy shift $\hbar\omega_q/2 - E_J$ from \hat{H}_0 .

The perturbed eigenenergies can be evaluated using the easily verified identity $\langle n | (\hat{c}^\dagger + \hat{c})^4 | n \rangle = 6n^2 + 6n + 3$, resulting in

$$E_n = \hbar\omega_q n - \frac{1}{2} E_C \left(n + \frac{1}{2} \right)^2.$$

As expected, the perturbation makes the spectrum of the transmon anharmonic. This is usually quantified by the *anharmonicity* parameter α , defined as $\alpha \equiv \omega_1 - \omega_0$, where $\omega_n \equiv (E_{n+1} - E_n)/\hbar$ are the transition frequencies between subsequent energy eigenstates. In a perfectly harmonic system, we would have $\alpha = 0$. As our perturbative calculation shows, the anharmonicity of a transmon can be approximated by $\alpha = -E_C/\hbar$ and the transition frequencies as

$$\omega_n = \omega_0 + n\alpha, \text{ with}$$

$$\omega_0 = \left(\sqrt{8E_J E_C} - E_C \right) / \hbar.$$

Conventionally, the energy eigenstates of a transmon are labeled in order of increasing energy as

$$\begin{aligned} |g\rangle &\equiv |\varphi_0\rangle, \\ |e\rangle &\equiv |\varphi_1\rangle, \\ |f\rangle &\equiv |\varphi_2\rangle, \\ |h\rangle &\equiv |\varphi_3\rangle, \\ &\vdots \end{aligned}$$

We will occasionally switch between these two notations. The letter-based one will be used mainly when we refer to specific states, while the indexed labeling $|\varphi_i\rangle$ is more convenient in expressions involving sums or relations which hold in general for all states.

The eigenbasis of the perturbed Hamiltonian differs from the bare Fock state basis. To first order in \hat{V} , each eigenstate $|\varphi_n\rangle$ is given by the corresponding Fock state $|n\rangle$ with a small admixture of the Fock states $|n-4\rangle$, $|n-2\rangle$, $|n+2\rangle$ and $|n+4\rangle$. This means that while the operators $\hat{n} - n_g$ and $\hat{\delta}$ only couple adjacent Fock states, the matrix elements $\langle\varphi_m|(\hat{n} - n_g)|\varphi_n\rangle$ and $\langle\varphi_m|\hat{\delta}|\varphi_n\rangle$ can in general be non-zero whenever $|m-n| = 1, 3, 5, 9$. The matrix elements with $|m-n| = 1$ are to zeroth order given by the corresponding matrix elements in the Fock basis. The ones with $|m-n| = 3, 5$ and $|m-n| = 7, 9$ are suppressed by a factor of the order $\mathcal{O}((E_C/E_J)^{1/2})$ and $\mathcal{O}(E_C/E_J)$, respectively.

If we continued developing the perturbation expansion in \hat{V} further, we would see that $\hat{n} - n_g$ couples in principle any pair of eigenstates $|\varphi_m\rangle$, $|\varphi_n\rangle$ for which $m-n$ is odd, albeit with matrix elements decreasing exponentially with $|m-n|$. In the transmon limit $E_J/E_C \gg 1$, the non-nearest-neighbor couplings approach zero and can be often neglected.

1.5 Jaynes-Cummings coupling

Many circuit QED experiments rely on coupling between a non-linear quantum system such as the transmon qubit and a quantized microwave field. In most cases, the field is confined in a transmission line resonator which increases its interaction with the qubit.

We will now describe the simplest coupled system of this type – one consisting of a single transmon and a single resonator mode. For convenience, we introduce the following short-hand notation for the basis vectors of the combined system:

$$|mn\rangle \equiv |m\rangle \otimes |n\rangle,$$

where $|m\rangle$ for $m \in \{g, e, f, \dots\}$ or $m \in \{\varphi_1, \varphi_2, \dots\}$ are the eigenstates of the transmon and $|n\rangle$ for $n \in \{0, 1, 2, \dots\}$ are the Fock states of the resonator.

The coupling can be modeled using a circuit of the form shown in Fig. 1.7(b) where the node indicated by the yellow dashed box is a node of the resonator, capacitively coupled to the qubit. The electrostatic energy of the circuit is given by eq. (A.1a)

derived in sec. A.1. Hence, the Hamiltonian term describing the effect of the bias voltage \hat{V}_r imposed by the resonator is

$$\hat{H}_{\text{int}} = 2e\beta_r\hat{V}_r\hat{n}. \quad (1.12)$$

Here β_r is a voltage division factor which depends on the geometry of the circuit. It is defined as the ratio $\Delta V/V_r$, where ΔV is the potential difference induced between the two transmon islands when the resonator node is fixed at a potential V_r .

The voltage \hat{V}_r at the resonator node can be expressed in terms of the ladder operators \hat{a}^\dagger, \hat{a} of the resonator:

$$\hat{V}_r = V_0(\hat{a}^\dagger + \hat{a}),$$

where V_0 is the root-mean-square voltage of the vacuum fluctuations. The resulting coupling Hamiltonian is therefore

$$\hat{H}_{\text{int}} = \frac{g}{n_0}(\hat{a}^\dagger + \hat{a})\hat{n}, \quad (1.13)$$

where $n_0 \equiv \langle g|\hat{n}|e \rangle$ and $g \equiv 2en_0\beta_rV_0$. This form is chosen to preserve the common convention denoting the matrix element $\langle g|1|\hat{H}_{\text{int}}|e0 \rangle$ as g .

For simplicity, we will assume that the offset charge n_g is zero, such that the diagonal elements of \hat{n} vanish. This is justified as we have seen that the transmon qubit is insensitive to variations in n_g .

In the eigenbasis of the resonator and the transmon, the full coupling Hamiltonian given by eq. (1.13) has a rather complicated structure. This is illustrated in Fig. 1.10(a). As discussed earlier, the operator \hat{n} couples all pairs of transmon states $|\varphi_m\rangle, |\varphi_n\rangle$ for which $|m-n|$ is odd. However, the non-nearest neighbor couplings with $|m-n| > 1$ are strongly suppressed in the limit $E_J/E_C \gg 1$, which allows us to ignore them. Examples of the transitions which we thus neglect are shown in Fig. 1.10(a) by light-red dashed arrows.

To express this approximation mathematically, we define operators \hat{b} and \hat{b}^\dagger as the nearest-neighbor components of \hat{n}/n_0 :

$$\hat{b} \equiv \frac{1}{n_0} \sum_n |\varphi_n\rangle \langle \varphi_{n+1}| \langle \varphi_n | \hat{n} | \varphi_{n+1} \rangle.$$

Then we approximate \hat{n} by $n_0(\hat{b}^\dagger + \hat{b})$ and replace the coupling Hamiltonian in eq. (1.13) by

$$\hat{H}_{\text{int}} = g(\hat{a}^\dagger + \hat{a})(\hat{b}^\dagger + \hat{b}). \quad (1.14)$$

The operators \hat{b} and \hat{b}^\dagger play the role of ladder operators for the transmon – they map each eigenstate of the transmon onto the next lower or higher eigenstate. In the limit $E_J/E_C \gg 1$, their matrix elements are identical to the standard ladder operators: $\langle \varphi_n | \hat{b} | \varphi_{n+1} \rangle = \sqrt{n+1}$. However, for finite E_J/E_C , they can substantially deviate from the $\sqrt{n+1}$ value, as shown in Fig. 1.9(b).

The terms $\hat{a}\hat{b}$ and $\hat{a}^\dagger\hat{b}^\dagger$ in eq. (1.14) couple states with a large energy difference on the order of $\omega_r + \omega_0$, where ω_r is the resonator frequency and ω_0 is, as before,

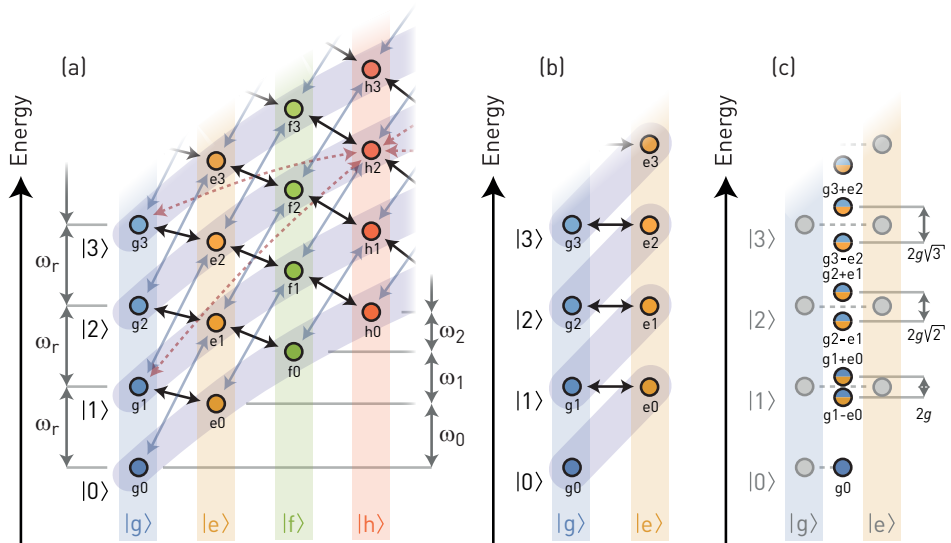


Figure 1.10: (a) Energy diagram of the bare eigenstates of a transmon-resonator system. The colored vertical bands indicate states of the transmon while the blue diagonal bands indicate states of the resonator. Matrix elements of the coupling Hamiltonian in eq. (1.13) are indicated by arrows. The light-red dashed and light-blue solid arrows represent examples of non-nearest-neighbor couplings and counter-rotating terms, respectively, both of which are neglected on the way to the Jaynes-Cummings Hamiltonian in eq. (1.15). The only coupling terms left are those which preserve the number of excitations in the system, here indicated by black solid arrows. (b) Analogous diagram for the Jaynes-Cummings Hamiltonian restricted to two states of the transmon in the resonant case $\omega_0 = \omega_r$. (c) Eigenstates of the resonant Jaynes-Cummings Hamiltonian from (b), forming the well-known Jaynes-Cummings ladder with the \sqrt{n} non-linearity.

the transition frequency between the transmon states $|g\rangle$ and $|e\rangle$. These transitions are represented in Fig. 1.10(a) by the grey arrows. If the coupling strength g is significantly smaller than $\omega_r + \omega_0$, which is typically the case in most circuit QED systems, we can perform the *rotating wave approximation* (Yamamoto & Imamoglu, 1999) and neglect $\hat{a}\hat{b}$ and $\hat{a}^\dagger\hat{b}^\dagger$. The coupling Hamiltonian from eq. (1.14) then reduces to the so-called *Jaynes-Cummings Hamiltonian* (Jaynes & Cummings, 1963; Shore & Knight, 1993)

$$\hat{H}_{\text{int}} = g(\hat{a}^\dagger\hat{b} + \hat{a}\hat{b}^\dagger) \quad (1.15)$$

whose non-zero matrix elements are shown in Fig. 1.10(a) by the black arrows.

Note that this form of \hat{H}_{int} commutes with the operator \hat{N} describing the number

of excitations in the system, defined as

$$\hat{N} \equiv \hat{a}^\dagger \hat{a} + \sum_n n |\varphi_n\rangle \langle \varphi_n|.$$

This is equivalent to the statement that \hat{H}_{int} does not mix different eigenspaces of \hat{N} . We can therefore diagonalize the system with the coupling Hamiltonian \hat{H}_{int} in each of the eigenspaces separately. Since the transmon qubit is a multi-level system, the dimensions of the individual eigenspaces \mathcal{E}_n grow with the number of excitations n . For example, the zero-excitation manifold \mathcal{E}_0 contains only the state $|g0\rangle$, the single-excitation manifold \mathcal{E}_1 consists of $|g1\rangle$ and $|e0\rangle$, \mathcal{E}_2 of $|g2\rangle$, $|e1\rangle$ and $|f0\rangle$, and so on.

The diagonalization can therefore be performed analytically only up to \mathcal{E}_3 . In practice, we can expect to get an exact solution in a reasonably tractable form only in \mathcal{E}_0 and \mathcal{E}_1 . However, one can often find a very good approximate solution.

One case in which this is possible is when the qubit transition frequency ω_0 is nearly resonant with the resonator frequency ω_r and the anharmonicity α of the qubit is large. More specifically, we require that $|\alpha| \gg |\omega_r - \omega_0|$ and $|\alpha| \gg g$. Under these conditions, we can approximate the transmon as a two-level system and neglect all its levels higher than $|e\rangle$. Consequently, all the excitation manifolds become at most two-dimensional, with each \mathcal{E}_n for $n > 0$ containing only states $|gn\rangle$ and $|e, n-1\rangle$, as illustrated in Fig. 1.10(b). The Hamiltonian of the system, restricted to the manifold \mathcal{E}_n becomes

$$\hat{H} = \hbar n \omega_r |gn\rangle \langle gn| + \hbar(n\omega_r + \Delta) |e, n-1\rangle \langle e, n-1| + g\sqrt{n}(|gn\rangle \langle e, n-1| + \text{H.c.}),$$

where $\Delta = \omega_0 - \omega_r$ is the detuning between the qubit and the resonator. This Hamiltonian is easily diagonalized (Blais *et al.*, 2004) as

$$\begin{aligned} \hat{H}/\hbar &= n\omega_r + \Delta/2 + \sum_{\pm} \pm \sqrt{ng^2 + \frac{\Delta^2}{4}} |\Phi_n^\pm\rangle \langle \Phi_n^\pm|, \text{ where} \\ |\Phi_n^+\rangle &= \sin \frac{\Theta_n}{2} |gn\rangle + \cos \frac{\Theta_n}{2} |e, n-1\rangle, \\ |\Phi_n^-\rangle &= \cos \frac{\Theta_n}{2} |gn\rangle - \sin \frac{\Theta_n}{2} |e, n-1\rangle \text{ and} \\ \Theta_n &\equiv \arctan \frac{2g\sqrt{n}}{\Delta}. \end{aligned}$$

The arctan function in the last equation is defined to take values between 0 and π .

In the special case when the resonator and the qubit are resonant with each other, we have $\Delta = 0$ which implies $\Theta_n = \pi/2$ and therefore the eigenstates of the coupled system $|\Phi_n^\pm\rangle$ are the symmetric and antisymmetric equal superpositions of $|gn\rangle$ and $|e, n-1\rangle$. The two corresponding eigenenergies are

$$E_n^\pm = \hbar(n\omega_r \pm g\sqrt{n}).$$

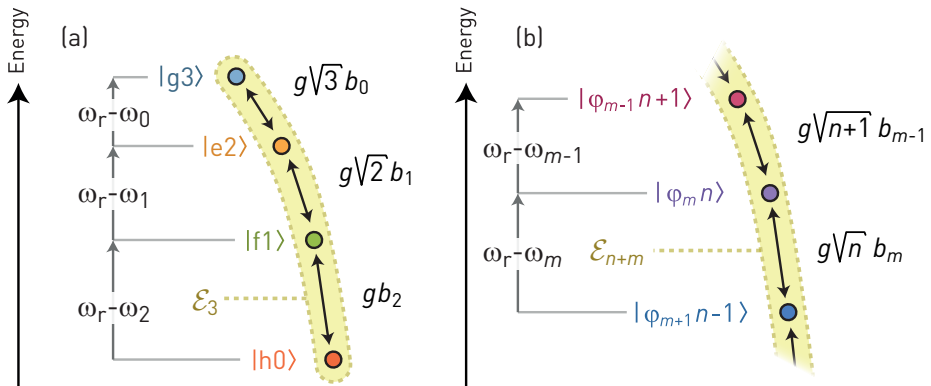


Figure 1.11: (a) Diagram of the three-excitation manifold \mathcal{E}_3 . Indicated are the bare eigenstates of the transmon-resonator system, the transition frequencies between them and the matrix elements of the Jaynes-Cummings coupling Hamiltonian from eq. (1.15). (b) Analogous diagram for the manifold \mathcal{E}_{n+m} , showing the transition frequencies and coupling matrix elements between a state $|\varphi_m n\rangle$ and its neighbors.

The resulting energy spectrum is shown in Fig. 1.10(c). It forms a ladder with rungs arranged in pairs (except for the ground state $|g0\rangle$) where the energy splitting of the pairs increases as \sqrt{n} . This splitting and its \sqrt{n} non-linearity, observed in early circuit QED experiments for example by Wallraff *et al.* (2004) and Fink *et al.* (2008), are a signature of the quantized nature of the resonator field.

1.6 Dispersive approximation

Another instance in which a system with a Jaynes-Cummings interaction can be diagonalized approximately is if the coupling Hamiltonian from eq. (1.15) can be treated as a perturbation of the uncoupled Hamiltonian.

The form of the coupled Hamiltonian is shown graphically in Fig. 1.11. A specific example of the three-excitation manifold \mathcal{E}_3 is illustrated in Fig. 1.11(a). The coupling has a linear structure – the bare eigenstates can be arranged in a sequence of increasing photon number where each state is coupled only to its nearest neighbors. The consecutive states differ by a swap of one excitation between the transmon and the resonator. The corresponding transition frequency is therefore given as the difference between the resonator frequency ω_r and the transmon transition frequency. The matrix elements coupling the consecutive states are expressed as products of the coupling strength g , a \sqrt{n} factor given by the resonator ladder operator \hat{a}^\dagger and a matrix element $b_i \equiv \langle \varphi_i | \hat{b} | \varphi_{i+1} \rangle$ of the transmon ladder operator \hat{b} .

In general, as illustrated in Fig. 1.11(b), a bare state $|\varphi_m n\rangle$ from a manifold \mathcal{E}_{n+m} is coupled to its two neighbors, unless $m = 0$ or $n = 0$. The coupling matrix

elements are $gb_{m-1}\sqrt{n+1}$ and $gb_m\sqrt{n}$, while the corresponding transition frequencies are $\omega_r - \omega_{m-1}$ and $\omega_r - \omega_m$.

If the coupling matrix elements are significantly smaller than the transition frequencies, we can use perturbation theory to approximate the dressed eigenenergy E_{mn} and eigenstate $||\varphi_m n\rangle$ corresponding to the bare state $|\varphi_m n\rangle$. Since we are typically interested in only the few lowest states of the transmon, we will assume that m is on the order of unity and therefore also $b_m \sim 1$. The condition for the validity of the perturbative solution can then be written as

$$g\sqrt{n} \ll |\omega_r - \omega_m|.$$

This means that the approximate diagonalization described here can be performed only for states with photon numbers n significantly below a certain *critical photon number*

The first non-zero correction to the eigenenergy E_{mn} is of second order in \hat{H}_{int} and is given by (Sakurai & Napolitano, 2010)

$$\delta E_{mn} = \frac{ng^2b_m^2}{\omega_r - \omega_m} - \frac{(n+1)g^2b_{m-1}^2}{\omega_r - \omega_{m-1}}.$$

In this so-called *dispersive approximation*, the diagonalized Hamiltonian can be written in the form

$$\hat{H}_{\text{disp}} = \sum_{m,n} \left(\tilde{E}_m + n\hbar(\tilde{\omega}_r + 2\chi_m) \right) ||\varphi_m n\rangle\langle\varphi_m n||. \quad (1.16)$$

Here $\tilde{\omega}_r \equiv \omega_r + g^2/(\omega_r - \omega_0)$ and $\tilde{E}_m \equiv E_m - \hbar g^2 b_{m-1}^2/(\omega_r - \omega_{m-1})$ are, respectively, the resonator frequency and the energy of the transmon state $|\varphi_m\rangle$, renormalized by the coupling to the resonator. The coefficient χ_m , defined as

$$\chi_m \equiv \frac{g^2b_m^2}{2(\omega_r - \omega_m)} - \frac{g^2b_{m-1}^2}{2(\omega_r - \omega_{m-1})} - \frac{g^2}{2(\omega_r - \omega_0)}, \quad (1.17)$$

is called the *dispersive shift*. How can we interpret the diagonalized Hamiltonian?

In the dispersive approximation, the transmon and the resonator can often be treated as decoupled in the following sense: The dressed eigenstates $||\varphi_m n\rangle$ differ from the bare ones $|\varphi_m n\rangle$ only by a small correction and the two subsystems are therefore nearly separable, that is, $||\varphi_m n\rangle \approx |\varphi_m\rangle \otimes |n\rangle$. Consequently, if for example the transmon is fixed to one of its eigenstates $|\varphi_m\rangle$, the resonator evolves as if it were isolated, except for the dispersive shift of its resonance frequency from its bare value ω_r to a dressed frequency $\tilde{\omega}_r + 2\chi_m$ which depends on the state of the transmon. This argument can be of course reversed and if the resonator is kept in one of the Fock states, the transmon can be treated separately, with its eigenenergies shifted by an amount which depends on the number of photons in the resonator.

These two interpretations of the dispersive coupling result from the two different ways in which we can write the dispersive Hamiltonian. We can put it in the form given in eq. (1.17) but we can also group the term $2n\hbar\chi_m$ with the transmon energies

\tilde{E}_m instead of with the resonator frequency $\tilde{\omega}_r$. This form is suggestive of the second interpretations where the transmon state energies change to $\tilde{E}_m + 2n\hbar\chi_m$, depending on the number of photons n .

Note that the definition of the dressed resonator frequency $\tilde{\omega}_r$ and the dispersive shift χ_m is not unique, as we can arbitrarily shift the two quantities by additive constants, as long as $\tilde{\omega}_r + 2\chi_m$ is kept unchanged. The particular definition we used is chosen such that $\chi_0 = 0$. In other words, $\tilde{\omega}$ is exactly the resonance frequency of the resonator when the transmon is in its ground state $|g\rangle$.

As a specific example, let us consider again the limit $E_J/E_C \rightarrow \infty$. The matrix elements b_m can then be approximated by $\sqrt{m+1}$ and the transition frequencies ω_m by $\omega_0 + m\alpha$. The dispersive shifts then become

$$\chi_m = \frac{m\alpha g^2(\Delta + (m-1)\alpha/2)}{\Delta(\Delta + m\alpha)(\Delta + (m-1)\alpha)},$$

where, once again, $\Delta \equiv \omega_0 - \omega_r$ is the detuning between the lowest transmon transition and the resonator. Particularly, for $m = 1$ we get $\chi_1 = \alpha g^2 / \Delta(\Delta + \alpha)$. Hence, if the transmon is excited from its ground state $|g\rangle$ to the first excited state $|e\rangle$, the frequency of the resonator shifts by χ_1 . In many applications, it is desirable for the dispersive shift to be as large as possible. Since the dispersive approximation requires that $g \ll |\Delta|$ and $g \ll |\Delta + \alpha|$, we see that for a transmon qubit, the shift χ_1 is limited by $|\chi_1| \ll |\alpha|$.

Note that this result is qualitatively different from the case of a genuine two-level system. In this instance, we can obtain the dispersive shift by taking the limit $\alpha \rightarrow \infty$, which yields $\chi_1 = g^2 / \Delta$. The dispersive approximation requirement $g \ll |\Delta|$ then sets the limit $|\chi_1| \ll g$, which is typically less restrictive than in the transmon case.

Chapter 2

Measurement setup and techniques

2.1 Cryogenic setup

Most of the experiments done in the Quantum Device lab are performed with a sample at a temperature of a few tens of millikelvin. This is needed to ensure that the materials are superconducting and the thermal equilibrium excitation of the various modes of the system is small.

To reach the necessary low temperatures, the samples are placed into a dilution cryostat (Pobell, 2006). This is a type of refrigeration system relying on the special thermodynamic properties of a mixture of two isotopes of helium: ^4He and ^3He . The phase diagram in Fig. 2.1(a) shows that below a temperature of approximately 0.87 K, the mixture separates into two phases with different concentrations of ^3He . Since the enthalpy of ^3He in the dilute phase is higher than in the concentrated phase, transferring ^3He from the concentrated to the dilute phase consumes energy in the form of heat. This results in cooling of the system, similarly to conventional household fridges where the refrigerant (analogous to ^3He here) is transferred from liquid (concentrated) to gaseous (dilute) phase while taking away heat from the environment. In practice, this process is utilized in the dilution cryostat as shown in a simplified way in Fig. 2.1(b).

The phase separation takes place in the so-called *mixing chamber*. The dilute phase is transported into a *still* where ^3He evaporates from it preferentially due to its higher vapor pressure. The nearly pure ^3He is then pumped out by a turbomolecular pump and returned into the system at high pressure through a flow impedance. Depending on the construction of a cryostat, the returning gas is pre-cooled either by means of a cryogen-free *pulse tube cooler* (Wang *et al.*, 1997) or using a liquid ^4He bath and a *1K pot* in which cooling is achieved by pumping on a volume of liquid ^4He . The high pressure ^3He then condenses, is further cooled down by thermal contact with the liquid dilute phase and returns back to the mixing chamber.

Modern cryogen-free (dry) dilution refrigerators typically contain a series of metal plates thermally connected to different parts of the dilution circuit. The Vericold DR200 cryostat shown in Fig. 2.1(c), in which I performed a majority of the experiments presented here, contains a 70 K-plate and a 4 K-plate which are thermally

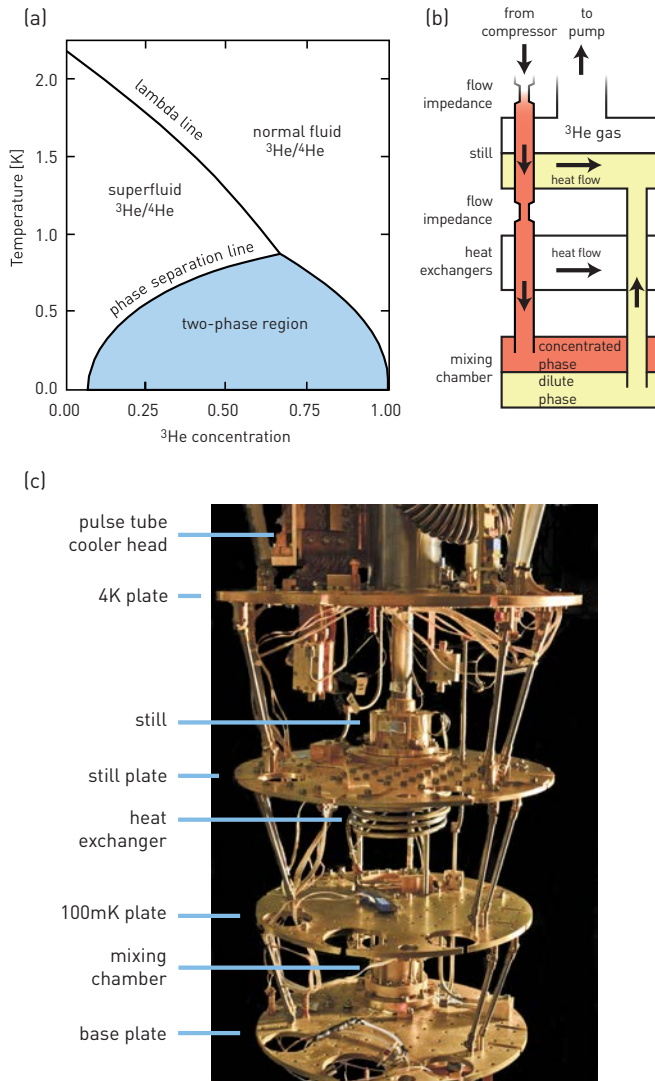


Figure 2.1: (a) Phase diagram of $^4\text{He}/^3\text{He}$ mixture and (b) diagram of a dilution refrigerator. Figures adapted from Pobell (2006). (c) Photograph of the inner parts of a Vericold DR200 cryostat without cryogenic shields microwave cabling. The top-most, 70 K-plate is out of the frame of the picture.

anchored to the two stages of the pulse tube cooler, a still plate, a 100 mK plate and a base plate which is in contact with the mixing chamber and reaches the lowest temperature. The plates provide space for mounting and thermalization of different components of the measurement setup (filters, attenuators, amplifiers).

When in operation, the temperature stages of the cryostat are enclosed in a series of nested thermal shields to prevent excessive heating of the colder stages by thermal radiation. The whole assembly is placed in an evacuated container to eliminate heat transport by convection.

2.2 Sample and its control lines

Sample preparation

The typical superconducting circuit samples studied in our lab are fabricated on 500 μm thick wafers of C-plane sapphire. The ground planes as well as a majority of RF lines in the circuit are then made out of niobium which is deposited on the wafers in a 150 nm layer by sputtering and patterned by optical lithography and reactive ion etching. After this, the wafer is diced into individual chips with sizes of $2 \times 7 \mu\text{m}$, $4 \times 7 \mu\text{m}$ or $6 \times 7 \mu\text{m}$.

The Josephson junctions and typically also the capacitor pads of the transmon qubits are fabricated by electron beam lithography followed by shadow evaporation of aluminium. In this process, the aluminium is deposited in two steps which are separated by controlled oxidation of the first aluminium surface. The resulting thin layer of aluminium oxide forms the tunnel barrier of the Josephson junction.

Afterwards, the finished chips are glued and bonded onto a copper printed circuit board (PCB) which breaks out the individual input and output lines of the chip to SMP connectors. The PCB with the chip is placed into a copper sampleholder box designed to shield the sample from stray electromagnetic radiation. The bottom side of the sampleholder underneath the PCB has cutouts for mounting coils which are used to apply magnetic flux bias to the sample. The top side contains openings to connect coaxial cables to the PCB. The whole sampleholder is mounted to the base plate of the cryostat and protected from stray magnetic field by one or two CryoPerm® high permeability shields.

Microwave input lines

The qubits and resonators in most circuit QED experiments are driven by microwave signals delivered through 50Ω coaxial cables installed in the cryostat. Stainless steel cables are used where low thermal conductivity is critical while copper cables offer lower microwave losses. Superconducting niobium-titanium cables combine the advantages of both at a higher cost. In most input lines, low microwave loss is not a priority and therefore stainless steel is used to connect components at different temperatures while copper may be used where both ends of the cable are at the same nominal temperature.

Signals used to drive circuit QED systems need to be heavily attenuated (as shown schematically in Fig. 2.2) to reduce the level of thermal noise in the line to sub-kelvin

levels. For this reason, the attenuators are placed inside the cryostat as attenuating the signal at room temperature would not reduce the noise temperature. The distribution of attenuators at the different temperature stages is chosen to achieve a good compromise between proper thermalization of the microwave field and low heat dissipation. A common configuration of attenuators is 20 dB at the 4 K plate, 20 dB at the 100 mK plate and 20 dB at the base plate.

Even though microwave attenuators can thermalize the electromagnetic field propagating along the cable, they can only do so reliably in their specified operating range of frequencies, typically up to about 20 GHz. This is enough to make sure that the modes at frequencies of the qubits or the resonators are not exceedingly hot. However, it has been recognized (Barends *et al.*, 2011) that stray radiation at much higher frequencies can also be detrimental to coherence properties of superconducting circuits. The proposed explanation of this phenomenon involves radiation in the 100 GHz range creating quasiparticles in the superconducting material which in turn contribute to dephasing in the circuit. To mitigate this effect, Córcoles *et al.* (2011) have successfully used shielding of the sampleholder box by a layer of Eccosorb® – an absorptive epoxy material. In our experiments, we attempt to block high frequency radiation propagating in the input lines by means of in-house made coaxial Eccosorb® filters.

Flux bias lines

Aside from microwave input lines described above, some measurement setups also contain flux lines (see Fig. 2.2). These are connected to lines on the chip which act as magnetic flux sources and are used to apply constant flux bias or low frequency (below 1 GHz) flux pulses to SQUID loops in the circuits. To minimize distortion of the pulses propagating from room temperature signal sources to the sample, flux lines are also built out of coaxial $50\ \Omega$ cables even though the end of the flux line on the chip is typically not $50\ \Omega$ -matched and therefore some amount of distortion is to be expected. Flux lines also contain low-pass filters to eliminate high-frequency noise, usually accompanied by Eccosorb® filters to suppress radiation above the maximum operating frequency of the standard filter and potential standing waves above its cutoff frequency.

Output lines

Like other microwave line in the setup, the output line (see Fig. 2.2) carrying the signal to be measured also consists of coaxial $50\ \Omega$ cables. It contains a low noise cryogenic amplifier based on high electron mobility transistors (HEMTs) (Pospieszalski *et al.*, 1988), placed at the 4 K stage of the cryostat, optionally preceded by a near-quantum-limited *Josephson parametric amplifier* (Yurke & Buks, 2006; Castellanos-Beltran & Lehnert, 2007) at the base plate. The attenuation of the section between the sample and the first amplifier needs to be kept as low as possible to preserve good signal-to-noise ratio. For this reason, output lines typically do not contain attenuators and are made of copper or niobium-titanium cables. To prevent signal and noise from propagating back from the amplifiers towards the sample, the line also contains cryogenic isolators and band-pass filters.

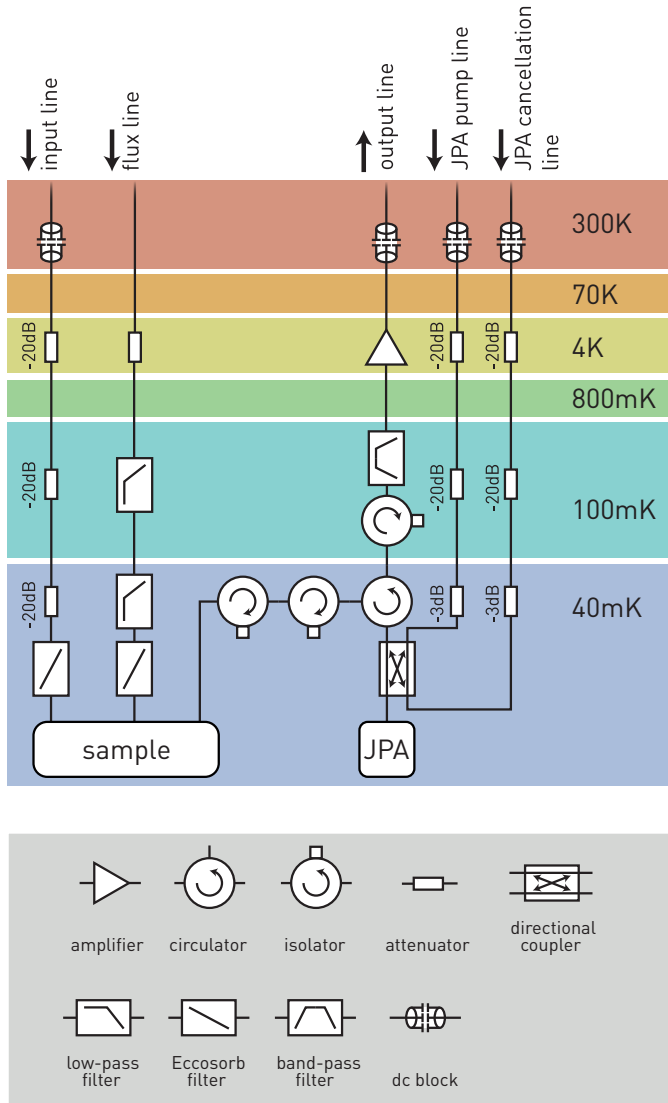


Figure 2.2: Schematic diagram of a typical microwave cryogenic setup used in the Quantum Device lab, shown together with the temperature stages in the cryostat at which the individual components are thermalized. The setup in this example has one microwave input line, one flux bias line and its output line is equipped with a Josephson parametric amplifier (JPA). The JPA requires two additional input line – one for applying a pump tone and one to suppress the reflected pump tone and prevent it from saturating the subsequent amplification chain.

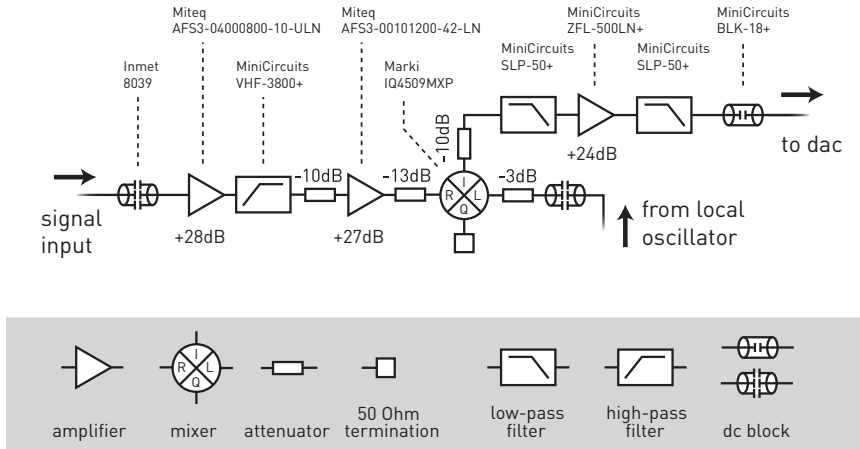


Figure 2.3: Schematic diagram of a typical down-conversion board used in the Quantum Device lab for heterodyne measurement of microwave signals.

2.3 Room-temperature electronics

The room-temperature part of a circuit QED measurement setup consists of several different types of electronic equipment: Microwave sources are used to generate continuous tones for probing the qubit and the resonators, precision dc voltage sources supply current for the flux bias coils and arbitrary waveform generators (AWGs) modulate analog microwave pulses and output digital pulses to trigger other equipment. All these devices are controlled by a LabVIEW-based measurement program called *CleanSweep*.

Down-conversion boards and FPGA

After leaving the cryostat, the output signal coming from the sample is first pre-processed by an in-house made down-conversion board and subsequently digitized and further processed by a *field-programmable gate array* (FPGA) programmed with firmware developed in our lab (Bozyigit, 2008; Salathé, 2011; Lang, 2014).

The down-conversion board consists of a pre-amplification chain containing two RF low-noise amplifiers, a microwave-frequency mixer which converts the signal to an intermediate frequency (IF) of 25 MHz and an IF amplifier. The gain of the individual stages needs to be limited with added attenuators to prevent saturating any of the amplifiers or the mixer. A typical configuration of a down-conversion board (Businger, 2015) is shown in Fig. 2.3.

The most common model of the data-acquisition FPGA currently in use in our lab is the *Virtex-4* from *Xilinx*. It is equipped with a fast analog-to-digital converter

(ADC) capable of sampling the incoming signal at a rate of 100 MS/s. The sampled time series of voltages V_j can be described as

$$V_j = A_j \cos(\omega_{\text{IF}} t_j + \phi_j),$$

where $t_j = j\Delta t$ with $\Delta t = 10$ ns are the sampling points and A_j and ϕ_j are the slowly varying amplitude and phase of the IF signal at a frequency of $\omega_{\text{IF}}/2\pi = 25$ MHz. To down-convert the IF signal to dc, the sampled voltages are then digitally multiplied by the complex 25 MHz wave $\exp(-i\omega_{\text{IF}} t_j)$. The resulting series is given by

$$\bar{V}_j = \frac{1}{2} A_j (\exp(i\phi_j) + \exp(-i\phi_j) \exp(-2i\omega_{\text{IF}} t_j)).$$

By convolving it with a suitable low-pass finite-impulse-response (FIR) filter with kernel f , the fast-oscillating component proportional to $\exp(-2i\omega_{\text{IF}} t_j)$ can be eliminated, leaving

$$v \equiv \bar{V} * f = \frac{1}{2} (I + iQ) * f,$$

where I_j and Q_j are the two quadratures $A_j \cos \phi_j$ and $A_j \sin \phi_j$ of the original signal. The two quadratures encoded thus in the complex time series v_j can be further processed by applying basic arithmetic operations to them (complex conjugation and multiplication of signals from different input channels of the ADC together). The results can then be stored in various ways by different FPGA applications. For example, they can be directly averaged and displayed as a function of time, their single-shot values can be stored in the form of a histogram or they can be correlated with another time series and only subsequently averaged.

In this way, for example the averaged voltage quadratures are accessible simply as $\langle v \rangle$, the power as $\langle v^* v \rangle$ or the power spectral density as the Fourier transform of the autocorrelation function $\langle \sum_{\tau} v_{\tau+t} v_{\tau}^* / N \rangle$.

Up-conversion boards

Microwave pulses used to manipulate the state of qubits and resonators can be created in the simplest case by gating microwave generators. However, this way only allows generation of pulses with a square envelope. To prepare pulses with arbitrary envelopes, we use a different method employing microwave mixers.

A mixer is an RF device which can be used to convert signals between different frequencies. The type used in our setups is a so-called *IQ mixer*. It has four ports acting as inputs or outputs depending on the application. For the *up-conversion* process where a low-frequency (typically around 100 MHz) signal is converted to microwave frequencies, the I (in-phase), Q (quadrature) and LO (local oscillator) ports of the mixer act as inputs and the RF (radio-frequency) port as an output. An ideal IQ mixer performs multiplication of the voltages at the input ports and adds the resulting signals together in the following way:

$$V_{\text{RF}} = A(V_{\text{I}}V_{\text{LO}} + V_{\text{Q}}\tilde{V}_{\text{LO}}),$$

where \tilde{V}_{LO} is the LO input signal phase-delayed by $\pi/2$.

The I and Q input signals are generated by two channels of the AWG and are given by

$$\begin{aligned} V_{\text{I}}(t) &= V(t) \cos(\omega_{\text{IF}}t + \phi(t)) \\ V_{\text{Q}}(t) &= V(t) \sin(\omega_{\text{IF}}t + \phi(t)), \end{aligned}$$

where ω_{IF} is the intermediate frequency, usually set to $\omega_{\text{IF}}/2\pi = 100$ MHz, and $V(t)$ and $\phi(t)$ are the slowly varying amplitude and phase of the signal. If the LO signal is a continuous tone $V_{\text{LO}} = V_0 \cos(\omega_{\text{LO}}t)$, the RF output of the mixer is

$$V_{\text{RF}} = AV_0V(t) \cos((\omega_{\text{LO}} + \omega_{\text{IF}})t + \phi(t)).$$

Hence, the output of the mixer is a signal at a frequency $\omega_{\text{LO}} + \omega_{\text{IF}}$ and with an amplitude and phase envelope inherited from the IF input. By choosing the opposite phase shift between the I and Q inputs, one can also generate the up-converted signal at a frequency $\omega_{\text{LO}} - \omega_{\text{IF}}$.

In practice, a real mixer will exhibit certain imperfections. To name the most important of these: the I and Q inputs of the mixer are not perfectly balanced in amplitude and the LO signal is not shifted exactly by $\pi/2$ and is not completely isolated from the RF output. These imperfections lead to the presence of unwanted signals at frequencies of ω_{LO} (so-called *LO leakage*) and $\omega_{\text{LO}} - \omega_{\text{IF}}$ (so-called *sideband leakage*) and one needs to account for them to achieve good up-conversion performance. This is usually done by introducing free scaling factors, phase shifts and dc offsets to the I and Q signals output by the AWG and adjusting these parameters to minimize the leakage signals. A more detailed account of the mixer calibration procedure is given for example by Abadal (2014) or Berger (2015).

2.4 Characterization measurements

When a new sample is installed in the measurement setup, its basic parameters need to be characterized and properties of the setup calibrated. This is done using a set of rather standard measurements (for a detailed overview in the case of a three-qubit sample, see Baur (2012)). The most basic of these rely on probing of the sample with continuous microwave tones and observing the response.

Continuous-tone measurements

For a simple circuit QED sample containing a qubit coupled to a resonator, the first characterization measurement to be done is usually resonator spectroscopy. The resonator is probed at its input port and the transmitted or reflected signal is measured. When measuring in transmission, it is enough to record the output signal amplitude $|I + iQ|$. As derived in eq. (1.5), its frequency-dependence is given by the Lorentzian function

$$|I + iQ| \propto \frac{1}{\sqrt{1 + \left(\frac{2(f_0 - f)}{\delta f}\right)^2}},$$

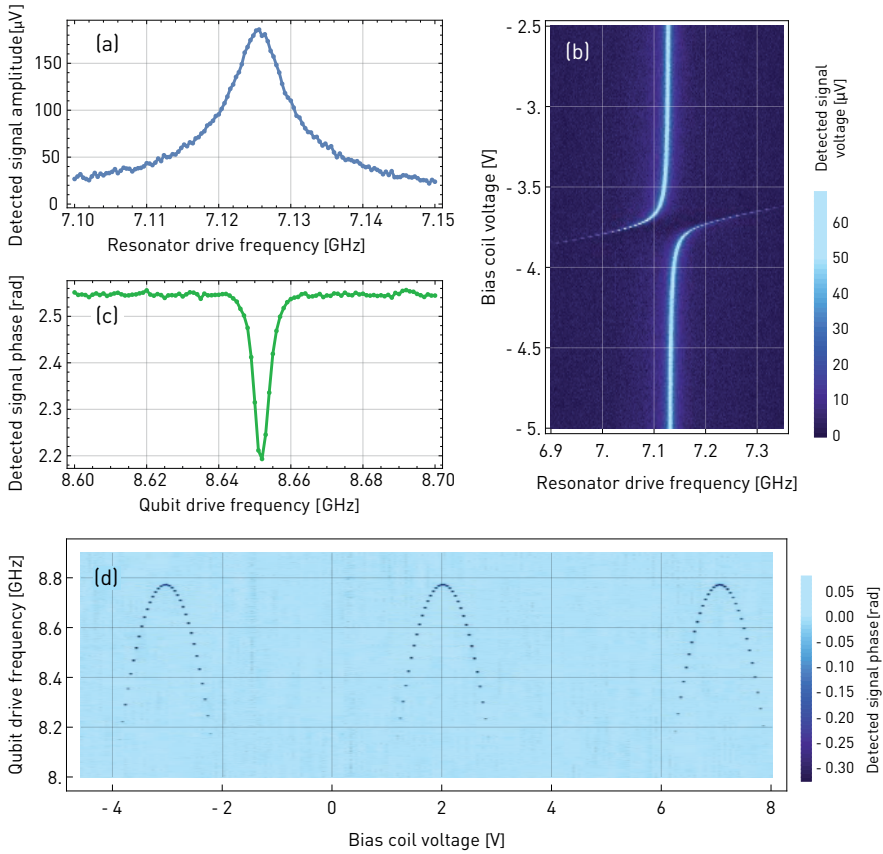


Figure 2.4: Examples of continuous-tone measurements for basic characterization of a sample. (a) Resonator spectroscopy in transmission. (b) Resonator spectrum as a function of voltage applied to a flux bias coil, showing an avoided crossing with a qubit. (c) Qubit two-tone spectroscopy. (d) Qubit spectrum as a function of voltage applied to a flux bias coil. Periodic modulation of qubit frequency is visible.

where f_0 is the resonance frequency of the resonator and δf its full-width-half-maximum (FWHM) linewidth. These two parameters can be extracted using a least-square fit. An example of data obtained in such a measurement is shown in Fig. 2.4(a). In the case of an overcoupled resonator with a single port probed in reflection, one needs to use a setup capable of recoding also the phase of the output signal. According to eq. (1.4), the two voltage quadratures are given by the complex Lorentzian

$$I + iQ \propto \frac{2i(f_0 - f) - \delta f}{2i(f_0 - f) + \delta f}.$$

The fact that $|I + iQ|$ is frequency-independent shows that measuring only the amplitude of the signal is not sufficient to extract the resonator parameters.

After finding the resonator frequency, one usually proceeds to test the magnetic-field tunability of the sample. In samples with tunable resonators, this means measuring their resonance frequencies as a function of voltages applied to the flux bias coils. Even if the resonator itself is not tunable, a spectroscopy measurement of the resonator while simultaneously tuning the qubit flux bias will show avoided crossings (as seen in an example data set in Fig. 2.4(b)), indicating where the qubit and the resonator frequencies coincide. This allows one to make a rough estimate of the qubit frequency as a function of flux bias which is useful for subsequent qubit spectroscopy measurements.

The qubit transition frequency can be found using a simple two-tone spectroscopy measurement once the resonator frequency is known. A constant probe tone is applied to the resonator at its resonance frequency and its transmission or reflection is measured as a function of frequency of a drive tone applied to the qubit. If the drive tone frequency matches the qubit transition, the excited state of the qubit gets populated and the dispersive coupling between the resonator and the qubit induces a shift of the resonator frequency. This in turn causes a change in the amplitude or phase of the detected signal. A result of a typical measurement of this type is shown in Fig. 2.4(c) where the dip in the signal phase reveals the transition frequency of the qubit. A two-tone spectroscopy measurement can be used to determine not only the qubit's frequency but also other properties such as its decoherence rate or its dispersive coupling to the resonator. The dependence of the measured signal on the drive signal frequency and the parameters of the system is rather complex and its calculation in general requires numerical simulations. It can, however, be treated analytically in certain special cases which are discussed in app. G.

Once the qubit spectroscopy measurement is set up properly, it is then performed for varying voltages applied to the flux bias coils. The qubit transition frequency varies periodically with the number of flux quanta threading the SQUID loop which in turn depends linearly on the coil voltages. A typical result of a spectroscopy measurement with a single coil voltage sweep is shown in Fig. 2.4(d).

In samples with $n > 1$ tunable elements, at least n coils are required for independent tuning of all their frequencies. As each of the coils generally couples to each of the tunable elements to some degree, we need to find the $n \times n$ matrix of coupling elements to have full control over the n frequencies. The coupling could of course be extracted from an n -dimensional sweep of all the coil voltages but this naive approach

is extremely time-consuming. Instead, the coupling matrix can be determined more efficiently as follows.

We choose one coil with which we will perform one-dimensional voltage sweeps. Usually, there is one big coil mounted to the sample-holder which couples relatively strongly to all tunable devices on the chip and it is advisable to choose this one. We then pick one of the tunable elements and measure its frequency as a function of the coil voltage. Typically, the obtained dependence has multiple maxima which occur when the flux through the SQUID loop is an integer number of flux quanta. As the flux is a linear function of the coil voltages, this condition can be expressed as

$$aV + b_1v_1 + b_2v_2 + \dots + c = k\Phi_0, \text{ where } k \in \mathbb{Z}. \quad (2.1)$$

Here V denotes the swept voltage, v_1, v_2, \dots the voltages on the other $n - 1$ coils which are kept constant, a, b_1, b_2, \dots are the unknown coupling constants, c a flux offset and Φ_0 the flux quantum.

From the difference ΔV between voltages corresponding to consecutive frequency maxima, we can extract a as $a = \Phi_0/\Delta V$. Furthermore, we can choose any of the maxima and assume without loss of generality that it corresponds to $k = 0$ ¹. The voltage V_0 at which this maximum occurs allows us to express $b_1v_1 + b_2v_2 + \dots + c$ as $-aV_0$. By repeating the measurement for n different sets of the $n - 1$ voltages v_1, v_2, \dots , we obtain a system of equations

$$b_1v_1^{(j)} + b_2v_2^{(j)} + \dots + c = -aV_0^{(j)},$$

which can be solved for b_1, b_2, \dots, c . For increased accuracy, the measurement may be performed for more than n sets of voltages, yielding an overdetermined system of equations from which the coefficients b_1, b_2, \dots, c can be extracted for example using the least squares method.

Note that while the choice of V_0 among the different frequency maxima is arbitrary for the first voltage sweep, in the subsequent measurements we are forced to pick the unique maximum corresponding to the same number of flux quanta. To make this possible, the sets of voltages $v_1^{(j)}, v_2^{(j)}, \dots$ should be chosen sufficiently close to each other such that the positions of the maxima change by significantly less than ΔV .

With the parameters a, b_1, b_2, \dots, c found, we can write the flux threading the SQUID loop as

$$\Phi = aV + b_1v_1 + b_2v_2 + \dots + c.$$

The same procedure then needs to be repeated for all remaining tunable elements, resulting in a set of $n \times n$ coupling coefficients and n offsets. The relations between the voltages and the fluxes can then be written in the matrix form

$$\Phi = \mathbf{M}\mathbf{V} + \mathbf{u},$$

where Φ and \mathbf{V} are vectors of SQUID fluxes and coil voltages, respectively, and \mathbf{u} is a vector of flux offsets. \mathbf{M} is a matrix containing the coupling elements.

¹The integer parameter k can be arbitrarily shifted by adding a multiple of Φ_0 to the flux offset c .

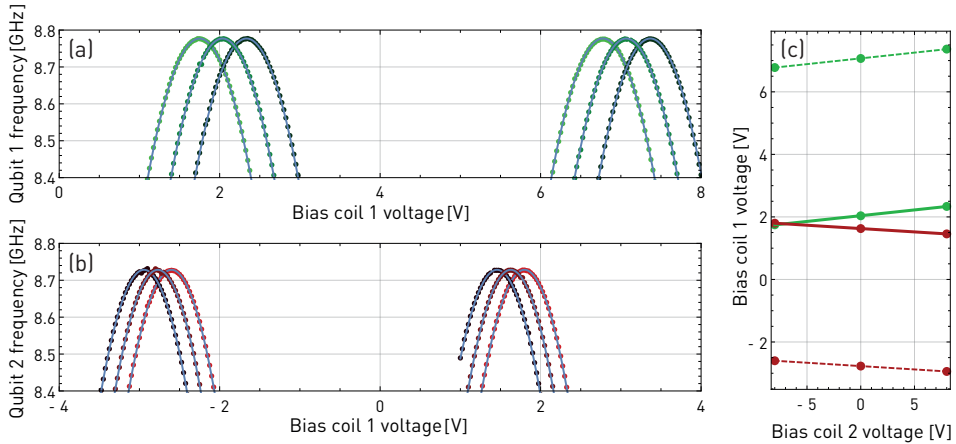


Figure 2.5: (a,b) Resonance frequencies of two qubits as a function of voltage applied to coil 1 for three different voltages applied to coil 2 (+8 V in dark green/red, 0 V in medium green/red and -8 V in light green/red). (c) Positions of the frequency maxima from plots (a,b) as a function of the voltage on coil 2. The lines connect maxima corresponding to the same numbers of flux quanta. The solid lines indicate the maxima chosen to correspond to $k = 0$ in eq. (2.1).

The plots in Fig. 2.5 illustrate the described procedure for a simple case of two qubit and two coils. The qubit frequencies, extracted from a measurement similar to that shown in Fig. 2.4(d), are displayed in Fig. 2.5(a,b) as a function of voltage applied to coil 1 for three discrete values of voltage applied to coil 2. The positions of the frequency maxima are then found and their spacing is used to determine the coupling parameter a of coil 1 as described above. The maxima corresponding to the same number of flux quanta can be easily identified because the additional flux applied by coil 2 shifts them by much less than ΔV . We can then display the maxima in the two-dimensional space of coil voltages as shown in Fig. 2.5(c). In this picture, eq. (2.1) describes a line on which the three points should lie. This condition yields a (over-determined) set of equations for the remaining unknown parameters b_1, c .

As soon as the dependence of Φ on \mathbf{V} is established, it is rather straightforward to determine the dependence of the qubit frequencies $\omega_1, \omega_2, \dots$ on the respective magnetic fluxes Φ_1, Φ_2, \dots which in the transmon limit $E_J \gg E_C$ can be approximated as $\omega_j = \omega_j^{\max} |\cos \pi \Phi_j / \Phi_0|^{1/2}$.

Pulsed measurements for qubit calibration

Unitary operations on qubits are performed by applying microwave pulses to the system. A pulse of sufficiently low amplitude at a frequency close to the energy difference between two neighbouring states $|i\rangle$ and $|j\rangle$ of the transmon will only induce transi-

tions between these two states. In a reference frame rotating at the pulse frequency, the Hamiltonian restricted to the two relevant states can be approximated as

$$\hat{H} = \frac{1}{2}\delta\hat{\sigma}_z + \frac{1}{2}(\Omega(t)\hat{\sigma}_- + \text{H.c.}),$$

assuming that the drive strength Ω is small in comparison with the transmon's anharmonicity α . In this equation, δ is the detuning of the transition between $|i\rangle$ and $|j\rangle$ from the drive frequency, $\hat{\sigma}_z$ and $\hat{\sigma}_-$ are the usual Pauli operators acting on the two states and $\Omega(t)$ is a quantity describing the strength of the drive. This drive strength parameter is related to the amplitude $V(t)$ and phase $\phi(t)$ of the pulse by

$$\Omega(t) = AV(t)e^{i\phi(t)},$$

where A is a proportionality constant depending on the attenuation of the drive line and the details of its coupling to the transmon.

If we represent the state of the transmon within the two-dimensional subspace by a vector on a Bloch sphere, the Hamiltonian written above induces rotations around an axis given by the vector $\mathbf{B} = (\Omega(t)\cos\phi(t), \Omega(t)\sin\phi(t), \delta)$ at a rate $|\mathbf{B}|$. This allows in principle to reach any state in the two-dimensional space from any other. In particular, applying resonant pulses with detuning $\delta = 0$ results in rotations around axes pointing along the equator of the Bloch sphere. Pulses of this type with $\int \Omega(t) dt = \pi$, known colloquially as π -pulses, realize rotations by π which map the two poles of the Bloch sphere onto each other. This is equivalent to swapping the populations of the states $|i\rangle$ and $|j\rangle$ and such pulses are therefore most often used to prepare higher transmon excited states.

Resonant pulses with an amplitude $\int \Omega(t) dt = \pi/2$ ($\pi/2$ -pulses) realize rotations which map a pole of the Bloch sphere onto a point on its equator. Starting from the state $|i\rangle$ or $|j\rangle$, they can be used to prepare equal superposition states of the form $(|i\rangle + e^{i\phi}|j\rangle)/\sqrt{2}$.

The amplitudes of these pulses need to be calibrated to relate them to the angles of rotation which they induce on the qubit Bloch sphere. Other parameters of the pulses are adjusted to suppress leakage to transmon levels other than the two between which we intend to drive the transition. Moreover, to achieve high fidelity of qubit operations, the qubit transition frequency usually has to be determined with more precision than offered by the simple qubit spectroscopy measurement described above which suffers from systematic errors due to ac Stark shifts.

A typical pulsed qubit measurement consists of a train of pulses designed to perform unitary operations on the transmon, followed by a pulse applied to the resonator to read out the state of the qubit. The transmon drive pulses are generated using sideband mixing with an IQ mixer and usually have a Gaussian envelope, optionally modified for leakage suppression (Motzoi *et al.*, 2009). The read-out pulse is rectangular and as such is generated by simple gating of the microwave generator with a digital modulation pulse. The response of the resonator to the read-out pulse depends on the state of the transmon. To extract the maximum amount of information from its measurement, one can optimize filtering of the signal and use reference measurements

of known transmon states to extract the individual populations. This topic is discussed in more detail in sec. 2.5. For purposes of the characterization measurements described here, it is very often sufficient to simply take the mean of the response signal over a suitable time window and use the fact that the result is a linear function of the transmon state populations which need not be further specified.

To calibrate the amplitude of the pulses, we perform a measurement of *Rabi oscillations*. Here a single pulse is applied at the qubit transition frequency, its amplitude is varied and the population of the transmon first excited state $|e\rangle$ is read out. A diagram of this scheme is shown in Fig. 2.6(a). As discussed above, the pulse induces a rotation around an axis lying in the equatorial plane of the Bloch sphere by an angle proportional to its amplitude V . The resulting excited state population is then $p_e(V) = \sin^2(\pi V/2V_\pi)$, where V_π is the pulse amplitude corresponding to a rotation by π . The mean read-out signal voltage is expected to be a linear function of $p_e(V)$. Its measured complex values fall along a line in the complex plane whose direction determines the quadrature which contains the maximum amount of information about the transmon state. We project the measured data onto this quadrature to obtain the real values plotted in Fig. 2.6(b). To determine the π -pulse amplitude, we simply fit a function of the form $a_1 \sin^2(\pi V/2V_\pi) + a_0$ to these data.

Once the amplitude of the π -pulse for the transition between $|g\rangle$ and $|e\rangle$ has been determined, the transmon can be initialized in the $|e\rangle$ state and an analogous procedure can be used to observe Rabi oscillations between the next pair of states $|e\rangle$ and $|f\rangle$. A diagram of this measurement is shown in the bottom part of Fig. 2.6(a).

An accurate measurement of the qubit transition frequency can be done by observing the so-called *Ramsey fringes*. In this measurement, the drive pulse frequency ω_d is detuned by a small amount $\Delta = \omega_d - \omega_{\text{est}}$ (typically a few MHz) from the transition frequency ω_{est} initially estimated by two-tone spectroscopy. This detuning needs to be significantly smaller than the Rabi rate Ω . In this limit, the axes of the rotations induced by the pulses still lie approximately in the equatorial plane. In the pulse sequence illustrated in Fig. 2.6(c), a $\pi/2$ -pulse is first applied to prepare the qubit in an equal superposition state $(|g\rangle + |e\rangle)/\sqrt{2}$, with a Bloch vector lying in the equatorial plane. Then, as the reference frame rotating at the drive frequency is detuned from the qubit transition ω_q by some amount $\delta = \omega_d - \omega_q$ (not necessarily equal to Δ , unless the initial estimate of the transition frequency was exactly correct), the Bloch vector starts to precess around the z -axis. After a waiting time τ , it has rotated by $\delta\tau$ and decreased in size by a factor $\exp(-\Gamma_\phi\tau)$ due to dephasing at a rate Γ_ϕ . Another $\pi/2$ -pulse then maps one of the equatorial components of the Bloch vector onto the z -component or, equivalently, onto the excited state population. Its dependence on the separation between the two $\pi/2$ -pulses is then $p_e(\tau) = (\cos(\delta\tau + \theta) \exp(-\Gamma_\phi\tau) + 1)/2$. Here the phase shift θ accounts for potential additional rotations caused by ac Stark shifts and by the Bloch vector precession starting already during the preparation pulse. The measured resonator response is again averaged and projected onto a suitably chosen quadrature. The result is plotted in Fig. 2.6(d) together with a fitted function of the form $a_1 \cos(\delta\tau + \theta) \exp(-\Gamma_\phi\tau) + a_0$ which is used to extract the parameters $|\delta|$ and Γ_ϕ .

Note that only the absolute value of the detuning can be determined because the protocol in this simple form is insensitive to the direction of the Bloch vector

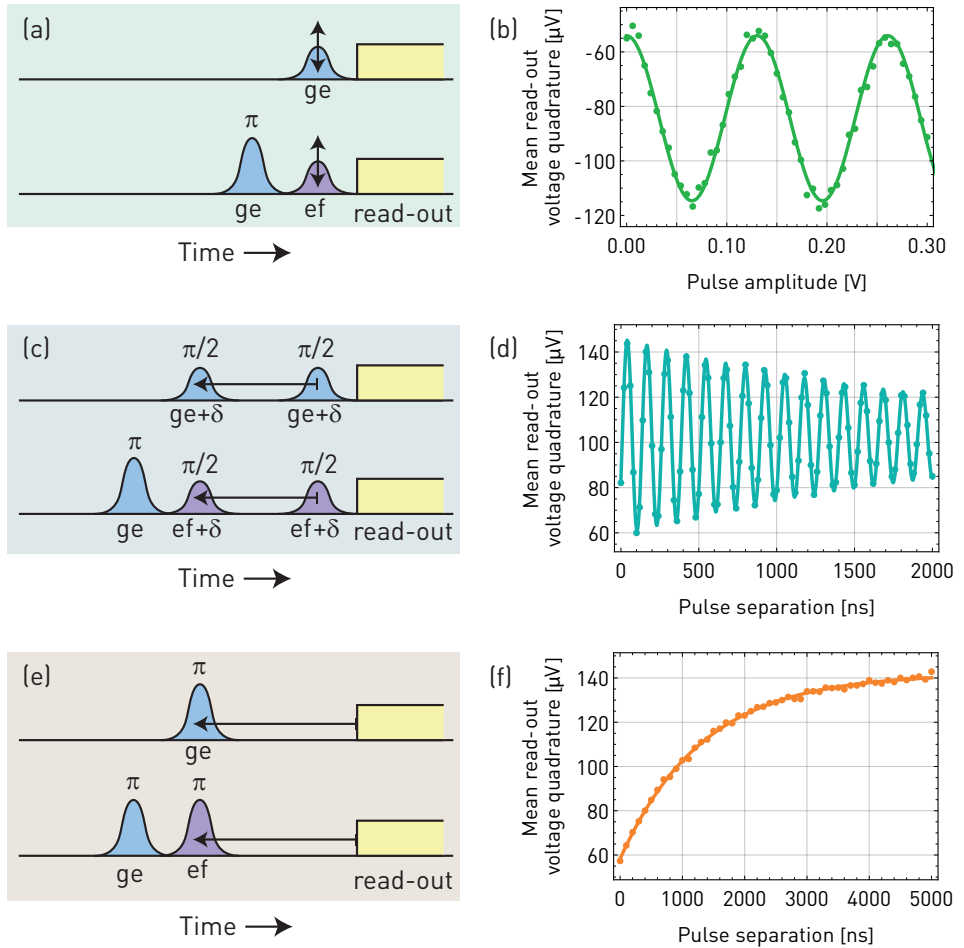


Figure 2.6: Diagrams of the pulses applied to measure (a) Rabi oscillations between states $|g\rangle$, $|e\rangle$ (top) and $|e\rangle$, $|f\rangle$ (bottom), (c) Ramsey fringes between states $|g\rangle$, $|e\rangle$ (top) and $|e\rangle$, $|f\rangle$ (bottom) and (e) relaxation of state $|e\rangle$ (top) and $|f\rangle$ (bottom). An example of the measured mean read-out voltage, projected onto the quadrature containing the maximum amount of information, is shown as a function of the pulse amplitude (in the case of Rabi oscillations) or pulse separation (in the case of Ramsey fringes and relaxation) in (b), (d) and (f), respectively.

precession. However, if the deviation of the estimated transition frequency from the real one is small compared with Δ , we can assume that Δ and δ have the same sign. In this way, δ can be fully recovered. This also shows why it is necessary to introduce a non-zero Δ – with $\Delta = 0$, we could not determine the sign of δ in a single measurement. Once δ is known, the corrected qubit frequency ω_q can then be expressed as $\omega_q = \omega_{\text{est}} + \Delta - \delta$.

As with the Rabi oscillation measurements, the scheme can be easily generalized to measure frequencies and dephasing times of higher transmon transitions, such as $|e\rangle$ to $|f\rangle$ by prepending an initial π -pulse to prepare the transmon in the $|e\rangle$ state (see Fig. 2.6(c)). In this case, however, relaxation out of the two-level subspace needs to be taken into account.

To characterize the relaxation rates of the excited transmon states, one simply needs to prepare the relevant state, wait and probe the system after a variable waiting time τ , as indicated in Fig. 2.6(d). The measured mean voltage quadrature plotted in Fig. 2.6(e) is then expected to be a linear function of the excited state population $\exp(-\Gamma\tau)$, where Γ is the sought relaxation rate.

At this point we should give a caveat, important when performing measurements like these with higher excited states. The simple forms of the read-out voltage quadrature are only correct if no more than two states of the transmon are involved. In general, this will not be the case if the transmon is initialized in the $|f\rangle$ state and beyond or if off-resonant driving of the higher transitions cannot be neglected. For example, in the measurement of the $|f\rangle$ state relaxation rate, the population p_f of this state is given by $\exp(-\Gamma\tau)$ but the populations p_e and p_g of $|e\rangle$ and $|g\rangle$ are more complicated functions of τ , involving the $|e\rangle$ state relaxation rate. The read-out voltage quadrature v will then be a linear combination of the form

$$v(\tau) = a_g p_g(\tau) + a_e p_e(\tau) + a_f \exp(-\Gamma\tau).$$

In most instances, this means that $v(\tau)$ has a more complicated dependence on τ than just the linear function of $\exp(-\Gamma\tau)$ which describes the simple case involving only two transmon states. Fortunately, there are situations in which the simple form of $v(\tau)$ is recovered. One of them is when relaxation from $|e\rangle$ to $|g\rangle$ can be neglected on the relevant time-scale. Then $p_g \approx 0$, $p_e \approx 1 - p_f$ and therefore $v \approx a_e + (a_f - a_e)p_f$. The same argument typically applies in the case of Rabi oscillation measurements where the pulse sequence is short enough to allow relaxation effects to be neglected. The other instance in which the dependence of v on p_g , p_e and p_f simplifies is if $a_g = a_e$. Then, since $p_g + p_e = 1 - p_f$, we again get $v = a_e + (a_e - a_g)p_f$.

While the condition $a_g = a_e$ is usually not satisfied unless the read-out procedure is specifically tailored to it, we can modify the measurement scheme using a simple trick to make a_g and a_e effectively equal. We perform the measurement twice and in one of the realizations we precede the read-out pulse by a π -pulse on the $|g\rangle$ to $|e\rangle$ transition to swap the populations of the two states. This means that the read-out quadrature is $a_g p_g + a_e p_e + a_f p_f$ in the measurement without the π -pulse and $a_g p_e + a_e p_g + a_f p_f$ in the one with it. If we average the two results together, we get $a_{ge} p_g + a_{ge} p_e + a_f p_f$, where $a_{ge} = (a_g + a_e)/2$. Hence, the averaged measurement can be described by a linear combination of the populations where the weights of

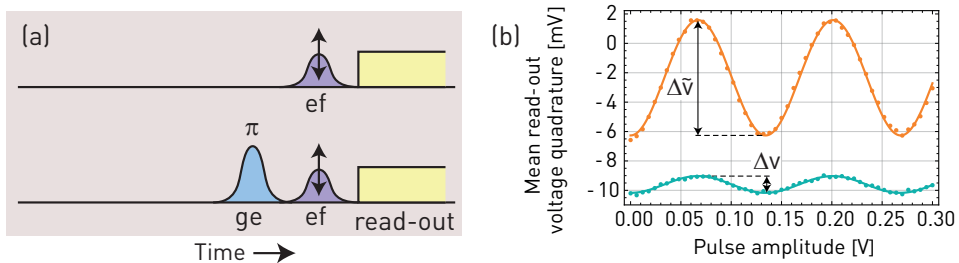


Figure 2.7: (a) Diagram of the pulses applied to measure the excited state thermal population with the method from Geerlings *et al.* (2013). (b) An example of the measured mean read-out voltage quadrature as a function of the pulse amplitude for the sequence with (orange) and without (cyan) the initial π -pulse. In the shown example, the thermal population was particularly high at approximately 12.6%.

p_g and p_e are equal, exactly as needed to be able to write the outcome in the form $v = a_{ge} + (a_f - a_{ge})p_f$.

This simple averaging process makes the measurement insensitive to any dynamics within the subspace spanned by $|g\rangle$ and $|e\rangle$ and thus isolates only the relaxation process from $|f\rangle$ to $|e\rangle$, making it significantly easier to analyze and extract the relaxation rate.

Thermal excitation measurement

Over the course of my work, I contributed to the already quite extensive tool-box of characterization measurements available in our lab by adapting and testing a simple scheme developed by Geerlings *et al.* (2013) for measuring the transmon thermal excitation.

The thermal population of the first excited state of the transmon is typically rather small – on the order of a few percent. It can be measured using single-shot projective measurements of the transmon but if these are not available, it is not particularly straightforward to extract. The main reason for this difficulty is that in averaged measurements, the transmon state populations are determined by comparison of the measured signal with references obtained for the transmon prepared in known states. Ideally, these reference states should be the pure transmon eigenstates. However, these cannot be easily prepared as the initial state obtained after waiting and letting the transmon relax is itself a thermal state.

To circumvent this problem, Geerlings *et al.* (2013) used a scheme where they observed Rabi oscillations between states $|e\rangle$ and $|f\rangle$. Assuming that the initial state is a mixed state of the transmon eigenstates, the peak-to-peak amplitude Δv of the Rabi oscillations is given by the difference between the response for a zero-amplitude pulse, equal to $a_g p_g + a_e p_e + a_f p_f$, and the response for a π -pulse, equal to $a_g p_g +$

$a_e p_f + a_f p_e$. As above, the coefficients a_g , a_e and a_f here denote the mean read-out voltage quadratures one would measure if the transmon were prepared in the pure $|g\rangle$, $|e\rangle$ and $|f\rangle$ state, respectively. The difference between the two responses can be expressed as $(a_e - a_f)(p_e - p_f)$. Assuming that the thermal population p_f of the $|f\rangle$ state is negligible, the amplitude of the oscillations is directly proportional to the first excited state population p_e . The proportionality constant is in principle unknown but by repeating the same measurement preceded by a π -pulse on the $|g\rangle$ to $|e\rangle$ transition, one measures Rabi oscillations with an amplitude $\Delta\tilde{v}$ proportional to $p_g = 1 - p_e$ with the same factor. Taking the ratio of the amplitudes then yields the equation

$$\frac{\Delta v}{\Delta\tilde{v}} = \frac{p_e}{1 - p_e}.$$

2.5 Transmon state read-out and tomography

Transmon read-out is most commonly performed by probing the resonator and observing the change of its response depending on the state of the transmon. This dependence is caused by the coupling between the transmon and the resonator which is usually of the dispersive type due to the large detuning between the two systems compared with their Jaynes-Cummings interaction strength. The dispersive coupling can be treated as an additional shift of the resonator frequency depending on the state of the transmon or, alternatively, as a shift of the transmon frequency depending on the number of photons in the resonator.

The first one of these two equivalent interpretations is more suitable to elucidate the nature of the dispersive read-out. The resonator is probed in the absence of any transmon drive and we will also for the moment neglect relaxation of the transmon. In this case, if the transmon is prepared in one of its energy eigenstates, its state will remain constant and the resonator will evolve in the same way as an isolated driven resonator with a frequency which is given by the transmon state.

Neglecting the transient response of the resonator at the onset of the drive pulse, the dependence of the steady state signal voltage v for a resonator probed in transmission on the drive frequency ω_d is given by the complex Lorentzian

$$v \propto \frac{1}{1 + 2i(\omega_r - \omega_d)/\kappa},$$

where ω_r is the resonance frequency of the resonator and κ its relaxation rate. Since ω_r is shifted by the dispersive coupling, the center of the Lorentzian peak changes with the state of the transmon $|j\rangle$ (where $j = g, e, f, \dots$) to $\omega_r^{(j)}$ and probing the resonator at a fixed frequency ω_d leads to a transmon-state-dependent read-out voltage $v^{(j)}$. This effect is illustrated in Fig. 2.8.

Depending on the signal-to-noise ratio of the measurement setup, the read-out may be performed in the *single-shot* regime or as *averaged read-out*. In the first case, the signal-to-noise ratio is high enough to allow the transmon state to be determined with an appreciable fidelity in a single realization of the measurement. This is important for example in experiments which rely on feedback or post-selection. In the following,

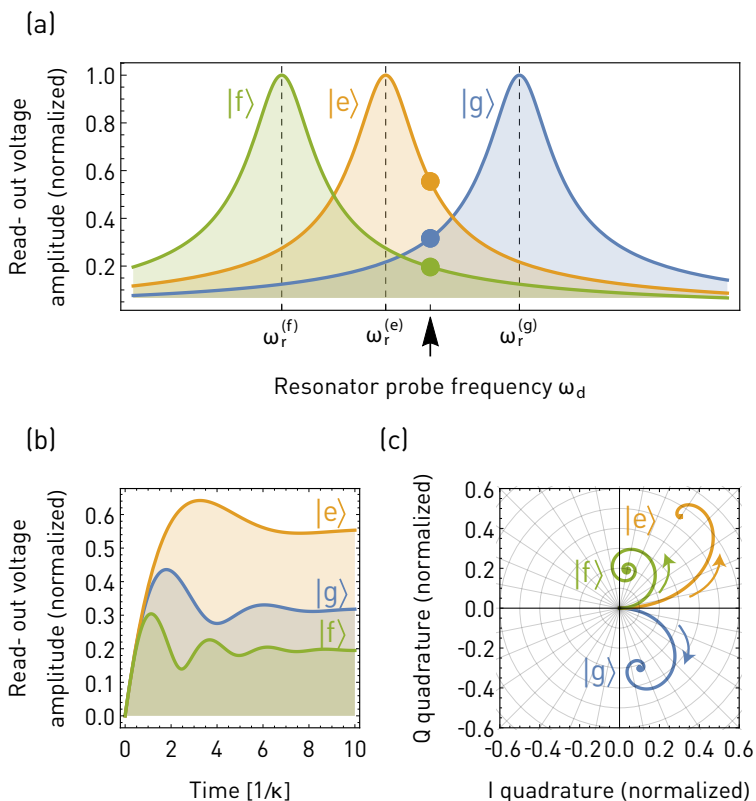


Figure 2.8: (a) Steady-state normalized read-out voltage amplitude as a function of drive frequency for a resonator probed in transmission, showing the differently shifted response curves depending on the state of the transmon. The steady-state response at a fixed drive frequency is the transmon-state-dependent, as indicated by the blue, orange and green point. In this particular example, the detunings of the resonator frequencies $\omega_r^{(g)}$, $\omega_r^{(e)}$ and $\omega_r^{(f)}$ from the drive frequency ω_d are 1.5κ , -0.75κ and -2.5κ , respectively. (b) Time-dependence of the read-out voltage when the drive signal is abruptly turned on at time $t = 0$. The curves show ringing at a frequency given by the drive-resonator detuning and asymptotically approach the steady-state values from (a). (c) Trajectories followed by the read-out voltages in the complex plane.

we will focus on the second case – averaged read-out which extracts expectation values such as state populations from a large number of individual measurements.

The dispersive read-out described here is insensitive to coherence between different transmon eigenstates because the dispersive coupling term is diagonal in the transmon eigenbasis. The averaged steady-state read-out voltage therefore depends only on the eigenstate populations p_g, p_e, p_f, \dots . As the expectation value of any physical measurement outcome needs to be a linear function of the system’s density matrix, the average measured voltage can be expressed as a linear combination of the form

$$v = a_g p_g + a_e p_e + a_f p_f + \dots \quad (2.2)$$

Provided that no more than three energy levels of the transmon are occupied, measuring the steady-state value v is in principle sufficient to calculate the populations. The two equations for the real and imaginary part of v together with the constraint $p_g + p_e + p_f = 1$ can be uniquely solved for p_g, p_e and p_f after a_g, a_e and a_f have been determined from calibration measurements of three known reference states.

Read-out in the presence of thermal excitations

This is not entirely trivial in practice since these reference states, typically chosen to be the eigenstates of the transmon, cannot be easily prepared in the presence of thermal excitations. The state to which the transmon relaxes after a sufficiently long time is not the pure ground state but a mixed state with small but non-zero unknown populations of the excited states. To calibrate the qubit readout process properly, that is, to extract the eigenstate responses a_g, a_e, a_f, \dots , the thermal populations need to be determined. This can be done either using the method developed by Geerlings *et al.* (2013), as described in sec. 2.4, or with a procedure which can be seen as its modification, requiring fewer measurements in total. The exact form of this measurement scheme depends on the assumptions which one can make about the thermal populations. We will analyze a simple instance in which we assume that the populations of transmon states higher than $|e\rangle$ are negligible.

In this case, one only needs to extend the minimal set of three reference measurements, which would be needed to determine a_g, a_e and a_f in the ideal case of zero thermal excitations, with a single additional one. The first three measurements are those which in said ideal case reduce to the standard set of measurements of the three eigenstates: In the first one, the transmon is simply left to relax to its steady state prior to the measurement. In the second one, an additional π -pulse is applied on the $|g\rangle$ to $|e\rangle$ transition to swap the populations of these two states. In the third one, the first π -pulse is followed by another one on the $|e\rangle$ to $|f\rangle$ transition, moving the population which was initially in the ground state to the $|f\rangle$ state. The expected read-out voltages for these three cases are

$$v_1 = a_g p_g + a_e p_e, \quad (2.3a)$$

$$v_2 = a_g p_e + a_e p_g, \quad (2.3b)$$

$$v_3 = a_g p_e + a_f p_g. \quad (2.3c)$$

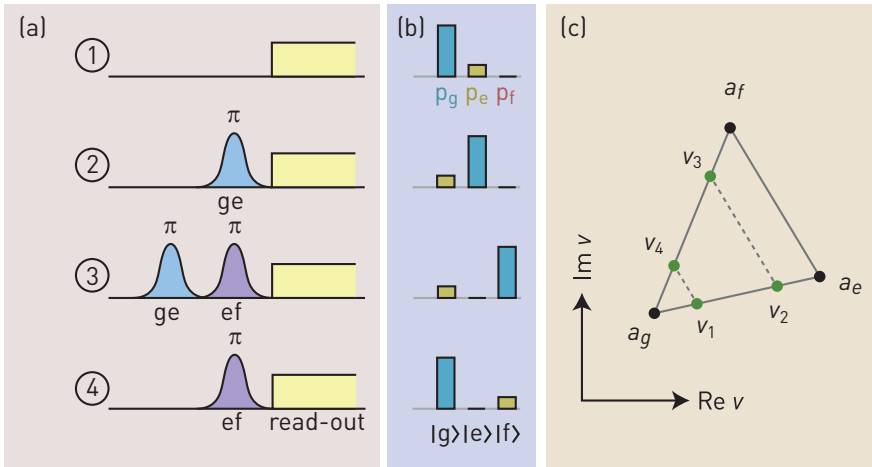


Figure 2.9: (a) Diagram of pulse sequences used in the read-out calibration measurements taking into account a non-zero thermal population of the excited state and (b) the corresponding populations of the three lowest transmon eigenstates before the read-out pulse. (c) Graphical complex-plane representation of the ideal eigenstate responses a_g , a_e , a_f (black dots) and the mixed state responses v_1 , v_2 , v_3 , v_4 (green dots) for the four calibration measurements.

We can see that if $p_e = 0$ and $p_g = 1$, we have simply $v_1 = a_g$, $v_2 = a_e$ and $v_3 = a_f$. For $p_e \neq 0$, we still have a bit of work to do. In the one additional measurement, we perform only a π -pulse on the $|e\rangle$ to $|f\rangle$ transition before probing the resonator. In the absence of thermal population, this would result in a read-out voltage $v_4 = a_g$ just like in the very first measurement. However, for non-zero p_e , we get

$$v_4 = a_g p_g + a_f p_e. \quad (2.3d)$$

The pulse sequences used in the four described measurements are summarized in the diagram in Fig. 2.9(a) while the resulting eigenstate populations before the start of the read-out pulse are shown in Fig. 2.9(b).

The relation between the ideal eigenstate responses a_g , a_e , a_f and the voltages v_1 , v_2 , v_3 , v_4 obtained in the four calibration measurements are shown graphically in Fig. 2.9(c). The outcome of the first measurement v_1 is a linear combination of a_g and a_e and therefore lies on the line connecting these two points. Its distances to a_g and a_e are in the ratio of the two thermal populations p_e and p_g . The voltage v_2 is then the reflection of v_1 with respect to the center-point between a_g and a_e since the π -pulse swaps the populations of $|g\rangle$ and $|e\rangle$. Furthermore, v_3 is obtained from v_2 by transporting it in the direction given by $a_f - a_e$ to the line connecting a_g and a_f . This construction ensures that v_2 and v_3 are linear combinations of a_g , a_e and a_g , a_f ,

respectively, with the same weights. The same construction then also transforms v_1 into v_4 .

From this geometric picture we see that knowledge of only the three points v_1, v_2, v_3 is not enough to reconstruct a_g, a_e, a_f . If we in addition also know v_4 , we can determine a_g as the intersection point between the lines connecting v_1, v_2 and v_3, v_4 . We can express this mathematically as

$$a_g = \eta v_2 + (1 - \eta)v_1 = \lambda v_3 + (1 - \lambda)v_4,$$

where η and λ are real parameters determining the position of a_g on the two lines. The real and imaginary part of this equation form a system which can be solved for η and λ , resulting in

$$\eta = \frac{\text{Im}((v_3 - v_4)^*v_1 + v_4^*v_3)}{\text{Im}(v_2 - v_1)^*(v_3 - v_4)},$$

$$\lambda = -\frac{\text{Im}((v_2 - v_1)^*v_4 + v_1^*v_2)}{\text{Im}(v_2 - v_1)^*(v_3 - v_4)}.$$

Note that η and λ are not expected to be independent because the positions of the points v_1, v_2 and v_3, v_4 on their respective lines are not arbitrary but are constrained by the fact that $v_4 - v_1$ and $v_3 - v_2$ are parallel. Indeed, from the form of v_1, v_2, v_3, v_4 in terms of a_g, a_e, a_f , as given by eq. (2.3), one can show that both η and λ should be equal to $p_e/(p_e - p_g)$. This can serve as a consistency check when processing experimental data. The calculated η and λ should be very similar. One can then use the mean of $\eta v_2 + (1 - \eta)v_1$ and $\lambda v_3 + (1 - \lambda)v_4$ to determine a_g . Once a_g is known, a_e and a_f can also be calculated using the relations $a_e = v_1 + v_2 - a_g$ and $a_f = v_4 + v_3 - a_g$ which are easily derived from eq. (2.3). Furthermore, the thermal population p_e can be expressed as $p_e = \eta/(2\eta - 1)$ or $p_e = \lambda/(2\lambda - 1)$ (or with the mean $(\eta + \lambda)/2$ in place of either η or λ). With the eigenstate responses a_g, a_e and a_f known, we can in principle analyze the measurement response of any unknown state and extract p_g, p_e and p_f .

Thus far, we have seen how at most three transmon state populations can be extracted if the outcome of each measurement is a single complex number – for example the steady-state response of the resonator. In practice, this is a slightly simplistic assumption. On the one hand, waiting for the resonator to reach its steady state may not be desirable because of the limited relaxation times of the transmon. At the same time, the transient response of the resonator which occurs just after the drive signal is abruptly turned on also contains information about the transmon state. The voltage of the signal transmitted through the resonator is proportional to the displacement α of its coherent state. In a reference frame rotating at the drive frequency ω_d , this displacement is governed by the Heisenberg equation

$$\dot{\alpha} = -i(\omega_r - \omega_d)\alpha - \frac{\kappa}{2}\alpha - \frac{i\varepsilon}{2},$$

where ε is a complex parameter describing the amplitude and phase of the drive signal. Starting in the vacuum state $\alpha = 0$, this equation can be easily solved, showing that

the read-out voltage has a time dependence of the form

$$v(t) \propto \frac{1 - e^{-i(\omega_r - \omega_d)t - \kappa t/2}}{i(\omega_r - \omega_d) + \kappa/2}.$$

Again, as the resonator frequency is shifted by the dispersive coupling, the read-out voltage trace depends on the state of the transmon in a not entirely trivial way. An example of such read-out traces is shown in Fig. 2.9(b,c). It exhibits ringing at the detuning frequency between the drive and the resonator which decays as the response settles to the steady state.

This analytical form of the time-dependent resonator response can give us a good insight into the effect the individual parameters ω_d , ω_r and κ have on the transients but it is still only an approximation. In real systems, the transmon may relax on a time-scale comparable with the resonator relaxation rate κ . In this case, the resonator response first converges to the steady-state corresponding to the initial state of the transmon but then, when relaxation occurs, it starts approaching the steady-state belonging to the next lower transmon state. In addition, the times at which the transmon relaxes are randomly distributed and one needs to average over them. The resulting voltage in general needs to be calculated numerically (Bianchetti *et al.*, 2009) but in the special (and fortunately very prevalent) case when the qubit is not driven while the resonator probe signal is applied, it can also be derived analytically, as presented in app. H.

To calculate the populations of n transmon states, the measured voltage trace somehow needs to be reduced to n real numbers. As the expectation value of the voltage is a linear combination of the eigenstate responses with coefficients given by the populations, the mapping we seek should be linear. Apart from this constraint and the requirement that it reproduces the correct populations when acting on a set of calibration measurements, we have a considerable freedom in choosing the exact form of this mapping. In fact, any mapping which satisfies the conditions mentioned above will give the correct results when acting on ideal, noiseless voltage traces. When noise enters the game, however, some mappings will become less suitable than others.

Typically, when very good signal-to-noise ratio is not extremely important, the mapping from voltage traces to populations may be chosen rather crudely. For example, by inspection of the eigenstate responses. In this case, one usually identifies a few time intervals in which the traces differ significantly from each other and integrates over them. The resulting vector of complex numbers is then linearly mapped onto populations in a way consistent with calibration measurements. If we wish to minimize noise in the populations obtained from a measurement, we need to choose the mapping more carefully. This task is discussed in more detail in app. H.

Transmon state tomography

As the dispersive read-out is only sensitive to transmon eigenstate populations, it is by itself not sufficient to fully reconstruct the density matrix of an unknown state. To accomplish this, one can use a procedure commonly known as *state tomography*. It consists of multiple read-out measurements in which the resonator probe signal is

preceded by different unitary operations \hat{U}_i acting on the transmon. The populations $p_j^{(i)}$ (where $j \in \{g, e, f, \dots\}$) extracted in each of these measurements are given by

$$p_j^{(i)} = \text{Tr} \hat{P}_j \hat{U}_i \hat{\rho} \hat{U}_i^\dagger,$$

where \hat{P}_j are projectors onto the transmon eigenstates. We can rewrite this equation as

$$p_j^{(i)} = \text{Tr} \hat{P}_j^{(i)} \hat{\rho},$$

where $\hat{P}_j^{(i)} = \hat{U}_i^\dagger \hat{P}_j \hat{U}_i$. The measurements therefore reveal expectation values of the unitarily rotated projection operators.

The expression $\text{Tr} \hat{A}^\dagger \hat{B}$ defines a scalar product $\langle \hat{A}, \hat{B} \rangle$ on the space of operators. Therefore, after performing the measurements, we know the scalar products $\langle \hat{P}_j^{(i)}, \hat{\rho} \rangle$. Additionally, the normalization condition $\text{Tr} \hat{\rho} = 1$ also tells us that $\langle \mathbb{1}, \hat{\rho} \rangle = 1$. Assuming that only up to n energy levels of the transmon are occupied, the density matrix can be extracted from these scalar products if the operators $\hat{P}_j^{(i)}$ together with the identity operator $\mathbb{1}$ span the whole space of $n \times n$ Hermitian matrices. To allow us find the density matrix with the smallest possible number of measurements, they should also be linearly independent or, in other words, form a basis. This shows us that at least $n^2 - 1$ measurements are needed to fully determine the density matrix.

As an example, if only the two lowest levels of the transmon $|g\rangle$ and $|e\rangle$ are involved, a possible set of measurement operators $\hat{P}_j^{(i)}$ is

$$\begin{aligned} \hat{P}_e &= \begin{pmatrix} 1 & 0 \\ 0 & 0 \end{pmatrix}, \\ \hat{U}_x^\dagger \hat{P}_e \hat{U}_x &= \frac{1}{2} \begin{pmatrix} 1 & -i \\ i & 1 \end{pmatrix}, \\ \hat{U}_y^\dagger \hat{P}_e \hat{U}_y &= \frac{1}{2} \begin{pmatrix} 1 & -1 \\ -1 & 1 \end{pmatrix}, \end{aligned}$$

where $\hat{U}_x = e^{-i\pi(|g\rangle\langle e| + \text{H.c.})/4}$ and $\hat{U}_y = e^{\pi(|g\rangle\langle e| - \text{H.c.})/4}$ are unitary operations corresponding to rotations on the Bloch sphere by $\pi/2$ around the x and y axis, respectively. Note that the three listed operators together with $\mathbb{1}$ form a basis in the space of Hermitian 2×2 matrices. This particular set of measurements has an intuitive geometrical interpretation which gives the tomography technique its name: The corresponding expectation values can be also written as $(1 + \langle \hat{\sigma}_z \rangle)/2$, $(1 + \langle \hat{\sigma}_y \rangle)/2$ and $(1 - \langle \hat{\sigma}_x \rangle)/2$ and can therefore be directly related to the expectation values of the three standard Pauli matrices. These are in turn equal to the three components of the Bloch vector representing the unknown state. Thus the Bloch vector is reconstructed from its three projections, similarly to how 3d scenes are reconstructed by tomographic imaging.

In the more complex case when three transmon levels are occupied (Bianchetti *et al.*, 2010), at least eight measurements need to be performed. These can be for

example

$$\begin{aligned}
\hat{P}_e &= \begin{pmatrix} 0 & 0 & 0 \\ 0 & 1 & 0 \\ 0 & 0 & 0 \end{pmatrix}, & \hat{P}_f &= \begin{pmatrix} 1 & 0 & 0 \\ 0 & 0 & 0 \\ 0 & 0 & 0 \end{pmatrix}, \\
\hat{U}_x^{(ge)\dagger} \hat{P}_e \hat{U}_x^{(ge)} &= \frac{1}{2} \begin{pmatrix} 0 & 0 & 0 \\ 0 & 1 & -i \\ 0 & i & 1 \end{pmatrix}, & \hat{U}_y^{(ge)\dagger} \hat{P}_e \hat{U}_y^{(ge)} &= \frac{1}{2} \begin{pmatrix} 0 & 0 & 0 \\ 0 & 1 & -1 \\ 0 & -1 & 1 \end{pmatrix}, \\
\hat{U}_y^{(ef)\dagger} \hat{P}_e \hat{U}_y^{(ef)} &= \frac{1}{2} \begin{pmatrix} 1 & i & 0 \\ -i & 1 & 0 \\ 0 & 0 & 0 \end{pmatrix}, & \hat{U}_y^{(ef)\dagger} \hat{P}_f \hat{U}_y^{(ef)} &= \frac{1}{2} \begin{pmatrix} 1 & 1 & 0 \\ 1 & 1 & 0 \\ 0 & 0 & 0 \end{pmatrix}, \\
\hat{U}_y^{(gf)\dagger} \hat{P}_f \hat{U}_y^{(gf)} &= \frac{1}{2} \begin{pmatrix} 1 & 0 & -i \\ 0 & 0 & 0 \\ i & 0 & 1 \end{pmatrix}, & \hat{U}_y^{(gf)\dagger} \hat{P}_f \hat{U}_y^{(gf)} &= \frac{1}{2} \begin{pmatrix} 1 & 0 & -1 \\ 0 & 0 & 0 \\ -1 & 0 & 1 \end{pmatrix}.
\end{aligned}$$

Here we have defined, analogously to \hat{U}_x and \hat{U}_y above, $\hat{U}_x^{(ij)} = e^{-i\pi(|i\rangle\langle j| + \text{H.c.})/4}$ and $\hat{U}_y^{(ij)} = e^{\pi(|i\rangle\langle j| - \text{H.c.})/4}$.

Even though linear reconstruction of an n -state density matrix is in principle possible from $n^2 - 1$ measurements and the procedure gives a unique result, the presence of measurement noise can render the resulting density matrix unphysical. To circumvent this problem, the density matrix can be estimated using maximum likelihood techniques (Smolin *et al.*, 2012) or other methods (Christandl & Renner, 2012; Faist & Renner, 2016).

The state tomography technique is not restricted to a single qubit or multi-level system but can be extended to extract density matrices of multi-qubit states, as described for example by Filipp *et al.* (2009).

Process tomography and verification procedures

In experiments where fidelity of the prepared quantum states is critical, as for example in many quantum information processing applications, one often needs a reliable way to characterize the performance of the individual unitary operations. This can be done using a process known as *quantum process tomography* (Chuang & Nielsen, 1997) which can be seen as an extension of the state tomography technique.

Arbitrary quantum operations can be seen as linear maps acting within the space of density matrices which additionally have the property of *complete positivity*. A map \mathcal{M} is called completely positive if any map of the form $\text{id} \otimes \mathcal{M}$ maps positive operators onto positive operators. According to *Choi's theorem* (Choi, 1975), any quantum operation \mathcal{M} acting on density matrices on a d -dimensional Hilbert space \mathcal{H} can be uniquely mapped onto a positive operator on a d^2 -dimensional Hilbert space $\mathcal{H} \otimes \mathcal{H}$:

$$\hat{C}_{\mathcal{M}} \equiv \sum_{i,j} |i\rangle\langle j| \otimes \mathcal{M}(|i\rangle\langle j|),$$

where $\{|i\rangle\}_{i=1}^d$ is an orthonormal basis of \mathcal{H} . This operator is often called the *Choi matrix* associated with \mathcal{M} . The action of \mathcal{M} can be written in terms of the Choi matrix as

$$\mathcal{M}(\hat{\rho}) = \text{Tr}_1 \hat{C}(\hat{\rho}^\text{T} \otimes \mathbb{1}),$$

where the transpose T of an operator is defined as $\hat{A}^\text{T} \equiv \sum_{i,j} |i\rangle\langle j| \langle j|\hat{A}|i\rangle$ and Tr_1 denotes the partial trace over the first Hilbert space \mathcal{H} in $\mathcal{H} \otimes \mathcal{H}$.

The Choi matrix characterizing an unknown operation can be determined with a technique similar to state tomography: A unitary operation \hat{U}_i is applied to an initial state (typically the steady state of the transmon) to prepare an input state for the operation. After the operation is performed, another unitary \hat{V}_j is applied and then the populations of the transmon are measured. The outcomes are given by

$$p_k^{(i,j)} = \text{Tr} \hat{P}_k \hat{V}_j \mathcal{M}(\hat{U}_i \hat{\rho} \hat{U}_i^\dagger) \hat{V}_j^\dagger$$

or, in terms of the Choi matrix:

$$p_k^{(i,j)} = \text{Tr} \hat{P}_k^{(i,j)} \hat{C},$$

where $\hat{P}_k^{(i,j)} = (\hat{U}_i \hat{\rho} \hat{U}_i^\dagger)^\text{T} \otimes \hat{V}_j^\dagger \hat{P}_k \hat{V}_j$. If these measurement operators together with the identity operator form a basis in the space of Hermitian $d^2 \times d^2$ matrices, \hat{C} can be uniquely determined from the measured populations.

This process tomography procedure has been used in a wide range of experiments to estimate fidelities of quantum gates (Bialczak *et al.*, 2010; Childs *et al.*, 2001). However, for systems with more than a few qubits, it becomes impractical rather quickly as the required number of measurements scales as 4^n with the number of qubits n .

An estimate of quantum operation fidelities in larger systems can be more easily obtained using the *randomized benchmarking* technique introduced by Emerson *et al.* (2007) and refined by Knill *et al.* (2008) and Magesan *et al.* (2012). In one version of this process, a sequence is built out of m copies of the quantum operation to be characterized, interleaved with m randomly chosen *Clifford gates*². Then one additional operation is appended, chosen to make the whole sequence result in the identity operation under the assumption that all of the constituent operations are ideal. The generated sequence is then applied to a fixed initial state and the probability that the system is again found in the same state is measured. The outcome is averaged over many realizations of the random gate sequence, giving the *sequence fidelity* F . This quantity is determined as a function of m and an exponential function $A_0 p^m + B_0$ is fitted to $F(m)$. The decay constant p is then related to the *error rate* of the studied operation.

The advantage of the randomized benchmarking protocol is that the scaling of the required number of measurements with the system size is more favorable than for full process tomography. Moreover, it is independent of state preparation and

²Quantum gates from a Clifford group – a group of unitary operations which map elements of the Pauli group onto each other.

measurement errors. On the other hand, it quantifies the error rate of the operation by a single number and therefore does not offer as much insight into the source of potential errors.

2.6 Microwave field measurements and state tomography

Just like transmons, microwave resonators are an essential ingredient of circuit QED systems. Unlike transmons, however, their physical state can be probed in a much more direct and intuitive way. As we have seen in sec. 2.5, transmon states are read out indirectly, using a resonator as an auxiliary system. On the other hand, the microwave field contained in a resonator radiates into transmission lines coupled to it and can be monitored directly using our measurement electronics. In fact, it may seem rather counter-intuitive that we can observe inherently quantum microwave signals with equipment which, perhaps with the exception of its price-tag and the fact that it is surrounded by somewhat exotic cryogenic paraphernalia, is essentially no different than what is found in any phone or GPS receiver. The principle of our measurement setup is as classical as can be – at its core, it is an oscilloscope. With very low noise and additional data processing features but still a device for recording voltages as a function of time.

This raises some obvious and yet quite intriguing questions: What does a quantum state of a microwave field look like on an oscilloscope? And can we fully characterize the state with this type of measurement? To be able to answer these questions, we first need to describe the full measurement process in more detail. The following explanation partially sacrifices rigor for the sake of clarity. An interested reader can fill in the gaps with the help of da Silva *et al.* (2010), Eichler *et al.* (2012a) or one of the available textbooks such as Walls & Milburn (2008) or Wiseman & Milburn (2010).

Let us consider a simple case where the measured signal is prepared by emission from a single-mode resonator which is initially in some state

$$|\psi\rangle = c_0|0\rangle + c_1|1\rangle + c_2|2\rangle + \dots, \quad (2.4)$$

where $|0\rangle, |1\rangle, |2\rangle, \dots$ are the usual Fock states of the resonator. The first question we need to answer is: How do we describe the field which the resonator emits, given its initial state?

Input-output formalism

We will assume that the transmission line into which the field is radiated is semi-infinite with an open boundary condition. The propagating field can then be quantized using the standard Lagrangian formalism and an approximate treatment of the interaction between the line and the resonator, as presented for example in Walls & Milburn (2008), leads to the standard Heisenberg-picture *input-output relations*:

$$\frac{d}{dt}\hat{c}(t) = i[\hat{H}_0(t), \hat{c}(t)] - \sqrt{\kappa}\hat{a}_{\text{in}}(t), \quad (2.5a)$$

$$\hat{a}_{\text{out}}(t) = \hat{a}_{\text{in}}(t) + \sqrt{\kappa}\hat{c}(t). \quad (2.5b)$$

Here \hat{H}_0 is the Hamiltonian of the resonator, \hat{c} its annihilation operator and κ is a parameter quantifying the strength of the coupling between the line and the resonator. The operators \hat{a}_{in} and \hat{a}_{out} represent the propagating field which can be interpreted in the following way:

Consider a dispersionless, semi-infinite transmission line with a propagation speed c . We can split the field into two components propagating towards and away from the end. We introduce operators \hat{a}_τ^\dagger which create photons localized at a distance $c|\tau|$ from the end of the line and propagating towards it for $\tau > 0$ and away from it for $\tau < 0$. A photon state $\hat{a}_\tau^\dagger|0\rangle$ created at time t will evolve into $\hat{a}_{\tau-\Delta\tau}^\dagger|0\rangle$ after a time interval Δt . We can visualize the propagation of the field as a “conveyor belt” of modes shown in Fig. 2.10.

The ladder operators are normalized such that $[\hat{a}_\tau, \hat{a}_{\tau'}^\dagger] = \delta(\tau - \tau')$ and are related to the voltage $\hat{V}(x)$ measured at a distance x from the end of the line by $\hat{V}(x) \propto \hat{a}_{x/c} + \hat{a}_{-x/c} + \text{H.c.}$

While the labeling of modes \hat{a}_τ which we have introduced is based on the location of the mode in the transmission line and its direction of propagation, in some sense it is even more natural to introduce a different, time-dependent labeling by

$$\hat{a}_\tau(t) \equiv \hat{a}_{\tau-t}.$$

With this definition, the state of mode $\hat{a}_\tau(t) = \hat{a}_{\tau-t}$ at time t will be shifted to mode $\hat{a}_{\tau-t-\Delta t} = \hat{a}_\tau(t + \Delta t)$ at time $t + \Delta t$. Whereas the original modes \hat{a}_τ are modes at fixed positions τ , the newly defined time-bin modes $\hat{a}_\tau(t)$ propagate with the field, as indicated in Fig. 2.10(b). This re-labeling can be seen equivalently as a transformation to an interaction picture with respect to free propagation of the field. Under this free propagation, the content of mode $\hat{a}_\tau(t)$ does not change with time t . The subscript label τ represents the time at which the mode arrives at the end of the transmission line.

We then define the input field $\hat{a}_{\text{in}}(\tau)$ as the limit of $\hat{a}_\tau(t)$ for $t \rightarrow -\infty$. This means that $\hat{a}_{\text{in}}(\tau)$ describes the distant past state of the time-bin which arrived at the end of the transmission line at time τ . Similarly, $\hat{a}_{\text{out}}(\tau)$ defined as $\hat{a}_\tau(t)$ in the limit $t \rightarrow +\infty$ represents the field in the same time-bin in the distant future.

Measurement of the quantum signal

To describe what happens to the output field as it propagates through the amplification and detection chain, we first need to specify at which point the quantum signal gets measured and converted into a c-number. This is not a simple question – the boundary between quantum and classical could presumably be drawn at the digitization step. But one could also argue that the quantum state of the full system including the measurement computer only collapses when a human looks at the resulting data. Fortunately, this rather philosophical distinction is of little consequence for the actual outcome of the measurement if one assumes that the signal was amplified with a large gain prior to observation. In fact, we may even assume that the signal is measured before any down-conversion process takes place.

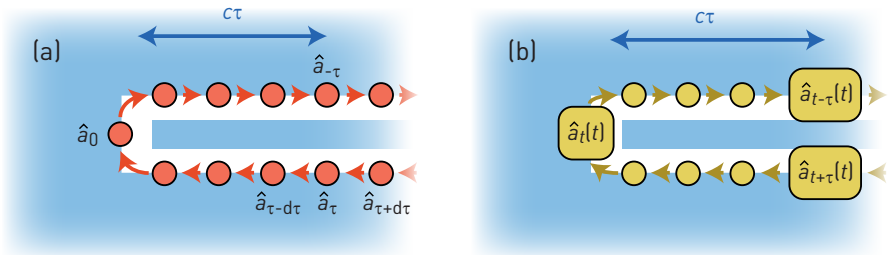


Figure 2.10: (a) Model of the semi-infinite transmission line as a “conveyor belt” of modes. The modes \hat{a}_{τ} and $\hat{a}_{-\tau}$ represent fields propagating towards and away from the end of the line, respectively, localized at a distance $c\tau$ from it. In each infinitesimal time step $d\tau$, the state of every mode is shifted along the “conveyor belt” to the next mode in line, as indicated by the arrows. (b) Time-dependent re-labeling of the modes $\hat{a}_{\tau}(t) \equiv \hat{a}_{\tau-t}$ such that the parameter τ is shifted together with the content of the mode. In this picture, $\hat{a}_{\tau}(t)$ denotes the mode which arrives at the end of the transmission line at time τ .

In this simplified picture, the only step which the output field undergoes while it is still quantum is amplification. In order to describe the amplification process, we could try to come up with a quantum-mechanical model of the amplifier and study its effect on the field. However, a detailed model is not really necessary as we can derive the action of a linear amplifier on a quantum field from simple considerations, independent of the actual physical implementation. This derivation follows a more detailed analysis presented for example in Clerk *et al.* (2010).

Our first naive guess about the amplification process may be that it simply transforms an input field \hat{a} into an amplified field $\hat{a}_{\text{amp}} = \sqrt{G}\hat{a}$, where G is the amplifier’s power gain. However, this process is not allowed by quantum mechanics as the output is not a valid field satisfying the required commutation relations $[\hat{a}_{\text{amp}}(t), \hat{a}_{\text{amp}}^{\dagger}(t')] = \delta(t - t')$. The simplest way we could possibly try to fix this shortcoming is to add another term, that is, $\hat{a}_{\text{amp}} = \sqrt{G}\hat{a} + \hat{\chi}$.

What conditions does $\hat{\chi}$ need to satisfy? If we assume that it commutes with \hat{a} , then the two-time commutator of the left-hand side needs to be $\delta(t - t')$ while for the right-hand side it is $G\delta(t - t') + [\hat{\chi}(t), \hat{\chi}^{\dagger}(t')]$. To make these equal, we have the condition $[\hat{\chi}(t), \hat{\chi}^{\dagger}(t')] = (1 - G)\delta(t - t')$. Since $1 - G < 0$, this can be satisfied if $\hat{\chi}(t) = \sqrt{G - 1}\hat{h}^{\dagger}(t)$ and $\hat{h}(t)$ is some field satisfying the standard commutation relations. Hence, the amplified output in our detection line can be described by the operator

$$\hat{a}_{\text{amp}}(t) = \sqrt{G}\hat{a}_{\text{out}}(t) + \sqrt{G - 1}\hat{h}^{\dagger}(t).$$

The added field $\hat{h}(t)$ represents the noise introduced by the amplifier. Its amount depends on the state of $\hat{h}(t)$ but it is non-zero even if $\hat{h}(t)$ is in its vacuum state. This shows that quantum mechanics requires any amplifier to add a minimal amount of noise. In the following, we will focus on this quantum-limited case, that is, $\hat{h}(t)|\psi\rangle = 0$.

The subsequent processing of the signal can be treated as purely classical. The steps, consisting of analog and digital down-conversion as described in sec. 2.3, effectively amount to multiplication of the signal by a homodyne local oscillator signal $\exp(i\omega_{\text{hom}}t)$ and subsequent low-pass filtering to obtain the complex voltage \hat{v} . In frequency space, the amplified signal is given by $\hat{V}(\omega) \propto \hat{a}_{\text{amp}}(\omega) + \hat{a}_{\text{amp}}^\dagger(-\omega)$ which after the down-conversion step becomes

$$\hat{v}(\omega) \propto \hat{a}_{\text{amp}}(\omega + \omega_{\text{hom}})f(\omega) + \hat{a}_{\text{amp}}^\dagger(-\omega - \omega_{\text{hom}})f(\omega),$$

where $f(\omega)$ is the frequency response of the low-pass filter. If its cut-off frequency ω_c is much lower than ω_{hom} , the second term can be neglected. The reason for this is that it could only be non-zero if $|\omega| \lesssim \omega_c$ which implies $-\omega - \omega_{\text{hom}} < 0$. But then $\hat{a}_{\text{amp}}^\dagger(-\omega - \omega_{\text{hom}}) = 0$ because there are no modes with negative energies. Thus, we can write the down-converted complex voltage in time domain as

$$\hat{v}(t) \propto \hat{a}_{\text{dc}}(t) + \hat{h}_{\text{dc}}^\dagger(t).$$

Here we have used the approximation $\sqrt{G-1} \approx \sqrt{G}$ and defined

$$\hat{a}_{\text{dc}}(t) \equiv (\hat{a}_{\text{out}}(t)e^{i\omega_{\text{hom}}t}) * f(t), \quad (2.6)$$

$$\hat{h}_{\text{dc}}^\dagger(t) \equiv (\hat{h}^\dagger(t)e^{i\omega_{\text{hom}}t}) * f(t). \quad (2.7)$$

A simple calculation reveals that the operators $\hat{a}_{\text{dc}}(t)$ and $\hat{h}_{\text{dc}}^\dagger(t)$ do not satisfy the standard commutation relations but instead

$$[\hat{a}_{\text{dc}}(t), \hat{a}_{\text{dc}}^\dagger(t')] = [\hat{h}_{\text{dc}}(t), \hat{h}_{\text{dc}}^\dagger(t')] = \int f(t-\tau)f(t'-\tau) d\tau.$$

If the filter is normalized such that $\int f(t) dt = 1$, then the expression in the second equation is a function $F(t-t')$ which is peaked around zero and whose integral is unity. In this sense, it approximates the Dirac delta function and we will therefore treat the operators $\hat{a}_{\text{dc}}(t)$ and $\hat{h}_{\text{dc}}^\dagger(t)$ as if they in fact do obey the normal commutation relations. We will, however, keep in mind that this is only an approximation, valid on time-scales significantly longer than the filter correlation time.

As we are dealing with quantum measurements, each single realization of the experiment has a random outcome. What is the probability distribution governing the measured voltage waveforms $v(t)$? To characterize it, let us investigate its moments – expectation values of the form $\langle \hat{v}(t_1) \dots \hat{v}(t_m) \hat{v}^\dagger(\tau_1) \dots \hat{v}^\dagger(\tau_n) \rangle$. Note that the order of the operators in this expectation value does not matter since they all commute with each other. We are therefore free to arrange them arbitrarily – for example in anti-normal order as shown here. As we have seen $\hat{v}(t) = \lambda(\hat{a}_{\text{dc}}(t) + \hat{h}_{\text{dc}}^\dagger(t))$, where λ is a proportionality constant relating the fields to voltages. Therefore the expectation value written above is equal to

$$\lambda^{m+n} \langle \psi | (\hat{a}_{\text{dc}}(t_1) + \hat{h}_{\text{dc}}^\dagger(t_1)) \dots (\hat{a}_{\text{dc}}^\dagger(\tau_1) + \hat{h}_{\text{dc}}(\tau_1)) \dots | \psi \rangle.$$

We factor out the product of operators and obtain a sum of 2^{m+n} terms. Since we assume that the noise mode \hat{h}_{dc} is in its vacuum state, any term which contains \hat{h}_{dc} or $\hat{h}_{\text{dc}}^\dagger$ results in a vanishing expectation value. We therefore get

$$\langle \hat{v}(t_1) \dots \hat{v}^\dagger(\tau_1) \dots \rangle = \lambda^{m+n} \langle \psi | \hat{a}_{\text{dc}}(t_1) \dots \hat{a}_{\text{dc}}^\dagger(\tau_1) \dots | \psi \rangle. \quad (2.8)$$

Spontaneously emitted non-classical state

We will now return to the simple example of a non-classical resonator state from eq. (2.4) being spontaneously emitted into a transmission line. The input-output formalism allows us to calculate the output field $\hat{a}_{\text{in}}(t)$ and eq. (2.6) then yields the down-converted field $\hat{a}_{\text{dc}}(t)$. The correspondence between the moments of $\hat{a}_{\text{dc}}(t)$ and the measured down-converted voltage $v(t)$, established in eq. (2.8), then indirectly characterizes the probability distribution of the measured voltage waveforms.

The resonator is prepared in a state $|\psi\rangle$ at time $t = 0$ and then continues to evolve freely. This means that $\hat{H}_0(t) = \omega_r \hat{c}^\dagger(t) \hat{c}(t)$ and the input-output relations in eq. (2.5) can be solved analytically. The output field can be expressed as:

$$\hat{a}_{\text{out}}(t) = \begin{cases} \sqrt{\kappa} \hat{c}(0) e^{-(i\omega_r + \frac{\kappa}{2})t} + \hat{a}_{\text{in}}(t) - \kappa \int_0^t \hat{a}_{\text{in}}(\tau) e^{-(i\omega_r + \frac{\kappa}{2})(t-\tau)} d\tau & \text{if } t \geq 0, \\ \hat{a}_{\text{in}}(t) - \kappa \int_{-\infty}^t \hat{a}_{\text{in}}(\tau) e^{-(i\omega_r + \frac{\kappa}{2})(t-\tau)} d\tau & \text{if } t < 0. \end{cases}$$

The term proportional to $\hat{c}(0)$ represents the initial state of the resonator being emitted into the transmission line with an exponential envelope, whereas the terms involving \hat{a}_{in} are the input field reflected from the resonator. For simplicity, we will combine them into a single operator $\hat{a}_{\text{refl}}(t)$ which satisfies

$$[\hat{a}_{\text{refl}}(t), \hat{a}_{\text{refl}}^\dagger(t')] = \delta(t - t') - \kappa \Theta(t) \Theta(t') e^{-i\omega_r(t-t') - \frac{\kappa}{2}(t+t')}.$$

Note that these commutation relations ensure that $[\hat{a}_{\text{out}}(t), \hat{a}_{\text{out}}^\dagger(t')] = \delta(t - t')$. The down-converted field \hat{a}_{dc} can now be written as

$$\begin{aligned} \hat{a}_{\text{dc}}(t) &= \hat{c}A(t) + \hat{a}_{\text{refl,dc}}(t), \text{ where} \\ A(t) &= \sqrt{\kappa} \Theta(t) e^{-\kappa t/2} * f(t) \text{ and} \\ \hat{a}_{\text{refl,dc}}(t) &= \hat{a}_{\text{refl}}(t) e^{i\omega_r t} * f(t). \end{aligned}$$

To simplify our notation, we have omitted the time argument from $\hat{c}(0)$ and from now on we will denote this operator only as \hat{c} .

According to eq. (2.8), the moments of the measured voltage waveform are given by the anti-normally ordered moments of $\hat{a}_{\text{dc}}(t)$. Now that we know the explicit form of $\hat{a}_{\text{dc}}(t)$, what does it reveal about the probability distribution of the random variable $v(t)$?

The so-called *optical equivalence theorem* (Cahill & Glauber, 1969) implies that there exists a quasi-probability distribution on the space of complex-valued functions $\alpha_{\text{dc}}(t)$ such that the moments of $\alpha_{\text{dc}}(t)$ under said distribution are identical to the anti-normally ordered moments of $\hat{a}_{\text{dc}}(t)$.

This distribution is the *Husimi Q function* which for a given state $\hat{\rho}$ is expressed as

$$Q(\alpha) = \frac{1}{\pi} \langle \alpha_{\text{dc}} | \hat{\rho} | \alpha_{\text{dc}} \rangle.$$

Here $|\alpha_{\text{dc}}\rangle$ is the multi-mode coherent state defined as the eigenstate of the operators $\hat{a}_{\text{dc}}(t)$ such that $\hat{a}_{\text{dc}}(t)|\alpha_{\text{dc}}\rangle = \alpha_{\text{dc}}(t)|\alpha_{\text{dc}}\rangle$.

As shown above, $\hat{a}_{\text{dc}}(t)$ is a sum of $\hat{c}A(t)$ and $\hat{a}_{\text{refl,dc}}(t)$. We will assume that the input field incident on the resonator is in the vacuum state, that is, the system is in a product state of the form $\hat{\rho}_r \otimes |0\rangle\langle 0|$, where $\hat{\rho}_r$ is the state of the resonator. This means that any moment of \hat{c} and $\hat{a}_{\text{refl,dc}}(t)$ factorizes into a product of the moments of the two operators. The quasi-probability generating the anti-normally ordered moments is therefore a convolution of the two corresponding Q functions. Consequently, the measured waveform $v(t)$ is, up to scaling by λ , the sum of two independent random functions:

$$\frac{1}{\lambda}v(t) = cA(t) + \alpha_{\text{refl,dc}}(t). \quad (2.9)$$

Here c is a random variable with a probability distribution

$$\Pi(c) = \frac{1}{\pi} \langle c | \hat{\rho}_r | c \rangle.$$

The second term $\alpha_{\text{refl,dc}}(t)$ is a random process whose moments are equal to the anti-normally ordered vacuum moments of $\hat{a}_{\text{refl,dc}}(t)$. According to *Wick's theorem* (Wick, 1950), each of these moments can be written as a sum of terms involving only second-order expectation values of the form $\langle 0 | \hat{a}_{\text{refl,dc}}(t) \hat{a}_{\text{refl,dc}}^\dagger(t') | 0 \rangle$. This property is fully analogous to that exhibited by Gaussian random variables, as expressed by *Isserlis' theorem* (Isserlis, 1918). From here it follows that $\alpha_{\text{refl,dc}}(t)$ is a Gaussian random process with zero mean, fully characterized by its covariances

$$\begin{aligned} \langle \alpha_{\text{refl,dc}}^*(t) \alpha_{\text{refl,dc}}(t') \rangle &= \langle 0 | \hat{a}_{\text{refl,dc}}(t) \hat{a}_{\text{refl,dc}}^\dagger(t') | 0 \rangle \\ &= \int f(t - \tau) f(t' - \tau) d\tau - A(t)A(t'). \end{aligned} \quad (2.10)$$

We can illustrate the results derived above with a plot of a randomly generated trace $v(t)$ for the resonator prepared in the single-photon Fock state $|1\rangle$. The exponential envelope $\sqrt{\kappa}\Theta(t)e^{-\kappa t/2}$ of the emitted state together with the filtered envelope $A(t)$ are shown in Fig. 2.11(a). A single realization of the detected waveform $v(t)$, generated according to eq. (2.9) as a sum of the reflected transmission-line noise $\alpha_{\text{refl,dc}}(t)$ and the resonator contribution $cA(t)$, is shown by the orange line in Fig. 2.11(b). The underlying density plot shows the marginal probability densities of one of the quadratures $v(t)$ for each individual t . We see that at times $t < 0$, before the emission of the photon, the distribution is stationary and Gaussian. Around time $t = 0$, the variance of the signal quadrature suddenly increases and then gradually falls off, approaching again the original level of the vacuum noise.

This example also illustrates that with the chosen filter, whose kernel is considerably shorter than $1/\kappa$, the signature of the single additional photon is rather subtle in comparison with the underlying noise. The nature of this problem can be seen from the form of eq. (2.9). Only the first term $cA(t)$ contains any information about the state of the resonator field. The second term represents added noise. The relative size of the two terms is influenced by the choice of the filter $f(t)$. A filter which is very wide in frequency space will fully transmit the signal but also a large amount of the white vacuum noise. A narrow-bandwidth filter will be more efficient at blocking

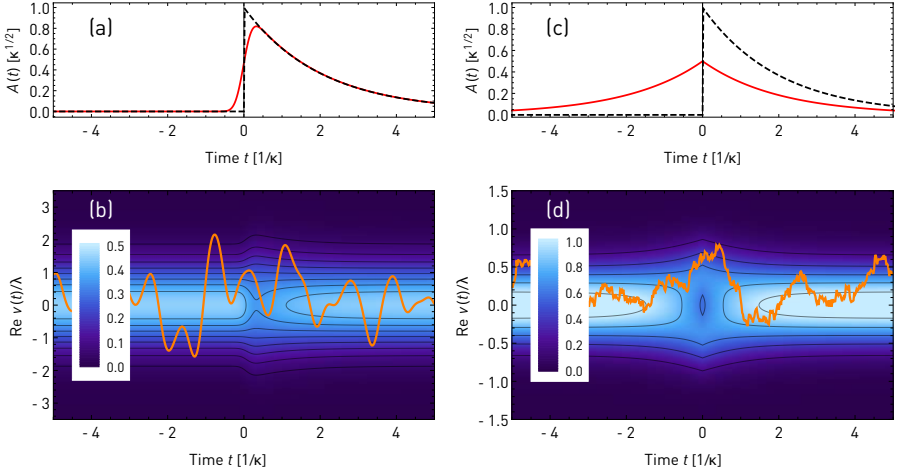


Figure 2.11: (a) The exponential envelope of the emitted field (dashed black) and the corresponding filtered envelope (solid red). The used filter is Gaussian with a kernel $f(t) \propto \exp(-4\kappa t^2)$. (b) One random realization of the observed waveform $v(t)$ (in orange) emitted by the resonator, initially prepared in the single-photon Fock state $|1\rangle$. The signal is filtered with the Gaussian filter from (a). Each vertical slice through the underlying density plot represents the marginal probability density of $v(t)$ at that particular time t . (c,d) Plots equivalent to (a,b) with the optimal filter given by $f(t) \propto \Theta(-t) \exp(\kappa t/2)$.

the noise but if it is too narrow, it may also block some of the signal. To see how to find a compromise between the two extremes, we will consider a single point of the measured waveform, say $v(t=0)$, and try to optimize its signal-to-noise ratio.

The signal component in eq. (2.9) depends on the filter through the scaling factor $A(0)$ while the variance of the added noise is given by eq. (2.10) as $\int f^2(\tau) d\tau - A^2(0)$. The noise variance relative to the signal is therefore proportional to

$$\frac{\int f^2(\tau) d\tau}{\left(\int f(\tau) \sqrt{\kappa} \Theta(-\tau) e^{\kappa\tau/2} d\tau\right)^2} - 1.$$

If we define a scalar product between two functions f and g as $\langle f, g \rangle \equiv \int f(\tau) g(\tau) d\tau$, the expression above can be written as $\langle f, f \rangle / \langle f, g \rangle^2 - 1$, where $g(\tau) = \sqrt{\kappa} \Theta(-\tau) e^{\kappa\tau/2}$. According to the Cauchy-Schwarz inequality, this expression is bounded from below by $1 / \langle g, g \rangle^2 - 1 = 0$. The minimal value of zero is reached if $f \propto g$. The optimal filter is therefore one whose kernel is the time-inverse of the exponentially decaying envelope of the emitted field.

Fig. 2.11(c,d) shows an example of a waveform and the corresponding marginal probability densities resulting from such optimal filtering. The distribution of the

voltage values at $t = 0$ clearly deviates from the classical Gaussian case much more than for the suboptimal filter presented in Fig. 2.11(a,b). This is true despite the fact that, as evidenced by the fast fluctuations in the trace shown in Fig. 2.11(d), the reverse exponential filter is not nearly as efficient at removing higher frequency noise components as the Gaussian filter used in Fig. 2.11(b).

We can also see that the optimal filter is perfectly mode-matched. Indeed, from eq. (2.10) we conclude that the variance of $\alpha_{\text{refl,dc}}(t)$ vanishes at $t = 0$ and this filter therefore completely eliminates all modes but the one into which the resonator field is emitted. Eq. (2.9) then simplifies to $v(0) \propto c$ and the measurement of $v(0)$ with the mode-matched filter directly reveals the Q function of the resonator's initial state.

Extracting field moments in the presence of noise

In real measurements, various imperfections of the detection process usually prevent us from reaching the ideal quantum limit. This is most often caused by losses in the detection chain and excess noise added by the amplifiers. Imperfect mode-matching also contributes to reduced efficiency of the measurement.

All these effects, even though very distinct from each other in their underlying mechanisms, can be described with a simple effective model: An imperfect detection chain is equivalent to a perfect one, followed by addition of noise to the measurement outcome. We have seen that in the quantum limit, a signal processed by an ideal mode-matched filter is distributed according to the photon state's Q function. This means that $v(0)$, which we will denote simply by v for the sake of brevity, can be described as an observable $\hat{v} = \lambda(\hat{c} + \hat{h}^\dagger)$ where the noise mode \hat{h} is in its vacuum state³. To generalize this result to a noisy detection chain, we simply allow the noise mode to be in an arbitrary state. The most typical case of excess noise which is Gaussian-distributed can be described by letting the noise mode be in a thermal state.

Since \hat{v} and \hat{v}^\dagger commute with each other, we have once again the freedom of arranging the terms in the moments $\langle (v^*)^m v^n \rangle = \langle (\hat{v}^\dagger)^m \hat{v}^n \rangle$ as we wish. Placing the operators \hat{v} on the right yields an expansion of the moment into a sum of products involving normally ordered moments of \hat{c} and anti-normally ordered moments of \hat{h} :

$$\langle (v^*)^m v^n \rangle = \lambda^{m+n} \sum_{i,j} \binom{m}{i} \binom{n}{j} \langle (\hat{c}^\dagger)^i \hat{c}^j \rangle \langle \hat{h}^{m-i} (\hat{h}^\dagger)^{n-j} \rangle. \quad (2.11)$$

If the moments of v are measured when the resonator is prepared in its vacuum state, the normally ordered moments of \hat{c} are all zero and the resulting expectation value $\langle (v^*)^m v^n \rangle_0$ simplifies to

$$\langle (v^*)^m v^n \rangle_0 = \lambda^{m+n} \langle \hat{h}^m (\hat{h}^\dagger)^n \rangle.$$

Such a reference measurement in the absence of the signal therefore allows us to determine the anti-normally ordered moments of the noise operator \hat{h} . Once these are

³Note that the proportionality constant λ is not the same as the one in eq. (2.8), since in the current context it also contains the filter coefficient $A(0)$.

known, eq. (2.11) can be inverted (Menzel *et al.*, 2010; Eichler *et al.*, 2012a; Eichler, 2013) to calculate the moments of \hat{c} . The scaling coefficient λ is usually determined from a calibration measurement in which one of the moments, typically $\langle \hat{c}^\dagger \hat{c} \rangle$, is assumed to be known.

It is important to note that this simple version of the subtraction scheme relies on \hat{c} being in the vacuum state during the reference measurement. In some instances, this assumption may not be completely justified. For example, if thermal excitations of the system cannot be neglected, it would be more appropriate to describe \hat{c} as being in a thermal state. In this case, we need to estimate the mean number of photons n_{th} in the thermal state and then calculate the noise moments of \hat{h} from the reference measurement moments of v by inverting the relations

$$\langle (v^*)^m v^n \rangle_0 = \lambda^{m+n} \sum_{i,j} \binom{m}{i} \binom{n}{j} \langle (\hat{c}^\dagger)^i \hat{c}^j \rangle_{\text{th}} \langle \hat{h}^{m-i} (\hat{h}^\dagger)^{n-j} \rangle,$$

where $\langle \cdot \rangle_{\text{th}}$ are thermal moments corresponding to n_{th} .

In practice, we obtain the moments using our FPGA-based setup by recording histograms of the single shot voltages and subsequently calculating the moments in software. In measurements of this type, it is extremely important for the detection chain to have good noise performance. As discussed in da Silva *et al.* (2010), the number of measurements needed to estimate a moment of order m with a given accuracy scales with the variance σ^2 of the added noise as σ^{2m} . For this reason, Josephson parametric amplifiers (JPA) are commonly used for measurements of higher order moments. Reducing σ^2 from the level of a few tens of noise photons to single photons by adding a JPA can easily shorten the needed measurement time from over a day to only a few minutes.

Photon state tomography

The techniques described so far allow us to measure the various moments of the resonator mode \hat{c} . To extract the density matrix of the resonator state, we can use one of several approaches described in more detail by Eichler *et al.* (2012a). One of these methods is based on a maximum likelihood estimate. Given a set of measured moments $\langle (\hat{c}^\dagger)^m \hat{c}^n \rangle$, we define a cost function which quantifies how well a given density matrix $\hat{\rho}$ reproduces these moments. This cost function is usually defined as

$$C(\hat{\rho}) \equiv - \sum_{m,n} \frac{1}{\sigma_{mn}^2} |\langle (\hat{c}^\dagger)^m \hat{c}^n \rangle - \text{Tr} \hat{\rho} (\hat{c}^\dagger)^m \hat{c}^n|^2$$

and can be interpreted as the log-likelihood function. The different moments are weighted inversely with their variances σ_{mn}^2 .

The density matrix is then estimated by maximizing $C(\hat{\rho})$. To ensure that the resulting density matrix is physical, that is, positive semi-definite and with a trace equal to one, we need to enforce these conditions in the optimization algorithm. This can be done using methods of semi-definite programming (Vandenberghe & Boyd,

1996) or by parametrizing the density matrix in a way which makes it satisfy the constraints identically.

One such parametrization is given by the Cholesky decomposition (James *et al.*, 2001): Any positive semi-definite matrix can be written in the form $\hat{T}^\dagger \hat{T}$, where \hat{T} is upper-triangular with real non-negative elements on the diagonal (in some orthonormal basis). Therefore any matrix of the form

$$\hat{\rho} \equiv \frac{\hat{T}^\dagger \hat{T}}{\text{Tr} \hat{T}^\dagger \hat{T}}, \text{ where}$$

$$\hat{T} = \begin{pmatrix} t_1 & t_2 + it_3 & t_4 + it_5 & \dots \\ 0 & t_{2d} & t_{2d+1} + it_{2d+2} & \dots \\ 0 & 0 & t_{4d-3} & \dots \\ \vdots & \vdots & \vdots & \ddots \end{pmatrix} \text{ with } t_j \in \mathbb{R}$$

is a valid density matrix and conversely, any valid density matrix can be parametrized in this form.

Experiments

Chapter 3

Multi-qubit gates induced by steered resonator field

The first experiment on which I worked as part of my PhD studies was an extension of my master thesis work (Pechal, 2011). There, we observed the geometric phase of a harmonic oscillator, using a transmon qubit as an auxiliary system to facilitate measurements of the phase. The results of this experiment are described in Pechal *et al.* (2012). In a follow-up work, we then realized a proof-of-principle measurement of the geometric phase in a system with a resonator coupled to two qubits. This experiment was motivated by the potential applications of such protocols for multi-qubit gates, such as have been demonstrated in systems of trapped ions by Leibfried *et al.* (2003).

3.1 Geometric phase

Geometric phase is an intriguing phenomenon arising in quantum mechanics due to certain non-trivial properties of complex Hilbert spaces. It reveals close and perhaps rather unexpected relations between quantum mechanics and differential geometry (Isham, 1999). Within the quantum-mechanical framework, it was first described by Berry (1984) but it was soon discovered to be intimately linked with other geometric phenomena in physics, such as the polarization of light (Pancharatnam, 1956). Even though it was first discussed in the context of adiabatic quantum evolution, it can be described more generally for any unitary evolution (Aharonov & Anandan, 1987).

Let us consider a quantum system evolving under the influence of a slowly varying Hamiltonian $\hat{H}(t)$. If the system is initially prepared in one of the energy eigenstates, then according to the adiabatic theorem (Born & Fock, 1928), its state will simply follow the instantaneous eigenstate of the changing Hamiltonian. The eigenstates of a Hamiltonian are, however, not uniquely defined – we have the freedom of multiplying them by arbitrary phase factors. The adiabatic theorem therefore does not fully describe the evolution of the system.

To illustrate the nature of this ambiguity, we can consider the problem at hand from a more abstract perspective of differential geometry. The Hilbert space \mathcal{H} ,

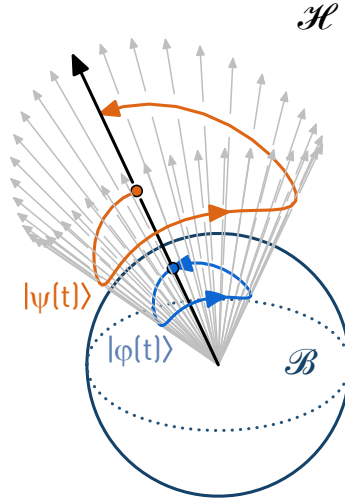


Figure 3.1: Illustration of the fiber bundle formalism. The Hilbert space \mathcal{H} is decomposed into fibers (some of which are represented by the grey arrows) of states differing only by a complex scaling factor. A single representative vector is chosen from each fiber to form the base space \mathcal{B} . Adiabatic evolution of the Hamiltonian specifies a trajectory $|\varphi(t)\rangle$ (in blue) in the base space. The evolution of the state vector is described by a path (in orange) in the Hilbert space such that its every point $|\psi(t)\rangle$ belongs to the same fiber as the corresponding $|\varphi(t)\rangle$.

consisting of all possible (not necessarily normalized) state vectors, can be naturally split into *fibers* – sets of vectors which differ only by multiplication with a complex coefficient. Vectors residing in the same fiber are physically indistinguishable from each other and we can therefore arbitrarily choose one vector from each fiber to represent all *physically distinct* states. The set of all these representative vectors then forms a *base space* \mathcal{B} and the full Hilbert space can be seen as a *fiber bundle* – a collection of fibers embedded at each point of the base space.

Taking some liberty with regard to mathematical accuracy, we can visualize this construction with the help of Fig. 3.1. The base space is represented by the surface of a sphere while the fibers are identified with rays emanating from the center. The evolution of the Hamiltonian determines a path $|\varphi(t)\rangle$ in the base space, shown in blue. The adiabatic theorem then states that the path taken by the state vector $|\psi(t)\rangle$ in the Hilbert space is such that its projection along the fibers onto the base space coincides with $|\varphi(t)\rangle$. There are infinitely many such paths, each of the form $|\psi(t)\rangle = e^{i\theta(t)}|\varphi(t)\rangle$, where $\theta(t)$ is an arbitrary function of time. One of the possible paths $|\psi(t)\rangle$ is indicated in Fig. 3.1 in orange. How can we find the one path which the state of the system actually takes in \mathcal{H} ?

To answer this question, we substitute $|\psi(t)\rangle = e^{i\theta(t)}|\varphi(t)\rangle$ into the Schrödinger equation and multiply the result from the left by $\langle\varphi(t)|$. This results in

$$\frac{d}{dt}\theta(t) = -\langle\varphi(t)|\hat{H}(t)|\varphi(t)\rangle + i\langle\varphi(t)|\frac{d}{dt}|\varphi(t)\rangle. \quad (3.1)$$

The first term on the right-hand side corresponds to the familiar *dynamical phase*, accumulated by a state at a rate given by its energy expectation value. The presence of a second term in this equation is not entirely surprising – in fact, it is necessary for the following reason: The phase on the left-hand side is *gauge-dependent*: it depends on the particular choice of our base space, that is, of the reference states $|\varphi(t)\rangle$ with respect to which the phase θ is specified. The expectation value $\langle\varphi(t)|\hat{H}(t)|\varphi(t)\rangle$, on the other hand, is gauge-independent. We should therefore expect there to be another gauge-dependent term on the right-hand side, in order to make the equation valid regardless of the gauge choice.

This could lead us to believe that the presence of the second term is an artifact of our gauge choice and that we could eliminate it by picking the “right” gauge. As it turns out, this is in general impossible. To see this, consider a case when the Hamiltonian evolves cyclically, such that $\hat{H}(T) = \hat{H}(0)$. Then the path $|\varphi(t)\rangle$ in the base space is closed and the phase difference $\Delta\theta \equiv \theta(T) - \theta(0)$ becomes gauge-independent. Thus, also the integral of the second term in eq. (3.1) from $t = 0$ to $t = T$ needs to be independent of the gauge.

This component of the phase $\Delta\theta$ accumulated by the state during a cyclic evolution is the *geometric phase*

$$\gamma \equiv \int_0^T i\langle\varphi(t)|\frac{d}{dt}|\varphi(t)\rangle dt.$$

From the form of the integrand, we can see that γ is invariant under re-parametrization of the path $|\varphi(t)\rangle$. That is, we can choose any parameter $\lambda = f(t)$ and replace the derivative d/dt by $d/d\lambda$ and integrate over λ instead of t . This means that γ is truly a geometric quantity in the sense that it depends only on the trajectory which $|\varphi(t)\rangle$ takes in the base space and not on the exact time evolution. We will emphasize this by rewriting the equation above in a parameter-less form

$$\gamma = \int_{\Gamma} i\langle\varphi|d|\varphi\rangle. \quad (3.2)$$

The integration is performed over the trajectory Γ of $|\varphi\rangle$ in \mathcal{B} .

It is widely believed that the independence of the geometric phase on the speed of the evolution and on the energy of the system makes it a useful resource for constructing quantum gates. Its geometric nature makes it insensitive to certain types of noise – a feature which has been demonstrated in recent experiments with transmon qubits by Berger *et al.* (2013).

3.2 Geometric phase in a harmonic oscillator

The evolution of a coherently driven harmonic oscillator is described by a time-dependent coherent state $|\psi(t)\rangle = e^{i\theta(t)}|\alpha(t)\rangle$. If its trajectory $\alpha(t)$ in the phase

space is known, the phase $\theta(t)$ can be calculated as a sum of the dynamical phase

$$\delta = - \int \langle \alpha(t) | \hat{H}(t) | \alpha(t) \rangle \quad (3.3)$$

and the geometric phase γ given by eq. (3.2). Coherent states defined in the standard way (Walls & Milburn, 2008) satisfy the identity $\langle \alpha | d | \alpha \rangle = (\alpha^* d\alpha - \alpha d\alpha^*)/2$. The geometric phase therefore takes the particularly simple form

$$\gamma = -2A_\Gamma, \quad (3.4)$$

where A_Γ is the area which the curve Γ traced by $\alpha(t)$ encloses in the phase space. This area is defined to be positive for counter-clockwise curves. If Γ is not closed, the area is calculated for a region obtained after extending Γ by two linear segments connecting its two end-points with the origin at $\alpha = 0$.

The phase θ is not directly observable and in the original single-qubit experiment (Pechal *et al.*, 2012), we made use of a transmon qubit whose dispersive coupling to the resonator causes the path Γ to depend on the state of the qubit. As a result, θ is also qubit-state-dependent. The qubit-resonator system evolves according to

$$\begin{aligned} |g\rangle \otimes |0\rangle &\xrightarrow{\text{following } \Gamma_g} e^{i\theta_g} |g\rangle \otimes |0\rangle, \\ |e\rangle \otimes |0\rangle &\xrightarrow{\text{following } \Gamma_e} e^{i\theta_e} |e\rangle \otimes |0\rangle, \\ &\vdots \end{aligned}$$

Here, we assume that the system is driven in such a way that all the individual trajectories $\Gamma_g, \Gamma_e, \dots$ are closed, starting and ending in the vacuum state $|0\rangle$. Thus, even though the qubit and the resonator are entangled with each other during the evolution, they return to a product state at the end. Effectively, this process implements a phase gate acting on the qubit and the induced phase $\theta_e - \theta_g$ can be measured by applying the gate to a superposition state $(|g\rangle + |e\rangle)/\sqrt{2}$ and performing qubit tomography (see sec. 2.5) on the resulting state.

The multi-qubit extension of this scheme is straightforward – the resonator mode is dispersively coupled to multiple qubits and the path Γ taken by the coherent state is therefore a function of the collective qubit state. In general, the resulting phase θ cannot be decomposed into a sum of single-qubit components and the phase gate implemented in this way is therefore a genuine multi-qubit operation.

In the case of two qubits, this statement can be expressed mathematically using the combination of phases

$$\theta_{2Q} \equiv \theta_{gg} + \theta_{ee} - \theta_{ge} - \theta_{eg}, \quad (3.5)$$

where $\theta_{gg}, \theta_{ee}, \dots$ are the phases accumulated by the resonator when the qubits are in the states $|gg\rangle, |ee\rangle, \dots$, respectively. It can be easily shown that any combination of single-qubit phase gates results in $\theta_{2Q} = 0$. Moreover, any two operations with the same value of θ_{2Q} can be converted to each other using single-qubit gates.

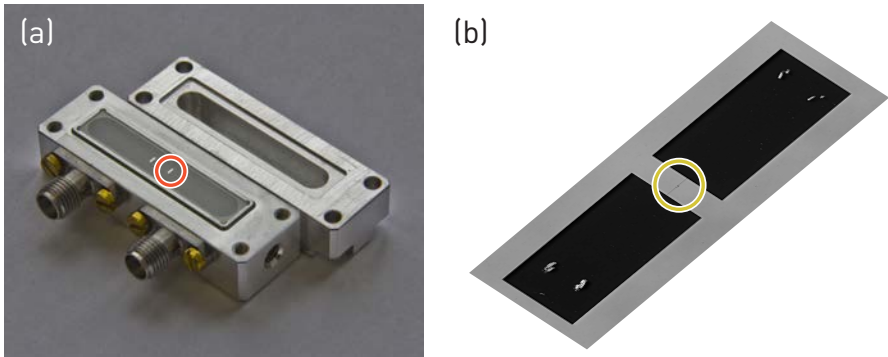


Figure 3.2: (a) Photograph of an open aluminium 3d cavity with a sapphire chip containing two transmon qubits. One of the qubits is indicated by the red circle. (b) Close-up photograph of the transmon qubit. The two rectangular pads are the transmon islands, connected by a Josephson junction whose position is indicated by the yellow circle. The light marks on the pads are scratches from the probes used in a room-temperature measurement of the junction resistance.

In the case of the driven harmonic oscillator, the displacement of the coherent state $\alpha(t)$ scales linearly with the drive amplitude ε . The accumulated phase therefore grows as ε^2 and by choosing a proper scaling of ε , we can in principle realize operations with arbitrary values of θ_{2Q} . This means that the protocol outlined above, augmented by single-qubit operations, can be used to implement *arbitrary two-qubit controlled phase gates*.

Unlike other types of multi-qubit gates (DiCarlo *et al.*, 2009; Mariantoni *et al.*, 2011b; Fedorov *et al.*, 2012), this realization does not require frequency tuning of the qubits. It is therefore very well suited for example for 3d cavity architectures which often operate with fixed-frequency qubits. It can also be generalized in a relatively straightforward way to gates operating on more than two qubits. However, these appealing features come at a cost: The weakness of the dispersive coupling in comparison with the resonant Jaynes-Cummings coupling means that gates based on the former are generally slower. The speed of dispersive gates is also restricted by the limited displacement of the resonator mode, which needs to be sufficiently low to keep the dispersive approximation valid.

We investigated two specific implementations of the outlined phase gate protocol: an adiabatic and a non-adiabatic one. Both were realized in systems consisting of a 3d cavity coupled to two transmon qubits. One of these samples is shown in Fig. 3.2.

The basic principle of the adiabatic protocol is very similar to the experiment described in Pechal *et al.* (2012). Due to the necessity to vary the Hamiltonian of the system adiabatically, we were forced to work with drive pulse lengths of 500 ns and longer – a significant fraction of the qubits’ coherence times which were on the order of a few microseconds. This severely limited the fidelities of the resulting operations

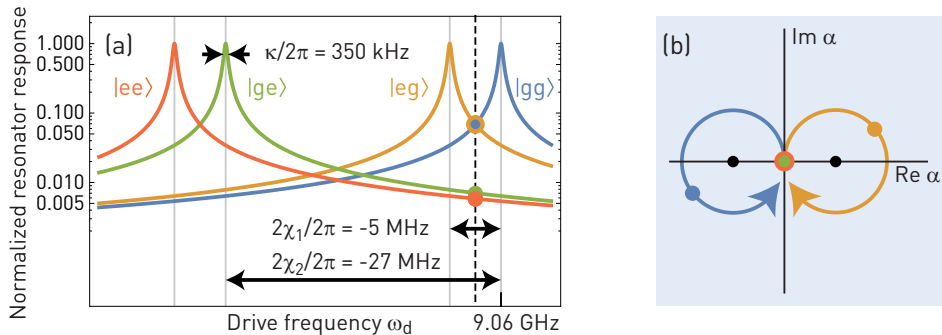


Figure 3.3: (a) Voltage response of the resonator in the non-adiabatic protocol, normalized to the on-resonance value, shown for the four two-qubit states. Indicated are the dispersive shifts $2\chi_1, 2\chi_2$ and the resonator FWHM linewidth κ . The drive frequency, shown by the black dashed line, was chosen to lie between the resonance frequencies of the resonator corresponding to two-qubit states $|eg\rangle$ and $|gg\rangle$. (b) Trajectories followed by the coherent state of the resonator in phase space for the two states $|eg\rangle$ and $|gg\rangle$. The black dots indicate the corresponding displaced ground states. For the other two states $|ge\rangle$ and $|ee\rangle$, the drive detuning is large enough that the resonator may be assumed to remain in the vacuum state.

and the reduced coherence led to significant uncertainties in the estimates of the accumulated phases. For these reasons, we singled out the non-adiabatic protocol as a more viable candidate for a potential implementation of a two-qubit gate.

3.3 Non-adiabatic protocol

For the non-adiabatic protocol, we employed a sample in which a mode of the 3d cavity at a frequency of 9.05 GHz and with a full-width-half-maximum linewidth of 350 kHz was dispersively coupled to two qubits at fixed frequencies of 8.09 GHz and 6.55 GHz. The measured anharmonicities of the qubits were -310 MHz and -380 MHz, respectively. The dispersive shifts of the qubit frequencies per single photon were $2\chi_1/2\pi = -5$ MHz and $2\chi_2/2\pi = -27$ MHz. The relations between the different frequencies are shown graphically in Fig. 3.3(a).

If we neglect dissipation effects in the resonator, the evolution of the system is described by the Hamiltonian

$$\hat{H}(t)/\hbar = \delta_r \hat{a}^\dagger \hat{a} + \frac{1}{2}(\varepsilon(t) \hat{a}^\dagger + \text{H.c.}).$$

Here δ_r is the detuning between the drive and the resonator frequency, dependent on the state of the qubits, and $\varepsilon(t)$ is the drive coefficient, related to the amplitude $V(t)$

and phase $\phi(t)$ of the drive signal by

$$\varepsilon(t) \propto V(t)e^{i\phi(t)}.$$

The proportionality constant in this relation depends on the details of the microwave line used to drive the resonator. In the scheme described here, the drive pulse has a square shape with a constant amplitude and phase. In this case, the Hamiltonian is time-independent and can be written as

$$\hat{H}/\hbar = \delta_r(\hat{a} - \beta)^\dagger(\hat{a} - \beta) - \delta_r|\beta|^2,$$

where $\beta = -\varepsilon/2\delta_r$. A coherent state $|\alpha(t)\rangle$ evolves under this Hamiltonian according to

$$\alpha(t) - \beta = (\alpha(0) - \beta)e^{-i\delta_r t}. \quad (3.6)$$

This means that the displacement $\alpha(t)$ of the coherent state in phase space rotates around the ground state β with an angular frequency δ_r . If the system is initially in the vacuum state, $\alpha(t)$ can be expressed as $\alpha(t) = \beta(1 - e^{-i\delta_r t})$. The coherent state then describes a circle with a radius $|\beta|$.

As mentioned above, the phase gate protocol relies on the state of the resonator returning back to the vacuum state at the end of its evolution, independently of the qubit state. This means that $\delta_r T$, where T is the duration of the drive pulse, needs to be an integer multiple of 2π for all the values of δ_r corresponding to the four two-qubit states. In general, this condition cannot be satisfied unless the two dispersive shifts are such that χ_1/χ_2 is a rational number. Additionally, for the required pulse time T to be reasonably short, χ_1/χ_2 should be equal to a ratio of two small integers.

Since this was not the case for our sample, we made use of the following approximation. We set the drive frequency to the mean of the resonance frequencies corresponding to the qubit states $|gg\rangle$ and $|eg\rangle$, as illustrated in Fig. 3.3(a). This choice ensures that $\delta_r^{(gg)} = -\delta_r^{(eg)}$. Moreover, as the dispersive shift of the resonator caused by qubit 2 is much larger than for qubit 1, we have $|\delta_r^{(eg)}|, |\delta_r^{(ee)}| \gg |\delta_r^{(gg)}|, |\delta_r^{(eg)}|$. Therefore, the radius of the circular trajectory described by the coherent state when the qubit is in one of the states $|eg\rangle, |ee\rangle$ is much smaller than when it is in $|gg\rangle$ or $|eg\rangle$. For this reason, we relax the periodicity condition in the cases of $|eg\rangle$ and $|ee\rangle$ and assume that even if the resonator state does not undergo an integer number of cycles, its displacement from the vacuum state can be neglected. Since the detunings $\delta_r^{(gg)}$ and $\delta_r^{(eg)}$ have the same magnitude, we can satisfy the periodicity condition for the remaining two states by choosing T such that $\delta_r^{(gg)}T = 2\pi$. In our case, this means $T = 390$ ns.

The resulting trajectories traced by the coherent states in phase space are shown in Fig. 3.3(b). For qubit states $|gg\rangle$ and $|eg\rangle$, they have the same radius of $|\varepsilon|/2|\delta_r^{(gg)}|$ but opposite orientations. As the resonator is blue-detuned from the drive when the qubits are in their ground states, the corresponding trajectory for $\delta_r > 0$ given by eq. (3.6) has a negative orientation. This implies that the geometric phase calculated from eq. (3.4) is $\gamma_{gg} = -\gamma_{eg} = \pi|\varepsilon|^2/2|\delta_r^{(gg)}|^2$. The expectation value of the Hamiltonian is constant and equal to zero and therefore the dynamical phase expressed by the

integral in eq. (3.3) vanishes. Hence, the total phase accumulated by the resonator for the four different two-qubit states is

$$\begin{aligned}\theta_{gg} &= -\theta_{eg} = \frac{\pi|\varepsilon|^2}{2|\delta_r^{(gg)}|^2}, \\ \theta_{ge} &= \theta_{ee} = 0.\end{aligned}$$

In the experiment, the phases accumulated by the two-qubit states were determined from a simple interferometric measurement. First, we prepared the system in the superposition state $(|gg\rangle + |eg\rangle + |ge\rangle + |ee\rangle)/2$ by applying $\pi/2$ pulses to both qubits. After the resonator undergoes its cyclic evolution, the resulting state

$$\frac{1}{2} (e^{i\theta_{gg}}|gg\rangle + e^{i\theta_{eg}}|eg\rangle + e^{i\theta_{ge}}|ge\rangle + e^{i\theta_{ee}}|ee\rangle)$$

was characterized using state tomography (see sec. 2.5). The phases are related to the off-diagonal elements of the reconstructed density matrix $\hat{\rho}$ by $\theta_i - \theta_j = \arg\langle i|\hat{\rho}|j\rangle$, where $i, j \in \{gg, eg, ge, ee\}$. The interaction phase θ_{2Q} defined by eq. (3.5) can therefore be expressed as

$$\theta_{2Q} = \arg\langle ge|\hat{\rho}|gg\rangle + \arg\langle eg|\hat{\rho}|gg\rangle - \arg\langle ee|\hat{\rho}|gg\rangle. \quad (3.7)$$

The measured dependence of θ_{2Q} on the amplitude V of the drive pulse is shown in Fig. 3.4(a). We can see that the data agree very well with a quadratic fit of the form $a_2V^2 + a_0$ represented by the solid black line. However, unlike the theoretical prediction of

$$\theta_{2Q} = \frac{\pi|\varepsilon|^2}{|\delta_r^{(gg)}|^2} \propto V^2,$$

the fitted quadratic function has a significant constant offset $a_0 \neq 0$. In other words, even for $V = 0$ when no pulse is applied, the two qubits become entangled. This is caused by direct $\sigma_z\sigma_z$ -type coupling between the two qubits which can be described by a term $J\hat{\sigma}_z \otimes \hat{\sigma}_z$ added to the Hamiltonian. This term induces frequency shifts of the four two-qubit states which cannot be decomposed into sums of single-qubit components. As a result, the states $|gg\rangle, |ee\rangle$ accumulate a phase $-JT$ over a time period T while the phase accumulated by $|ge\rangle$ and $|eg\rangle$ is $+JT$. This leads to an additional contribution of $-4JT$ to the two-qubit phase θ_{2Q} .

To verify this, we performed a measurement where the qubits were again prepared in an equal superposition of the four computational states and then their state was read out after a variable waiting time T by qubit tomography. The resulting two-qubit phase θ_{2Q} as a function of T is plotted in Fig. 3.4(b). As expected, its dependence on T is linear, corresponding to $J/2\pi = -77.4$ kHz.

The two-qubit phase component induced by the resonator drive pulse reaches a value of π at a pulse amplitude of approximately 0.31. The resulting state of the two qubits. We extracted the density matrix of the resulting two-qubit state and plotted the absolute values of its matrix elements in Fig. 3.4(c). For an ideal equal superposition state of all four computational states, all 16 of these values should be equal to

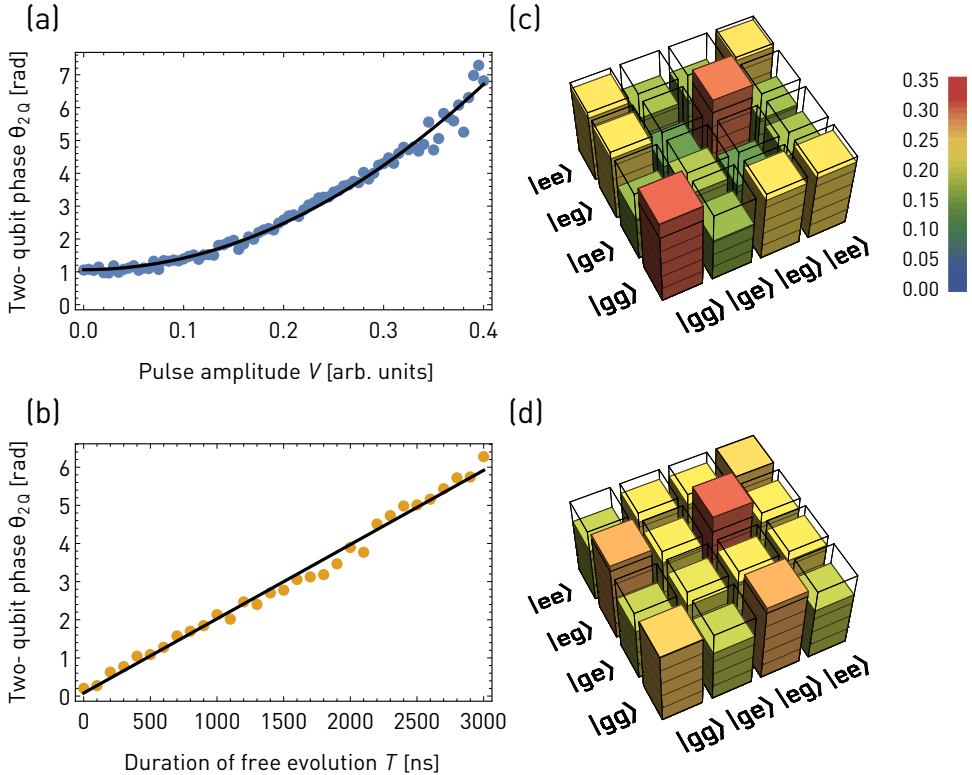


Figure 3.4: (a) Two-qubit phase θ_{2Q} calculated from eq. (3.7) as a function of the pulse amplitude V in the non-adiabatic protocol. The amplitude is expressed relative to the full range of the arbitrary waveform generator output, in this case ± 400 mV. The black line represents a quadratic fit of the form $a_2 V^2 + a_0$. (b) Two-qubit phase accumulated during free evolution due to $\sigma_z \sigma_z$ -type coupling between the qubits. The black line is a linear fit. (c) Absolute values of the density matrix elements of the final state for a pulse amplitude of 0.31 at which the two-qubit phase induced by the pulse equals π . The fidelity of this state with respect to an ideal equal superposition state is 0.81. (d) Absolute values of the density matrix elements at a zero pulse amplitude. The calculated fidelity is 0.88.

1/4. Deviation from this ideal case indicate decoherence effects. In particular, reduction of off-diagonal elements as seen in the figure are caused by dephasing processes. To quantify these effects, we calculated the fidelity of the extracted density matrix relative to the ideal superposition state $(|gg\rangle + e^{i\phi_1}|eg\rangle + e^{i\phi_2}|ge\rangle + e^{i\phi_3}|ee\rangle)/2$ and found its maximum with respect to the phases ϕ_1, ϕ_2, ϕ_3 , obtaining a value of 0.81. For comparison, in Fig. 3.4(d) we also show an analogous plot for free evolution of the qubits at zero pulse amplitude. In this case, the extracted maximum fidelity was 0.88.

From these results, we can conclude that the presence of the resonator drive pulse leads to dephasing, resulting in a reduction of fidelity by a factor of approximately 0.92. This drive-induced dephasing arises mainly from resonator dissipation where the microwave field emitted from the resonator carries information about the qubit state, effectively causing dephasing by measurement. It is also partially caused by the residual entanglement between the qubit and the resonator at the end of the drive pulse, due to the fact that the resonator does not remain exactly in the vacuum state when the qubits are in $|eg\rangle$ or $|ee\rangle$.

The reduced fidelity of 0.88 in the absence of a drive pulse shows that decoherence of the qubits significantly degrades the performance of the phase gate and makes it impractical for quantum information applications at the current stage. It may become a viable method to generate entanglement in qubits with significantly improved coherence times. Additionally, modifications of the drive scheme with a drive amplitude which is ramped up and down smoothly instead of being turned on and off abruptly could lead to improved performance by making the process adiabatic for the qubit states $|eg\rangle$ and $|ee\rangle$.

Chapter 4

Generation of shaped microwave photons and active qubit cooling

Circuit QED systems have been successfully used as versatile sources of non-classical microwave signals. For example, as demonstrated by Hofheinz *et al.* (2009), by making use of the resonant Jaynes-Cummings interaction between a qubit and a resonator, one can in principle prepare the resonator field in arbitrary superpositions of Fock states. While this protocol shows good control over the photon number degree of freedom, another important aspect of the field emitted from the resonator – its temporal profile – has only recently started to draw attention in the circuit QED community.

The temporal shape of a field emitted from a resonator undergoing spontaneous relaxation is typically exponential, independently of whether the state of the resonator is classical or non-classical. By driving the system in specific ways during the emission of the field, one can engineer its waveform – an ability which is useful for quantum communication protocols. Specifically, if a system can be driven such that the emitted field is symmetric in time, then by time-reversal symmetry, an identical system may be in principle used to perfectly absorb the field.

It is chiefly for this reason that protocols for generating single photons with controllable temporal profiles have received considerable attention. They were first developed in atomic systems (Kuhn *et al.*, 2002; Keller *et al.*, 2004; Nisbet-Jones *et al.*, 2011) where they were also shown to enable exchange of single photons between two atoms, albeit with a limited efficiency (Ritter *et al.*, 2012).

In the field of circuit QED, approaches to single photon shaping can be categorized into two types. In one of them, the single energy quantum is first prepared by means of a quick qubit excitation followed by a resonant exchange interaction between the qubit and the resonator, similarly to Hofheinz *et al.* (2009). A tunable coupler between the resonator and the output line, such as demonstrated by Yin *et al.* (2013), can then be used to control the emission rate of the single photon. In an alternative approach presented by Srinivasan *et al.* (2014), the coupling of the resonator to the line is constant and instead, the coupling between the qubit and the resonator is tunable, facilitated by a special version of a transmon qubit (Srinivasan *et al.*, 2011).

Both these implementations of photon shaping rely on flux-tuning of a SQUID loop to achieve control over the qubit-resonator or resonator-transmission line coupling. However, because of the varying Josephson inductance of the loop, the frequency of the resonator changes along with the coupling. Therefore, to control the phase of the emitted photon as well as its amplitude envelope, the frequency shift needs to be compensated by an additional tunable parameter, such as the qubit-resonator detuning (Srinivasan *et al.*, 2014).

We therefore set out to implement another, fully microwave-based approach to photon shaping which does not rely on fast flux tuning. In our protocol, described in more detail below and in Pechal *et al.* (2014), both the amplitude and the phase of the emitted photon are controlled by a single phase- and amplitude-modulated microwave signal.

4.1 Photon shaping

The basic principle of most photon shaping schemes is that the photon-generating system (typically implemented as a coupled atom-resonator system) is prepared in an initial state belonging to a certain manifold of states \mathcal{M} and driven in a way which does not induce transitions into or out of \mathcal{M} . Additionally, a state $|\varphi_e\rangle$ from \mathcal{M} can then relax into a state $|G\rangle$ *not* belonging to \mathcal{M} by emitting a single photon at a rate κ . This ensures that the state is trapped outside of \mathcal{M} after emitting exactly one photon. This scheme is illustrated in Fig. 4.1(a). The theory of photon shaping processes is discussed in more detail in app. E.

Our particular system consists of a transmon coupled to a resonator via a Jaynes-Cummings interaction. The energy diagram of this system, truncated to the lowest three levels of the transmon and the lowest two levels of the resonator, is shown in Fig. 4.1(b). As we can see, the matrix elements of the Hamiltonian connect the states $|f0\rangle$ and $|g1\rangle$ via a second order process which proceeds through the intermediate states $|e0\rangle$ and $|e1\rangle$. Therefore, if the frequency of the drive applied to the transmon matches the energy difference between $|f0\rangle$ and $|g1\rangle$ and if the drive is sufficiently weak with respect to the detuning of the intermediate transitions, we can resonantly drive the system between $|f0\rangle$ and $|g1\rangle$ without significantly populating either $|e0\rangle$ or $|e1\rangle$. Effectively, we can describe this process as a transition with a matrix element \tilde{g} which is given by

$$\tilde{g} = \frac{g\Omega\alpha}{\sqrt{2}\Delta(\Delta + \alpha)}. \quad (4.1)$$

The theoretical aspects of this second-order process are discussed in our paper by Zeytinoglu *et al.* (2015).

If we neglect any unitary transitions outside of the two-level subspace spanned by $|f0\rangle$ and $|g1\rangle$, we can approximate the system by the setting shown in Fig. 4.1(c). This configuration is clearly of the general type illustrated in Fig. 4.1(a). The manifold \mathcal{M} is formed by $|f0\rangle$ and $|g1\rangle$, the emitting state $|\varphi_e\rangle$ is $|g1\rangle$ and the ground state $|G\rangle$ is $|g0\rangle$. As the transition element \tilde{g} is proportional to the drive parameter Ω , we have full control over it and can therefore in principle fully control the population of the

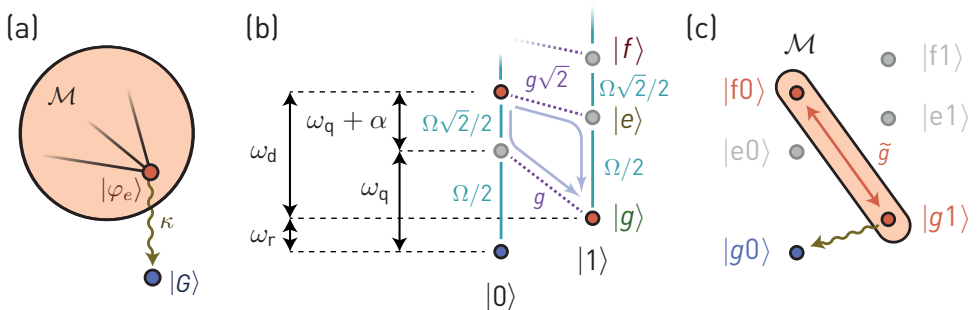


Figure 4.1: (a) Basic principle of the general photon shaping scheme. The system evolves coherently within a manifold \mathcal{M} , one of whose states can relax by photon emission into a ground state $|G\rangle$. (b) Realization of this scheme in an off-resonant transmon-resonator system. The energy diagram indicates the resonator and qubit transition frequencies ω_r and ω_q , as well as the drive frequency ω_d applied to induce transitions between the states $|f0\rangle$ and $|g1\rangle$. The matrix elements of the transmon drive are shown by the solid cyan lines while the Jaynes-Cummings matrix elements are represented by the dashed purple lines. The light-blue arrows indicate the second-order transitions between $|f0\rangle$ and $|g1\rangle$ via the intermediate states $|e0\rangle$ and $|e1\rangle$. (c) Simplification of the transmon-resonator system where all coherent transitions out of the two-level subspace spanned by $|f0\rangle$ and $|g1\rangle$ are neglected. The system is then equivalent to (a).

state $|g1\rangle$ and thus also the photon emission rate. For a more detailed explanation of how the time dependence of \tilde{g} relates to the resulting photon waveform, I refer the reader to sec. E.1.

First photon shaping experiments

To test the photon shaping protocol, we prepared a sample containing a single qubit coupled to a $\lambda/2$ resonator whose photograph is shown in Fig. 4.2(a). It was installed in a measurement setup with the configuration outlined in Fig. 4.3(a), built inside the Vericold cryostat. The basic parameters of the sample were obtained using standard characterization measurements as described in sec. 2.4. The transmon was tuned to a transition frequency of $\omega_q/2\pi = 8.640$ GHz and its measured anharmonicity was $\alpha/2\pi = -421$ MHz. The resonator frequency and full-width-half-maximum linewidth were $\omega_r/2\pi = 7.224$ GHz and $\kappa/2\pi = 24$ MHz while the Jaynes-Cummings coupling strength between the transmon and the resonator was estimated to be $g/2\pi = 35$ MHz.

The relaxation times of the first and second transmon excited state were found to be $T_1^e = (2000 \pm 200)$ ns and $T_1^f = (550 \pm 5)$ ns, respectively. The measured dephasing times of the various superposition states were $T_2^{ge} = (1640 \pm 50)$ ns, $T_2^{ef} = (557 \pm 8)$ ns and $T_2^{gf} = (580 \pm 30)$ ns.

After the basic characterization measurements, we performed two-tone spectroscopy with the qubit drive tone frequency varied around the theoretically expected

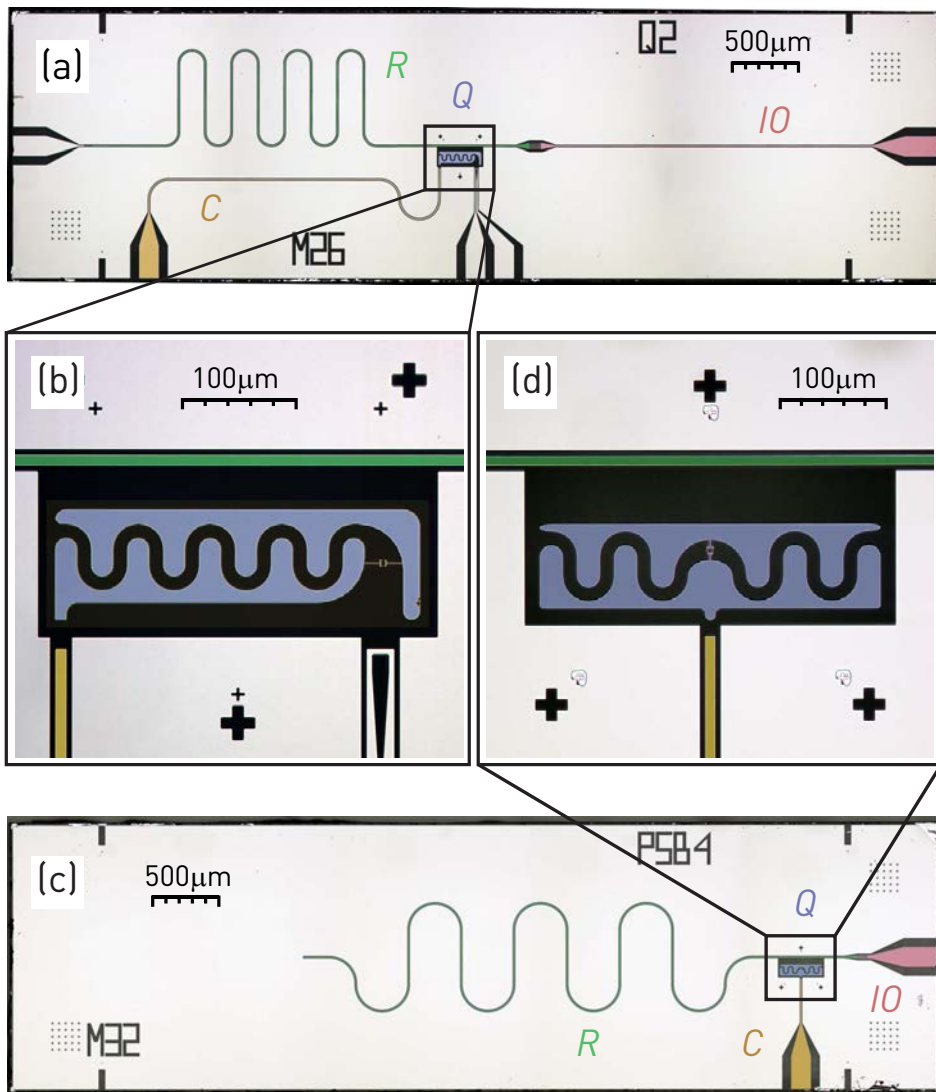


Figure 4.2: (a) False-color micrograph of the sample used in the first experiment to demonstrate the photon shaping protocol. The resonator (R) is indicated in green, the input and output line (IO) in red, the charge line used to drive the qubit (C) in yellow and the transmon (Q) in blue. (b) Close-up view of the transmon with the resonator line at the top, the charge line on the bottom left and the unused flux line on the bottom right. (c) False-color micrograph of one of the two nominally identical samples used in the experiments with photon emission and reabsorption. The individual components of the sample are labeled in the same way as in (a). (d) Close-up view of the transmon.

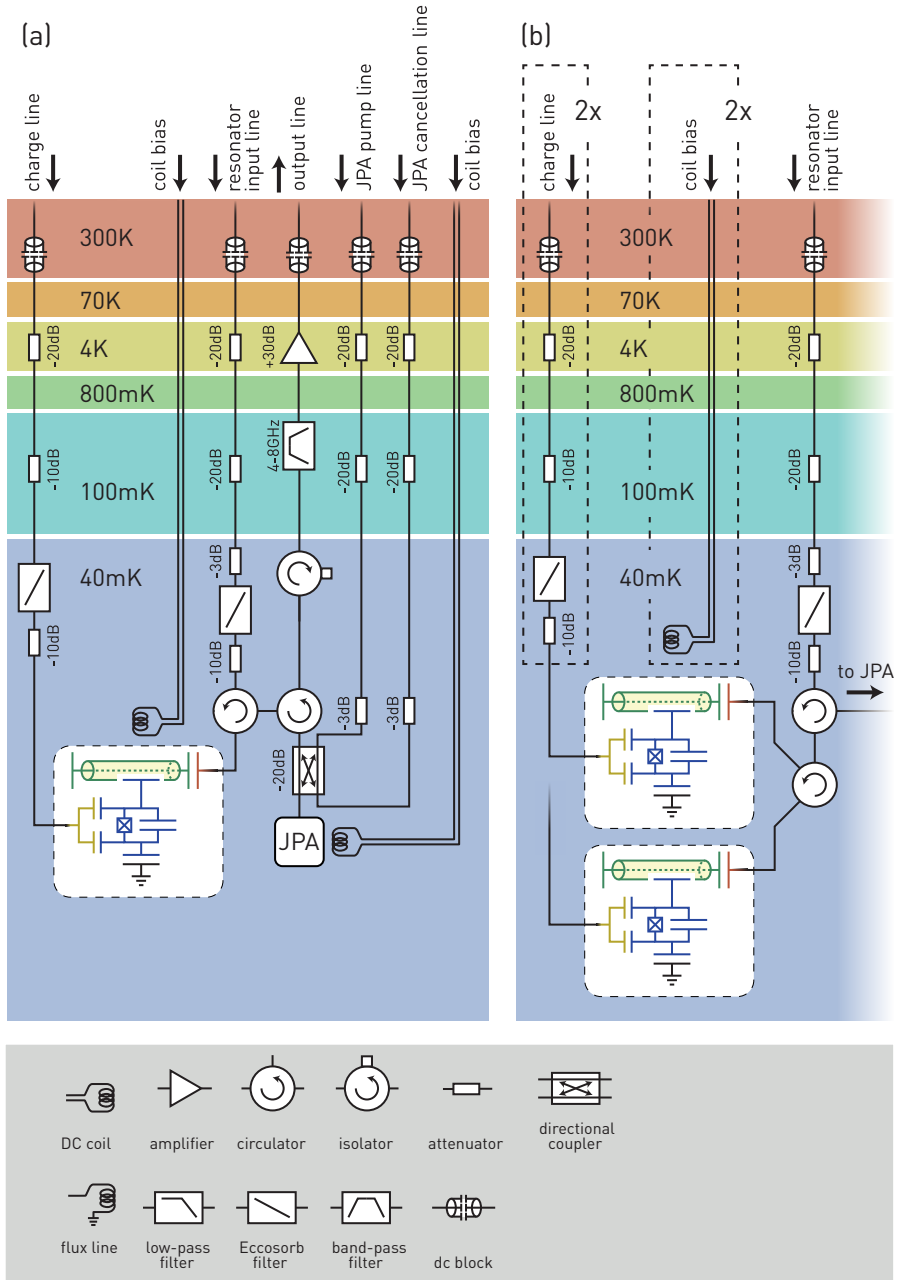


Figure 4.3: (a) Diagram of the setup used for the photon shaping experiment in the Vericold cryostat. (b) Modified version of the setup for the photon reabsorption experiment. The output line with the parametric amplifier is the same as in (a).

frequency of the $|f0\rangle \leftrightarrow |g1\rangle$ transition $2\omega_q + \alpha - \omega_r$. When the drive frequency matches the transition, the phase of the reflected resonator probe signal changes, as shown in Fig. 4.1. In this plot, we can also observe that the transition frequency shifts with increasing power of the drive signal. This is caused by ac Stark shifts of the system's energy levels induced by the strong drive.

In the experiment presented in Pechal *et al.* (2014), the Stark shift was taken into account using a heuristic method: We approximated the functional dependence of the Stark shift Δ on the drive amplitude Ω by the quadratic function $\Delta = c_0 + c_2|\Omega|^2$ and treated its parameters c_0, c_2 as free parameters to be adjusted to optimize the resulting photon waveform.

The temporal mode of the photon state $|1\rangle$ is characterized by its wavefunction $\psi(t)$, given by the relation

$$|1\rangle = \int \psi(t) \hat{a}_{\text{out}}^\dagger(t) |0\rangle dt.$$

To measure $\psi(t)$, we prepared the emitted field in the superposition state $(|0\rangle + |1\rangle)/\sqrt{2}$. This can be done by initializing the transmon in the state $(|g\rangle + |f\rangle)/\sqrt{2}$ before inducing the $|f0\rangle \leftrightarrow |g1\rangle$ transition, using a pulse sequence illustrated in Fig. 4.5(a). It can be easily verified that the expectation value $v(t)$ of the downconverted measured voltage, which is proportional to $\langle \hat{a}_{\text{out}}(t) \rangle$ (see sec. 2.6), then satisfies $v(t) \propto \psi(t)$. The proportionality constant between ψ and v is not important for the calculation of the symmetry parameter s .

To establish that our protocol is suitable for generating symmetric photon pulses, we defined a figure-of-merit s as the overlap between the photon wavefunction $\psi(t)$ and its time-inverse:

$$s \equiv \max_{t_0} \frac{|\int (\psi(2t_0 - t))^* \psi(t) dt|}{\int |\psi(t)|^2 dt}.$$

This quantity lies in the interval $0 \leq s \leq 1$ and is equal to 1 for exactly symmetric waveforms. It is therefore a suitable measure of the photon's temporal symmetry.

We chose the shape of the transmon $|f0\rangle \leftrightarrow |g1\rangle$ drive pulse to be given by

$$\Omega(t) = \Omega_0 \sin^2(\pi t/T) \exp(i\phi(t)),$$

where the phase is calculated as the time-integral of the Stark shift $\Delta = c_0 + c_2|\Omega|^2$. This particular functional dependence of $\Omega(t)$ was chosen as a particularly simple continuous function with only two free parameters describing its envelope and – unlike other candidates such as a Gaussian function – with no need for an arbitrary cut-off. We could then observe the effect variation of the four parameters Ω_0, T, c_0 and c_2 has on the shape of the resulting photon pulses and experimentally optimize the symmetry parameter s . To this end, we sampled the pulse length T from a range between 60 ns and 500 ns and the drive amplitude $\Omega_0/2\pi$ between 0 MHz and 1000 MHz. We found values of s close to one for various combinations of these parameters, as shown in Fig. 4.5(b). For comparison, the dashed lines represent the simulated photon waveforms obtained by solving the master equation for the full Jaynes-Cummings

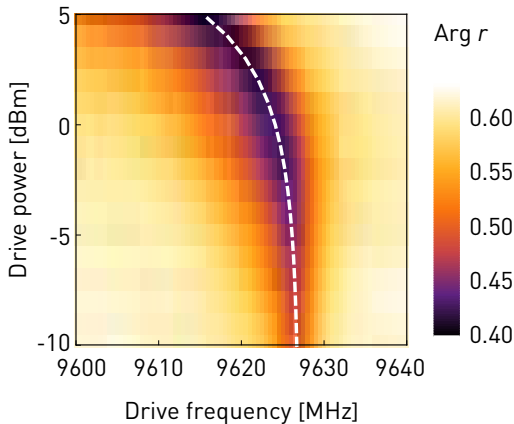


Figure 4.4: Phase of the reflected resonator probe signal in a two-tone spectroscopy measurement as a function of the transmon drive tone frequency and power. The white dashed line shows the position of the minimum as it shifts to lower frequencies with increasing drive power due to ac Stark shift.

Hamiltonian including three resonator and six transmon levels and evaluating the output field. This model takes into account imperfections of the second-order transition as well as transmon decoherence. The scaling factor between the measured voltages and the expectation value of the field $\langle \hat{a}_{\text{out}}(t) \rangle$ is treated as a fit parameter here and so is the relative timing between the measured and the simulated waveforms.

Performing qubit tomography measurements after the photon emission process shows that for the two longer photon pulses ($T = 200$ ns, $T = 500$ ns) the initial $|f0\rangle$ state is nearly emptied by the drive pulse, having a residual population on the order of 1 – 2%. On comparable time scales the reduction of the population due to relaxation is negligible. The peak drive strengths for these pulses are $\Omega_0/2\pi = 700$ MHz and $\Omega_0/2\pi = 600$ MHz, respectively. The corresponding peak amplitudes of the effective coupling $\tilde{g}/2\pi$ given by eq. (4.1) are 5.2 MHz and 4.4 MHz, consistent with numerical diagonalization of the Hamiltonian which yields values of $\tilde{g}/2\pi = 5.5$ MHz and 4.6 MHz. The symmetry parameter s reaches a value of 0.98 for both longer pulses. This high symmetry can only be obtained for pulses much longer than the cavity rise time $1/\kappa \approx 7$ ns. For comparison, we show a short pulse with $T = 20$ ns. This photon pulse is not long enough for a complete population transfer from $|f0\rangle$ to $|g1\rangle$ with the drive pulse amplitudes used which leads to a reduced emission efficiency. Its symmetry parameter $s = 0.92$ also does not reach the high values obtained for the longer pulses.

To prepare a symmetric photon state which can be easily reabsorbed by a quantum node, it is important that not only its amplitude but also its phase is symmetric in time. By optimizing the Stark shift parameters c_0 and c_2 , we made the phase of the photon pulse constant in time, as illustrated in the inset of Fig. 4.5(b), noting that the ratio of the two signal quadratures is in good approximation time-independent for each of the three pulses.

The observed effect of the drive pulse length on the length of the photon pulse and the efficiency of its emission, which is reflected in the amplitude of the detected voltage, is illustrated in Fig. 4.5(c). Shorter drive pulses lead to shorter photon

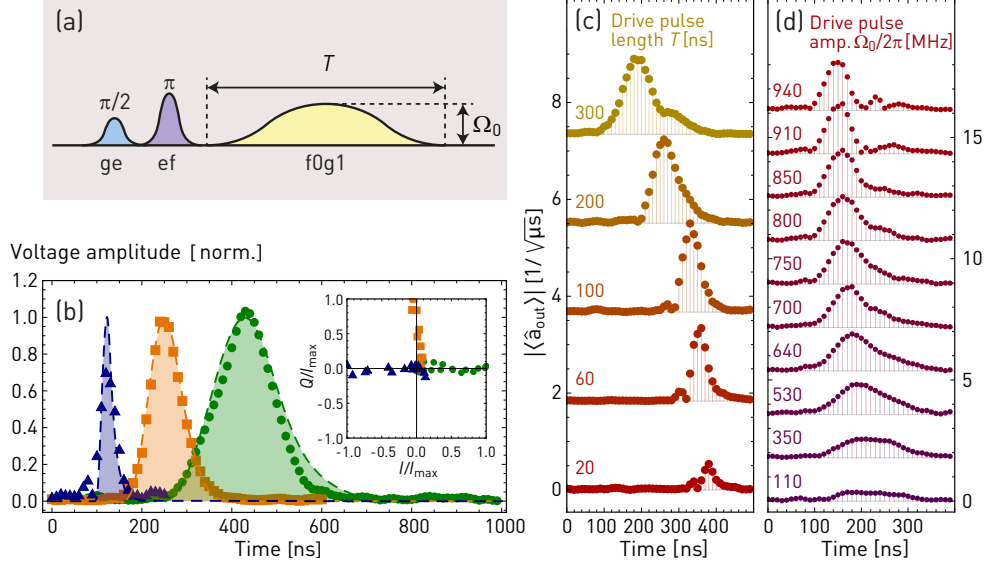


Figure 4.5: (a) Amplitude of the drive signal used to initialize the transmon and transfer the excitation into the resonator to generate a symmetric photon shape. (b) Normalized voltage amplitude of the shaped photons obtained for drive pulses with $T = 20$ ns, $\Omega_0/2\pi = 680$ MHz (blue triangles), $T = 200$ ns, $\Omega_0/2\pi = 700$ MHz (orange squares) and $T = 500$ ns, $\Omega_0/2\pi = 600$ MHz (green circles). The dashed lines show the simulated photon shapes scaled to normalize their peak values to unity. The measured traces are fitted to the simulation with only the time-shifts and scaling factors as fit parameters. The inset shows both voltage quadratures I and Q of the photon pulses. (c) The measured voltage waveform of the photon superposition state $(|0\rangle + |1\rangle)/\sqrt{2}$ for the indicated length of the drive pulse T at a fixed pulse amplitude $\Omega_0/2\pi = 420$ MHz and (b) for the indicated amplitude of the pulse Ω_0 at a fixed pulse length $T = 300$ ns.

waveforms (curves at the bottom of the plot) and vice versa. The influence of the drive pulse amplitude is shown in Fig. 4.5(d). Photon shapes generated with stronger drive pulses are shorter and display signatures of Rabi oscillations (the smaller side-peaks in the two curves at the top of the plot). On the other hand, weak pulses result in an incomplete population transfer and therefore reduced efficiency of the emission process, as illustrated by the reduced amplitude of the bottom-most waveform.

To demonstrate the single photon nature of the emitted field, we measured its moments using the propagating field tomography method described in more detail in Eichler *et al.* (2012a); Menzel *et al.* (2010) and in sec. 2.6 of this thesis. We first determined the mode function $\psi(t)$ of the photon pulse which is proportional to the observed averaged coherent signal $\langle v(t) \rangle$. Then in each realization of the experiment, the measured single-shot voltage $v(t)$ was processed by a digital Chebyshev filter with a shape approximately matched to $\psi(t)$ and the result V was recorded in a 2D histogram. The observable \hat{V} can be described by an operator $\hat{a} + \hat{h}^\dagger$ where \hat{a} is the temporal field mode $\hat{a} = \int \psi^*(t) \hat{a}_{\text{out}}(t) dt$ and \hat{h} is a noise mode, assumed to be in a thermal state which is characterized by the effective noise temperature of the amplification chain. The moments $\langle (V^*)^m V^n \rangle$ extracted from the recorded histogram and the noise moments $\langle (\hat{h}^\dagger)^k \hat{h}^l \rangle$ determined in an equivalent measurement with only vacuum at the input of the detection chain were used to calculate the field moments $\langle (\hat{a}^\dagger)^i \hat{a}^j \rangle$ (Eichler *et al.*, 2012a).

For both the symmetrically shaped photon superposition state $(|0\rangle + |1\rangle)/\sqrt{2}$ and the single photon Fock state $|1\rangle$ described above, we found the normalized fourth order moments $g^{(2)}(0) = \langle \hat{a}^\dagger \hat{a}^\dagger \hat{a} \hat{a} \rangle / \langle \hat{a}^\dagger \hat{a} \rangle^2$ of 0.03 ± 0.07 and 0.06 ± 0.02 , respectively, which lie well below the classical limit of $g^{(2)}(0) = 1$ expected for coherent states, showing a high degree of antibunching. The density matrices $\hat{\rho}$ with fidelities $F = 86\%$ and 76% to the respective photon states were extracted from the measured moments (Eichler *et al.*, 2012a) by employing a maximum likelihood algorithm. From the numerical simulation of the emission process, we found the normalization conditions $\langle A^\dagger A \rangle = 0.39$ and 0.79 . This is lower than the values of $\langle A^\dagger A \rangle = 1/2$ and 1 expected for the ideal states $(|0\rangle + |1\rangle)/\sqrt{2}$ and $|1\rangle$ due to the reduced photon emission efficiency of $(79 \pm 1)\%$, limited by the finite lifetime $T_1^f = (550 \pm 5)$ ns of the $|f\rangle$ state. This accounts for the deviation of the diagonal elements of $\hat{\rho}$ from the theoretical values while the off-diagonal elements are reduced due to the loss of coherence between the qubit states $|g\rangle$ and $|f\rangle$ on a time scale of $T_2^{gf} = (580 \pm 30)$ ns. This estimate of the emission efficiency assumes perfect initialization of the transmon in the $|f\rangle$ state in order to evaluate the shaping process separately from the preparation procedure. The total efficiency including a realistic initial state preparation is approximately 76% , that is, about 6% lower. We attribute this to relaxation during the initialization pulses and thermal population of the excited states, measured to be approximately 13% . This thermal population significantly exceeds the theoretical equilibrium value 0.2% corresponding to the physical base temperature of 50 mK. The source of this anomalous thermal excitation is likely due to undesired elevated temperatures of the still and 100 mK stages of the Vericold cryostat.

To demonstrate the rapid amplitude and phase modulation capability of our all-microwave photon shaping scheme we prepared six-peaked single photon pulses

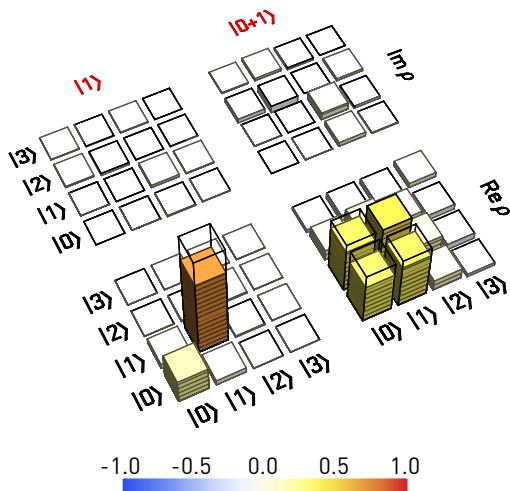


Figure 4.6: The real and imaginary part of the measured density matrices $\hat{\rho}$ of the symmetric temporal photon mode with fidelities $F = 76\%$ and $F = 86\%$ to the respective ideal states $|1\rangle$ and $(|0\rangle + |1\rangle)/\sqrt{2}$. The wire frames show the single-photon Fock state $|1\rangle$ (all density matrix elements equal to 1 or 0) and the ideal superposition state $(|0\rangle + |1\rangle)/\sqrt{2}$ (all density matrix elements equal to $1/2$ or 0). The ticks in the bars represent increments of 0.1.

similar to the double-peaked pulses demonstrated with optical frequency photons (Keller *et al.*, 2004). For this purpose the transmon was again prepared in the state $(|g\rangle + |f\rangle)/\sqrt{2}$. The subsequent photon shaping signal consists of a train of six identical \sin^2 pulses of amplitude $\Omega_0/2\pi \approx 350$ MHz and length $T = 60$ ns separated by 170 ns, as shown in Fig. 4.7(a). These parameters are adjusted to make the overlap between the photon peaks small while keeping the overall duration of the pulse train short to minimize decoherence.

We then verified that the phases of the individual peaks in the photon waveform can be controlled independently. As an example, we changed the phase of any one of the subsequent photon peaks by π by adjusting the phase of the corresponding drive pulses leading to a change of sign in the detected voltage, Fig. 4.7(b). This phase control can be achieved while keeping the emitted power unchanged, as illustrated in Fig. 4.7(c). The power was measured as a function of time by squaring and subsequent averaging of the digitized and filtered voltages. The noise power was then subtracted in post-processing.

A photon $|1\rangle$ with a waveform $\psi(t)$ consisting of multiple peaks can be equivalently interpreted as a superposition state of multiple single-photon states $|1_j\rangle$, each described by a single-peaked wavefunction $\psi_j(t)$. If $\psi(t) = \sum_j \psi_j(t)$, we can write

$$\begin{aligned}
 |1\rangle &= c_1|1_1\rangle + c_2|1_2\rangle + \dots, \text{ where} \\
 c_j|1_j\rangle &= \int \psi_j(t) \hat{a}_{\text{out}}^\dagger(t) |0\rangle dt \text{ and} \\
 |c_j|^2 &= \int |\psi_j(t)|^2 dt.
 \end{aligned}$$

Thus, the photon states shown in Fig. 4.7(b,c) can also be viewed as time-bin superposition states. This shows that the described photon shaping technique could

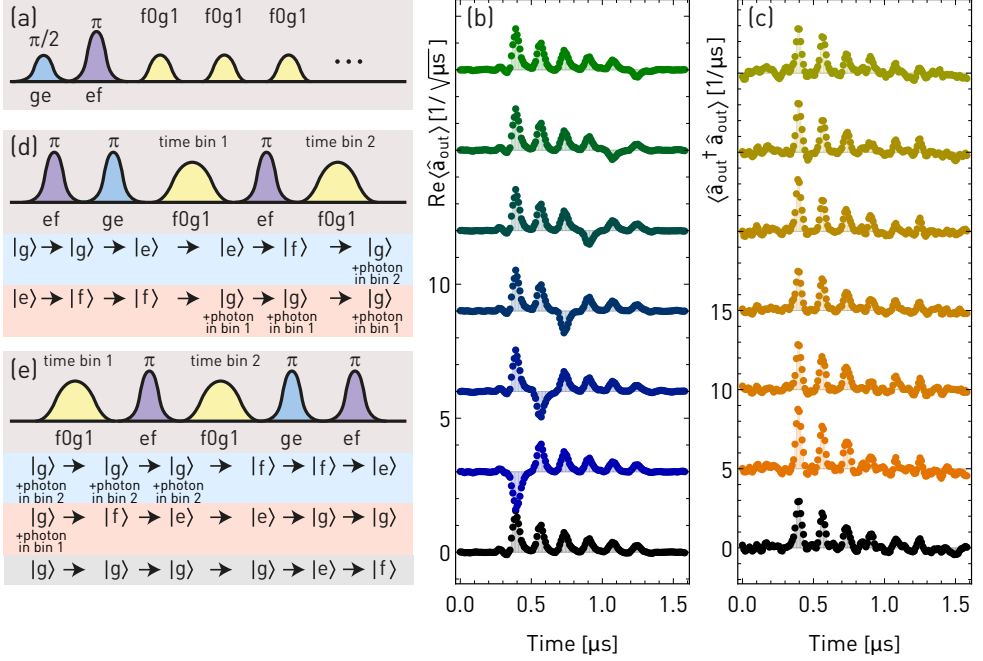


Figure 4.7: (a) Pulse sequence used to generate the multiple-peaked photon states whose coherent voltage waveforms are shown in (b) and power waveforms in (c). The bottom-most trace in (b) and (c), shown in black, corresponds to a train of drive pulses which are all in phase. The colored traces above result from flipping the phase of each one of the drive pulses by π . (d) Protocol for mapping a qubit state onto a time-bin superposition state of a single photon. (e) The reverse protocol, mapping the time-bin superposition back onto the qubit state. Photon loss can be detected in this scheme if a projective measurement in the transmon eigenbasis, which does not distinguish between $|g\rangle$ and $|e\rangle$, observes the transmon in the $|f\rangle$ state.

also be used to realize time-bin encoding of quantum information. Such encoding can provide a useful alternative to the simple scheme which uses the vacuum state $|0\rangle$ and the single-photon Fock state $|1\rangle$ as its computational states. In the presence of dissipation in the communication channel, the simple protocol is unable to detect the loss of a photon since the relaxed state $|0\rangle$ is identical to one of the encoding states. On the other hand, mapping the state of a qubit onto a superposition of two time-bin photon states $|1_1\rangle$ and $|1_2\rangle$ allows the detection of a photon loss event. This could in turn enable heralded protocols to achieve high transmission efficiency in a subset of post-selected measurements even for a lossy communication channel where the average transmission success probability is reduced.

An theoretical example of such a time-bin encoding protocol is illustrated in Fig. 4.7(d,e). The two lowest states $|g\rangle$ and $|e\rangle$ of the transmon are mapped onto the two time-bin photon states by means of the pulse sequence shown in Fig. 4.7(d). The first three pulses map the excited state $|e\rangle$ onto a photon whose emission is induced by the first $|f0\rangle \leftrightarrow |g1\rangle$ drive pulse, shown in yellow. Meanwhile, the ground state $|g\rangle$ is simply transferred into $|e\rangle$ which is unaffected by the first drive pulse. It is then mapped to $|f\rangle$ and subsequently to a photon by the second drive pulse.

The transfer of the time-bin photon states back to a transmon state can be done simply by reversing the pulse scheme, as shown in Fig. 4.7(e). If the photon is absent, the transmon is not excited by any of the first three pulses and ends up in the state $|f\rangle$ at the end of the sequence. The final step of the protocol is a projection measurement in the transmon eigenbasis which distinguishes $|f\rangle$ from $|g\rangle$ and $|e\rangle$ but not $|g\rangle$ and $|e\rangle$ from each other. This allows one to detect the absence of the incoming photon while simultaneously preserving the coherence of the encoded state if the transfer was successful.

Second generation of photon shaping experiments

Since the first generation of the photon shaping experiment described above, significant effort was devoted in our lab to design a sample optimized for quantum networking by single-photon exchange. This development was led by a team of doctoral students Philipp Kurpiers, Theo Walter and Paul Magnard. Together with them, we set out to replicate the photon shaping experiment with the improved samples, with a particular focus on developing a more reliable and convenient way of calibrating and controlling the shaped photon emission.

The new samples were equipped with a Purcell filter (Reed *et al.*, 2010; Sete *et al.*, 2015), designed to suppress Purcell relaxation of the transmon into the output line of the resonator. This is a key improvement, since the decay of the transmon's $|f\rangle$ state is one of the main factors limiting the efficiency of the photon exchange process.

Instead of the heuristic approach described above, where the parameters of the Stark shift correction had been adjusted to optimize the shape of the emitted photon, the Stark shift was now measured more rigorously using a pulsed measurement. This scheme was developed for the photon reabsorption experiment and is described in ch. 5. In this way, we could calibrate the Stark shift and the effective matrix element of the $|f0\rangle \leftrightarrow |g1\rangle$ transition as a function of the applied pulse amplitude. By inverting these relations, we then generated pulses for which \tilde{g} has the time-dependence

described by eq. (E.10). In a simplified model involving only the three states $|f0\rangle$, $|g1\rangle$ and $|g0\rangle$, this drive pulse shape leads to a photon with a waveform

$$f(t) = \frac{\sqrt{\kappa_{\text{eff}}}}{2 \cosh(\kappa_{\text{eff}}t/2)}.$$

4.2 Qubit cooling

The exchange of excitation between the transmon and the resonator facilitated by the $|f0\rangle \leftrightarrow |g1\rangle$ drive can be used for other purposes than just photon shaping. In the experiment by Gasparinetti *et al.* (2016), it was utilized to prepare Fock states of the resonator field and implement an effectively tunable Jaynes-Cummings interaction between the transmon and the resonator.

In the photon shaping experiment, the elevated thermal population of the transmon excited states, though in principle undesirable, provided us with a fortuitous opportunity to study an active cooling scheme based on the $|f0\rangle \leftrightarrow |g1\rangle$ transition.

Provided that the effective temperature of the resonator mode is lower and the relaxation time shorter than those of the transmon, one can drive the transmon closer to its ground state by a sequence of two steps which can be repeated if needed: In the first one, a π -pulse is applied to the $|e\rangle \leftrightarrow |f\rangle$ transition to transfer the thermal population of $|e\rangle$ into $|f\rangle$. In the second step, the $|f0\rangle \leftrightarrow |g1\rangle$ transition is driven for a period of time such that the excitation is emitted into the transmission line with high probability and the system is left in the ground state $|g0\rangle$.

To test this process, we implemented a pulse sequence shown in Fig. 4.8(a). A π -pulse driving the $|e\rangle \leftrightarrow |f\rangle$ transition, followed by a square pulse at the $|f0\rangle \leftrightarrow |g1\rangle$ transition frequency, are repeated $N + 1$ times. The square pulses have an amplitude corresponding to an equivalent resonant Rabi rate of approximately $\Omega/2\pi = 300$ MHz, as estimated from a comparison of the measurements with a master equation simulation. The first N square pulses have a fixed length $T_{\text{max}} = 400$ ns and the last one has a variable length T .

We measured the populations of the transmon states $|e\rangle$ and $|f\rangle$ at the end of the sequence to investigate their dependence on the pulse length T and the number of repetitions. The results, plotted in Fig. 4.8, show that the initial thermal population of approximately 11%, transferred into the $|f\rangle$ state, decreases with increasing length of the pulse. At the same time, however, the population of the $|e\rangle$ state increases as the transmon thermalizes due to interactions with its environment.

We can see that the performance of the cooling scheme slightly improves when the cycle is repeated two or three times but additional repetitions do not lead to any further improvement. Moreover, beyond approximately $T = 150$ ns, the total population of both states $|e\rangle$ and $|f\rangle$ no longer decreases with increasing T , as the thermalization rate exceeds the effective cooling rate. The minimum thermal population reached in this measurement was 2.8%. This represents a reduction by a factor of 4 with respect to the steady state value.

Thus, in the particular sample investigated here, the cooling scheme led to a significant decrease in the effective temperature of the transmon. In future devices,

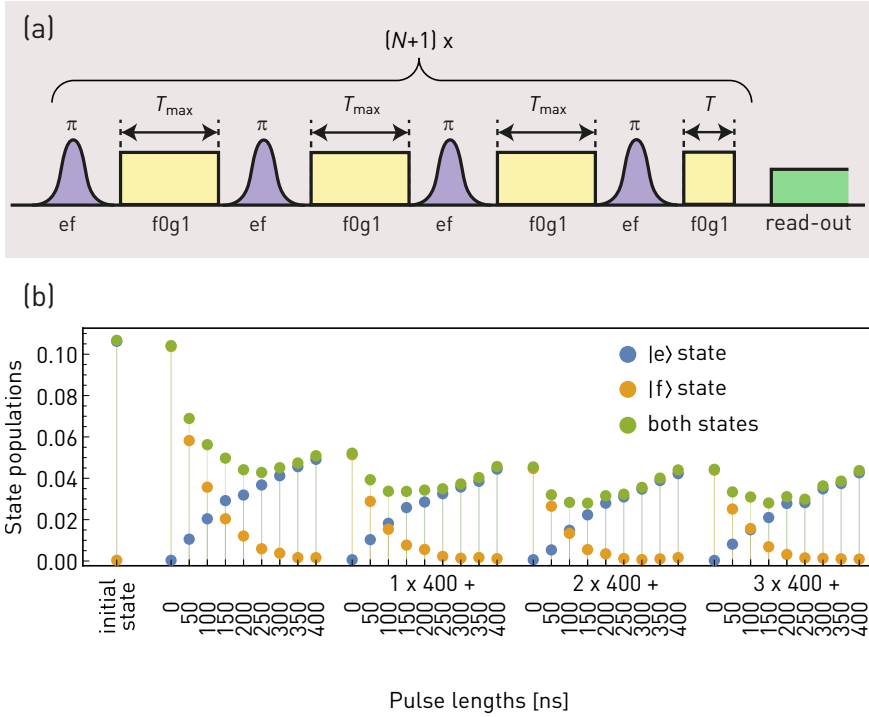


Figure 4.8: (a) Pulse scheme used to test the cooling protocol. A π -pulse on the $|e\rangle \leftrightarrow |f\rangle$ transition and a $|f0\rangle \leftrightarrow |g1\rangle$ square drive pulse are repeated $N + 1$ times, where the first N repetitions of the $|f0\rangle \leftrightarrow |g1\rangle$ pulse have a fixed length $T_{\max} = 400$ ns while the last one has a variable length T . (b) Populations of the $|e\rangle$ and the $|f\rangle$ state as a function of the last pulse length T for different numbers of repetitions.

it could be used in combination with a special low Q dump resonator (similar to the *zeroing registers* employed by Mariantoni *et al.* (2011a)) to initialize the transmon in its ground state on a time-scale much shorter than its spontaneous relaxation time.

Chapter 5

Reabsorption of single microwave photons

Following the photon shaping demonstration presented in Pechal *et al.* (2014), we extended the experimental setup to include a second identical sample of the type shown in Fig. 4.2(c). The two samples were connected to each other and to the input/output line via a circulator, as illustrated in Fig. 5.1. The configuration of the measurement setup, presented in Fig. 4.3(b), was similar to that of the photon shaping experiment.

In this setting, the resonators of both samples are probed in reflection. The reflected signal receives a phase shift upon scattering from each resonator and the sum of the two phases is then measured. As the circulator allows the signal to pass only in one direction, the two resonators do not hybridize even though their frequencies are nearly identical. This allows us to characterize the two samples independently of

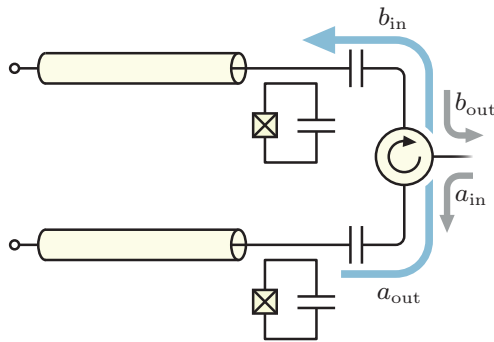


Figure 5.1: Simplified diagram of the photon reabsorption setup with two qubit-resonator systems connected by coaxial cables and a circulator.

each other using measurement techniques similar to the standard ones described in sec. 2.4.

In the following, we number the samples and their respective qubits and resonators as 1 and 2 according to the order of propagation of the probe signal. The measured resonance frequencies of the resonators were both approximately $\omega_{r1}/2\pi = \omega_{r2}/2\pi = 7.255$ GHz. Their full-width-half-maximum linewidth was measured to be about $\kappa_1/2\pi = \kappa_2/2\pi \approx 4$ MHz. This parameter could not be estimated very accurately due to the frequency-dependent phase shifts in the setup obscuring the Lorentzian shape of the ideal resonator spectrum. The stated value of 4 MHz is close to the linewidth of $\kappa/2\pi = 4.7$ MHz determined in an earlier dipstick measurement at 4.2 K. The transition frequencies of qubits 1 and 2 were set to $\omega_{q1}/2\pi = 8.575$ GHz and $\omega_{q2}/2\pi = 8.450$ GHz, respectively. Their maximum frequencies were both approximately 9 GHz. The measured anharmonicities were $\alpha_1/2\pi = -443$ MHz and $\alpha_2/2\pi = -445$ MHz. The Jaynes-Cummings couplings to the respective resonators, extracted from vacuum Rabi splitting measurements were $g_1/2\pi = g_2/2\pi \approx 40$ MHz. For reasons similar to the resonator linewidth measurements, this value could not be determined with very high accuracy.

The relaxation times obtained from measurements were $T_1^{1e} = (1620 \pm 50)$ ns, $T_1^{1f} = (930 \pm 20)$ ns for qubit 1 and $T_1^{2e} = (1960 \pm 80)$ ns and $T_1^{2f} = (1630 \pm 80)$ ns for qubit 2. The dephasing times of the various superposition states were $T_2^{1ge} = (1330 \pm 180)$ ns, $T_2^{1ef} = (610 \pm 40)$ ns, $T_2^{1gf} = (480 \pm 130)$ ns for qubit 1 and $T_2^{2ge} = (1200 \pm 110)$ ns, $T_2^{2ef} = (680 \pm 50)$ ns, $T_2^{2gf} = (500 \pm 70)$ ns for qubit 2.

To characterize the Stark shift as a function of the drive amplitude, we employed a pulsed calibration measurement. The transmon was initialized in the $|f\rangle$ state. We then applied a square pulse of duration $T = 100$ ns, amplitude A and detuning δ from the $|f0\rangle \leftrightarrow |g1\rangle$ transition frequency and measured the final transmon state populations. The results of this measurement for system 1 are presented in Fig. 5.2(a).

If the drive frequency matches the $|f0\rangle \leftrightarrow |g1\rangle$ transition frequency, the transmon is driven from $|f\rangle$ to $|g\rangle$ and we observe depletion of the $|f\rangle$ state population. At the same time, we note that the first excited state $|e\rangle$ remains unoccupied which justifies our treatment of the second-order transition as operating directly between the states $|f0\rangle$ and $|g1\rangle$ without populating the intermediate states $|e0\rangle$ and $|e1\rangle$. Due to the ac Stark shift, the frequency at which the $|f\rangle$ state population drops depends on the pulse amplitude. This dependence is plotted in Fig. 5.2(b). We can see that while the Stark shift starts off as quadratic for small pulse amplitudes, it soon becomes roughly linear. This indicates that the $|f0\rangle \leftrightarrow |g1\rangle$ transition in this regime cannot be described simply by the lowest-order perturbative expansion.

With the amplitude-dependence of the Stark shift established, we performed a measurement where the frequency of the square pulse was tied to its amplitude to keep it resonant with the $|f0\rangle \leftrightarrow |g1\rangle$ transition. We then varied the length and the amplitude of the pulse and again recorded the resulting transmon populations, obtaining for system 1 the data presented in Fig. 5.3(a). These results show that with a sufficiently long pulse, the transmon is driven almost completely into the ground state. Note that this is not simply the result of spontaneous relaxation, as the bottom-

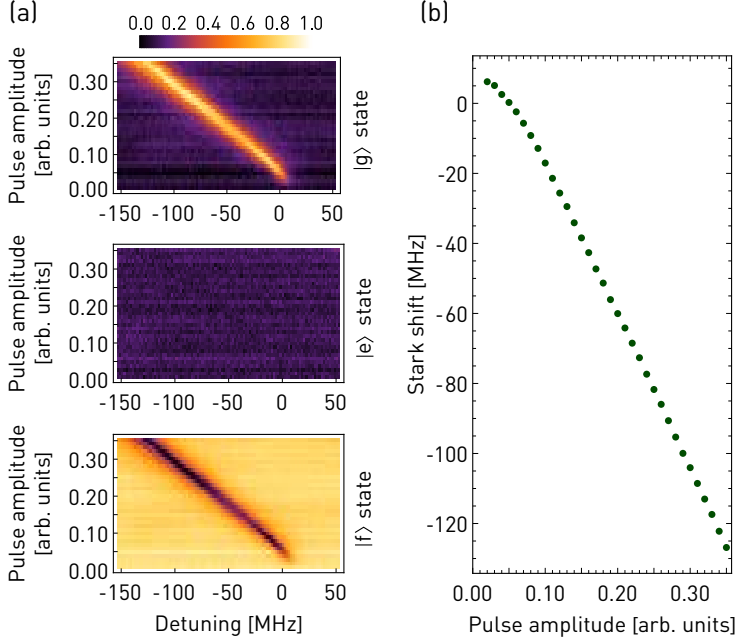


Figure 5.2: (a) Transmon state populations as a function of the detuning and amplitude of the square pulse applied to induce the $|f0\rangle \leftrightarrow |g1\rangle$ transition. The length of the pulse is $T = 100$ ns and its amplitude is expressed relative to the full output range of the arbitrary waveform generator which in this case was ± 600 mV. (b) Stark shift as a function of the drive amplitude, extracted from the minima of the $|f\rangle$ state population in (a).

most line in the density plots shows that this process, occurring in the absence of the drive signal, is significantly slower.

For stronger pulses, the population transfer between $|f\rangle$ and $|g\rangle$ shows signs of Rabi oscillations, damped mainly by the resonator relaxation process and to a smaller extent by the transmon relaxation. We modeled the transition in a simplified picture neglecting all coherent transitions out of the two-level subspace spanned by $|f0\rangle$ and $|g1\rangle$. The total population of the subspace is not constant in time but decreases due to the relaxation of $|g1\rangle$ into the ground state $|g0\rangle$ at a rate κ and $|f0\rangle$ into $|e0\rangle$ at a rate Γ . The evolution equations for the probability amplitudes c_{f0} and c_{g1} are

$$\begin{aligned} \frac{d}{dt}c_{f0} &= -i\tilde{g}c_{g1} - \frac{\Gamma}{2}, \\ \frac{d}{dt}c_{g1} &= -i\tilde{g}c_{f0} - \frac{\kappa}{2}, \end{aligned}$$

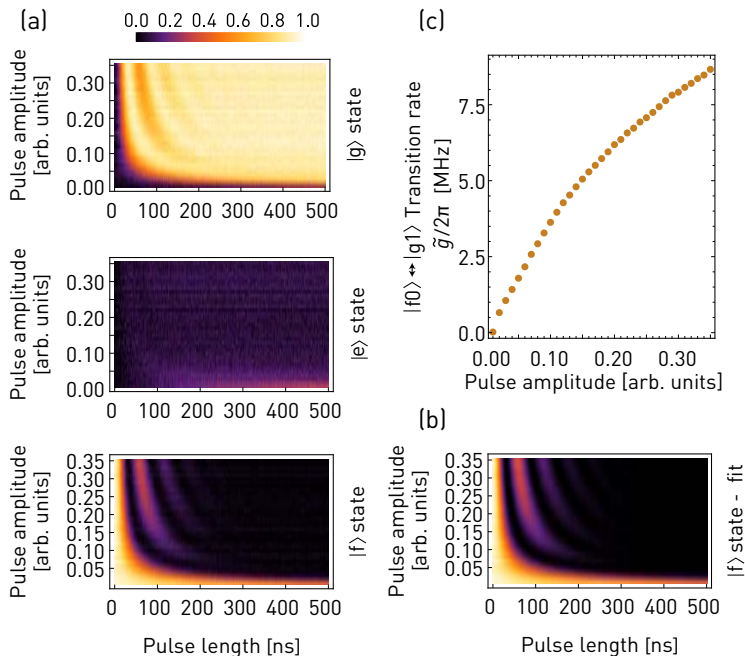


Figure 5.3: (a) Transmon state populations as a function of the length and amplitude of the square pulse applied to induce the $|f0\rangle \leftrightarrow |g1\rangle$ transition. The frequency of the pulse is set to be resonant with the transition, based on the measurement from Fig. 5.2. (b) Least-squares fit of a dissipative two-level model to the measured $|f\rangle$ state populations. (c) The transition rate \tilde{g} extracted from the fit as a function of the pulse amplitude.

where \tilde{g} is the $|f0\rangle \leftrightarrow |g1\rangle$ transition rate induced by the drive. This system of differential equations can be solved analytically. We fitted the solution to the measured $|f\rangle$ state population. In this fit, Γ was taken from a previous relaxation time measurement, κ was a fit parameter common for the whole data set and \tilde{g} was fitted separately for each line of constant pulse amplitude. The resulting optimal value of κ was $\kappa/2\pi = 4.8$ MHz. The fit function agrees very well with the measured data, as shown in Fig. 5.3(b). The fitted values of \tilde{g} are plotted in Fig. 5.3(c) as a function of the applied pulse amplitude. In the weak drive limit, the transition rate scales linearly with the amplitude, as suggested by eq. (4.1). The deviation from linearity again indicates a break-down of the lowest-order perturbative approximation.

To observe single photon exchange between the two systems, we prepared qubit 1 in its $|f\rangle$ state while qubit 2 was left in its ground state $|g\rangle$. We then applied drive pulses to both systems at their respective $|f0\rangle \leftrightarrow |g1\rangle$ transition frequencies and measured the final populations of transmon 2 to investigate how the transfer efficiency

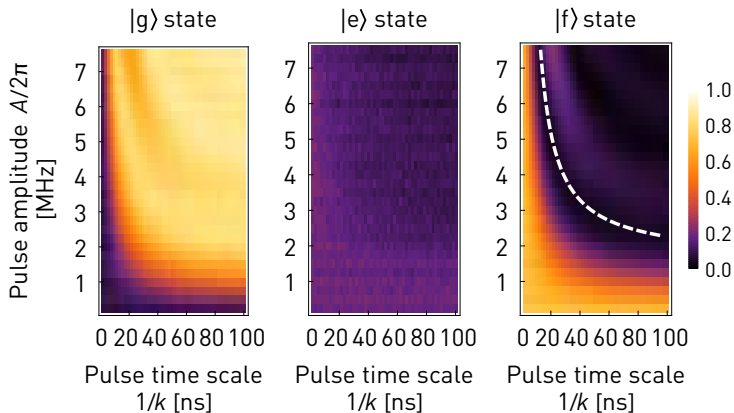


Figure 5.4: Transmon state populations as a function of the time-scale $1/k$ and amplitude A of the $1/\cosh$ pulse defined by eq. (5.1), applied to induce the $|f0\rangle \leftrightarrow |g1\rangle$ transition. The frequency of the pulse varies with its instantaneous amplitude to keep it resonant with the transition. The dashed white line in the right-most plot indicates points of high transfer efficiency from $|f\rangle$ to $|g\rangle$.

depends on the parameters of the $|f0\rangle \leftrightarrow |g1\rangle$ drive pulses. Setting these parameters optimally presents a number of challenges in comparison with the simpler photon shaping experiment. This is chiefly due to the large parameter space which needs to be explored. We expected that many of the relevant aspect of the system, such as the transmittivity of the line connecting the two samples or potential impedance mismatches could not be controlled well enough to set up the measurement parameters simply from first principles. We therefore once more decided to adopt a heuristic approach, similarly to ch. 4.

As derived in sec. E.1, if the transition rate \tilde{g} varies in time as $\kappa/2 \cosh(\kappa t/2)$, the emitted photon is symmetric with a waveform proportional to $1/\cosh(\kappa t/2)$. For this reason, we chose to parametrize the pulses by four numbers $A_{1,2}$ and $k_{1,2}$ such that

$$\tilde{g}_{1,2} = \frac{A_{1,2}}{\cosh k_{1,2}t}. \quad (5.1)$$

The dependence of \tilde{g} on the drive amplitude, obtained from the measurement illustrated in Fig. 5.3, was then inverted and used to find the corresponding time-dependence of the arbitrary waveform generator's output amplitude. Furthermore, the Stark shift measurement shown in Fig. 5.2 was used to calculate the time-dependence of the drive pulse's phase necessary to compensate the Stark shift.

By separately applying the pulse to each of the systems prepared in the $|f0\rangle$ state and measuring the final state populations, we determined a relation between the pulse amplitude A and the time-scale $1/k$ which results in a high-efficiency transfer of the

excitation into the transmission line. The results of this measurement for system 1 are shown in Fig. 5.4. As A and $1/k$ are varied, we observe alternating bands of low and high transfer efficiency, similarly to the case of a square pulse presented in Fig. 5.3. We extracted the positions of the first minima in the $|f\rangle$ state population and described them by an interpolating function indicated by the white dashed line. In the subsequent measurements, we always kept the pulse amplitude and time-scale related to each other by this function.

We then proceeded to set up measurements of the excitation transfer efficiency between the two systems as a function of the two pulse parameters $k_{1,2}$ and the detunings $\delta_{1,2}$ added to the pulse frequencies. These corrections were added to counteract potential deviations of the qubit frequencies from the initially measured values due to long-term drifts. We fixed the detunings to the values leading to the highest transfer efficiencies – $\delta_1/2\pi = 0$ MHz, $\delta_2/2\pi = 1$ MHz – and repeated the measurement, this time sweeping $k_{1,2}$ and the relative delay between the pulses applied to the two systems.

A selection of the obtained data is presented in Fig. 5.5. As we can see, for large delays Δt , the efficiency is optimized when the two pulses have significantly unequal lengths. Fig. 5.5(b) presents the efficiency values maximized over $1/k_1$ and $1/k_2$ as a function of the delay Δt . These data suggest that the efficiency is not extremely sensitive to small variations in relative timing between the pulses. The maximum efficiency reached in these measurements was approximately 37%.

Efficiency analysis

While the photon exchange efficiency achieved in our measurements is significantly higher than that demonstrated with optical photons by Ritter *et al.* (2012), it is still too low for many quantum communication applications such as generation of entanglement. To determine how the performance of our protocol could be improved in future devices, we analyzed the likely factors contributing to the reduced efficiency, as summarized in Tab. 5.1.

The more straightforward sources of inefficiency to estimate are dissipation and insertion loss in the elements connecting the two samples. Based on the length of the coaxial cables and their typical attenuation constant at cryogenic temperatures, we estimated the power transmission in the cabling to be 0.95. From a 4.2 K dipstick network analyzer measurement of a PCB through with a length equal to the total length of the input/output traces in the two used samples, we extracted the transmittivity of the PCB and its SMP connectors as approximately 0.95. The cryogenic circulator used between the two samples is the model CTH1184 from QuinStar (formerly Pamtech). We did not directly measure its microwave properties at base temperature as that would require cryogenic calibration standards. The maximum insertion loss reported by the manufacturer is 0.4 dB, corresponding to a transmittivity of 0.91. The total efficiency of the connection between the two samples is therefore approximately 0.82. This value excludes potential impedance mismatches at the wire bonds of the chip for which we do not have a good estimate.

Using a master equation simulation of the cascaded system (as described in more detail in sec. E.3, we found that Purcell decay of the $|f0\rangle$ state reduces the transfer

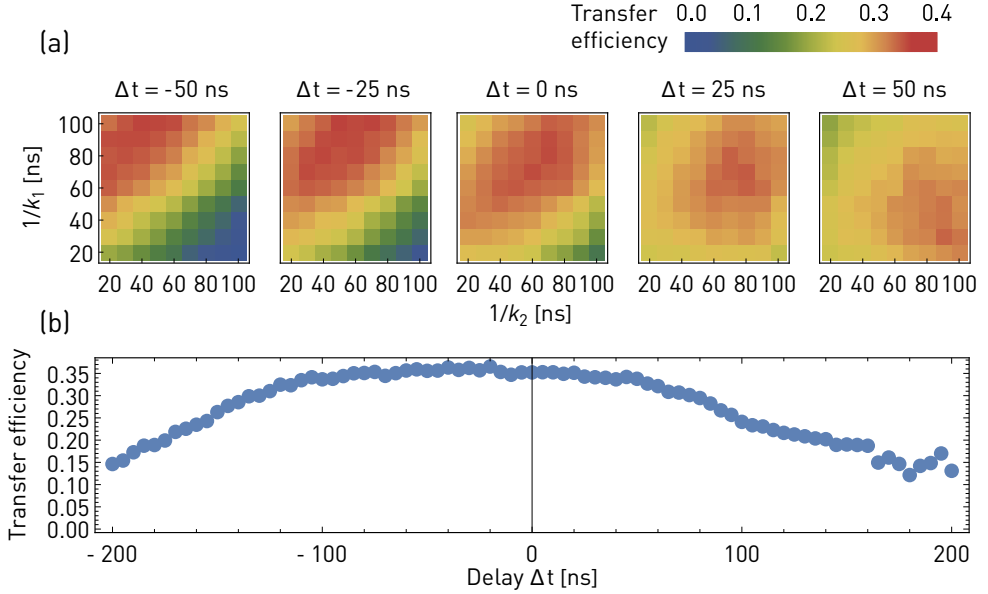


Figure 5.5: (a) Measured transfer efficiency given by the final $|f\rangle$ state population of transmon 2 as a function of the two pulse time-scales $1/k_1$ and $1/k_2$ for several different delays Δt between the pulses. (b) The efficiency maximized over $1/k_1$ and $1/k_2$ as a function of the delay Δt .

transmittivity of coaxial cables	0.95
transmittivity of the PCB	0.95
transmittivity of the circulator	0.91
total connection efficiency	0.82
efficiency reduction due to Purcell decay	0.95
efficiency reduction due to qubit dissipation	0.69
efficiency reduction due to qubit dephasing	0.78
total efficiency due to decoherence	0.52
overall estimated efficiency	0.43
measured efficiency	0.37

Table 5.1: Summary of the different estimated loss mechanisms in the photon reabsorption experiment.

efficiency with respect to the ideal case, where the photon emission process is artificially restricted to link only the states $|g1\rangle$ and $|g0\rangle$, by a factor of approximately 0.95. Including qubit relaxation in the simulations decreases the efficiency further by a factor of 0.69 and qubit dephasing by 0.78. All these effects combined then result in an efficiency of 0.52.

Assuming that we can treat the transmission channel losses and the efficiency reduction due to decoherence as independent and simply multiply the two factors together to get the overall efficiency, we arrive at an estimate of 0.43. This number is reasonably close to the highest measured efficiency of 0.37. This analysis shows that in order to improve the performance of the photon reabsorption scheme, we first need to improve the coherence properties of our transmon qubits. In addition, Purcell decay of the transmon $|f\rangle$ state can be significantly suppressed by using a suitable Purcell filter. The attenuation in the connecting line may be reduced by using superconducting materials or 3d waveguides instead of coaxial cables, as well as employing a circulator optimized for low insertion loss. Operation of the scheme without a circulator is also in principle possible but will most likely involve additional difficulties due to the presence of discrete modes supported by the line. To suppress formation of these standing wave modes, the use of a circulator is preferable.

The remaining unexplained efficiency deficit of $0.37/0.43 \approx 0.86$ could be attributed to one of several factors. For example, the fact that the resonators are not exactly equal in their frequency and linewidth or that the line connecting the two samples is not perfectly dispersionless.

Chapter 6

On-chip microwave switch

Many circuit QED experiments and in particular the ones studying propagating quantum fields could benefit from a possibility to route the microwave signals directly at the base stage of the cryostat. A suitable switching element can have a wide range of applications, ranging from fairly technical ones (saving resources by sharing a single output line among several experiments) to ones where it enables otherwise unfeasible types of experiments and devices (single-photon transistor).

Commercially available, mechanically operated microwave switches have been used for routing of signals inside a cryostat (Ranzani *et al.*, 2013) but these suffer from slow switching times and significant heat dissipation which can disturb the operation of the cryostat. The latter problem can be at least partially mitigated by custom modifications of the switch, as described in app. K, while the former may be circumvented by using a different type of switch, such as a MEMS- or pin-diode-based one. Nevertheless, neither of these options is particularly well suited for integration with superconducting circuits on a single chip.

A simple single-pole single-throw (SPST) switch capable of routing a signal towards an output line or reflecting it back to the input can be implemented for example using a tunable symmetrically coupled resonator, as shown in Fig. 6.1(a,b). Alternatively, other approaches can be used to build a device with a larger bandwidth, as recently demonstrated by Naaman *et al.* (2016) or Chapman *et al.* (2016). A single-pole double-throw (SPDT) switch which connects a single input to either of two distinct outputs (or vice versa) as illustrated in Fig. 6.1(c) is a much more versatile component in many practical applications. It can be realized for example by adding a circulator to the SPST switch in a configuration shown in Fig. 6.1(d). However, this particular version of the SPDT switch is non-reciprocal which may be undesirable in some applications.

One could ask whether a reciprocal SPDT switch can also be realized using some circuit with a single tunable element. It turns out that the answer is “no”, based on rather general arguments about the properties of S-parameter matrices. A detailed proof of this statement is given in app. I. The minimal number of independently tunable elements required to build a reciprocal SPDT switch is two.

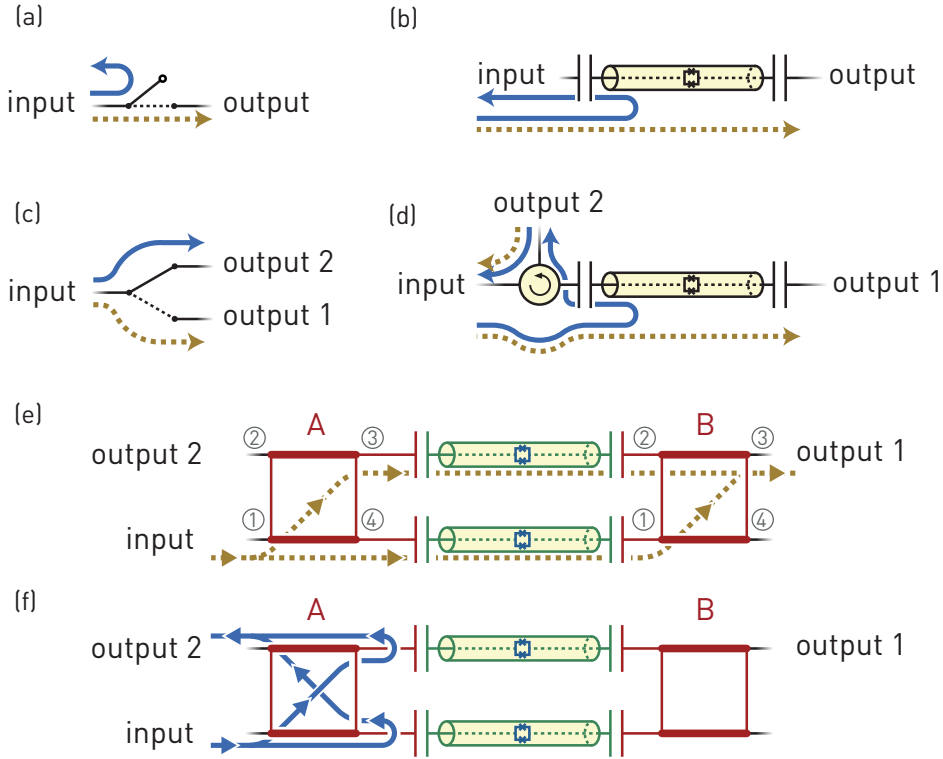


Figure 6.1: (a) Diagram of a single-pole single-throw (SPST) switch, toggling between transmission (dashed yellow line) and reflection (solid blue line). (b) Realization of the SPST switch using a tunable transmission-line resonator. (c) Diagram of a single-pole double-throw (SPDT) switch and (d) its non-reciprocal implementation using a tunable resonator and a circulator. (e,f) Implementation of a reciprocal SPDT switch with two tunable resonators and two $\pi/2$ hybrids (labeled here as A and B). (e) and (f) illustrate its operation in the resonant and off-resonant state, respectively.

An example of a circuit realizing such a switch is shown in Fig. 6.1(e,f). It consists of two tunable resonators placed between two $\pi/2$ -hybrids in a Mach-Zehnder configuration. A $\pi/2$ -hybrid is one of several types of RF circuits which act as microwave analogues of optical beamsplitters. Its S -parameters are given by the matrix

$$\mathbf{S} = -\frac{1}{\sqrt{2}} \begin{pmatrix} 0 & 0 & 1 & i \\ 0 & 0 & i & 1 \\ 1 & i & 0 & 0 \\ i & 1 & 0 & 0 \end{pmatrix} \quad (6.1)$$

A more detailed analysis of this circuit and its properties is presented in app. J. The tunable resonators are realized as $\lambda/2$ resonators (see sec. 1.2) with an array of

SQUID loops in its center. As discussed in sec. 1.3, a SQUID loop can be modeled as an inductor whose inductance depends on the magnetic flux threading the loop. By tuning the inductance of the array, we can vary the resonance frequency of the resonator.

As shown in Fig. 6.1(e), signal entering port 1 of hybrid A is split equally into ports 3 and 4. When the two resonators are both tuned to be resonant with the signal, they are fully transmissive and the signal arrives at hybrid B where it recombines in its port 3.

If the resonators are off-resonant with the signal, it gets reflected back into hybrid A, as illustrated in Fig. 6.1(f). The form of the S -parameters given in eq. (6.1) implies that the signal in the bottom arm of the device is phase-shifted by $\pi/2$ with respect to the top arm. Assuming that both resonators are tuned to the same frequency, the phase difference between the two components of the signal does not change upon reflection from the resonators. The phase relations between the transmission coefficients of the hybrid then imply that the signal interferes destructively at port 1 and constructively at port 2. Thus, the hybrid serves to isolate the reflected signal from the input line.

In this way, by tuning both resonators in or out of resonance with the signal, we can realize an SPDT switch where the input is port 1 of hybrid A and the outputs are port 3 of hybrid B and port 2 of hybrid A. Since the device is reciprocal, the role of the input and outputs can of course be reversed. The symmetry of the device also implies that when the resonators are resonant with the signal and port 1 of hybrid A is connected to port 3 of hybrid B, there is simultaneously a connection between port 2 of hybrid A and port 4 of hybrid B. Similarly, in the off-resonant state, the switch connects together not only ports 1 and 2 of hybrid A but also ports 3 and 4 of hybrid B.

In fact, the S -parameters of the device with respect to ports 1,2 of hybrid A and ports 3,4 of hybrid B can be written in general as

$$\mathbf{S} = i \begin{pmatrix} 0 & r & t & 0 \\ r & 0 & 0 & t \\ t & 0 & 0 & r \\ 0 & t & r & 0 \end{pmatrix},$$

where r and t are the reflection and transmission coefficient of the two resonators. Here we again assume that the resonators are tuned to the same frequency and therefore their S -parameters are identical. This form of the S -parameter matrix is that of an unbalanced beamsplitter. The switch can therefore be operated not only in the two discrete states where r and t are either zero or one, but also in an intermediate regime where the resonators are partially transmissive. In this case, it acts as a tunable beamsplitter.

6.1 Basic characterization of the switch

We have implemented the circuit outlined above on a 7×4 mm niobium-on-sapphire chip, as shown in Fig. 6.2(a). The sample was prepared using the standard fabrication

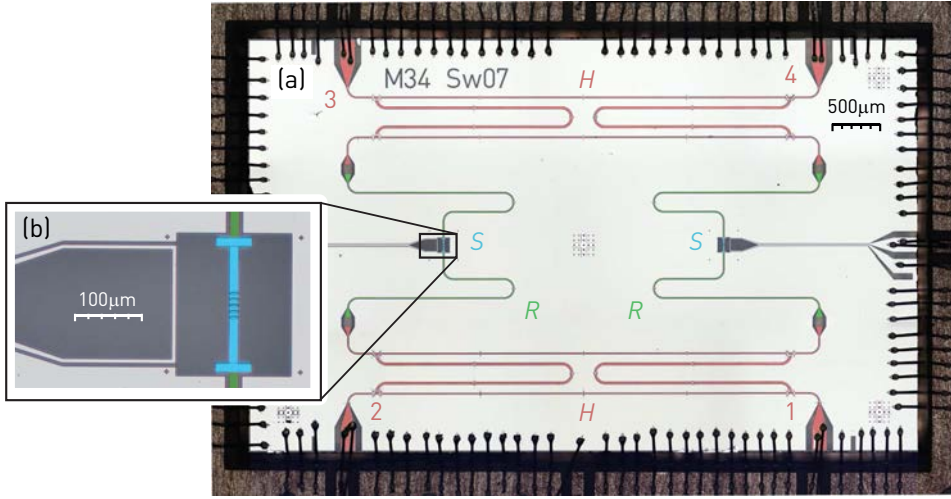


Figure 6.2: (a) False-color microscope picture of the on-chip switch sample, with the $\pi/2$ hybrids (H) in red, the tunable resonators (R) in green and their SQUID arrays (S) in cyan. The ports of the device labeled as 1,2,3,4 correspond to ports 1,2 of hybrid A and ports 3,4 of hybrid B in Fig. 6.1(e,f). (b) Enlarged view of one of the arrays with five SQUID loops. The loop on the left is the on-chip flux line which can be used for flux-biasing the array.

process employed in our lab (see sec. 2.2). The resonators and the hybrids were patterned in niobium using optical lithography and dry etching. The SQUID arrays in the centers of the resonators, consisting each of $N = 5$ SQUID loops, were deposited by electron beam lithography and evaporation of aluminium. The SQUIDs are designed to be asymmetric with a ratio of Josephson energies of 2 : 3. This reduces the tuning range of the resonators to suppress the sensitivity of the resonator frequencies to external magnetic flux noise.

The sample was then glued and wire-bonded on a copper printed circuit board which was placed into a copper sample-holder. Two coils, each with a diameter of 4 mm and 3000 windings of superconducting wire were mounted to the sampleholder, positioned approximately underneath the two SQUID arrays.

The sample-holder was placed at the base temperature stage of the Vericold cryostat and the sample connected to a measurement setup whose cryogenic part is outlined schematically in Fig. 6.3(a). For practical reasons, we decided to characterize the device in a setting which is the reverse of that represented in Fig. 6.1(e,f). That is, instead of routing a signal from a single input to one of two outputs, we measured the signal transmission from two inputs to one output.

We numbered the ports of the switch such that port 1 was connected to the output line and ports 2 and 3 to the input lines. Port 4 was not connected to any microwave

line but instead was terminated with a cryogenic $50\ \Omega$ load. To enable measurements of reflections from the device, we additionally connected port 1 to another input line via a circulator.

Calibration of S -parameter measurements

In most circuit QED experiments, the overall scaling of the measured signal is irrelevant. For example, to find the resonance frequency of a resonator or a qubit, we are only interested in the position of the feature of interest in the frequency spectrum and not in its amplitude. However, to characterize the performance of the switch, we seek to determine its S -parameters in absolute terms. Therefore, somewhat unusually for typical circuit QED setups, we need to calibrate the transmission of the input and output lines. Since these are temperature-dependent, the calibration measurement needs to be done while the cryostat is cold.

Full calibration of an S -parameter measurement of a multi-port device, for example using the *thru-reflect-line* (TRL) technique (Pojar, 2011), requires many individual measurements in which different standards are connected to the setup. This makes such a calibration extremely time consuming in a cryogenic setting since the cryostat needs to be warmed up and opened every time the standard is to be exchanged. This obstacle could be circumvented using a setup in which the calibration standards can be exchanged remotely, for example by means of a microwave switch. Such an approach was demonstrated for example by Ranzani *et al.* (2013).

Since this was not an option in our measurements setup, we settled for a simpler calibration scheme which is not completely general but suffices under the assumption that the input and output lines are well impedance-matched. In this case, the setup can be fully characterized by the attenuation of the individual lines. For our setup with only a single output line, it is enough to determine the total attenuation of the output line in combination with each of the inputs.

To this end, we performed three calibration measurements which are schematically shown in Fig. 6.3(b,c,d). These were done in three separate cool-downs of the cryostat but in order to save time, the system was only pre-cooled to approximately 10 K with the pulse tube cooler and the $^3\text{He}/^4\text{He}$ mixture was not condensed into the dilution unit. This approach is justified by a separate measurement where the transmissions through the input and output lines at 10 K and at the base temperature were found to be nearly identical. The first two calibration measurements illustrated in Fig. 6.3(b,c) were done with input lines 2 and 3 connected directly to the output line via a short coaxial cable. They served as a reference for full transmission through the device-under-test. The third measurement represented in Fig. 6.3(d) was done with the end of input line 1 / output line left open to give us a normalization for full reflection from the device under test. By dividing the signal measured with the switch connected to the setup by these calibration data, we could then obtain the normalized S -parameters S_{11} , S_{12} and S_{13} .

To estimate impedance mismatches in the setup, we performed one additional measurement as shown in Fig. 6.3(e). Here, input line 1 was terminated with a $50\ \Omega$ load. In the ideal case, the signal from input line 1 would be perfectly absorbed by

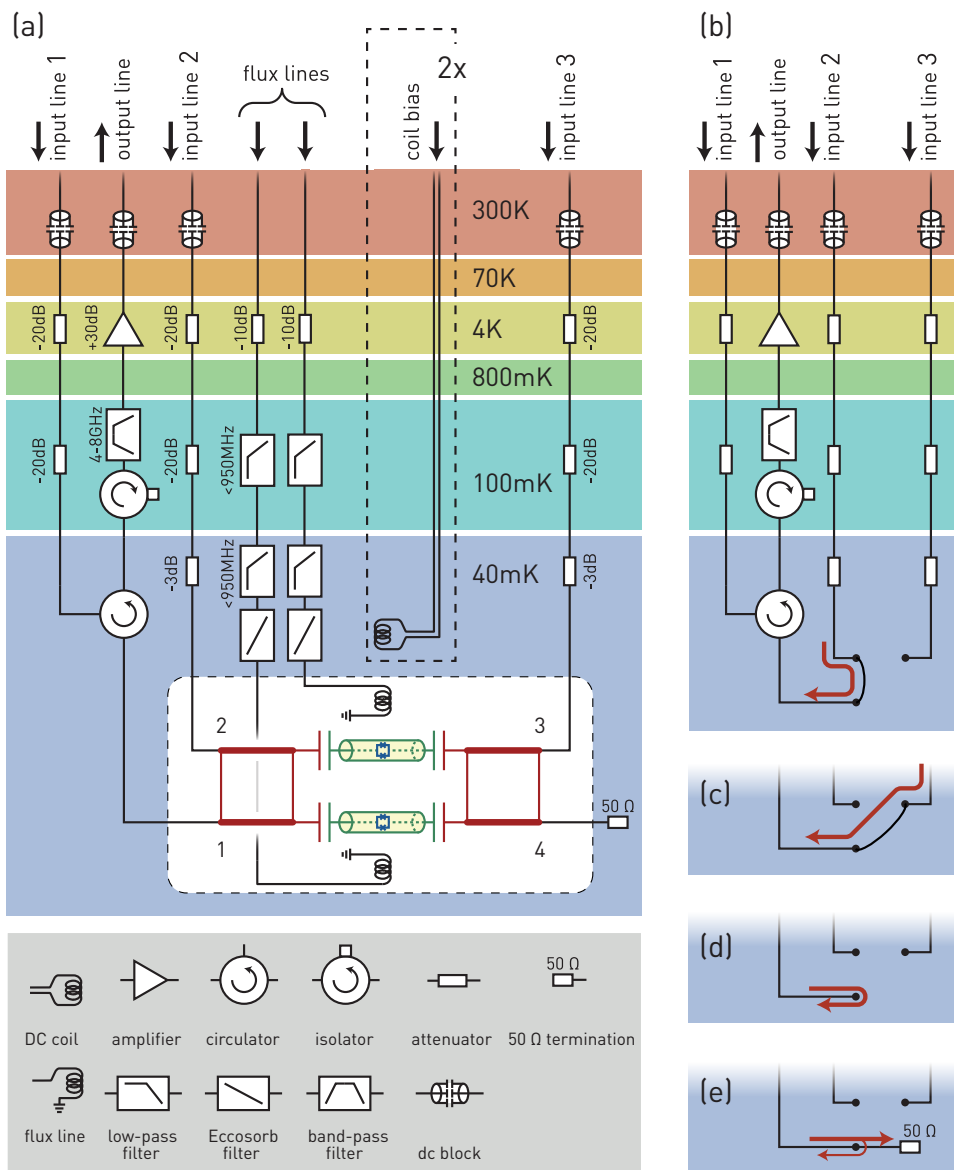


Figure 6.3: (a) Diagram of the setup used in characterization measurements of the on-chip switch in the Vericold cryostat. (b,c,d) Illustration of the calibration measurements used to normalize the S -parameters of the switch: Through measurements with the output line connected by a short cable directly to (b) input line 2 and (c) input line 3. (d) Full reflection measurement with the end of input line 1 left open. (e) Spurious reflection measurement with the end of line 1 terminated with a $50\ \Omega$ load.

the load. In reality, imperfections in impedance matching in the line between the bottom-most circulator and the sample lead to spurious reflections into the output line which in our setup varied between -20 dB and -10 dB in power. While this level of reflections is significant, it does not seem to be atypical – similar values were reported in our lab by van Loo (2014).

Tuning of the resonators

To characterize the sample, we started by measuring the transmission coefficient S_{12} as a function of the signal frequency and the voltage applied to one of the flux bias coils. If the resonators are off-resonant with the signal, we expect high transmission between ports 1 and 2. This transmission will decrease if the signal frequency matches either of the two resonators. We therefore observe the resonators as dips in the S -parameter S_{12} , as shown in Fig. 6.4(a).

We see that the frequency of one of the resonances is more sensitive to the coil voltage than the other. This is due to the asymmetric coupling of the two coils to the SQUID arrays. Each coil couples significantly more to the array which is physically closer to it.

The dependence of the resonance frequency on the coil voltage is approximately periodic, as expected due to the periodicity of the SQUID array inductance as a function of applied magnetic flux. The deviation from an exactly periodic dependence, which we clearly observe in Fig. 6.4(a), is the effect of non-uniformity of the magnetic field across the SQUID array. The following model, represented in Fig. 6.4(a) by the dashed line, matches the measured data very well:

The inductance L of an asymmetric SQUID loop in its linear regime can be tuned between its minimum and maximum value L_{\min} and L_{\max} . Its dependence on the applied magnetic flux Φ is given by

$$L_S(\phi) = \frac{L_{\min}L_{\max}}{\sqrt{L_{\max}^2 \cos^2 \frac{\phi}{2} + L_{\min}^2 \sin^2 \frac{\phi}{2}}}, \quad (6.2)$$

where $\phi = 2\pi\Phi/\Phi_0$ and Φ_0 is the magnetic flux quantum. We assume that the Josephson energies of the junctions comprising the five individual SQUID loops in the array are identical but we allow for the possibility that the fluxes Φ_1, \dots, Φ_5 threading the loops are unequal. However, we will constrain them to satisfy $\Phi_1 = \Phi_5$ and $\Phi_2 = \Phi_4$ due to symmetry of the sample. We will further take the fluxes to be linear functions of the applied coil voltage V of the form $\Phi_1 = \Phi_5 = \Phi_0(V - V_0)/V_1$, $\Phi_2 = \Phi_4 = \Phi_0(V - V_0)/V_2$ and $\Phi_3 = \Phi_0(V - V_0)/V_3$. The total inductance of the SQUID array is then

$$\begin{aligned} L(V) = & 2L_S(2\pi(V - V_0)/V_1) \\ & + 2L_S(2\pi(V - V_0)/V_2) \\ & + L_S(2\pi(V - V_0)/V_3). \end{aligned} \quad (6.3)$$

To calculate the dependence of the resonator frequency on the SQUID array inductance, we consider the circuit model of the system shown in Fig. 6.5. The symmetry

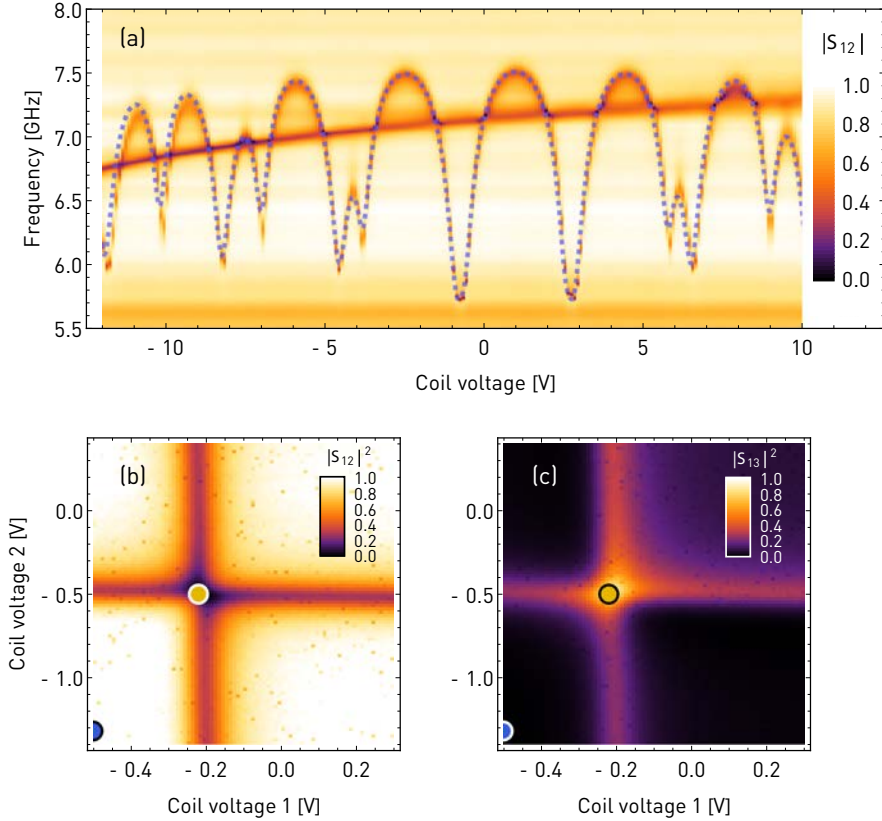


Figure 6.4: (a) Measured S -parameter $|S_{12}|$ as a function of the signal frequency and the voltage applied to one of the flux bias coils. Measured transmittances (b) $|S_{12}|^2$ and (c) $|S_{13}|^2$ as a function of the voltages applied to the two coils. The optimal operating points of the switch found from these data are indicated by the yellow circle for the resonant state and by the blue circle for the off-resonant state.

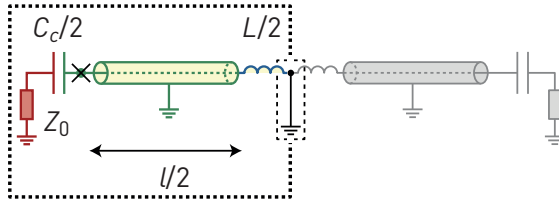


Figure 6.5: Schematic diagram of the tunable resonator, with the SQUID array inductance L and the coupling capacitance C_c between the resonator and its environment modeled as a lumped impedance $Z_0 = 50 \Omega$. For calculation of the fundamental mode frequency, the center point is connected to ground, as indicated in the dashed box. The dotted box shows the reduced circuit whose resonance frequency is to be found. The node chosen for the admittance calculation is marked by \times .

of the resonator with respect to its center implies that the fundamental mode has a voltage node at the center point. Therefore, for the purposes of further circuit analysis, we can connect this point to ground and analyze only one of the two halves of the resulting circuit, as illustrated in the figure.

As derived in sec. B.1, the resonance frequency can be determined by expressing the admittance of the circuit as a function of frequency and finding its zero. The node at which the admittance is taken can be chosen arbitrarily as long as the mode of interest has a non-zero voltage amplitude there. Here we choose the node at the end of the resonator indicated in Fig. 6.5 by \times . The admittance is found to be

$$Y = \frac{i}{Z_0} \left(\frac{x_c \delta}{ix_c \delta + 1} - \frac{1 - x_L \delta \tan \delta}{x_L \delta + \tan \delta} \right),$$

where $\delta = \omega l/2v$ is the phase accumulated by the signal upon propagation over a distance $l/2$, half the length of the resonator, v is the propagation velocity in the transmission line and $x_c = 2vC_c Z_0/l$, $x_L = vL/Z_0 l$ are dimensionless parameters quantifying the coupling capacitance C_c and the SQUID array inductance L . The equation $Y = 0$ takes a particularly simple form (Eichler & Wallraff, 2014) in the limit $C_c \rightarrow 0$:

$$\delta \tan \delta = \frac{1}{x_L}.$$

Taking this limit is justified in our case since the coupling, characterized by the linewidth of the resonator, is small in comparison with the resonance frequency. If the inductance L vanishes, we get $\delta = \pi/2$ and the circuit resonates at the bare resonator frequency $\omega_{r0} = \pi v/l$. We can eliminate the resonator parameters v and l from the expression for δ by writing it as $\delta = \pi \omega/2\omega_{r0}$. The relation between the resonance frequency ω_r and the SQUID array inductance L is then

$$\tan \frac{\pi \omega_r}{2\omega_{r0}} = \frac{2Z_0}{\omega_r L}. \quad (6.4)$$

To find the bare resonance frequency ω_{r0} , we measured a sample with an identical resonator except with the SQUID array replaced by a short niobium wire whose inductance we neglect. A micrograph of this test sample is presented in Fig. 6.6. Its resonance frequency and linewidth determined in a dipstick measurement at 4.2 K using a vector network analyzer (VNA) were $\omega_{r0}/2\pi = 8.3$ GHz and $\kappa_0/2\pi = 305$ MHz. Eq. (6.2) together with eq. (6.3) and eq. (6.4) then allow us to calculate the resonance frequency as a function of the coil voltage V . The parameters of this models are the minimum and maximum inductance L_{\min} and L_{\max} , the coupling parameters V_1 , V_2 , V_3 and the voltage offset V_0 . A fit of the model to the data plotted in Fig. 6.4(a) provides a very good match, as shown by the dashed line in the plot. The optimal fit parameters are $V_0 = 0.984$ V, $V_1 = 3.192$ V, $V_2 = 3.686$ V, $V_3 = 3.686$ V, $L_{\min} = 0.064$ nH and $L_{\max} = 0.354$ nH. These inductances correspond to Josephson energies of 2.55 THz and 0.46 THz, respectively.

Another dipstick measurement in liquid helium was used to determine the optimal operating frequency of the $\pi/2$ hybrid. Here, the S -parameters of a sample containing a single hybrid, shown in Fig. 6.6(c), were measured with a VNA and found to best match the ideal beamsplitter values at a frequency of approximately 7.2 GHz. This operating frequency differs by about 3% from the designed value of 7 GHz which may be due to a mismatch between the assumed and the actual effective dielectric constant of the transmission lines or due to unaccounted-for boundary effects at the junctions between the lines.

With the signal frequency fixed to the hybrids' operation point of 7.2 GHz, we then measured the S -parameters S_{12} and S_{13} as a function of the voltages applied to the two coils. The corresponding transmittances $|S_{12}|^2$ and $|S_{13}|^2$ are plotted in Fig. 6.4(b,c). We see that the transmission between ports 1 and 2 approaches unity and between ports 1 and 3 zero unless either of the two resonators is tuned close to the signal frequency. The resonance condition occurs at approximately -0.2 V for the resonator which is strongly coupled to coil 1 and at -0.5 V for the resonator coupled to coil 2. When both resonators are resonant with the signal, $|S_{12}|^2$ reaches its minimum while $|S_{13}|^2$ is maximal.

In the ideal case, the switch should reach $|S_{12}|^2 = 0$, $|S_{13}|^2 = 1$ in the resonant state and $|S_{12}|^2 = 1$, $|S_{13}|^2 = 0$ in the off-resonant state. We defined the ratio $|S_{12}|^2/|S_{13}|^2$ as a figure of merit to quantify how well the real device approximates these ideal values. We then minimized and maximized this quantity to find the settings for the resonant and off-resonant state of the switch, respectively. The operating points found in this way are marked in Fig. 6.4(b,c) by the yellow and the blue circle. In the resonant state, we find $|S_{12}|^2 = 0.005$, $|S_{13}|^2 = 0.93$ and in the off-resonant state $|S_{12}|^2 = 1.03$, $|S_{13}|^2 = 0.001$. The clearly unphysical value of a transmittance higher than one can be attributed to imperfect calibration data, for example due to long-term drifts in the properties of the measurement lines. The ability of the switch to block the unwanted transmission channel can be characterized by the on/off ratios between the transmittances in the switch states. From the values stated above, we calculate these to be 23.1 dB between ports 1 and 2 and 29.7 dB between ports 1 and 3.

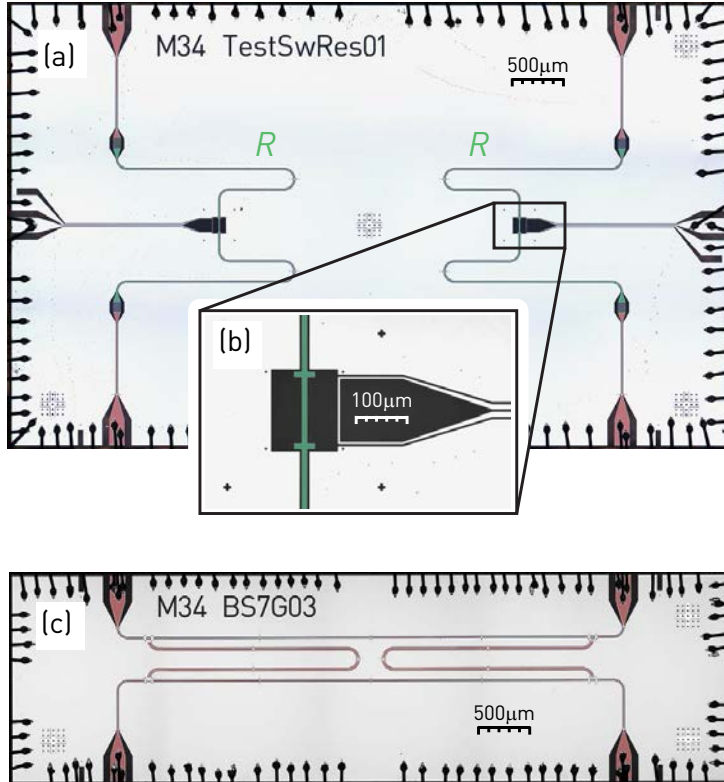


Figure 6.6: (a) False-color microscope picture of the test sample without SQUID arrays used to characterize the bare resonator parameters in a dipstick measurements at 4.2 K. The chip contains two resonators (R) shown in green. Its input and output lines are indicated in red. (b) Enlarged view of one of the center areas where the SQUID array is replaced by a strip of niobium, directly connecting the two halves of the resonator. (c) False-color microscope picture of the test sample containing a $\pi/2$ hybrid, used to characterize its S -parameters and find its optimal operating frequency.

Frequency spectrum

After finding the two operating points of the switch, we characterized its bandwidth by measuring the transmittances $|S_{12}|^2$ and $|S_{13}|^2$ as a function of frequency. The obtained data, plotted in Fig. 6.7(a,b), show that in the off-resonant state (blue), the transmittivities are relatively insensitive to frequency changes. This is to be expected because the signal is detuned from the resonance frequencies of the two resonators by more than 1 GHz, that is, by nearly ten times their linewidth. On the other hand, in the resonant state (yellow), the bandwidth of the device is determined by the linewidth of the tunable resonators. The data closely match the expected Lorentzian frequency response given by $|S_{13}|^2 = 1 - |S_{12}|^2 = 1/(1 + 4(f - f_0)^2/\Delta f^2)$. The least-squares fit indicated in Fig. 6.7(a,b) by the dashed line, yields the center frequency $f_0 = 7.20$ GHz and the bandwidth $\Delta f = \kappa/2\pi = 149$ MHz.

The values of $|S_{12}|^2$ above unity which can be seen in Fig. 6.7(a) are obviously unphysical for a passive device such as ours. We attribute these to imperfections of the calibration procedure. Specifically, we have observed that the total transmittance of the input and output lines can vary by up to 10% between subsequent cool-downs of the cryostat. It is therefore reasonable to implicitly assume a relative uncertainty of this order of magnitude for all stated transmittances and reflectances.

To characterize the impedance-matching of the switch, we measured the signal reflected from port 1, obtaining the data plotted in Fig. 6.7(c). Within the bandwidth of the switch, the reflections are below 10% and they do not exceed 20% over the measured frequency range. For comparison, the spurious reflections of the measurement setup itself, as characterized by the calibration measurement outlined above, are shown by the green curve in Fig. 6.7(c). The reflections from the switch seem to be of the same order of magnitude as those of the setup and they are nearly identical in both states of the switch. This suggests that they may originate from impedance mismatches between the PCB connectors and the hybrids on the chip.

It can seem counterintuitive that the reflectivity measured with the device connected is lower than in the calibration measurement. However, we need to keep in mind that the reflections in the measurement setup may interfere destructively with those in the sample, leading to total reflections smaller than if the sample is replaced by a 50Ω load.

Compression point

As the switch relies on Josephson junctions for its operation, we should expect it to become non-linear at sufficiently high levels of power. The non-linearity of the device can be estimated in a simplified model where the resonators are approximated as Duffing oscillators with the Hamiltonian

$$\hat{H}/\hbar = \omega_r \hat{a}^\dagger \hat{a} + \frac{1}{2} K \hat{a}^\dagger \hat{a}^\dagger \hat{a} \hat{a}, \quad (6.5)$$

where the Kerr non-linearity K is the lowest-order anharmonic correction to the resonator energy levels due to the non-linearity of the Josephson junctions.

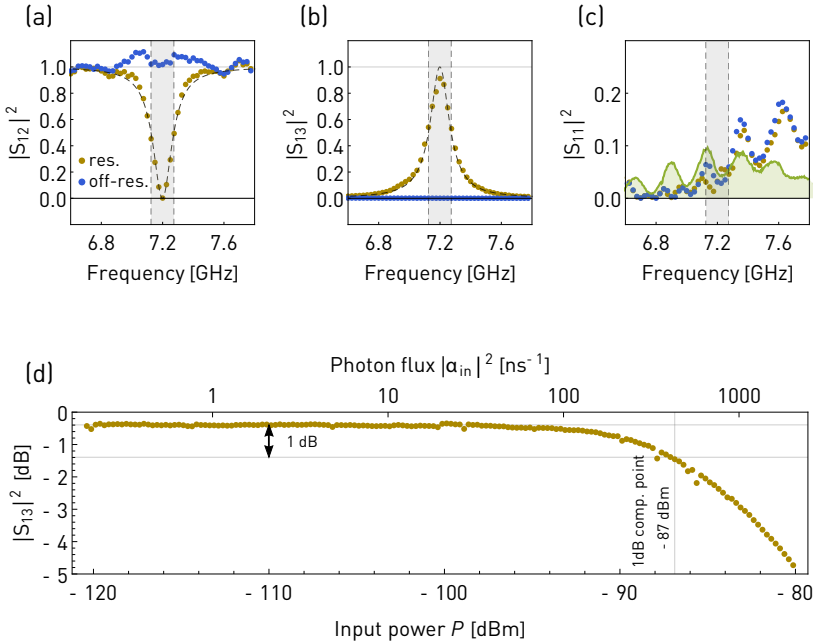


Figure 6.7: Frequency dependence of the transmittances (a) $|S_{12}|^2$, (b) $|S_{13}|^2$ and (c) the reflectance $|S_{11}|^2$ for the resonant (yellow points) and the off-resonant (blue points) state of the switch. The FWHM bandwidth of the device is indicated by the gray bar. The dashed lines in (a,b) represent a Lorentzian fit while the green solid line in (c) is the spurious reflectance of the measurement lines (see Fig. 6.3(e)). (d) Power dependence of the transmittance $|S_{13}|^2$, showing the onset of non-linearity. The indicated 1 dBm compression point is found at an input power of -87 dBm.

We will study the case when the resonators are driven resonantly. In a rotating frame at the signal frequency $\omega_s = \omega_r$, the input-output relations (Walls & Milburn, 2008) for the resonator probed in transmission are

$$\begin{aligned} \frac{d}{dt} \hat{a} &= -iK \hat{a}^\dagger \hat{a} \hat{a} + \sqrt{\frac{\kappa}{2}} \hat{a}_{\text{in}} - \frac{\kappa}{2} \hat{a}, \\ \hat{b}_{\text{out}} &= \sqrt{\frac{\kappa}{2}} \hat{a}. \end{aligned}$$

In the classical approximation, we replace the operators \hat{a} , \hat{b}_{in} and \hat{b}_{out} by c -numbers α and β_{in} and β_{out} and get the steady state equations

$$\alpha = \frac{\sqrt{\frac{\kappa}{2}} \alpha_{\text{in}}}{iK |\alpha|^2 + \frac{\kappa}{2}} = \beta_{\text{out}} \sqrt{\frac{2}{\kappa}}.$$

Its solution can be found to lowest order in K as

$$\frac{\beta_{\text{out}}}{\alpha_{\text{in}}} = \frac{1}{\frac{4iK|\alpha_{\text{in}}|^2}{\kappa^2} + 1}.$$

Therefore, the power transmission is suppressed by 1 dB, that is, a factor of $\epsilon = 10^{1/10}$ when $16K^2|\alpha_{\text{in}}|^4/\kappa^4 + 1 = \epsilon$. The power $P_{\text{cp}} = 2\hbar\omega_r|\alpha_{\text{in}}|^2$ entering the switch at its 1 dB compression point is then given by

$$P_{\text{cp}} = \frac{\hbar\kappa^2\omega_r\sqrt{\epsilon-1}}{2|K|}. \quad (6.6)$$

To evaluate this quantity, we need to find the Kerr non-linearity K . We first notice that it is by definition (see eq. (6.5)) equal to d^2E_n/dn^2 , where E_n are the energy levels of the non-linear oscillator. To zeroth order, the Hamiltonian \hat{H}_0 of the system is that of a linear system where the SQUID array was linearized and represented by its equivalent inductance L . The non-linear correction to the linear system is comprised of the fourth and higher order terms in the expansion of the array's energy $-NE_J \cos(\hat{\delta}/N)$. Here E_J is the Josephson energy of each individual SQUID loop and $\hat{\delta}$ is the operator of the phase drop across the array. To lowest order, the correction \hat{V} is given by

$$\hat{V} = -\frac{1}{24N^2L} \left(\frac{\Phi_0}{2\pi} \right)^2 \hat{\delta}^4,$$

where Φ_0 is the magnetic flux quantum.

We can express the phase drop $\hat{\delta}$ in terms of the ladder operators \hat{a} and \hat{a}^\dagger as $\hat{\delta} = \delta_{\text{vac}}(\hat{a} + \hat{a}^\dagger)$. The vacuum amplitude of the phase drop δ_{vac} can be calculated by considering the fraction η of the circuit's energy stored in the SQUID array. On the one hand, this can be expressed as the ratio of the array's vacuum energy $\langle 0|\hat{\Phi}^2|0\rangle/2L$, where $\hat{\Phi} = \Phi_0\hat{\delta}/2\pi$, and the total vacuum energy of the circuit $\hbar\omega_r/2$. From here, we can write δ_{vac} as $2\pi\sqrt{\hbar\omega_r L\eta}/\Phi_0$. On the other hand, a classical circuit analysis of the system gives

$$\eta = \frac{1}{1 + (y + 1/y) \arctan y},$$

where $y = 2Z_0/\omega_r L$. According to eq. (6.4), we can calculate this parameter as $y = \tan(\pi\omega_r/2\omega_{r0})$. The Kerr non-linearity, expressed as $K = \hbar^{-1}d^2\langle n|\hat{V}|n\rangle/dn^2$, can then be written in the form

$$K = -\frac{\delta_{\text{vac}}^4}{2\hbar N^2 L} \left(\frac{\Phi_0}{2\pi} \right)^2 = -\frac{4e^2 Z_0 \omega_r}{\hbar N^2} \frac{1}{y(1 + (y + 1/y) \arctan y)^2}, \quad (6.7)$$

which after substitution into eq. (6.6) yields the following expression for the input power at the 1 dB compression point:

$$P_{\text{cp}} = \frac{\hbar^2 \kappa^2 N^2 \sqrt{\epsilon-1}}{8Z_0 e^2} y(1 + (y + 1/y) \arctan y)^2. \quad (6.8)$$

This equation shows us how the different parameters of the system influence its non-linearity. Assuming that the bare resonator frequency ω_{r0} and the operating frequency ω_r are fixed, the 1 dB compression point scales as $P_{\text{cp}} \propto \kappa^2 N^2$. That is, we can improve the linearity of the device by increasing its bandwidth κ or the number of SQUID loops in the array. The upper limit on κ is determined by the tunability of the resonators since a good on/off ratio can be achieved only if the resonators can be tuned by significantly more than κ . The number of SQUID loops is ultimately limited by the used fabrication process and by the homogeneity of the applied magnetic field which is required over the extent of the array. In the tested sample, we chose $N = 5$ as a reasonable compromise between these requirements.

For the parameters of our device, which are $y = 4.73$, $\kappa/2\pi = 149$ MHz and $N = 5$, eq. (6.8) gives the value $P_{\text{cp}} = 3.42$ pW = -84.7 dBm. This power corresponds to a photon flux of approximately 7×10^5 per microsecond.

The measured dependence of the transmittivity $|S_{13}|^2$ on the input power is plotted in Fig. 6.7(d). As expected, it is constant at low powers but starts to decrease when the power becomes sufficiently high. The measured power level at which the transmittivity drops by 1 dB with respect to the low-power limit is -86.9 dBm. This is close to the theoretically predicted value of -84.7 dBm derived above. We attribute the difference of approximately 2 dB to the reduced losses in the microwave input line at low temperatures. The transmittivity of the input line, which is used to relate the output power of the microwave generator to the power arriving at the sample, was measured at room temperature. It is reasonable to assume that when the cryostat is cooled down, this transmittivity increases. This means that the values of power on the horizontal axis of Fig. 6.7(d) are in fact slightly underestimated.

The fact that the obtained 1 dB compression point is rather high when compared with typical signal powers in circuit QED experiment means that our switch can be treated as a linear device in most realistic settings.

Switching speed

After the continuous-tone characterization measurements described above, we investigated the switching speed of the device. To this end, we connected the measurement setup to a room-temperature data acquisition system with a higher sampling rate of 1 GS/s. This is based on the Virtex 6 field-programmable gate array (FPGA) and provides a measurement bandwidth of approximately 500 MHz. Here, the digitized waveforms were averaged and their mean was recorded without any further processing by the FPGA. All subsequent data analysis was then done in software. After digital down-conversion of the signal from its intermediate frequency of 250 MHz to dc, we convolved it with a filter which has a sinc shape in time domain. This corresponds to a boxcar function in the frequency domain, centered around zero with a width of 500 MHz. Such a filter therefore removes all frequency components above 250 MHz. In addition, to remove artifacts of the digital processing attributed to cross-talk of digital signals in the FPGA, we explicitly set frequency components at 250 and 125 MHz to zero.

We flux-biased the sample with the dc coils to set the switch to its resonant state. Using a Tektronix 5014 arbitrary waveform generator (AWG) with an output

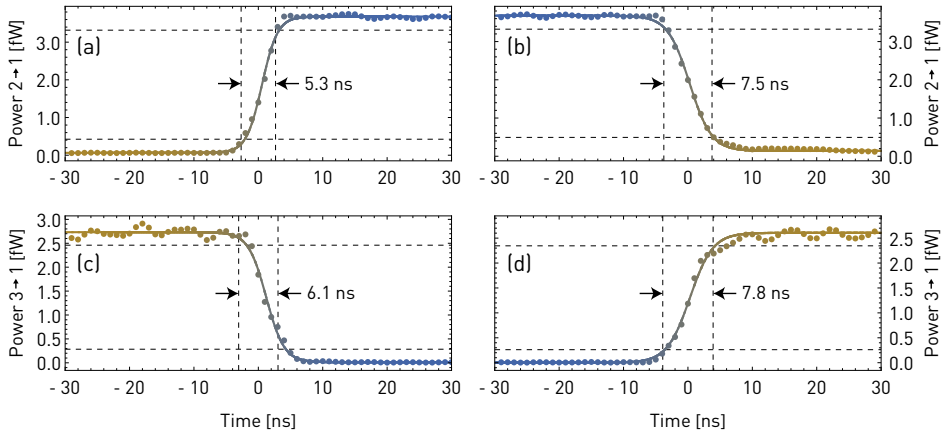


Figure 6.8: Demonstration of the device’s switching speed. Recorded waveforms of (a) the rising and (b) the falling edge of the signal transmitted from port 2 to port 1 and (c,d) from port 3 to port 1. The colors of the points represent the two switch states. Solid lines are fits to a tanh step used to estimate the rise/fall times. Dashed lines represent the 10% and 90% signal level used to extract the indicated switching times.

bandwidth of 250 MHz, we applied nominally square pulses to the flux lines of the sample. We then found the combination of amplitudes of these pulses which brought the switch closest to the ideal off-resonant state. The obtained optimal amplitudes were approximately -370 mV for both lines at the output of the AWG. Based on room-temperature measurements of the flux line’s S -parameters, this corresponds to a current of approximately 5 mA in the on-chip flux line loop.

To observe the switching waveforms, we applied a continuous microwave tone at 7.2 GHz to either of the two input lines 2 and 3 and recorded the output signal while the state of the switch was being toggled by the flux pulse. The obtained data are plotted in Fig. 6.8. We fitted a tanh step to the waveform to extract the 10% to 90% rise times of 5.3 ns for transmission from port 2 and 7.8 ns from port 3. The corresponding fall times are 7.5 ns and 6.1 ns.

The detection chain, the AWG and the coaxial section of the flux line have bandwidths of approximately 500 MHz, 250 MHz and 950 MHz, respectively. We therefore expect that the switch resonators’ narrower bandwidth of 150 MHz should be the main limit on the speed of the switching process. The transmittivity of a continuously driven resonator with a full-width-half-maximum bandwidth $\kappa/2\pi$ whose frequency suddenly changes from far off-resonant to resonant is expected to be given by $(1 - e^{-\kappa t/2})^2$. The time-scale on which this function reaches its new steady state is characterized by a 10% to 90% rise time of approximately $5/\kappa$. When the resonator is tuned from resonance to a far off-resonant frequency, the transmittivity falls off as $e^{-\kappa t}$ and the corresponding 90% to 10% fall time is roughly $2/\kappa$. In our case

where $\kappa/2\pi = 149$ MHz, this simple theory predicts that the switching times should be approximately 5.5 ns from the off-resonant to the resonant state and 2.3 ns for the opposite transition. The measured values are 7 – 8 ns and 5 – 6 ns. We attribute the excess of 2 – 3 ns to the bandwidth limit of the flux line, the detection chain and the AWG. The on-chip section of the fluxline, which could not be characterized separately from the coaxial cabling, may be a potential source of additional bandwidth limitations. This could be investigated in future generations of the switch by means of finite element simulations.

The demonstrated nanosecond switching speed of the device means that it can become a useful tool for applications where on-chip routing of signals needs to be controlled by real-time feedback on time-scales significantly shorter than the typical circuit QED coherence times.

6.2 Single photon source

To demonstrate the operation of the switch in the quantum regime and its integration with other quantum systems, we prepared a proof-of-principle sample which combines the switch with a single photon source on one chip. The finished device is presented in Fig. 6.9. The switch is completely analogous to the first generation device described above, except for the arrangement of its elements on the chip and the design of the $\pi/2$ -hybrid which we made more compact to facilitate easier scaling in future devices.

The single photon source is of the type presented by Peng *et al.* (2015). It is based on a transmon qubit, shown in Fig. 6.9(b), directly capacitively coupled to the input line of the switch. If the operation of the switch is ideal, its input line presents a 50Ω load to the qubit. Effectively, it can be regarded as a Markovian dissipative environment which induces energy relaxation of the qubit, as described by the standard master equation (Walls & Milburn, 2008). The concept of dissipation in electrical circuits is analyzed in more detail in app. B and a closer study of the single photon source circuit is presented in sec. A.3.

After the qubit is prepared in a superposition state $\alpha|g\rangle + \beta|e\rangle$ of its ground and first excited state, it spontaneously relaxes by emitting a photon into the input line of the switch. The state of the emitted field is given by the superposition $\alpha|0\rangle + \beta|1\rangle$ of the vacuum state and the single-photon Fock state. Its temporal mode is described by an exponential envelope which in the tested device has a time constant of approximately 90 ns.

The qubit is initialized in the superposition state by applying a microwave pulse at its transition frequency through a drive line which can be seen at the top of Fig. 6.9(b) in blue. The mutual capacitance of the qubit to the drive line is designed to be smaller than to the switch input line by approximately a factor of 7. Due to this asymmetry, the probability of the photon being emitted into the drive line is expected to be only about 2.3%. This value is derived from the relaxation rates of the qubit into the two lines, calculated in sec. A.3. As also discussed in sec. A.3, we additionally estimated the direct coupling between the drive line and the switch input line. This coupling, if strong enough, can lead to a significant fraction of the qubit initialization pulse leaking directly into the switch input line, thus compromising the operation of the

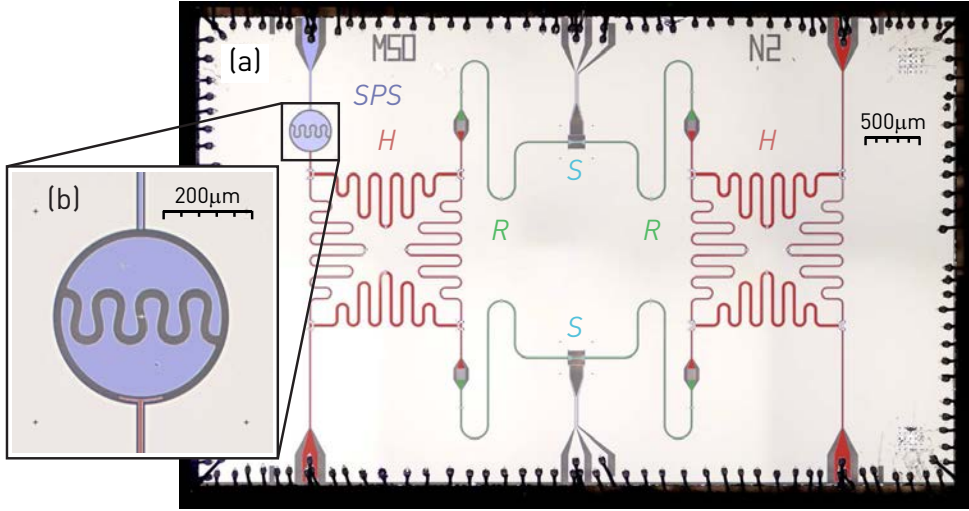


Figure 6.9: (a) False-color microscope picture of the on-chip switch integrated with the single photon source. The $\pi/2$ hybrids (H) are shown in red, the tunable resonators (R) in green, their SQUID arrays (S) in cyan and the single photon source (SPS) in blue. (b) Enlarged view of the transmon qubit acting as the single photon source. At the top in blue is shown the weakly coupled qubit drive line and at the bottom in red the strongly coupled input line of the switch.

device as a single photon source. For the device tested here, the calculation suggests that the leakage should be suppressed by more than 70 dBm.

In reality, this level of suppression would be difficult to reach due to other potential transmission channels between the two lines, such as spurious modes present in the chip or the sample-holder. We characterized the drive signal leakage experimentally in a test sample which contains only the single photon source, with its drive line and output line connected directly to the measurement setup. We applied a continuous signal to the drive line and recorded the power spectral density of the signal detected in the output line. As the drive strength is low in comparison with the anharmonicity of the transmon, it can be treated as a two-level system and the power spectral density therefore takes the form of the usual *Mollow triplets* (Walls & Milburn, 2008).

We performed this measurement for different values of the drive power, obtaining the power spectral densities plotted in Fig. 6.10(a). The standard Mollow triplets with parameters obtained using a least-squares fit match the observed data very well, as seen in the figure. We used the fit to scale the measurements from the rather arbitrary units which depend on the details of the detection chain to units of photons per microsecond per megahertz at the qubit output line. Moreover, it allowed us to extract the relation between the microwave generator output power and the Rabi rate

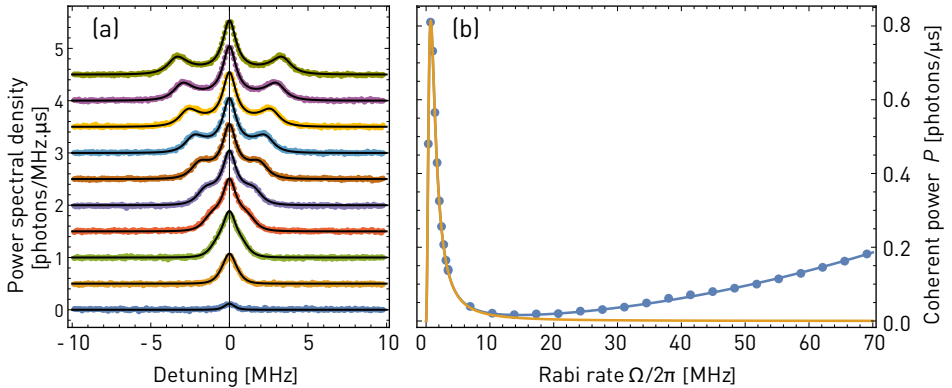


Figure 6.10: (a) Measured power spectral densities for different drive powers, with the coherent delta peak at zero frequency omitted. The bottom-most set of data corresponds to a drive power of approximately -36 dBm at the output of the microwave generator. The other datasets are obtained for signal amplitudes which are integer multiples ($2\times, 3\times, \dots$) of the amplitude in the first measurement. The black curves represent a fit of the standard Mollow triplet expression (Walls & Milburn, 2008) to all the displayed datasets simultaneously. (b) The coherent component of the detected power as a function of the Rabi rate extracted from the Mollow triplet fit in (a). The yellow line shows the expected theoretical dependence with parameters extracted from the fit in (a), in the absence of any direct coupling from drive to output. The blue line is a dependence which contains in addition a cross-talk signal whose amplitude is proportional to the Rabi rate. The proportionality constant is obtained as a fit parameter.

Ω experienced by the qubit. We could then plot the power of the coherent signal in the output line as a function of the Rabi rate, as shown in Fig. 6.10(b).

For low drive powers, the measured data closely follow the theoretical dependence expected for resonance fluorescence, represented by the yellow line. At higher powers, they start to deviate. As indicated by the good match between the data points and the blue curve, this deviation can be explained by an additional term in the output signal with an amplitude proportional to the Rabi rate Ω . The proportionality constant is obtained by least-squares fitting and is equal to

$$\frac{P_{\text{leakage}}}{(\Omega/(2\pi))^2} = 3.8 \cdot 10^{-5} \frac{\text{photons} \cdot \mu\text{s}^{-1}}{\text{MHz}^2}.$$

From this value, we can estimate that if we wish to excite the qubit by a Gaussian pulse with a standard deviation σ , the total number of photons transmitted into the output line due to the cross-talk is approximately $0.003 \text{ ns}/\sigma$. For typical pulses with σ on the order of several nanoseconds, this number is well below 1% and therefore negligible for most practical purposes.

6.3 Routing of single photons

In measurements with the sample combining the switch with the single-photon source, we used the setup outlined in Fig. 6.11, installed in the Triton cryostat. In contrast with the switch characterization measurements discussed above, here we use two input lines and two output lines equipped with Josephson parametric amplifiers (JPA).

One of the input lines is used as a qubit drive. Therefore, its signal is not transmitted unless either the qubit is resonant with the signal or if the applied power is sufficiently high to result in a significant cross-talk. For this reason, the input line connected to port 4 of the switch is useful in the initial characterization measurements of the resonator frequencies. Using this line, we could observe the resonances in transmission between ports 4 and 3 in the same way as in Fig. 6.4(a), without needing to tune the qubit into resonance with the signal. The qubit resonance could then be found in transmission between ports 1 and 2, provided that at least one of the resonators is detuned from the qubit. By measuring the resonance frequencies of the qubit and the two resonators as a function of the voltages applied to the three flux bias coils, we then obtained the coil matrix of the system (see sec. 2.4) which allowed us to tune the three elements independently of each other.

To show routing of single photons by the switch, we prepared the single-photon Fock state $|1\rangle$ by initializing the qubit in its excited state $|e\rangle$ and waiting until it relaxes. We then measured the power at the two output ports of the switch in both the resonant and the off-resonant state. In these measurements, we did not use the (JPA) in order to keep the measurement bandwidth as wide as possible. After subtracting the noise background obtained in an analogous measurement with the photon source off, we got the waveforms of the photon power shown in Fig. 6.12(a,b). The plotted data clearly show that we can route the photon to either of the two outputs of the switch while the cross-talk to the other output is strongly suppressed.

As the next step, we verified the non-classical nature of the switched signal by measuring the moments of the field. In this process, described in more detail in sec. 2.6, the digitized downconverted signal is first filtered with a kernel chosen to match the waveform of the photon state. After this *mode matching* step, the resulting complex voltage v is recorded in a histogram. When sufficiently many single-shot measurements have been recorded, the histogram is used to calculate moments of the voltage such as $\langle (v^*)^m v^n \rangle$. The voltage can be seen as the result of a measurement of an observable described by an operator proportional to $\hat{a} + \hat{h}^\dagger$, where \hat{a} is the annihilation operator acting on the photon mode and \hat{h}^\dagger is the creation operator of a noise mode. By systematic subtraction of the noise terms involving \hat{h} and \hat{h}^\dagger which are obtained in measurements with the signal source off, one can extract moments of the photon mode. For example, the moments $\langle \hat{a} \rangle$ and $\langle \hat{a}^\dagger \hat{a} \rangle$ can be expressed as

$$\begin{aligned} \lambda \langle \hat{a} \rangle &= \langle v \rangle - \langle v \rangle_0, \\ \lambda^2 \langle \hat{a}^\dagger \hat{a} \rangle &= \langle v^* v \rangle - \langle v^* v \rangle_0 - 2\text{Re}(\langle v \rangle - \langle v \rangle_0) \langle v^* \rangle_0, \end{aligned}$$

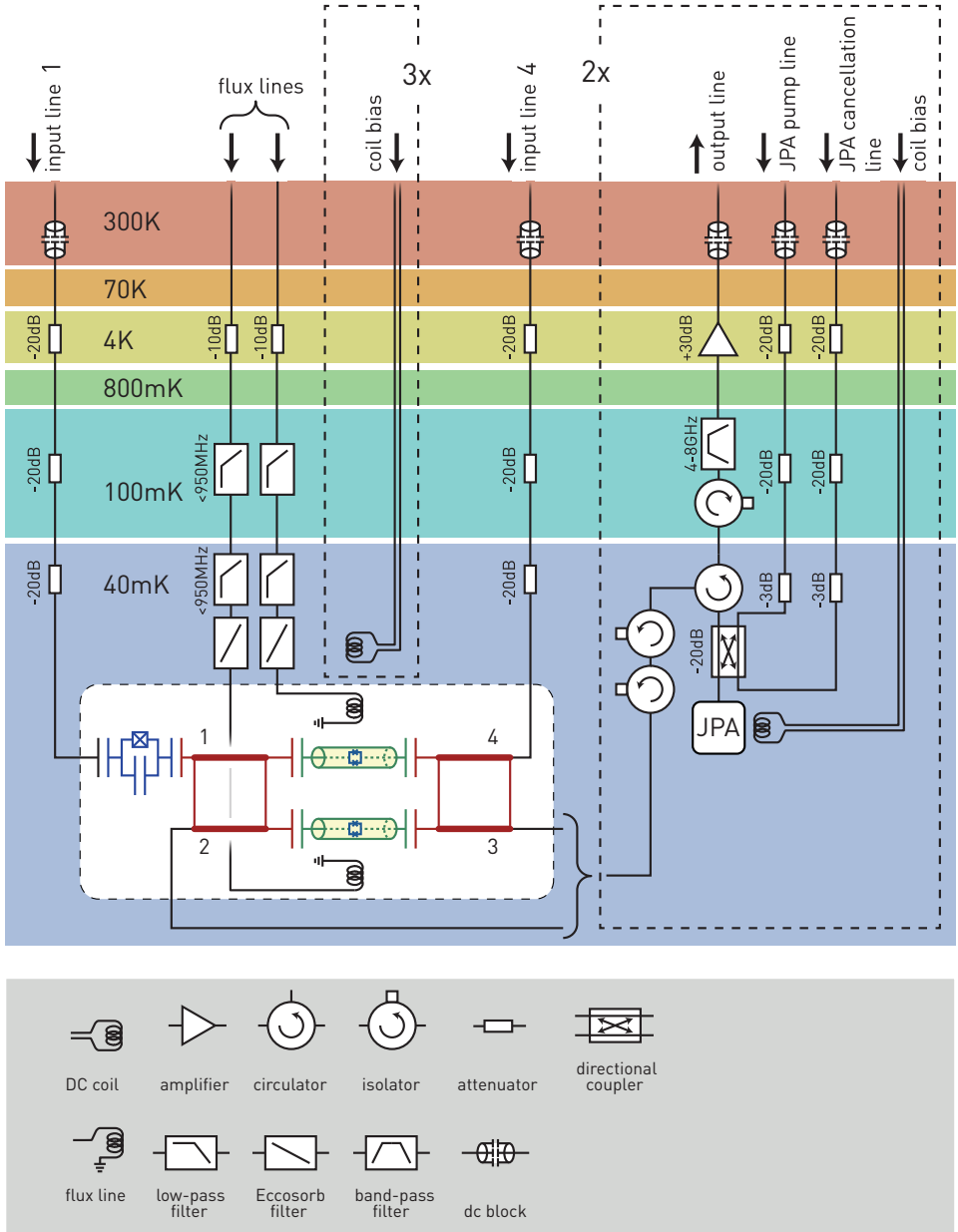


Figure 6.11: Diagram of the setup used in characterization measurements of the on-chip switch with the single photon source in the Triton cryostat.

where λ is the proportionality constant between $\hat{a} + \hat{h}^\dagger$ and v and the subscript 0 denotes the expectation values obtained from the reference measurements with the signal off.

To be able to extract the moments of \hat{a} , one first needs to determine the scaling factor λ , which is typically done by measuring a reference state for which some of the moments are assumed to be known. We did this by measuring the moments for a series of different photon states, prepared by exciting the qubit with pulses of varying amplitude A . A resonant preparation pulse rotates the Bloch vector describing the qubit state by an angle $\theta \propto A$ around an axis lying in the equatorial plane of the Bloch sphere. The prepared qubit state is $\cos(\theta/2)|g\rangle + e^{i\phi} \sin(\theta/2)|e\rangle$ which, after the qubit spontaneously relaxes, results in the photon state $|\psi\rangle = \cos(\theta/2)|0\rangle + e^{i\phi} \sin(\theta/2)|1\rangle$. The corresponding expectation values $\langle \hat{a} \rangle$ and $\langle \hat{a}^\dagger \hat{a} \rangle$ are

$$\begin{aligned}\langle \hat{a} \rangle &= \frac{1}{2} e^{i\phi} \sin \theta, \\ \langle \hat{a}^\dagger \hat{a} \rangle &= \sin^2 \frac{\theta}{2}.\end{aligned}$$

We further take into account that dephasing of the qubit can lead to a reduction of the coherent signal $\langle \hat{a} \rangle$ by some factor $k < 1$. We denote the proportionality factor between the rotation angle θ and the applied pulse amplitude by $c = \theta/A$. The expected relation between the moments of v and the pulse amplitude A is therefore

$$\begin{aligned}| \langle v \rangle - \langle v \rangle_0 | &= \frac{1}{2} k \lambda | \sin cA |, \\ \langle v^* v \rangle - \langle v^* v \rangle_0 - 2 \text{Re} (\langle v \rangle - \langle v \rangle_0) \langle v^* \rangle_0 &= \lambda^2 \sin^2 \frac{cA}{2}.\end{aligned}$$

We fitted these dependences to the measured moments to obtain the unknown parameters λ , k and c . We then verified our measurement and analysis by plotting the extracted moments of a as a function of the rotation angle θ and comparing them with the theory. The plot in Fig. 6.12(c) shows a good match of the extracted moments with theory, indicating that our single photon source as well as the analysis procedure work as expected.

Next, we specifically analyzed the Fock state $|1\rangle$ and the superposition state $(|0\rangle + |1\rangle)/\sqrt{2}$ (which we denote for the sake of brevity by $|0+1\rangle$) whose relevant moments are shown in Fig. 6.12(d). The first and second order moments agree well with the predicted values $\langle \hat{a}^\dagger \hat{a} \rangle = 1$, $|\langle \hat{a} \rangle| = 0$ for $|1\rangle$ and $\langle \hat{a}^\dagger \hat{a} \rangle = 1/2$, $|\langle \hat{a} \rangle| = 1/2$ for $|0+1\rangle$. As expected for a single-photon field, in contrast to a coherent or thermal state, the higher order moments such as $\langle \hat{a} \hat{a} \rangle$ or $\langle \hat{a}^\dagger \hat{a}^\dagger \hat{a} \hat{a} \rangle$ are close to zero. The non-classical nature of the switched signal is corroborated by the negative values of the Wigner function shown in Fig. 6.12(e), which is extracted from the measured moments by means of a maximum likelihood method (Eichler *et al.*, 2012a).

The slightly reduced value of $|\langle \hat{a} \rangle| \approx 0.46$ for $|0+1\rangle$ can be explained as a result of dephasing of the photon-source qubit. The qubit's pure dephasing rate γ_ϕ can be estimated from the decay rate Γ_2 of the coherent signal $\langle v \rangle$ for the superposition state $|0+1\rangle$. In the absence of pure dephasing, this rate is expected to be half of the

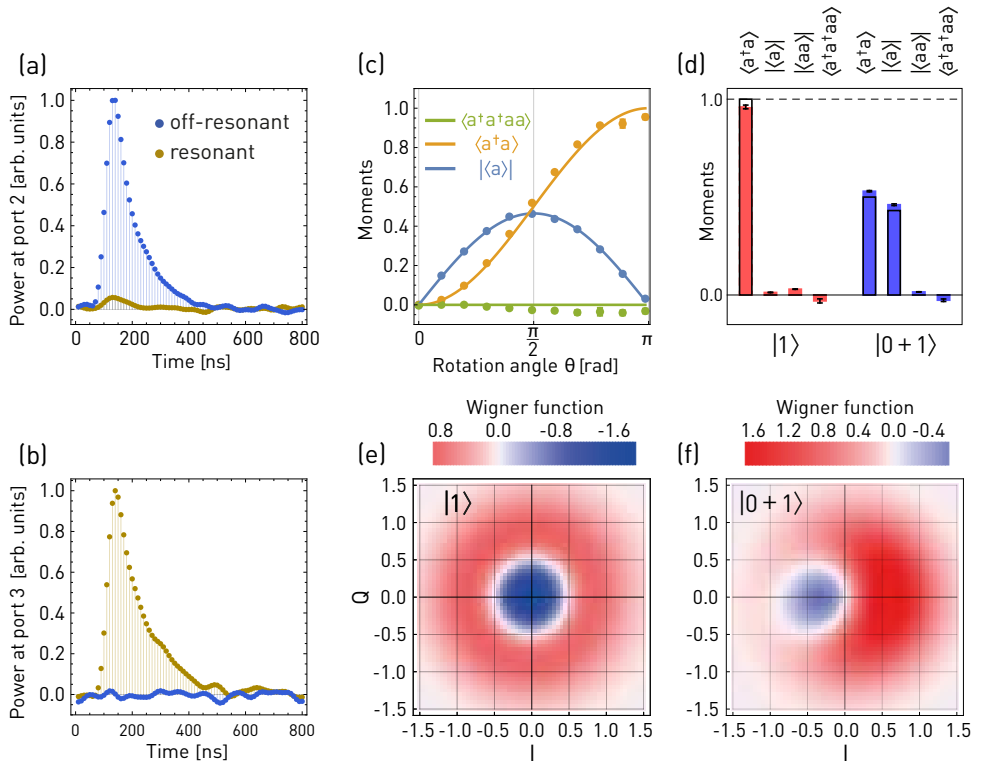


Figure 6.12: The single photon power waveforms measured at the output ports (a) 2 and (b) 3 in the resonant (yellow points) and off-resonant (blue points) state of the switch. (c) Calibration measurements of the moments $|\langle a \rangle|^2$, $\langle a^\dagger a \rangle$ and $\langle a^\dagger a^\dagger a a \rangle$ as a function of the rotation angle in the qubit initialization step. (d) Measured moments of a single photon state $|1\rangle$ (red) and a superposition state $(|0\rangle + |1\rangle)/\sqrt{2}$ (blue) transmitted through the switch. (e) Wigner functions corresponding to the moments from (d), obtained from them using a maximum likelihood method.

decay rate Γ_1 of the signal power $\langle v^*v \rangle$. The excess $\Gamma_2 - \Gamma_1/2$ then determines the pure dephasing γ_ϕ . Our measurements result in the value $\gamma_\phi = 6.1 \mu\text{s}^{-1}$. A simple calculation then shows that the moment $|\langle \hat{a} \rangle|$ of a field emitted by a qubit prepared in the equal superposition state $|g + e\rangle$ is given by

$$|\langle \hat{a} \rangle| = \frac{1}{2} \sqrt{\frac{2\gamma_f + \Gamma}{2\gamma_f + \Gamma + \gamma_\phi}},$$

where Γ is the relaxation rate of the qubit, γ_ϕ is the pure dephasing rate and γ_f is the decay constant of the used mode-matched filter. In our case with $\Gamma = 11.5 \mu\text{s}^{-1}$ and $\gamma_f = 3.1 \mu\text{s}^{-1}$, this formula leads to a prediction of $|\langle \hat{a} \rangle| \approx 0.43$.

Of particular interest is the normalized zero-time-delay intensity correlation function $g^{(2)} \equiv \langle \hat{a}^\dagger \hat{a}^\dagger \hat{a} \hat{a} \rangle / \langle \hat{a}^\dagger \hat{a} \rangle^2$. Its value of -0.03 ± 0.01 for both $|1\rangle$ and $|0 + 1\rangle$ is very close to zero, showing nearly ideal anti-bunching of the switched microwave field. The fact that the value extracted from the experiments is slightly negative is most likely an artifact of the data analysis procedure which we ascribe to a non-vanishing thermal field in the off-measurement used as a reference.

The non-classical nature of the switched signal is corroborated by the negative values of the Wigner function shown in Fig. 6.12(e), which we extracted from the measured moments by means of a maximum likelihood method (Eichler *et al.*, 2012a).

Chapter 7

Outlook

Most of the experiments described above offer interesting possibilities of follow-up work to further expand the toolbox for generating and manipulating non-classical photonic states. Some of these follow-ups were already described in the sections dealing with the individual experiments, such as for example the protocol to encode quantum information into a time-bin superposition of single photons, outlined at the end of sec. 4.1. A few additional ones are discussed in more detail below.

The photon reabsorption process from sec. 5 provides one method for transferring the state of an itinerant photon to a stationary qubit. An alternative way can be realized as described by Reiserer *et al.* (2013). In this scheme, the qubit-resonator system is set up such that the interaction between the resonator and the qubit modifies the resonator's reflection coefficient r depending on the state of the qubit. If the phase of r differs by π between the two qubit states, this implies that the state of the system evolves upon reflection of a single photon according to $|g\rangle \otimes |1\rangle \rightarrow |g\rangle \otimes |1\rangle$ and $|e\rangle \otimes |1\rangle \rightarrow -|e\rangle \otimes |1\rangle$. Consequently, if the qubit is prepared in one of the superposition states $|\pm\rangle \equiv (|g\rangle \pm |e\rangle)/\sqrt{2}$, the system evolves as $|+\rangle \otimes |1\rangle \rightarrow |-\rangle \otimes |1\rangle$. In the absence of a photon, the state of the qubit remains unchanged. Using an appropriate projective measurement, the two mutually orthogonal states $|+\rangle$ and $|-\rangle$ can be distinguished from each other, determining whether a single photon was reflected or not.

This non-demolition photon detection scheme, originally demonstrated with optical photons, could be implemented with superconducting circuits in a relatively straightforward way. A simple analysis shows that for higher Fock states, the described protocol performs a measurement of the photon number parity¹. In combination with single-shot qubit read-out and post-selection, such a measurement could be used to prepare interesting non-classical photon states.

An important distinction to be made between this scheme and the photon reabsorption described in sec. 5 is that the former does not absorb the photon and

¹It is important to note that this is true only if the qubit-dependence of the reflection coefficient is realized in a way which is independent of the number n of reflected photons, at least approximately in the low n limit. This is the case for example when the scheme is based on the dispersive shift but not in the original version by Reiserer *et al.* (2013) which relies on photon blockade.

therefore cannot be directly used to transfer the state of a photon to the qubit. Indeed, if the reflected field is in the superposition state $(|0\rangle + |1\rangle)/\sqrt{2}$, the resulting state is $(|+\rangle \otimes |0\rangle + |-\rangle \otimes |1\rangle)/\sqrt{2}$ and the photon remains entangled with the qubit. If this is not desired, the scheme can be extended as shown by (Kalb *et al.*, 2015). Here, the phase shift of the reflection coefficient is dependent on the polarization of the light such that the evolution upon reflection is modified to

$$\begin{aligned} |+\rangle \otimes |R\rangle &\rightarrow |+\rangle \otimes |R\rangle, \\ |+\rangle \otimes |L\rangle &\rightarrow |-\rangle \otimes |L\rangle, \end{aligned}$$

where R and L describe the handedness of the photon's circular polarization. After being reflected from the qubit-resonator system, the polarization of the photon is measured in the linear basis consisting of the states $|\uparrow\rangle = (|R\rangle + |L\rangle)/\sqrt{2}$ and $|\downarrow\rangle = (|R\rangle - |L\rangle)/\sqrt{2}$ and a NOT operation is applied to the qubit if the state $|\downarrow\rangle$ is measured. It can be easily verified that if the incoming photon was in the state $\alpha|R\rangle + \beta|L\rangle$, the resulting qubit state is $\alpha|+\rangle + \beta|-\rangle$.

To adapt this scheme to a superconducting circuit system, we need to find a replacement for the polarization degree of freedom which does not exist in standard coplanar waveguides. This can be done if instead of the two circularly polarized photons $|R\rangle$ and $|L\rangle$ we use the even and odd Schrödinger cat state $|\mathcal{C}_\pm\rangle \equiv (|\alpha\rangle \pm |-\alpha\rangle)/\sqrt{2}$ for $|\alpha| \gg 1$. In this case, if the reflection coefficient r of the resonator is again qubit-dependent such that $r = 1$ for $|g\rangle$ and $r = -1$ for $|e\rangle$, we naturally get the desired evolution

$$\begin{aligned} |+\rangle \otimes |\mathcal{C}_+\rangle &\rightarrow |+\rangle \otimes |\mathcal{C}_+\rangle, \\ |+\rangle \otimes |\mathcal{C}_-\rangle &\rightarrow |-\rangle \otimes |\mathcal{C}_-\rangle. \end{aligned}$$

The equivalent of the linear polarization basis are then the two coherent state $|\alpha\rangle$ and $|-\alpha\rangle$ which can be easily distinguished from each other in the standard heterodyne measurement scheme. In this way, an itinerant cat-state-encoded qubit $\alpha|\mathcal{C}_+\rangle + \beta|\mathcal{C}_-\rangle$ can be mapped onto the stationary qubit state $\alpha|+\rangle + \beta|-\rangle$.

A natural extension of the non-demolition photon detection scheme could be the construction of a single photon transistor, in which the presence or absence of a single control photon controls routing of a target state (which may be either a single photon or a classical coherent field). Such a device could be based on a principle similar to the one described by (Manzoni *et al.*, 2014). In the first step of its operation, the presence or absence of the control photon is encoded in the states $|+\rangle$ and $|-\rangle$ of the qubit as described above. In the second step, the superposition states are mapped onto the computational basis states $|g\rangle$ and $|e\rangle$ by a $\pi/2$ -pulse. Next, the target field is reflected from the resonator, receiving a phase shift which depends on the presence of the control photon. Finally, the target field needs to be routed to one of two output lines, based on the acquired phase.

This last step can be accomplished by placing the qubit-resonator at the end of one arm in a Michelson interferometer, which can be implemented using a $\pi/2$ -hybrid (see app. J). The hybrid, however, presents a complication since the control photon needs to be sent to the resonator directly without being split. This problem

can be resolved for example with one of the following approaches. One can use two resonators coupled to the qubit, one for the control photon and the other for the target field. Alternatively, the on-chip switch presented in ch. 6 can be used as a tunable beamsplitter – set to act as a direct through connection for the control photon and as a balanced beamsplitter for the target field.

Another possible direction of further development could be devoted to improving the properties of the on-chip switch. For instance, to increase its bandwidth, which is currently limited by the linewidth of the used resonators. A system consisting of multiple resonators could be engineered to have a larger 3 dB bandwidth but it may be challenging to implement convenient tuning of such a system with a small number of control lines. Since the switch can be also interpreted as an element which multiplies the incoming signal by a tunable transmission coefficient, modulation of this device or some suitable modification thereof with a periodic signal could be used to implement microwave frequency mixing at the single photon level.

Appendices

Appendix A

Designing a qubit

Several crucial parameters of a circuit QED system are determined by the design of the qubit. The most important ones are the Josephson energy, the charging energy and the coupling of the qubit to the resonator(s). In addition, the relaxation rates of the qubit into its control lines (charge line, flux line) are also determined by the qubit design. The Josephson energy has a special place among these since it depends almost exclusively on the parameters of the Josephson junction itself and is practically independent of the qubit capacitor design. Similarly, the design of the junction has very little effect on the charging energy and the couplings apart from adding a small parallel capacitance between the two qubit islands.

A.1 Calculating qubit parameters analytically

Given the design of the qubit capacitor, the resonator and the control lines, it is possible to determine the capacitance matrix of the system using a finite element solver. In the QuDev lab, the software of choice during my doctoral project was ANSYS Maxwell. Assuming that the physical size of the qubit is much smaller than the wavelength at the qubit transition frequency, the qubit as well as the sections of the resonator and the charge line coupled to it behave as capacitive elements and their inductance can be neglected. This is why an electrostatic solver such as Maxwell can be reliably used to model the qubit. For more extended structures, the lumped element model is not valid anymore and a true RF solver such as Sonnet by AWR needs to be used.

An example of a qubit design is shown in Fig. A.1(a) and its equivalent circuit in Fig. A.1(b). The mutual capacitances relevant for the qubit parameters are those between the two qubit islands (which we will denote by a and b) and the remaining three nodes representing the resonator, the charge line and the ground plane. Their values for this particular geometry extracted from the finite element simulation in Maxwell are given in Tab. A.1.

To calculate the coupling of the qubit to the resonator and the charge line, we imagine that their potentials are forced to constant values V_r and V_c by external ideal voltage sources. We now need to determine the energy of the system *excluding the*

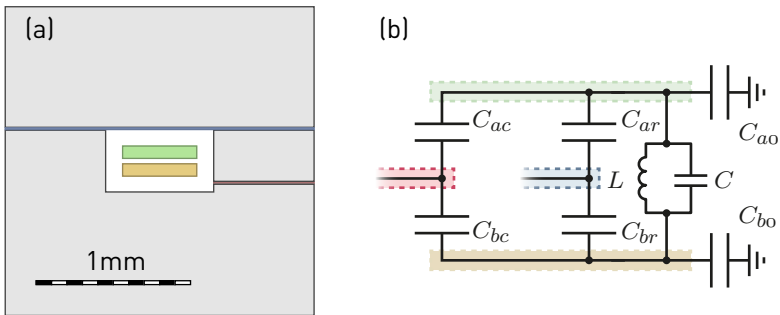


Figure A.1: (a) Example of a very simple qubit design. The qubit islands a and b are shown in green and yellow, respectively, the resonator in blue and the charge line in red. (b) Equivalent circuit of the qubit.

	island a	island b	resonator	charge line	ground
island a	×	31 fF	7.4 fF	0.13 fF	44 fF
island b	×	×	1.5 fF	0.25 fF	50 fF

Table A.1: Mutual capacitances between the individual parts of the circuit QED system.

Josephson junction, whose energy will be added later, as a function of the number of excess Cooper pairs on the qubit islands. Assuming that the charges on islands a and b are q and $-q$, respectively, we can calculate the potentials of the two islands by solving the system of equations

$$\begin{aligned}
 C(V_a - V_b) + C_{ar}(V_a - V_r) + C_{ac}(V_a - V_c) + C_{a0}V_a &= q, \\
 C(V_b - V_a) + C_{br}(V_b - V_r) + C_{bc}(V_b - V_c) + C_{b0}V_b &= -q.
 \end{aligned}$$

The energy of the system for given charges Q and $-Q$ on the qubit islands can then be calculated as the integral

$$E = \int_0^Q (V_a - V_b) dq,$$

leading to the expression

$$E = \frac{Q^2}{2C_\Sigma} + \beta_r V_r Q + \beta_c V_c Q, \text{ where} \quad (\text{A.1a})$$

$$C_\Sigma \equiv \frac{C_a C_b}{C_a + C_b} + C, \quad (\text{A.1b})$$

$$C_a \equiv C_{ar} + C_{ac} + C_{a0}, \quad (\text{A.1c})$$

$$C_b \equiv C_{br} + C_{bc} + C_{b0}, \quad (\text{A.1d})$$

$$\beta_r \equiv \frac{C_{ar} C_b - C_{br} C_a}{(C_a + C_b) C_\Sigma}, \quad (\text{A.1e})$$

$$\beta_c \equiv \frac{C_{ac} C_b - C_{bc} C_a}{(C_a + C_b) C_\Sigma}. \quad (\text{A.1f})$$

Note that the total capacitance C_Σ and the voltage division ratios β_r and β_c appearing here are the same parameters used to express the system's relaxation rates in eq. (B.7).

A.2 Black-box quantization

Circuit QED systems in planar geometries can be in most cases accurately described by circuit models, allowing their properties to be studied analytically. Other types of systems, such as those based on the 3d cavity architecture introduced by Paik *et al.* (2011), are not amenable to this approach since they cannot be easily mapped to an equivalent circuit.

In the case of a 3d cavity, one can of course attempt to quantize its normal modes and then describe their coupling to a qubit placed inside the cavity. However, the resulting calculation quickly becomes very cumbersome due to the large number of modes involved.

As a transmon qubit is to a good approximation an anharmonic LC oscillator, one can approach the quantization of the coupled system using an elegant alternative method developed by Nigg *et al.* (2012). Instead of quantizing the transmon and the cavity separately and only then introducing their mutual coupling, one linearizes the transmon, finds the normal modes of the coupled transmon-cavity system and only then adds the non-linearity as a perturbation.

This approach is very general and can be used to treat a significantly wider class of systems than just transmons coupled to cavities. In fact, within this framework, one can describe in principle any linear circuit coupled to any number of weakly anharmonic oscillators. The technique was dubbed *black-box quantization* by Nigg *et al.* (2012) because the linear part of the circuit is treated as a black box, characterized by its impedance matrix.

The impedance of the black box can be obtained in a number of ways – for example as the result of finite element simulations or from an analytical calculation. To illustrate the procedure, let us consider the case of a single transmon in a 3d cavity – the system for which the method was used in Nigg's original paper. A diagram of this system is shown in Fig. A.2(a). The qubit consists of two metal capacitor pads which

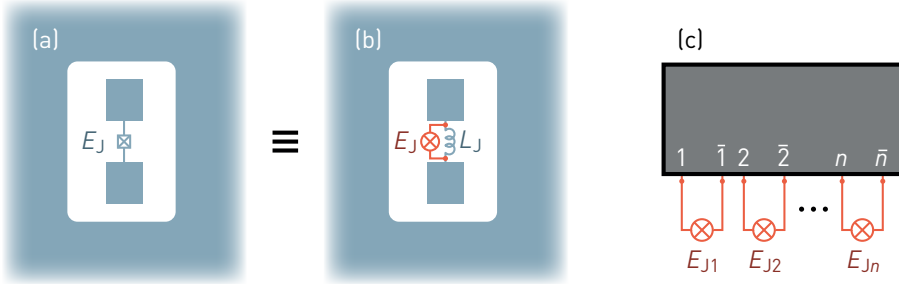


Figure A.2: (a) Diagram of a cross-section through a 3d cavity (in white) containing a transmon qubit. The qubit consists of two capacitor pads (blue rectangles) connected by a Josephson junction. (b) The same system, now with the Josephson junction formally split into its linear part (inductor) and a non-linear component (in red) representing the terms ϕ^4, ϕ^6, \dots from the Junction's Hamiltonian. The red points indicate the nodes at which the impedance matrix of the linear part of the system (in blue) is evaluated (c) A generic setting with the linear part of the system, represented by the black box, connected to n non-linear components via its $2n$ external nodes.

are connected together by a Josephson junction, in full analogy with the standard planar transmon. The potential energy of the junction depends on the phase drop δ across it as $E = -E_J \cos \delta$, where E_J is the Josephson energy of the junction. By expanding E into a power series in δ around $\delta = 0$, we can formally split the junction into two fictitious components connected in parallel. One of them is a linear inductor with inductance $L_J \equiv \hbar^2/4e^2 E_J$. Its energy is given by the quadratic term in E . The other component does not have a real-life counterpart and we define it such that its energy contains all terms of order 4 and higher from the expansion of E . This split is illustrated by Fig. A.2(b) where the non-linear component is denoted by a crossed circle.

The linear part of the circuit, consisting of the cavity, the qubit capacitor pads and the linearized Josephson junction, is then considered separately. Its impedance is calculated with respect to the two nodes at which it connects to the non-linear component. This can be done for example by analyzing the cavity with the qubit capacitor pads in a finite element Maxwell equations solver and then combining the resulting impedance matrix with that of a lumped element inductor. Once the impedance is known as a function of frequency, the quantized model of the linear system can be derived from the properties of the impedance poles. A deeper discussion of this step is presented in app. C.

To see how the non-linearity is incorporated back into the model, let us further consider a slightly more general setting, of which the cavity-transmon system is a special case. As shown in Fig. A.2(c), we can have a black box with $2n$ external nodes, labeled as $1, \bar{1}, 2, \bar{2}, \dots, n, \bar{n}$. Each pair j, \bar{j} is connected to one non-linear component with a Josephson energy E_{Jj} .

The resonance frequencies of the black box can be found as the poles of its impedance matrix, as derived in sec. B.1. The individual modes can then be quantized, giving rise to ladder operators $\hat{a}_k^\dagger, \hat{a}_k$. The voltages at the external nodes can be expressed in the form of eq. (C.1) as

$$\hat{V}^{(j)} = \sum_k V_k^{(j)} \hat{a}_k^\dagger + V_k^{(j)*} \hat{a}_k,$$

where $j \in \{1, \bar{1}, \dots\}$ and $V_k^{(j)}$ are the voltage vacuum fluctuation amplitudes which are related to the residues of the impedance matrix by eq. (C.3).

The phase drops $\hat{\delta}_j$ across the non-linear components are related to the voltages by $\Phi_0 \hat{\delta}_j / 2\pi = \int \hat{V}^{(j)} - \hat{V}^{(\bar{j})} dt$, where $\Phi_0 = \pi \hbar / e$ is the flux quantum. We can transform this relation into

$$\hat{\delta}_j = \sum_k \delta_k^{(j)} \hat{a}_k^\dagger + \delta_k^{(j)*} \hat{a}_k,$$

where the vacuum fluctuation amplitudes $\delta_k^{(j)}$ satisfy the equation

$$|\delta_k^{(j)}|^2 = \frac{i(2e)^2}{\hbar \omega_k} \text{res}_{\omega_k} (Z_{jj} + Z_{\bar{j}\bar{j}} - Z_{j\bar{j}} - Z_{\bar{j}j}), \quad (\text{A.2})$$

derived from eq. (C.3). The combination of impedances on the right-hand side represents the impedance which would be measured between nodes j and \bar{j} if all other nodes were left disconnected. We will denote it by Z_j .

The Hamiltonian of the non-linear components is given by

$$\hat{H}_{\text{nl}} = - \sum_j E_{Jj} \left(\frac{1}{4!} \hat{\delta}_j^4 - \frac{1}{6!} \hat{\delta}_j^6 + \frac{1}{8!} \hat{\delta}_j^8 - \dots \right).$$

We will treat it as a perturbation of the linear system and find the eigenenergies of the system including the non-linearities to lowest order in perturbation theory (Sakurai & Napolitano, 2010). To this end, we will retain only the δ^4 terms in \hat{H}_{nl} .

The eigenstates of the linear unperturbed system are the multi-mode Fock states $|n_1 n_2 \dots\rangle$. The corrections of their eigenenergies induced by the perturbation are, to first order in \hat{H}_{nl} ,

$$\begin{aligned} \Delta E_{n_1 n_2 \dots} &= -\frac{1}{24} \sum_j E_{Jj} \langle n_1 n_2 \dots | \hat{\delta}_j^4 | n_1 n_2 \dots \rangle \\ &= -\frac{1}{24} \sum_j E_{Jj} \langle n_1 n_2 \dots | \left(\sum_k \delta_k^{(j)} \hat{a}_k^\dagger + \delta_k^{(j)*} \hat{a}_k \right)^4 | n_1 n_2 \dots \rangle. \end{aligned}$$

The matrix elements on the right-hand side can be evaluated using Wick's theorem (Wick, 1950). The resulting expression can be cast into the form

$$\frac{1}{\hbar} \Delta E_{n_1 n_2 \dots} = \sum_k \Delta_k n_k + \sum_k \alpha_k n_k (n_k - 1) + \sum_{k>l} \chi_{kl} n_k n_l.$$

The various factors in this equation have a very natural interpretation: Δ_k is the frequency renormalization of mode k , α_k is its anharmonicity and χ_{kl} is the cross-Kerr coupling between modes k and l . They are related to the vacuum amplitudes $\delta_k^{(j)}$ by

$$\begin{aligned}\Delta_k &= -\frac{1}{2\hbar} \sum_j E_{Jj} |\delta_k^{(j)}|^2 \sum_l |\delta_l^{(j)}|^2, \\ \alpha_k &= -\frac{1}{2\hbar} \sum_j E_{Jj} |\delta_k^{(j)}|^4, \\ \chi_{kl} &= -\frac{1}{\hbar} \sum_j E_{Jj} |\delta_k^{(j)}|^2 |\delta_l^{(j)}|^2.\end{aligned}$$

Eq. (A.2) then allows us to express these parameters in terms of impedance residues and the inductances L_{Jj} of the linearized Josephson junctions:

$$\Delta_k = \frac{2e^2}{\hbar} \sum_j \frac{1}{L_{Jj}} \frac{\text{res}_{\omega_k} Z_j}{\omega_k} \sum_l \frac{\text{res}_{\omega_l} Z_j}{\omega_l}, \quad (\text{A.3a})$$

$$\alpha_k = \frac{2e^2}{\hbar} \sum_j \frac{1}{L_{Jj}} \left(\frac{\text{res}_{\omega_k} Z_j}{\omega_k} \right)^2, \quad (\text{A.3b})$$

$$\chi_{kl} = \frac{4e^2}{\hbar} \sum_j \frac{1}{L_{Jj}} \frac{\text{res}_{\omega_k} Z_j}{\omega_k} \frac{\text{res}_{\omega_l} Z_j}{\omega_l}. \quad (\text{A.3c})$$

Example – transmon qubit

We will illustrate the application of eq. (A.3) with a simple example: a transmon qubit. In this case, we have only a single Josephson junction and the black box consists of a single capacitance C in parallel with the linearized junction's inductance L_J . The impedance Z_1 is then equal to $(i\omega C + 1/(i\omega L_J))^{-1}$ and its residue at the resonance frequency $\omega_1 = 1/\sqrt{L_J C}$ is

$$\text{res}_{\omega_1} Z_1 = -\frac{i}{2C}.$$

Using eq. (A.3), we easily obtain

$$\begin{aligned}\Delta = \alpha &= -\frac{2e^2}{\hbar} \frac{1}{L_J} \frac{1}{4C^2\omega^2} \\ &= -\frac{e^2}{2C\hbar}.\end{aligned}$$

This shows that, in agreement with the result derived in sec. 1.4, both the resonance frequency renormalization and the anharmonicity are equal to $-E_C/\hbar$, where $E_C \equiv e^2/2C$ is the charging energy of the transmon.

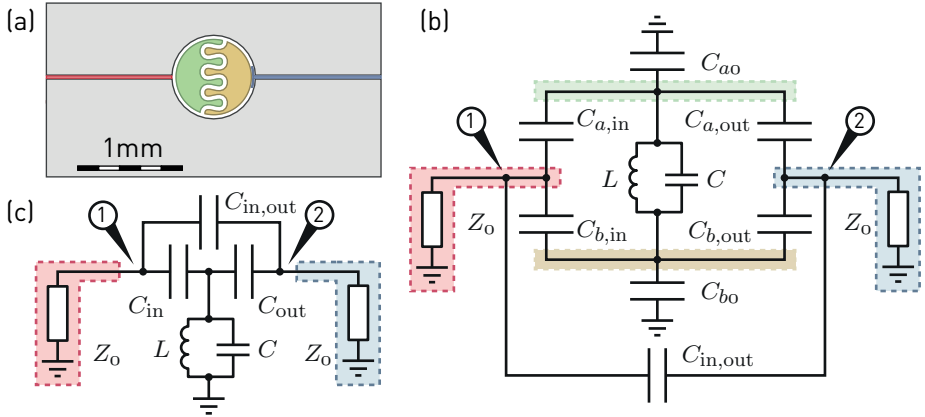


Figure A.3: (a) Design of a qubit as a single-photon source. The qubit islands *a* and *b* are shown in green and yellow, respectively, the input line in red and the output line in blue. (b) Equivalent circuit of the qubit and the lines. (c) Simplified circuit with one side of the qubit LC circuit grounded.

A.3 Qubit as a single-photon source: Analysis of direct drive leakage

A transmon qubit coupled to two semi-infinite waveguides can be used as a single-photon source which has been demonstrated by Peng *et al.* (2015). One of the two lines is coupled weakly and serves as a charge line for driving the qubit into its excited state. Following this, the qubit spontaneously relaxes, emitting a photon predominantly into the other, strongly coupled line. When designing a system like this, care must be taken to ensure that the emission probability of the photon back into the drive line as well as the direct leakage of the coherent drive signal into the output line are negligible.

This section demonstrates how such a system can be analyzed. We start by noting that in the weak drive limit, the qubit can be replaced by a linear *LC* circuit without altering the response of the system (see sec. B.1). We will then compare the classical expression for the transmission through the system with an approximately equivalent input-output quantum model. Finally, we will transform the linear input-output relations to non-linear ones for a real two-level qubit, based on the requirement of equivalence in the weak drive limit.

The design considered here is shown in Fig. A.3(a) and its equivalent circuit diagram in Fig. A.3(b). The values of the eight mutual capacitances determined from a finite element simulation in Maxwell are given in Tab. A.2. Note that the capacitances between the two lines and ground are not stated as they are taken into account when the whole semi-infinite line is replaced by an equivalent real impedance Z_0 .

	island a	island b	input	output	ground
island a	×	42 fF	1.1 fF	0.17 fF	68 fF
island b	×	×	0.10 fF	6.9 fF	65 fF
input	×	×	×	0.0052 fF	×
output	×	×	×	×	×

Table A.2: Mutual capacitances between the individual parts of the single-photon source circuit.

The form of the result for the realistic circuit in Fig. A.3(b) is rather complicated and does not provide good insight into the dependence on the individual capacitances. We will therefore also study a simplified circuit shown in Fig. A.3(c). In both cases, we start by considering the 2×2 impedance matrix \mathbf{Z} of the circuit defined between two of its nodes indicated in Fig. A.3(b,c). The impedance matrix $\tilde{\mathbf{Z}}$ of the circuit excluding the waveguides is related to the S -matrix by $\mathbf{S} = (\tilde{\mathbf{Z}} - Z_0)/(\tilde{\mathbf{Z}} + Z_0)$. Using the relation $\mathbf{Z}^{-1} = \tilde{\mathbf{Z}}^{-1} + 1/Z_0$, we can rewrite \mathbf{S} as $\mathbf{S} = 2\mathbf{Z}/Z_0 - 1$. This results in the simple equation for the transmission coefficient S_{21}

$$S_{21} = \frac{2Z_{21}}{Z_0}.$$

Let us now assume that the system is driven from the input side by a signal V_{in} which has mainly frequency components very close to the qubit resonance frequency ω_0 . As discussed in sec. B.1, the resonant frequencies of a circuit's modes are given by the poles of its impedance matrix. For $\omega \approx \omega_0$, we can therefore approximate Z_{21} by its Laurent series truncated at zeroth order in $\omega - \omega_0$:

$$Z_{21}(\omega) \approx Z_{21}^{(0)} + \frac{\text{res}_{\omega_0} Z_{21}}{\omega - \omega_0}.$$

The transmitted signal V_{out} can then be written as

$$V_{\text{out}} = \frac{2Z_{21}^{(0)}}{Z_0} V_{\text{in}} + \frac{2\text{res}_{\omega_0} Z_{21}}{(\omega - \omega_0)Z_0} V_{\text{in}}. \quad (\text{A.4})$$

The input-output relations for this system have the form

$$\begin{aligned} \hat{b}_{\text{out}} &= c\hat{a}_{\text{in}} + \sqrt{\Gamma_{\text{out}}}\hat{a}, \\ -i\omega\hat{a} &= -i\omega_0\hat{a} - \sqrt{\Gamma_{\text{in}}}\hat{a}_{\text{in}}, \end{aligned}$$

where \hat{a}_{in} and \hat{b}_{out} are the input and the output field, respectively, and \hat{a} is the qubit field. Note that in addition to the field emitted by the qubit, the expression for the transmitted field contains the term $c\hat{a}_{\text{in}}$ which represents the direct coupling between the input and the output line. Solving these equations for \hat{a} and \hat{b}_{out} gives us

$$\hat{b}_{\text{out}} = c\hat{a}_{\text{in}} + \frac{\sqrt{\Gamma_{\text{in}}\Gamma_{\text{out}}}}{i(\omega - \omega_0)}\hat{a}_{\text{in}}.$$

Comparison with eq. (A.4) shows that we can identify the first term on its right-hand side with the directly transmitted signal while the second term is the signal emitted by the qubit. The transmission coefficient c is then given by

$$c = \frac{2Z_{21}^{(0)}}{Z_0}. \quad (\text{A.5})$$

Treating the qubit as a real two-level system instead of a harmonic oscillator, we need to replace the ladder operators \hat{a} by the Pauli operator $\hat{\sigma}_-$. The relation between \hat{b}_{out} and \hat{a}_{in} then becomes

$$\hat{b}_{\text{out}} = c\hat{a}_{\text{in}} + \sqrt{\Gamma_{\text{out}}}\hat{\sigma}_-,$$

while the Heisenberg equation for $\hat{\sigma}_-$ will be

$$\frac{d}{dt}\hat{\sigma}_- = -i\omega_0\hat{\sigma}_- - \sqrt{\Gamma_{\text{in}}}\hat{\sigma}_z\hat{a}_{\text{in}}.$$

Assuming that the input field is in a coherent state such that $\langle\hat{a}_{\text{in}}\rangle = a_{\text{in}}$, we can identify the expression $\sqrt{\Gamma_{\text{in}}}a_{\text{in}}$ with the Rabi rate Ω . The contribution to the output field coupled directly from the input line is therefore equal to $c\Omega/\sqrt{\Gamma_{\text{in}}}$ and the total number of photons n_{leak} in this undesirable coherent signal is

$$n_{\text{leak}} = \int \frac{|c|^2\Omega^2}{\Gamma_{\text{in}}} dt.$$

For simplicity, let us consider a square drive pulse of length T and amplitude $\Omega = \pi/T$ which drives the qubit from the ground state to the excited state. The number of leakage photons then becomes

$$n_{\text{leak}} = \frac{|c|^2\pi^2}{\Gamma_{\text{in}}T}.$$

Other sources of error in the single-photon generation process are the emission from the qubit into the output line during the drive pulse and the emission back into the input line. As the emission rate into the output line is given by $\Gamma_{\text{out}}p_e$, where p_e is the population of the qubit excited state, the mean number of photons emitted during the drive pulse is approximately $\Gamma_{\text{out}}T/2$. The desired single photon will be emitted back into the input with a probability equal to the branching ratio $\Gamma_{\text{in}}/(\Gamma_{\text{in}} + \Gamma_{\text{out}})$.

We can define the error \mathcal{E} of the single-photon emission process by summing the numbers of photons coupled directly from the input to the output, emitted during the drive pulse and emitted into the input line:

$$\mathcal{E} = \frac{|c|^2\pi^2}{\Gamma_{\text{in}}T} + \frac{\Gamma_{\text{out}}T}{2} + \frac{\Gamma_{\text{in}}}{\Gamma_{\text{in}} + \Gamma_{\text{out}}}. \quad (\text{A.6})$$

From this expression, we see that minimization of the direct input-to-output leakage favors longer drive pulses and stronger input couplings (which leads to the required drive power being lower). On the other hand, if we want to keep the probability to

emit the single photon into the input line low, we need a weak input coupling and a strong output coupling. Lastly, to minimize the number of photons emitted while the qubit is being driven into its excited state, a shorter drive pulse and a weaker output coupling. Clearly, the three sources of errors individually put very different constraints on the parameters of the system and we will need to find some kind of trade-off between them.

As the drive pulse length T is a free parameter, we can start by minimizing the error with respect to T . The minimum is achieved when $|c|^2\pi^2/\Gamma_{\text{in}}T = \Gamma_{\text{out}}T/2$, that is, $T = |c|\pi\sqrt{2/\Gamma_{\text{in}}\Gamma_{\text{out}}}$. The corresponding value of \mathcal{E} is

$$\mathcal{E} = |c|\pi\sqrt{\frac{2\Gamma_{\text{out}}}{\Gamma_{\text{in}}}} + \frac{\Gamma_{\text{in}}}{\Gamma_{\text{in}} + \Gamma_{\text{out}}}. \quad (\text{A.7})$$

To evaluate the theoretical performance of the system as a single photon source, we need to calculate the direct input-to-output transmission coefficient c given by eq. (A.5) and the relaxation rates $\Gamma_{\text{in}}, \Gamma_{\text{out}}$.

We can determine Γ_{in} and Γ_{out} using a method analogous to that employed in sec. B.1 to derive eq. (B.7). After expanding the admittance of the circuit from Fig. A.3(c) to first order in the small parameters $x_{\text{in}} \equiv \omega Z_0 C_{\text{in}}$ and $x_{\text{out}} \equiv \omega Z_0 C_{\text{out}}$, we find the imaginary part of its zero which is equal to $\Gamma/2$. We split the resulting expression into terms proportional to C_{in}^2 and C_{out}^2 to obtain Γ_{in} and Γ_{out} . Even though our circuit differs from that considered in sec. B.1, it turns out that the first-order expressions for the relaxation rates have the same form as eq. (B.7), that is

$$\begin{aligned} \Gamma_{\text{in}} &= \omega_0^2 C_{\Sigma} Z_0 \beta_{\text{in}}^2, \\ \Gamma_{\text{out}} &= \omega_0^2 C_{\Sigma} Z_0 \beta_{\text{out}}^2, \text{ where} \\ C_{\Sigma} &= C + C_{\text{in}} + C_{\text{out}}, \\ \beta_{\text{in}} &= C_{\text{in}}/C_{\Sigma}, \\ \beta_{\text{out}} &= C_{\text{out}}/C_{\Sigma}, \\ \omega_0 &= 1/\sqrt{LC_{\Sigma}}. \end{aligned}$$

The residue $\text{res}_{\omega_0} Z_{21}$ can be calculated in a similar fashion. We expand the impedance to second order in the coupling capacitances and calculate the limit $\lim_{\omega \rightarrow \omega_0} (\omega - \omega_0) Z_{21}$ which yields

$$\text{res}_{\omega_0} Z_{21} = \frac{iZ_0^2 \beta_{\text{in}} \beta_{\text{out}}}{2L}. \quad (\text{A.8})$$

We can then express the regular part of Z_{21} and calculate the direct transmission coefficient c using eq. (A.5):

$$c = 2i\omega_0 Z_0 (C_{\text{in},\text{out}} + 5\beta_{\text{in}}\beta_{\text{out}}C_{\Sigma}/4).$$

The term proportional to $C_{\text{in},\text{out}}$ represents transmission mediated by the direct capacitance between the input and output line which can be in principle made arbitrarily

small by increasing their distance. The second term, on the other hand, quantifies transmission through the input and output coupling capacitances and is therefore intrinsically related to Γ_{in} and Γ_{out} . We can rewrite the absolute value of c as

$$|c| = 2\omega_0 Z_0 C_{\text{in,out}} + \frac{5\sqrt{\Gamma_{\text{in}}\Gamma_{\text{out}}}}{2\omega_0}.$$

Substituting into eq. (A.6) then gives us the following expression for the error of the photon emission process:

$$\mathcal{E} = 2\pi\omega_0 Z_0 C_{\text{in,out}} \sqrt{\frac{2\Gamma_{\text{out}}}{\Gamma_{\text{in}}}} + \frac{5\pi\Gamma_{\text{out}}}{\omega_0\sqrt{2}} + \frac{\Gamma_{\text{in}}}{\Gamma_{\text{in}} + \Gamma_{\text{out}}}.$$

Under the assumption that $\Gamma_{\text{in}} \ll \Gamma_{\text{out}}$, we can approximate the last term on the right-hand side by $\Gamma_{\text{in}}/\Gamma_{\text{out}}$ and minimize the resulting expression with respect to Γ_{in} . The minimum is achieved for

$$\frac{\Gamma_{\text{in}}}{\Gamma_{\text{out}}} = \left(\sqrt{2}\pi C_{\text{in,out}} Z_0 \omega_0 \right)^{2/3}$$

and is equal to

$$\mathcal{E} = 3(\sqrt{2}\pi C_{\text{in,out}} Z_0 \omega_0)^{2/3} + \frac{5\pi\Gamma_{\text{out}}}{\omega_0\sqrt{2}}. \quad (\text{A.9})$$

The error is therefore determined by two factors – the direct capacitance $C_{\text{in,out}}$ between the input and output line and the ratio of the output coupling and the qubit frequency $\Gamma_{\text{out}}/\omega_0$. The first can be minimized by choosing a suitable geometry of the device, the second by making the output coupling weaker and thus the photon pulse longer. Clearly, the error cannot be reduced to an arbitrarily low level by decreasing Γ_{out} because the emission efficiency will ultimately become limited by the internal losses Γ_{int} in the qubit. Assuming that the error due to the direct capacitance $C_{\text{in,out}}$ can be made negligible, the remaining error, now including the internal losses, can be estimated as

$$\mathcal{E} = \frac{5\pi\Gamma_{\text{out}}}{\omega_0\sqrt{2}} + \frac{\Gamma_{\text{int}}}{\Gamma_{\text{int}} + \Gamma_{\text{out}}}.$$

In the limit $\Gamma_{\text{int}} \ll \Gamma_{\text{out}}$, we can minimize this expression with respect to Γ_{out} by choosing $\Gamma_{\text{out}}^2 = \Gamma_{\text{int}}\omega_0\sqrt{2}/5\pi$. The resulting minimal error is

$$\mathcal{E} = 2\sqrt{\frac{5\pi\Gamma_{\text{int}}}{\omega_0\sqrt{2}}} = 2\sqrt{\frac{5\pi}{Q_{\text{int}}\sqrt{2}}},$$

where Q_{int} is the internal quality factor of the qubit. For realistic values of $1/\Gamma_{\text{int}} = 5 \mu\text{s}$ and $\omega_0/2\pi = 7 \text{GHz}$, we get $\mathcal{E} \approx 0.014$ for $1/\Gamma_{\text{out}} \approx 36 \text{ns}$. To keep the error due to direct capacitance in eq. (A.9) from dominating the total error, $C_{\text{in,out}}$ needs to be sufficiently small. For the stated numerical value, this means approximately $C_{\text{in,out}} \lesssim 0.02 \text{fF}$.

For the realistic circuit in Fig. A.3(b), the relaxation rates can be again determined from eq. (B.7), where the parameters C_Σ , β_{in} and β_{out} are defined by eq. (B.4) and eq. (B.5) and the resonance frequency of the qubit is given by $\omega_0 = 1/\sqrt{LC_\Sigma}$.

Their numerical values obtained from the capacitances stated in Tab. A.2 are

$$\begin{aligned} C_\Sigma &= 77 \text{ fF}, \\ \beta_{\text{in}} &= 0.0066, \\ \beta_{\text{out}} &= -0.043. \end{aligned}$$

For a qubit frequency $\omega_0/2\pi = 7 \text{ GHz}$ we get relaxation rates

$$\begin{aligned} \Gamma_{\text{in}} &= 3.3 \times 10^5 \text{ s}^{-1}, \\ \Gamma_{\text{out}} &= 1.4 \times 10^7 \text{ s}^{-1}, \end{aligned}$$

corresponding to time constants $T_{\text{in}} \equiv 1/\Gamma_{\text{in}} = 3.1 \mu\text{s}$ and $T_{\text{out}} \equiv 1/\Gamma_{\text{out}} = 74 \text{ ns}$.

The residue $\text{res}_{\omega_0} Z_{21}$ takes the same form as for the simpler circuit, given by eq. (A.8). The regular part of Z_{21} can be expressed as

$$\begin{aligned} Z_{21}^{(0)} &= i\omega_0 C_{\text{in,out}} Z_0^2 + \frac{i\omega_0 Z_0^2}{4C_\Sigma(C_{a0} + C_{b0})^2} (\\ &4C(C_{a0} + C_{b0})(C_{a,\text{in}} + C_{b,\text{in}})(C_{a,\text{out}} + C_{b,\text{out}}) + \\ &5(C_{a0}^2 C_{b,\text{in}} C_{b,\text{out}} + C_{b0}^2 C_{a,\text{in}} C_{a,\text{out}}) + \\ &5C_{a0} C_{b0} (C_{a,\text{in}} - C_{b,\text{in}})(C_{a,\text{out}} - C_{b,\text{out}})/2 + \\ &3C_{a0} C_{b0} (C_{a,\text{in}} + C_{b,\text{in}})(C_{a,\text{out}} + C_{b,\text{out}})/2), \end{aligned} \quad (\text{A.10})$$

The numerical value of the direct transmission coefficient we obtain for our particular design is

$$c = 0.00018i.$$

Using eq. (A.7), we find that the error of the emission process is approximately $\mathcal{E} \approx 0.029$.

To clarify the dependence of the rather complicated expression in eq. (A.10) on the input and output coupling, we will consider a realistic situation where island a couples predominantly to the input line and island b to the output line. This means that the capacitances $C_{a,\text{out}}$ and $C_{b,\text{in}}$ can be neglected. In this case, the resulting expression for c can be approximated by

$$c = 2i\omega_0 C_{\text{in,out}} Z_0 + i \frac{C_{a0} C_{b0} - 4(C_{a0} + C_{b0})C}{2C_{a0} C_{b0}} \frac{\sqrt{\Gamma_{\text{in}} \Gamma_{\text{out}}}}{\omega_0}.$$

The direct transmission through the coupling capacitances has a similar form as for the simpler circuit from Fig. A.3(c), that is, it is proportional to $\sqrt{\Gamma_{\text{in}} \Gamma_{\text{out}}}/\omega_0$. In addition, however, it contains the dimensionless term $(C_{a0} C_{b0} - 4(C_{a0} + C_{b0})C)/2C_{a0} C_{b0}$ which depends on the capacitances between the qubit islands and ground. As the two terms in its numerator have opposite signs, it is in principle possible to design these capacitances to greatly suppress the direct transmission.

Appendix B

Dissipation in electrical circuits

Dissipation in circuit QED systems is an extremely important phenomenon. It can be an undesirable obstacle on the way to long-lived quantum coherence but also an intended feature of the system. For example, a superconducting qubit will, despite our best efforts, eventually relax to its ground state because of dielectric losses and other dissipation mechanisms. On the other hand, the energy of a microwave resonator coupled to a coplanar waveguide is to all appearances lost when we consider the resonator on its own, yet in fact it was merely radiated into the waveguide. It still exists as a propagating field, possibly to be reabsorbed by another quantum system. To understand these effects, we will first look how they can be treated in classical linear circuit consisting of capacitors, inductors and resistors. The second part of this appendix will then give an overview of the quantum master equation formalism.

B.1 Classical analysis

It might seem like studying classical circuits will not be of much use for understanding dissipation in circuit QED systems. However, results derived using high-school physics are surprisingly applicable. This is especially clear in the case of transmon qubits. They are essentially LC resonant circuits where the role of the inductor is played by a Josephson junction, operating in a regime where its behaviour is very nearly linear. It is then not surprising that circuits with transmons can often be modelled as linear systems, possibly with the weak non-linearity of the junction added as a perturbation (Nigg *et al.*, 2012).

But even for strongly anharmonic qubits, we can make the following argument: Let us assume that we are not adding energy into the system by driving it and instead let it evolve freely. If, furthermore, the interaction between the qubit(s) and the linear part of the circuit is of the Jaynes-Cummings type, the number of energy quanta in the system will not increase. Provided that we have started with only a single excitation in the system, its state will never get outside the zero- and one-excitation subspace of the Hilbert space. Therefore, the structure of the higher excitation subspaces does not have an effect on the dynamics of the system. We can then replace the anharmonic systems by harmonic oscillators, as long as we keep the

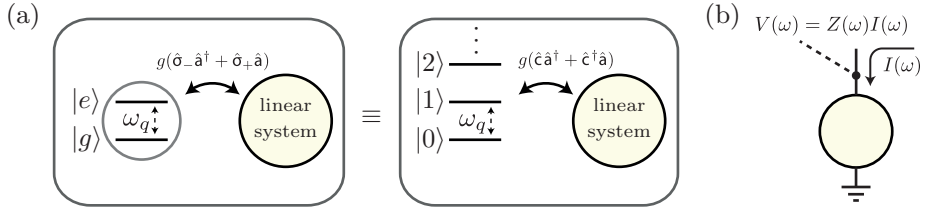


Figure B.1: (a) Equivalence of an anharmonic and a harmonic system when studying relaxation of single excitations. (b) A “black box” circuit with impedance $Z(\omega)$ and its voltage response $V(\omega)$ to a current excitation $I(\omega)$.

energy separation of the two lowest frequency states and their coupling to the rest of the circuit unchanged. This is a rather useful result worth pointing out once more: The free dissipation of single excitations can be studied using a linear model where the non-linear qubits are replaced by equally coupled harmonic oscillators with the same frequency, as illustrated in Fig. B.1(a).

To analyze the free dynamics of a circuit, we will consider it as a black box with a single node exposed to the outside, as shown in Fig. B.1(b). If we probe the system by a short current pulse $I(t) = A\delta(t)$, its voltage response in frequency space will be given by $V(\omega) = Z(\omega)I(\omega) = AZ(\omega)$, where $Z(\omega)$ is the impedance of the circuit. After Fourier-transforming the voltage back into time domain, we get

$$V(t) = \int \frac{d\omega}{2\pi} AZ(\omega)e^{i\omega t}.$$

We are interested in the voltage at times $t > 0$. Assuming that the impedance as a function of a complex variable ω is well-behaved and falls off to zero for $|\omega| \rightarrow \infty$, we can close the integration contour in the complex upper half-plane. If, in addition, the impedance has only simple poles, we can evaluate the contour integral as

$$V(t) = iA \sum_{\omega \in P} \text{res}_{\omega} Z e^{i\omega t}, \quad (\text{B.1})$$

where we sum over the set of poles P . From this expression we see that the evolution of the voltage response consists of damped oscillations $\exp(i\omega_0 t - \Gamma t/2)$ with frequencies $\omega_0 = \text{Re } \omega$ and decay constants $\Gamma/2 = \text{Im } \omega$. Hence, we can obtain the frequencies and decay constants of the circuit’s resonant modes from the poles of its impedance considered as a function of a complex frequency ω . We have defined the decay constant of the voltage oscillations as $\Gamma/2$ because the decay rate of the energy stored in the system, which falls off with the square of the voltage, is typically denoted by Γ .

Transmission-line resonator connected to an environment

We can now use this result to analyze dissipation in a simple $\lambda/2$ transmission line resonator with an open boundary condition at one end and capacitively connected to

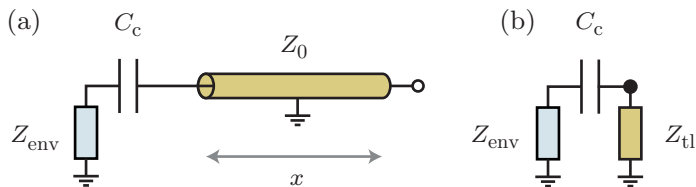


Figure B.2: (a) Circuit diagram of a $\lambda/2$ resonator capacitively coupled to its environment. (b) Modified version of the circuit where the open-ended transmission line is replaced by its equivalent lumped-element impedance. The black dot indicates the node of the circuit whose impedance to ground is evaluated to find the eigenfrequencies of the resonator.

its environment at the other. We will model the environment as a lumped element with an impedance $Z_{\text{env}}(\omega)$, leading to the effective circuit diagram shown in Fig. B.2(a).

Using eq. (1.2) with $Z_L \rightarrow \infty$, we get the equivalent lumped element impedance of the open-ended transmission line section

$$Z_{\text{tl}} = -iZ_0 \cot \frac{\omega x}{c}.$$

If we replace the transmission line by this equivalent impedance, we get the simple circuit shown in Fig. B.2(b). As derived above, the resonance frequencies ω_i and relaxation rates κ_i of a circuit's modes can be found as the poles $\omega_i + i\kappa_i/2$ of its impedance $Z(\omega)$ viewed as a function of a complex variable ω . The exact choice of the node at which the impedance is evaluated is not important since they all yield the same set of poles¹. We choose the node indicated by the black dot in Fig. B.2(b). Its impedance to ground is given by $Z_{\text{tl}}(Z_{\text{env}} + Z_c)/(Z_{\text{tl}} + Z_{\text{env}} + Z_c)$, where $Z_c = 1/i\omega C_c$. The condition for a pole of this impedance is therefore

$$-iZ_0 \cot \frac{\omega x}{c} + \frac{1}{i\omega C_c} + Z_{\text{env}}(\omega) = 0.$$

We know that the uncoupled $\lambda/2$ resonator has resonance frequencies of the form $\omega_n^{(0)} = n\pi c/x$. If the coupling capacitance C_c is small, we expect the modified resonance frequencies to be close to $\omega_n^{(0)}$. Let us therefore write the complex frequency as $\omega = \omega_n^{(0)} + \delta\omega_n$ and expand the left-hand side of the resonance condition to lowest order in $\delta\omega_n$. This gives us

$$-iZ_0 \frac{c}{x\delta\omega_n} + \frac{1}{i\omega_n C_c} + Z_{\text{env}}(\omega_n) = 0,$$

which can be solved for $\delta\omega_n$. Furthermore, we expand the result to second order in C_c which yields

$$\delta\omega_n = -\frac{1}{\pi}\omega_1\omega_n C_c Z_0 (1 - i\omega_n C_c Z_{\text{env}}(\omega_n)).$$

¹That is, provided that all modes have a non-zero voltage amplitude at the chosen node.

The shifted resonance frequency ω_n , given by the real part of $\omega_n^{(0)} + \delta\omega$, can therefore be expressed to first order in C_c as

$$\omega_n = \omega_n^{(0)} - \frac{1}{\pi}\omega_1\omega_n C_c Z_0, \quad (\text{B.2a})$$

while the relaxation rate κ_n , given by $2\text{Im}(\omega_n^{(0)} + \delta\omega)$, is

$$\kappa_n = \frac{2}{\pi}\omega_1\omega_n^2 C_c^2 Z_0 \text{Re} Z_{\text{env}}(\omega_n). \quad (\text{B.2b})$$

We see that the frequency of a transmission line resonator mode is decreased by its coupling to the environment. To lowest order, this shift is linear in the coupling capacitance and independent of the environment impedance.

The relaxation rate introduced by the environmental coupling is to lowest order quadratic in the coupling capacitance and proportional to the real part of the environment impedance at the mode frequency.

LC oscillator connected to an environment

As a second example, we will study a simple parallel *LC* circuit, representing a linearized qubit, capacitively coupled to a dissipative environment. The circuit diagram of the system is displayed in Fig. B.3(a), while the more realistic drawing in Fig. B.3(b) shows an example of a chip design with a qubit and highlights the parts of the chip corresponding to the main components of the idealized circuit.

The two islands of the qubit, corresponding in the schematic to the nodes marked by red circles, are capacitively coupled to impedances Z_1, Z_2, \dots representing the different dissipation channels. In the example in Fig. B.3, Z_1 is the dissipative resonator and Z_2 the charge line. However, the following derivation holds for essentially any linear circuit coupled to the qubit. For instance, capacitive coupling to flux lines or Purcell-filtered resonators can be analyzed using the same approach.

A straightforward analysis shows that the admittance of the circuit between the two qubit islands is given by

$$Y(\omega) = i\omega \left(\frac{\bar{C}_a \bar{C}_b}{\bar{C}_a + \bar{C}_b} + C \right) + \frac{1}{i\omega L} - \omega^2 K, \text{ where}$$

$$\bar{C}_a = \sum_{i \geq 0} \frac{C_{ai}}{1 + i\omega Z_i^{\text{env}}(C_{ai} + C_{bi})},$$

$$\bar{C}_b = \sum_{i \geq 0} \frac{C_{bi}}{1 + i\omega Z_i^{\text{env}}(C_{ai} + C_{bi})},$$

$$K = \sum_{i \geq 0} \frac{C_{ai} C_{bi} Z_i^{\text{env}}}{1 + i\omega Z_i^{\text{env}}(C_{ai} + C_{bi})},$$

where we have defined $Z_0^{\text{env}} \equiv 0$ to keep the form of the expression simple. To simplify it further, we will assume that the coupling to the environment is weak, i.e.

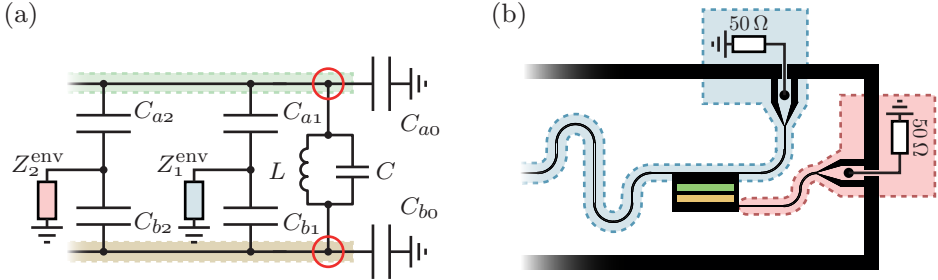


Figure B.3: (a) Schematic of a circuit with a linearized qubit as an LC circuit capacitively coupled to a number of environments represented by the impedances Z_1, Z_2, \dots . The total impedance of the circuit is calculated between the two nodes indicated by red circles. (b) Simplified diagram of a realistic qubit-resonator chip with its different components corresponding to the identically color-coded parts in (a). In blue the resonator and its output line, in red the charge line and in green and orange the two islands of the qubit.

the capacitances C_{ai}, C_{bi} are small, satisfying $x_i \equiv \omega Z_i (C_{ai} + C_{bi}) \ll 1$. We can then expand the expression for $Y(\omega)$ to first order in the small dimensionless parameters x_i and obtain

$$Y(\omega) = i\omega C_\Sigma + \frac{1}{i\omega L} + \omega^2 C_\Sigma^2 \sum_{i>0} \beta_i^2 Z_i^{\text{env}}, \text{ where} \quad (\text{B.3})$$

$$C_\Sigma \equiv \frac{C_a C_b}{C_a + C_b} + C, \quad (\text{B.4})$$

$$C_a \equiv \sum_{i \geq 0} C_{ai},$$

$$C_b \equiv \sum_{i \geq 0} C_{bi},$$

$$\beta_i \equiv \frac{C_a C_{bi} - C_b C_{ai}}{C_\Sigma (C_a + C_b)}. \quad (\text{B.5})$$

It is worth pointing out that the quantities C_Σ and β_i defined here have a very natural interpretation. If all the environmental impedances Z_i^{env} are replaced by direct connections to ground, then the remaining capacitance network composed of C , C_{ai} and C_{bi} is equivalent to a total capacitance C_Σ between the two qubit islands. In other words, if all the dissipation channels are considered to be grounded, the resonance frequency of the circuit will be $\omega_0 = 1/\sqrt{LC_\Sigma}$. Now consider that we replace one of the impedances Z_i^{env} by an ideal source of voltage V , the rest by connections to

ground and remove the inductor. The voltage between the qubit islands will then be $\beta_i V$.

To calculate the qubit resonance frequency ω_q and dissipation rate Γ , we need to find the pole of $Z(\omega) = 1/Y(\omega)$ by solving the equation $Y(\omega) = 0$. The coupling to the environment will cause the pole to shift by a small amount $\Delta\omega$ from its value $\omega_0 = 1/\sqrt{LC_\Sigma}$ which it takes in the limit $Z_i^{\text{env}} \rightarrow 0$. We will expand the first two terms on the right-hand side of eq. (B.3) to first order in $\Delta\omega$, getting the equation

$$2i\Delta\omega C_\Sigma + \omega^2 C_\Sigma^2 \sum_{i>0} \beta_i^2 Z_i^{\text{env}}(\omega) + \mathcal{O}((\Delta\omega)^2) = 0.$$

Its inspection shows us that the second term in it has to be of the order $\mathcal{O}(\Delta\omega)$. Therefore, to first order in $\Delta\omega$, we can replace ω by ω_0 . Solving for $\Delta\omega$ then yields the result

$$\omega_q = \text{Re}(\omega_0 + \Delta\omega) = \omega_0 - \frac{1}{2}\omega_0^2 C_\Sigma \sum_{i>0} \beta_i^2 \text{Im} Z_i^{\text{env}}(\omega_0) \quad (\text{B.6})$$

$$\Gamma = 2\text{Im}(\omega_0 + \Delta\omega) = \omega_0^2 C_\Sigma \sum_{i>0} \beta_i^2 \text{Re} Z_i^{\text{env}}(\omega_0). \quad (\text{B.7})$$

These expressions allow us to calculate the transition frequency and the dissipation rate of a qubit weakly capacitively coupled to lossy environments with given impedances. The degree to which these influence the qubit is given by simple multiplicative coupling constants β_i . These parameters characterize the network of coupling capacitances and can be interpreted as ratios between a fictitious voltage presented by the environment and the resulting voltage across the qubit.

B.2 Quantum description of dissipation

This section gives a brief introduction into open quantum systems, the density matrix formalism and a (hopefully educational) step-by-step derivation of the quantum master equation, following those of for example Walls & Milburn (2008) or Breuer (2012). In its second part we will show how this framework can be applied to circuit QED systems and use it to arrive at some of the previous section's results from a different angle.

Schrödinger equation is one of the cornerstones of quantum mechanics and, to the best of our knowledge, can be used to model the dynamics of any closed system. However, dissipative systems which we would like to describe here, are far from closed. They lose energy to their environment and even though the combined system including this environment is closed, its complexity makes it difficult if not impossible to solve its corresponding Schrödinger equation. To circumvent this problem, it would be desirable to write an effective equation of motion for the dissipative (open) system alone. But since dissipative processes are inherently irreversible, the evolution of an open system has to be governed by an equation of a different kind than the Schrödinger equation. Moreover, since dissipation is a random process, the state of an open system

also has to be represented in a different way than that of a closed system undergoing unitary evolution. For example, a lossy two-level system prepared in its excited state will lose its energy and relax to the ground state at a random point in time. After one half-life, it will either still be in the excited state, or it will have already relaxed, both cases occurring with probability 1/2. Whatever formalism we use to describe this process, it needs to be able to express statistical mixtures like this – states where the system is represented by one of multiple state vectors with given probabilities.

Density matrix formalism

Let us consider a pure quantum state described by a state vector $|\psi\rangle$. We can equally well characterize this state by giving the projector $|\psi\rangle\langle\psi|$ onto its state vector instead of the vector itself. This object is called the *density matrix* of the state and is commonly denoted by $\hat{\rho}$. The expectation value of an observable \hat{X} in this state can be expressed as $\text{Tr } \hat{X}\hat{\rho}$.

To describe a mixed state $\hat{\rho}$ created by preparing pure states $\hat{\rho}_i$ with probabilities p_i , we simply take the weighted mean

$$\hat{\rho} = \sum_i p_i \hat{\rho}_i.$$

As expected, the expectation value $\text{Tr } \hat{X}\hat{\rho}$ will then be a weighted mean of the individual expectation values in states $\hat{\rho}_i$. This definition of the density matrix implies that it is necessarily Hermitian, positive semi-definite and its trace is equal to one. Conversely, any operator with these properties is a density matrix of some mixed state because it can be diagonalized as $\sum_i p_i |\phi_i\rangle\langle\phi_i|$ and its eigenvalues p_i are positive and sum up to one.

Moreover, the density matrix fully characterizes a mixed state. Note that this is not a trivial statement. Mixed states with a given density matrix can be prepared as a mixture of pure states in different ways. For example, a mixture of states $|0\rangle$ with probability 1/3 and $|1\rangle$ with probability 2/3 has the same density matrix as a mixture of $\sqrt{1/3}|0\rangle + \sqrt{2/3}|1\rangle$ and $\sqrt{1/3}|0\rangle - \sqrt{2/3}|1\rangle$, both with probability 1/2. At first glance, these differently prepared mixtures should be treated as different states, which the density matrix formalism clearly fails to do. In fact, this is not true. Even though they were prepared in a different way, the fact that expectation values of all observables are uniquely determined by the density matrix means that states with the same density matrix are truly indistinguishable. This justifies our treatment of them as effectively identical mixed states and the density matrix as their full description.

The evolution of a pure state's density matrix under the action of a Hamiltonian \hat{H} is given by

$$\begin{aligned} \frac{d\hat{\rho}}{dt} &= \frac{d}{dt} |\psi\rangle\langle\psi| = \left(\frac{d}{dt} |\psi\rangle \right) \langle\psi| + |\psi\rangle \left(\frac{d}{dt} \langle\psi| \right) \\ &= -\frac{i}{\hbar} [\hat{H}, \hat{\rho}]. \end{aligned}$$

This *von Neumann equation* describes unitary dynamics of density matrices not only for pure states but by extension also for arbitrary mixed states.

Another useful feature of the density matrix formalism is its ability to describe the state of a single part of a composite system. Consider two subsystems A and B with Hilbert spaces \mathcal{H}_A and \mathcal{H}_B , constituting a larger system whose states form the Hilbert space $\mathcal{H}_A \otimes \mathcal{H}_B$. If the total system is in an entangled state, there is no single state vector in \mathcal{H}_A which could be reasonably said to describe the state of the subsystem A in isolation from B .

On the other hand, if we have a density matrix $\hat{\rho}$ of the composite system, there exists a density matrix $\hat{\rho}_A$ on \mathcal{H}_A which characterizes the state of A alone in the following sense: An experimentalist who does not have access to subsystem B can only measure observables of subsystem A , that is, quantities given by operators of the form $\hat{X} \otimes \mathbb{1}$. The result of measuring the expectation value of $\hat{X} \otimes \mathbb{1}$ on the composite system in state $\hat{\rho}$ will be exactly the same as that of measuring the expectation value of \hat{X} on the subsystem A in a state $\hat{\rho}_A$. This property can be written as

$$\text{Tr}(\hat{X} \otimes \mathbb{1})\hat{\rho} = \text{Tr} \hat{X} \hat{\rho}_A.$$

How do we get $\hat{\rho}_A$ from $\hat{\rho}$ then? The density matrix $\hat{\rho}$ can always be written in the form

$$\hat{\rho} = \sum_i \hat{\rho}_{Ai} \otimes \hat{\rho}_{Bi}.$$

The defining condition of $\hat{\rho}_A$ then becomes $\sum_i (\text{Tr} \hat{X} \hat{\rho}_{Ai})(\text{Tr} \hat{\rho}_{Bi}) = \text{Tr} \hat{X} \hat{\rho}_A$. This equation is clearly satisfied by $\hat{\rho}_A = \sum_i \hat{\rho}_{Ai} \text{Tr} \hat{\rho}_{Bi}$. The operation leading from $\hat{\rho}$ to $\hat{\rho}_A$ is called the *partial trace* where we have *traced out* or *traced over* the subsystem B . In short, this is typically written as $\hat{\rho}_A = \text{Tr}_B \hat{\rho}$ and $\hat{\rho}_A$ is called a *reduced density matrix* of the subsystem A .

Master equation

To describe the evolution of an open system with a Hilbert space \mathcal{H}_S coupled to the an environment \mathcal{H}_E without tracking the dynamics of the complete system, we need to derive an equation of motion for the reduced density matrix $\hat{\rho}_S$. We would like this equation to be local in time, that is, of the form

$$\frac{d\hat{\rho}_S(t)}{dt} = \mathcal{L}[\hat{\rho}_S(t)],$$

where \mathcal{L} is a superoperator – a linear operation acting on the space of operators in \mathcal{H}_S – generating the evolution of the system, often called the *Liouville superoperator* or in short *Liouvillian*. Clearly, with an equation of motion of this form, future evolution of the system is fully determined by its current state and does not depend on its history.

In general, such an evolution equation may not exist, as the environment can act as a “memory”, causing the time derivative of $\hat{\rho}_S(t)$ at time t depend on $\hat{\rho}_S(\tau)$ for $\tau < t$. However, under certain simplifying assumptions applicable to many realistic environments, the system can be described by a time-local *master equation*.

To derive it, we will start by assuming that the coupling between the open system \mathcal{H}_S and the environment \mathcal{H}_E is described by the interaction-picture Hamiltonian $\hat{H}(t) = \hat{X}(t) \otimes \hat{F}(t)$, where $\hat{X}(t)$ and $\hat{F}(t)$ are Hermitian operators acting on the open system and the environment, respectively. The choice of the letters F and X comes from an interpretation of these as, respectively, a force with which the environment acts on the open system and a generalized coordinate of the system coupling to this force. In the context of circuit QED systems, one can imagine \hat{F} to be for instance the voltage presented to the qubit by a capacitively coupled transmission line and \hat{X} the charge on the qubit electrodes. With this Hamiltonian, the density matrix evolution of the combined system is described by the von Neumann equation

$$\frac{d\hat{\rho}(t)}{dt} = -\frac{i}{\hbar}[\hat{X}(t) \otimes \hat{F}(t), \hat{\rho}(t)].$$

Integrating this equation from t_0 to t , substituting the resulting expression for $\hat{\rho}(t)$ back into the right-hand side of the equation and tracing over the environment Hilbert space yields the following equation for the reduced density matrix of the system

$$\frac{d\hat{\rho}_S(t)}{dt} = -\frac{i}{\hbar}\text{Tr}_E \left[\hat{X}(t) \otimes \hat{F}(t), \hat{\rho}(t_0) - \frac{i}{\hbar} \int_{t_0}^t [\hat{X}(\tau) \otimes \hat{F}(\tau), \hat{\rho}(\tau)] d\tau \right].$$

We will now assume that entanglement between the system and the environment can be neglected and the environment is in a time-independent steady state $\hat{\rho}_E$. This means that $\hat{\rho}(t)$ can be written as a tensor product $\hat{\rho}_S(t) \otimes \hat{\rho}_E$. Furthermore, we assume that the expectation value of $\hat{F}(t)$ in the steady state $\hat{\rho}_E$ is zero. Under these conditions, the term in the previous equation involving $\hat{\rho}(t_0)$ vanishes and the rest becomes

$$\begin{aligned} \frac{d\hat{\rho}_S(t)}{dt} &= -\frac{1}{\hbar^2} \int_{t_0}^t d\tau \text{Tr}_E \left[\hat{X}(t) \otimes \hat{F}(t), [\hat{X}(\tau) \otimes \hat{F}(\tau), \hat{\rho}_S(\tau) \otimes \hat{\rho}_E] \right] \\ &= -\frac{1}{\hbar^2} \int_{t_0}^t d\tau [\hat{X}(t), \hat{X}(\tau) \hat{\rho}_S(\tau)] \langle \hat{F}(t) \hat{F}(\tau) \rangle_E \\ &\quad + [\hat{\rho}_S(\tau) \hat{X}(\tau), \hat{X}(t)] \langle \hat{F}(\tau) \hat{F}(t) \rangle_E, \end{aligned}$$

where the expectation values of the autocorrelation functions $\langle \hat{F}(t) \hat{F}(\tau) \rangle_E$ are evaluated in the state $\hat{\rho}_E$.

Next we assume that the coherence time of the environment is much shorter than the dynamic time-scale of the system. In other words, the autocorrelation function $\langle \hat{F}(t) \hat{F}(\tau) \rangle_E$ falls off to zero with increasing $|t - \tau|$ at a time-scale t_E much shorter than the characteristic time-scale t_S at which $\hat{\rho}_S$ evolves. This means that we can approximate the product $\hat{\rho}_S(\tau) \langle \hat{F}(t) \hat{F}(\tau) \rangle_E$ by $\hat{\rho}_S(t) \langle \hat{F}(t) \hat{F}(\tau) \rangle_E$. At this point, the right-hand side of our evolution equation no longer depends on $\hat{\rho}_S$ at times other than t , so it is now in the desired time-local form. The subsequent approximations only serve to cast the master equation into its most familiar, the so-called *Lindblad form*.

As the open system density matrix evolves on a timescale t_S and $t_S \gg t_E$, we will typically want to use the master equation for $t - t_0 \gg t_E$. In this case, the value of

the integrand on its right-hand side is negligible for $\tau < t_0$ because then $t - \tau \gg t_E$. We can therefore replace the lower integration bound t_0 by $-\infty$ without changing the value of the integral significantly. This results in

$$\begin{aligned} \frac{d\hat{\rho}_S(t)}{dt} = & -\frac{1}{\hbar^2} \int_{-\infty}^t d\tau [\hat{X}(t), \hat{X}(\tau) \hat{\rho}_S(t)] \langle \hat{F}(t) \hat{F}(\tau) \rangle_E \\ & + [\hat{\rho}_S(t) \hat{X}(\tau), \hat{X}(t)] \langle \hat{F}(\tau) \hat{F}(t) \rangle_E. \end{aligned}$$

The interaction-picture operator $\hat{X}(t)$ can be written in terms of the Schrödinger-picture one \hat{X} as $\hat{X}(t) = \sum_{i,j} \exp(i(E_i - E_j)t/\hbar) \hat{P}_i \hat{X} \hat{P}_j$, where \hat{P}_i are projectors onto the eigenspaces of the system's free Hamiltonian with eigenenergies E_i . We now group the terms with the same frequency of oscillations $(E_i - E_j)/\hbar$ together, defining

$$\begin{aligned} \hat{X}_\omega & \equiv \sum_{E_i - E_j = \omega} \hat{P}_i \hat{X} \hat{P}_j, \\ \hat{X}(t) & = \sum_{\omega} \hat{X}_\omega \exp(i\omega t), \end{aligned} \tag{B.8}$$

where the sum in the second line is over the set of all different frequencies $(E_i - E_j)/\hbar$. Inserting this form of $\hat{X}(t)$ and $\hat{X}(\tau)$ into the master equation results in a summation over two frequencies ω and ω' of terms involving combinations of \hat{X}_ω and $\hat{X}_{\omega'}$. We will now perform the rotating wave approximation, that is, we neglect all of those terms for which $\omega + \omega' \neq 0$.

$$\begin{aligned} \frac{d\hat{\rho}_S(t)}{dt} = & -\frac{1}{\hbar^2} \sum_{\omega} \int_{-\infty}^t d\tau [\hat{X}_\omega, \hat{X}_{-\omega} \hat{\rho}_S(t)] e^{i\omega(t-\tau)} \langle \hat{F}(t) \hat{F}(\tau) \rangle_E \\ & + [\hat{\rho}_S(t) \hat{X}_{-\omega}, \hat{X}_\omega] e^{i\omega(t-\tau)} \langle \hat{F}(\tau) \hat{F}(t) \rangle_E. \end{aligned}$$

Expressing the autocorrelation function of \hat{F} in terms of its corresponding spectral density S_{FF} (as defined for example in Clerk *et al.* (2010)) as

$$\left. \begin{aligned} \langle \hat{F}(\tau) \hat{F}(t) \rangle_E \\ \langle \hat{F}(t) \hat{F}(\tau) \rangle_E \end{aligned} \right\} = \int \frac{d\omega'}{2\pi} S_{FF}(\omega') e^{\pm i\omega'(t-\tau)}$$

yields an expression where the integration of $\exp(i(\omega \pm \omega')(t - \tau))$ over τ can be performed analytically, resulting in

$$\begin{aligned} \frac{d\hat{\rho}_S(t)}{dt} = & -\frac{1}{\hbar^2} \sum_{\omega} \int \frac{d\omega'}{2\pi} [\hat{X}_\omega, \hat{X}_{-\omega} \hat{\rho}_S(t)] \frac{S_{FF}(\omega')}{-i(\omega - \omega') + \epsilon} \\ & + [\hat{\rho}_S(t) \hat{X}_{-\omega}, \hat{X}_\omega] \frac{S_{FF}(\omega')}{-i(\omega + \omega') + \epsilon}. \end{aligned}$$

After making a substitution $\omega \rightarrow -\omega$ in the second summand in the integral and using the identity $1/(\mp i(\omega - \omega') + \epsilon) = \pm i\mathcal{P}/(\omega - \omega') + \pi\delta(\omega - \omega')$, we separate the

terms with the delta function from those including the principal value and get

$$\begin{aligned} \frac{d\hat{\rho}_S(t)}{dt} = & -\frac{i}{\hbar^2} \sum_{\omega} \int \frac{d\omega'}{2\pi} ([\hat{X}_{\omega}, \hat{X}_{-\omega} \hat{\rho}_S(t)] - [\hat{\rho}_S(t) \hat{X}_{\omega}, \hat{X}_{-\omega}]) \mathcal{P} \frac{S_{FF}(\omega')}{\omega - \omega'} \\ & - \frac{1}{2\hbar^2} \sum_{\omega} ([\hat{X}_{\omega}, \hat{X}_{-\omega} \hat{\rho}_S(t)] + [\hat{\rho}_S(t) \hat{X}_{\omega}, \hat{X}_{-\omega}]) S_{FF}(\omega). \end{aligned}$$

It can be easily shown that the combination of commutators in the first line is equal to $[\hat{X}_{\omega} \hat{X}_{-\omega}, \hat{\rho}_S(t)]$ while those in the second line can be written as $-2\mathcal{D}_{\hat{X}_{-\omega}}[\hat{\rho}_S(t)]$, where \mathcal{D} is a superoperator defined as

$$\mathcal{D}_{\hat{A}} \hat{B} \equiv \hat{A} \hat{B} \hat{A}^{\dagger} - \frac{1}{2} \hat{A}^{\dagger} \hat{A} \hat{B} - \frac{1}{2} \hat{B} \hat{A}^{\dagger} \hat{A}.$$

If we further define

$$\Delta \hat{H} \equiv \frac{1}{\hbar} \sum_{\omega} \int \frac{d\omega'}{2\pi} \hat{X}_{\omega} \hat{X}_{-\omega} \mathcal{P} \frac{S_{FF}(\omega')}{\omega - \omega'}, \quad (\text{B.9})$$

$$\mathcal{L}_d \equiv \frac{1}{\hbar^2} \sum_{\omega} S_{FF}(-\omega) \mathcal{D}_{\hat{X}_{\omega}}, \quad (\text{B.10})$$

we can write the master equation in the final form

$$\frac{d\hat{\rho}_S(t)}{dt} = -\frac{i}{\hbar} [\Delta \hat{H}, \hat{\rho}_S(t)] + \mathcal{L}_d[\hat{\rho}_S(t)]. \quad (\text{B.11})$$

The first term represents a correction to the unitary evolution of the system – a renormalization of its Hamiltonian. The second term generates non-unitary evolution. The quantum noise in the generalized force \hat{F} whose spectral density is given by S_{FF} induces transitions in the open system. These can be interpreted as discrete *quantum jumps* where the state of the system changes from $|\psi\rangle$ to $\hat{X}_{\omega}|\psi\rangle$ and the probability of this event per unit time is proportional to the intensity of the noise $S_{FF}(-\omega)$ at the transition frequency.

Quantum dissipation in a qubit coupled to a circuit

Let us apply the derived result to the case of a transmon qubit coupled to a lossy electrical circuit. We will consider a circuit similar to the one analyzed in sec. B.1 but with only one environmental impedance for simplicity. Its schematic is shown in Fig. B.4(a). The lossy environment with impedance Z^{env} is a source of quantum (and, if its temperature $T > 0$, also thermal) fluctuations \hat{V}^{env} . As shown in our previous discussion of eq. (B.3), we can define a voltage division ratio β given by eq. (B.5) which relates the voltage \hat{V}^{env} presented by the environment to an offset in the voltage across the qubit capacitance. The qubit can be represented by an equivalent circuit displayed in Fig. B.4(b). Its capacitance C_{Σ} arises as a combination of all the capacitances in the original network. If the charges on the two qubit electrodes are $\pm\hat{Q}$, the potential

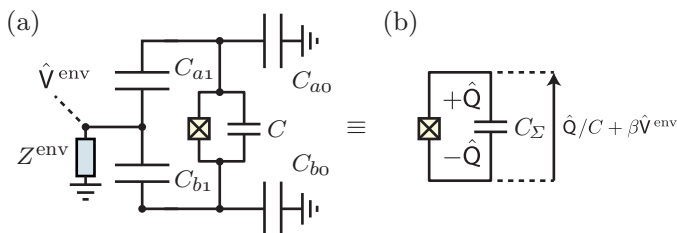


Figure B.4: (a) Circuit of a qubit capacitively coupled to a dissipative environment of impedance Z^{env} . The qubit is equivalent to a simpler circuit (b) where the voltage \hat{V}^{env} presented by the environment causes a shift $\beta\hat{V}^{\text{env}}$ in the voltage across the qubit capacitor with effective capacitance C_{Σ} .

difference \hat{V} between them can be expressed as a sum of the usual term \hat{Q}/C_{Σ} and an additional voltage shift $\beta\hat{V}^{\text{env}}$ caused by the mutual capacitance between the qubit and the environment.

It follows that the Hamiltonian describing the interaction of the qubit with the environment has the form $\hat{H} = 2e\hat{n} \otimes \beta\hat{V}^{\text{env}}$, where $2e\hat{n}$ is the charge \hat{Q} on the qubit electrodes expressed in terms of the number of Cooper pairs \hat{n} . Then $\beta\hat{V}$ is the generalized force \hat{F} and $2e\hat{n}$ its corresponding coordinate \hat{X} . To express the dissipative part of the master equation, we need to decompose \hat{X} into its frequency components \hat{X}_{ω} defined in eq. (B.8) and calculate the spectral density S_{FF} related to the spectral density of the environment voltage \hat{V}^{env} by $S_{FF} = \beta^2 S_{VV}$.

In the transmon limit $E_J \gg E_C$, the number operator \hat{n} couples only neighbouring eigenstates and can be written as $\hat{n} = \sum_i n_0 \sqrt{i+1} (|i\rangle\langle i+1| + \text{H.c.})$, where $|0\rangle, |1\rangle, \dots$ are the eigenstates of the transmon and $n_0 = (E_J/32E_C)^{1/4}$ (Koch *et al.*, 2007). The possible transition frequencies are $\pm\omega_1, \pm\omega_2, \dots$, where $\omega_i = (E_{i+1} - E_i)/\hbar$ and the corresponding frequency components of \hat{X} are $\hat{X}_{\omega_i} = 2en_0\sqrt{i+1}|i+1\rangle\langle i|$ and $\hat{X}_{-\omega_i} = (\hat{X}_{\omega_i})^\dagger$.

The spectral density S_{VV} of the environment voltage \hat{V}^{env} can be calculated in terms of the circuit's impedance Z , as shown in app. C, eq. (C.4). Just like in sec. B.1, we assume that the coupling capacitances are small compared with $1/\omega Z^{\text{env}}$. In this limit, the impedance at the node where the environment connects with the capacitive network is close to Z^{env} .

Now we can substitute \hat{X}_{ω_i} and S_{VV} into eq. (B.10). Furthermore, we express n_0 in terms of the $|0\rangle \rightarrow |1\rangle$ transition frequency $\omega_0 = \sqrt{8E_J E_C}/\hbar$ and the charging energy $E_C = e^2/2C_{\Sigma}$. The resulting expression for the dissipative part of the Liouvillian \mathcal{L}_d is

$$\mathcal{L}_d = \omega_0 C_{\Sigma} \beta^2 \sum_i \omega_i (i+1) \text{Re} Z^{\text{env}}(\omega_i) (N_i \mathcal{D}_{|i+1\rangle\langle i|} + (N_i + 1) \mathcal{D}_{|i\rangle\langle i+1|}), \quad (\text{B.12})$$

where $N_i = 1/(\exp(\hbar\omega_i/k_B T) - 1)$ is the mean number of photons in a harmonic mode of frequency ω_i .

To relate this result to the relaxation rates in the system, we can consider a diagonal density matrix $\hat{\rho} = \sum_i p_i |i\rangle\langle i|$, that is, a mixture of the transmon eigenstates. We substitute this form of the density matrix into the evolution equation $d\hat{\rho}/dt = \mathcal{L}_d[\hat{\rho}]$ where we have neglected the unitary evolution. By comparing the factors of the density matrix components $|i\rangle\langle i|$ for each i on both sides of the equation, we get

$$\frac{dp_i}{dt} = \Gamma_{i-1}^\uparrow p_{i-1} + \Gamma_{i+1}^\downarrow p_{i+1} - (\Gamma_i^\uparrow + \Gamma_i^\downarrow) p_i, \text{ where} \quad (B.13)$$

$$\Gamma_i^\uparrow \equiv (i+1)\omega_0\omega_i C_\Sigma \beta^2 N_i \text{Re } Z^{\text{env}}(\omega_i), \quad (B.14)$$

$$\Gamma_{i+1}^\downarrow \equiv (i+1)\omega_0\omega_i C_\Sigma \beta^2 (N_i + 1) \text{Re } Z^{\text{env}}(\omega_i). \quad (B.15)$$

This is a rate equation where Γ_i^\uparrow and Γ_i^\downarrow are the transition rates from state $|i\rangle$ to $|i+1\rangle$ and $|i-1\rangle$, representing excitation and relaxation processes, respectively. Specifically, at zero temperature when $N_i = 0$, the relaxation rate from the first excited state $|1\rangle$ to the ground state $|0\rangle$ is

$$\Gamma_1^\downarrow = \omega_0^2 C_\Sigma \beta^2 \text{Re } Z^{\text{env}}(\omega_0).$$

This result is identical to the one shown in eq. (B.7) derived from purely classical considerations in sec. B.1. Compared with the classical formula, however, eq. (B.12) provides additional insight. It tells us how the transition rates change for higher energy levels and how they depend on the temperature of the environment.

B.3 Example - qubit coupled to a transmission line

The simplest possible example of a dissipative environment is a semi-infinite transmission line. Despite being in principle lossless, the fact that energy can propagate in it without ever returning back means that it can be effectively described as a lossy element. The center conductor at the end of the line can be capacitively coupled to the qubit as illustrated in Fig. B.5(a). A $50\ \Omega$ chargeline coupled to a superconducting qubit is a typical example of such a configuration.

The impedance Z_0 of a semi-infinite lossless transmission line is frequency-independent and real, making it equivalent to an ideal resistor. The excitation and relaxation rates given by eq. (B.13) and eq. (B.14) then simplify to

$$\Gamma_i^\uparrow \equiv (i+1)\omega_0\omega_i C_\Sigma \beta^2 N_i Z_0,$$

$$\Gamma_{i+1}^\downarrow \equiv (i+1)\omega_0\omega_i C_\Sigma \beta^2 (N_i + 1) Z_0.$$

B.4 Example - Purcell effect

Another important instance of qubit relaxation induced by the circuit environment is the so-called *Purcell decay*. When a qubit is coupled to a resonator which itself

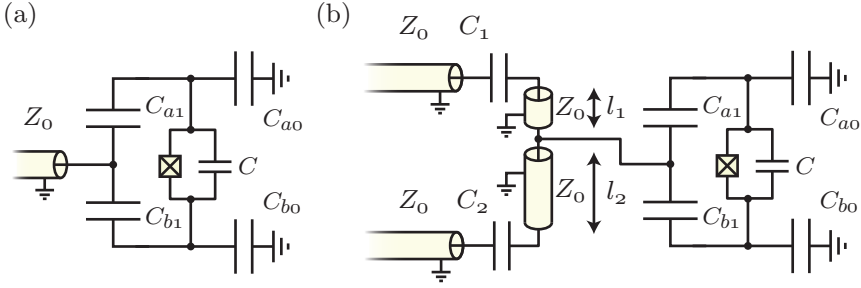


Figure B.5: (a) Schematic of a qubit capacitively coupled to a transmission line. (b) Schematic of a qubit capacitively coupled to a transmission line resonator.

couples to an outside environment – for example a transmission line, the qubit can lose its energy to the line via the resonator. This can happen even if the two are not resonant with each other and the dependence of the qubit relaxation rate on frequency will be heavily influenced by the presence of the resonator. Generally speaking, the relaxation rate decreases with increasing detuning of the qubit from the resonator modes.

This effect can be interpreted in many different ways. As the qubit and the environment exchanging virtual photons via the resonator. As the qubit acting like an antenna, oscillating at its transition frequency and transmitting an off-resonant signal through the resonator. Or as the vacuum fluctuations of the environment, filtered by the resonator, inducing relaxation of the qubit. All of these are equally valid ways of gaining insight into the problem. The second one is perhaps closest to the way we have derived the relaxation rates in sec. B.1 while the last one is rather in the spirit of sec. B.2.

The schematic of the circuit in question is shown in Fig. B.5b. The resonator is a finite section of a transmission line connected at its two ends to semi-infinite input and output transmission lines via capacitances C_1 and C_2 . An arbitrary point somewhere along the resonator is capacitively coupled to the qubit. The admittance of such environment is given by

$$Y^{\text{env}}(\omega) = Y_0 \left(\frac{Y_1(\omega)/Y_0 - i \tan(\omega l_1/v)}{1 - i Y_1(\omega) \tan(\omega l_1/v)/Y_0} + \frac{Y_2(\omega)/Y_0 - i \tan(\omega l_2/v)}{1 - i Y_2(\omega) \tan(\omega l_2/v)/Y_0} \right),$$

where $Y_1(\omega) = 1/(Z_0 + 1/i\omega C_1)$, $Y_2(\omega) = 1/(Z_0 + 1/i\omega C_2)$ are the admittances of the loads at the ends of the resonator composed of the coupling capacitors and the outside transmission lines. Furthermore, l_1 and l_2 are the lengths of the two sections of the resonator between its ends and the qubit and v is the propagation speed of the field in the transmission line. With a rather tedious calculation, one can show that in the limit of weak coupling, that is for $C_{1,2} \ll 1/\omega Z_0$, the real part of $Z^{\text{env}}(\omega) = 1/Y^{\text{env}}(\omega)$ becomes

$$\text{Re } Z^{\text{env}}(\omega) = Z_0^3 \omega^2 \frac{C_1^2 \cos^2(\omega l_2/v) + C_2^2 \cos^2(\omega l_1/v)}{\sin^2(\omega l/v)}.$$

After substitution into eq. (B.14), we get an equation which can be used to model the expected Purcell-limited relaxation rates Γ_i^\downarrow as a function of the qubit frequency. Most of the quantities appearing in this expression, such as the capacitances C_1 and C_2 , are not directly measurable in an experiment. However, some of them are related to easily measurable quantities. For example, the voltage division ratio can be extracted from the resonant Jaynes-Cummings coupling strength g and the capacitances C_1 and C_2 from the linewidth κ of the resonator's fundamental mode and its resonant insertion loss L_0 .

Appendix C

A shortcut to circuit quantization

In general, the way to quantize a linear lossless electrical circuit is rather straightforward and well-understood. One starts by writing the Lagrangian describing the dynamics of the circuit and derives the corresponding Hamiltonian. Thanks to the linearity of the circuit, this will be a quadratic function of the canonical variables. Using a suitable canonical transformation, one can diagonalize the Hamiltonian, thus separating the dynamics of the system into independent harmonic modes. These are then quantized in the standard way by replacing the dynamical variables with operators obeying the canonical commutation relations.

Arguably, despite its conceptual simplicity, this process can become rather cumbersome for realistic circuits. In this appendix I present a less well known procedure which will allow us to extract the frequencies and the vacuum voltage amplitudes of the individual modes from a purely classical quantity – the impedance of the circuit. The connection between the properties of the quantum model and the impedance is provided by the correspondence principle which states that the expectation values of the canonical variables of a linear system obey the classical equations of motion. We will describe the evolution of the circuit using both the quantum and the classical model and obtain the main result of this appendix by requiring the two predictions to be equal.

To probe the system, we connect its node i to an ideal source of current $I_e(t)$ and measure the voltage response at node j , as shown in Fig. C.1a. We can then obtain the voltage $V^{(j)}(t)$ at a node j from the impedance matrix $\mathbf{Z}(\omega)$ of the circuit. In the frequency domain, we have $V^{(j)}(\omega) = Z_{ji}(\omega)I_e(\omega)$. In the following, we will consider specifically a delta pulse excitation $I_e(t) = A\delta(t)$, or in frequency domain $I_e(\omega) = A$, for which we get the simple result

$$V^{(j)}(\omega) = AZ_{ji}(\omega).$$

To calculate the voltage $V^{(j)}$ within the framework of quantum mechanics, we first need to determine the Hamiltonian describing the interaction of the circuit with the current source. The dynamics of a network of nodes connected by capacitors and inductors can be expressed in terms of flux variables $\Phi^{(k)}(t) = \int V^{(k)}(t) dt$ and a

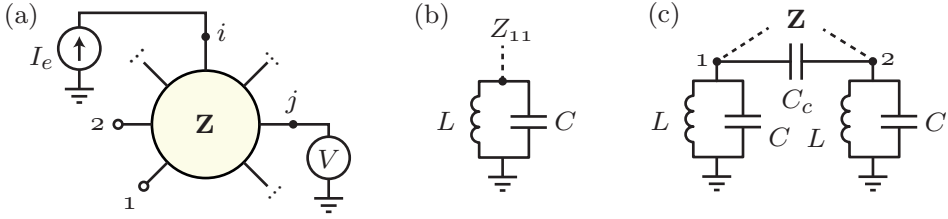


Figure C.1: (a) Diagram of the multi-port circuit characterized by the impedance matrix \mathbf{Z} . A current source drives node i of the circuit and its voltage response is monitored at node j . (b) LC oscillator as an example of a simple single-mode circuit. (c) A system of two coupled LC oscillators as an example of a circuit with multiple modes. The impedance matrix is evaluated at the two indicated nodes.

Lagrangian

$$\mathcal{L}_0 = \frac{1}{2} \dot{\Phi} \cdot \mathbf{C} \cdot \dot{\Phi} - \frac{1}{2} \Phi \cdot \mathbf{L}^{-1} \cdot \Phi,$$

where \mathbf{C} and \mathbf{L} are the capacitance and inductance matrices of the circuit. It is not difficult to show that the left-hand side of the Euler-Lagrange equation

$$\frac{d}{dt} \frac{\partial \mathcal{L}_0}{\partial \dot{\Phi}^{(i)}} - \frac{\partial \mathcal{L}_0}{\partial \Phi^{(i)}} = 0$$

then represents the net current flowing out of node i . After connecting the current source, this is no longer equal to zero but is instead given by I_e . This modification is equivalent to the addition of a term

$$\delta \mathcal{L} = \Phi^{(i)} I_e$$

to the Lagrangian. The variables $\Pi^{(k)}$ conjugate to the fluxes $\Phi^{(k)}$ are then $\mathbf{\Pi} = \mathbf{C} \cdot \dot{\Phi}$ and the Hamiltonian

$$\begin{aligned} H &= \mathbf{\Pi} \cdot \dot{\Phi} - \mathcal{L}_0 - \delta \mathcal{L} \\ &= \frac{1}{2} \mathbf{\Pi} \cdot \mathbf{C} \cdot \mathbf{\Pi} + \frac{1}{2} \Phi \cdot \mathbf{L}^{-1} \cdot \Phi - \Phi^{(i)} I_e. \end{aligned}$$

We can see that the coupling term has the form $H_c = -\Phi^{(i)} I_e$.

The linear circuit can be modelled as a collection of N harmonic modes with annihilation (creation) operators \hat{a}_k (\hat{a}_k^\dagger), where $k = 1, 2, \dots, N$. To describe the system fully, we need to specify the eigenfrequencies ω_k of all the modes and their vacuum flux amplitudes $\Phi_k^{(i)}$ which define the fluxes $\hat{\Phi}^{(j)}$ at each node j of the circuit as

$$\hat{\Phi}^{(j)} = \sum_k \Phi_k^{(j)} \hat{a}_k^\dagger + \Phi_k^{(j)*} \hat{a}_k.$$

Similarly, we can also expand the voltages at each node as

$$\hat{V}^{(j)} = \sum_k V_k^{(j)} \hat{a}_k^\dagger + V_k^{(j)*} \hat{a}_k, \quad (\text{C.1})$$

where the vacuum amplitudes $V_k^{(j)}$ are related to $\Phi_k^{(j)}$ by $V_k^{(j)} = i\omega_k \Phi_k^{(j)}$ in order to satisfy the identity $d\hat{\Phi}^{(j)}/dt = \hat{V}^{(j)}$.

The current delta pulse is represented by the Hamiltonian $\hat{H}_c = -\hat{\Phi}^{(i)} A \delta(t)$ which results in a unitary operation $U = \exp(iA\hat{\Phi}^{(i)}/\hbar)$ acting at $t = 0$. Starting with the circuit in the vacuum state, this displacement operator drives the system into the coherent state $|\alpha_1 \alpha_2 \dots\rangle$ where $\alpha_k = iA\Phi_k^{(i)}$. After that, the state evolves freely and at time $t > 0$ is

$$|\psi(t)\rangle = |\alpha_1(t) \alpha_2(t) \dots\rangle, \text{ where}$$

$$\alpha_k(t) = \frac{iA\Phi_k^{(i)}}{\hbar} e^{-i\omega_k t}.$$

If we measure the voltage at a node j , we obtain the expectation value

$$\begin{aligned} \langle \hat{V}^{(j)}(t) \rangle &= \sum_k V_k^{(j)} \langle \hat{a}_k \rangle^* + V_k^{(j)*} \langle \hat{a}_k \rangle \\ &= -\frac{iA}{\hbar} \sum_k V_k^{(j)} \Phi_k^{(i)*} e^{i\omega_k t} - V_k^{(j)*} \Phi_k^{(i)} e^{-i\omega_k t}. \end{aligned}$$

Its Fourier transform (in the electrical engineering notation) is then

$$\begin{aligned} \langle \hat{V}^{(j)}(\omega) \rangle &= \int \langle \hat{V}^{(j)}(t) \rangle e^{-i\omega t} dt \\ &= -\frac{iA}{\hbar} \int_0^\infty dt \sum_k V_k^{(j)} \Phi_k^{(i)*} e^{i(\omega_k - \omega)t} - V_k^{(j)*} \Phi_k^{(i)} e^{-i(\omega_k + \omega)t} \\ &= \frac{A}{\hbar} \sum_k V_k^{(j)} \Phi_k^{(i)*} \frac{1}{\omega_k - \omega + i\epsilon} + V_k^{(j)*} \Phi_k^{(i)} \frac{1}{\omega_k + \omega - i\epsilon}. \end{aligned}$$

From the correspondence principle, comparison of the classical and the quantum mechanical expression gives us

$$\begin{aligned} \sum_k V_k^{(j)} \Phi_k^{(i)*} \left(\pi \delta(\omega_k - \omega) + \mathcal{P} \frac{i}{\omega_k - \omega} \right) \\ - V_k^{(j)*} \Phi_k^{(i)} \left(\pi \delta(\omega_k + \omega) - \mathcal{P} \frac{i}{\omega_k + \omega} \right) = i\hbar Z_{ji}(\omega), \end{aligned}$$

which finally leads to the central result of this appendix, namely that

$$\sum_k V_k^{(j)} V_k^{(i)*} \delta(\omega_k - \omega) - V_k^{(j)*} V_k^{(i)} \delta(\omega_k + \omega) = \frac{\hbar\omega}{2\pi} (Z_{ji}(\omega) + Z_{ij}^*(\omega)). \quad (\text{C.2})$$

This identity links a classical quantity – the impedance matrix \mathbf{Z} – to the vacuum voltage amplitudes $V_k^{(j)}$ of the modes and their frequencies ω_k . To understand how these quantities can be extracted from the impedance matrix, let us consider a finite lossless circuit whose impedance $\mathbf{Z}(\omega)$ is symmetric and purely imaginary for $\omega \in \mathbb{R}$, has simple poles at frequencies $\pm\omega_1, \pm\omega_2, \dots, \pm\omega_N \in \mathbb{R}$ and can be expanded in the form

$$\mathbf{Z}(\omega) = \sum_k \frac{\text{res}_{\omega_k} \mathbf{Z}}{\omega - \omega_k} + \frac{\text{res}_{-\omega_k} \mathbf{Z}}{\omega + \omega_k}.$$

Causality dictates that the poles of any response function, of which impedance is one example, all lie in the upper¹ half of the complex plane. We will therefore shift all the poles $\pm\omega_k$ by an infinitesimal amount $i\epsilon$. The right-hand side of eq. (C.2) is then zero everywhere except at the poles where the terms $1/(\omega \mp \omega_k \mp i\epsilon) - 1/(\omega \mp \omega_k \pm i\epsilon)$ yield a delta function $\pm 2\pi i \delta(\omega - \omega_k)$. A simple comparison of the terms on both sides of eq. (C.2) then tells us that the poles ω_k are exactly the eigenfrequencies of the modes and the products of the vacuum voltage amplitudes on the left-hand side are related to the residues of $\mathbf{Z}(\omega)$ by

$$V_k^{(j)} V_k^{(i)*} = i\hbar \omega_k \text{res}_{\omega_k} Z_{ji}. \quad (\text{C.3})$$

According to this equation, we can determine the absolute values of the vacuum amplitudes $|V_k^{(j)}|$ from the residues of the diagonal impedance matrix elements Z_{jj} . The off-diagonal elements allow us to find the relative phases between each pair of amplitudes $V_k^{(i)}$ and $V_k^{(j)}$ belonging to the same mode k . This determines all the amplitudes up to a phase shift which may be different for each mode. These phase shifts can be chosen arbitrarily which corresponds to choosing the phases of the ladder operators \hat{a} and \hat{a}^\dagger . Eq. (C.3) therefore fully specifies the coefficients in the expansion of the voltage operators $\hat{V}^{(j)}$ in terms of the ladder operators, as given by eq. (C.1).

C.1 Example – LC oscillator

To illustrate the use of eq. (C.3), we will start with a very simple example – a parallel LC circuit as shown in Fig. C.1(b). This circuit has a single ungrounded node $i = 1$ and the corresponding impedance Z_{11} can be readily calculated as

$$\begin{aligned} Z_{11}(\omega) &= \frac{1}{i\omega C + \frac{1}{i\omega L}} \\ &= -\frac{i\omega}{\omega^2 - \frac{1}{LC}}. \end{aligned}$$

This function has two poles at $\omega = \pm\omega_1$, where $\omega_1 = 1/\sqrt{LC}$. The circuit therefore has a single resonant mode with frequency ω_1 . The residue of the impedance at this

¹Or lower, depending on the definition of the Fourier transform.

frequency is given by

$$\text{res}_{\omega_1} Z_{11} \equiv \lim_{\omega \rightarrow \omega_1} (\omega - \omega_1) Z_{11}(\omega) = \lim_{\omega \rightarrow \omega_1} \frac{-\frac{i\omega}{C}}{\omega + \frac{1}{\sqrt{LC}}} = -\frac{i}{2C}.$$

Application of eq. (C.3) then gives us

$$|V_1^{(1)}|^2 = i\hbar\omega_1 \text{res}_{\omega_1} Z_{11} = \frac{\hbar\omega_1}{2C}.$$

This vacuum fluctuation amplitude can be also derived in the more usual way by considering that half of the vacuum energy $\hbar\omega_1/2$ is stored as the electrostatic energy of the capacitor, i.e. $C|V_1^{(1)}|^2/2 = \hbar\omega_1/4$.

C.2 Example – two coupled LC oscillators

Let us now consider a more interesting example – a system of two LC oscillator as discussed above, coupled together via a capacitance C_c (see Fig. C.1(c)). The 2×2 admittance matrix \mathbf{Y} corresponding to the two ungrounded nodes can be written as a sum of the admittance matrices of the individual LC circuits and the coupling capacitor

$$\mathbf{Y}(\omega) = \begin{pmatrix} i\omega C + 1/i\omega L & 0 \\ 0 & 0 \end{pmatrix} + \begin{pmatrix} 0 & 0 \\ 0 & i\omega C + 1/i\omega L \end{pmatrix} + \begin{pmatrix} i\omega C_c & -i\omega C_c \\ -i\omega C_c & i\omega C_c \end{pmatrix}.$$

The impedance matrix is its inverse

$$\mathbf{Z}(\omega) = -\frac{\omega^2}{(\omega^2 C - 1/L)(\omega^2(C + 2C_c) - 1/L)} \begin{pmatrix} i\omega C_{\text{tot}} + 1/i\omega L & i\omega C_c \\ i\omega C_c & i\omega C_{\text{tot}} + 1/i\omega L \end{pmatrix},$$

where $C_{\text{tot}} = C + C_c$. It has four poles $\pm\omega_{1,2}$, where $\omega_1 = 1/\sqrt{LC}$ and $\omega_2 = 1/\sqrt{L(C + 2C_c)}$ are the frequencies of the two resonant modes. The residues of the impedance matrix at the two poles are straightforward, even if slightly tedious, to calculate:

$$\begin{aligned} \text{res}_{\omega_1} \mathbf{Z} &= -\frac{i}{4C} \begin{pmatrix} 1 & 1 \\ 1 & 1 \end{pmatrix} \\ \text{res}_{\omega_2} \mathbf{Z} &= -\frac{i}{4(C + 2C_c)} \begin{pmatrix} 1 & -1 \\ -1 & 1 \end{pmatrix} \end{aligned}$$

Using eq. (C.3), we then get $|V_1^{(1)}|^2 = |V_1^{(2)}|^2 = V_1^{(1)} V_1^{(2)*} = V_1^{(2)} V_1^{(1)*} = \hbar\omega_1/4C$ and $|V_2^{(1)}|^2 = |V_2^{(2)}|^2 = -V_2^{(1)} V_2^{(2)*} = -V_2^{(2)} V_2^{(1)*} = \hbar\omega_1/4(C + 2C_c)$. As discussed above, this determines the voltage amplitudes up to a phase which can be chosen arbitrarily and separately for each mode. We will choose $V_1^{(1)}$ and $V_2^{(1)}$ to be positive

real which gives us

$$\begin{aligned}
V_1^{(1)} &= \sqrt{\frac{\hbar\omega_1}{4C}}, \\
V_1^{(2)} &= \sqrt{\frac{\hbar\omega_1}{4C}}, \\
V_2^{(1)} &= \sqrt{\frac{\hbar\omega_2}{4(C+2C_c)}}, \\
V_2^{(2)} &= -\sqrt{\frac{\hbar\omega_2}{4(C+2C_c)}}.
\end{aligned}$$

From the symmetry of the circuit, we would expect that its modes are either symmetric or antisymmetric under exchange of the two LC oscillators. We can see that the results of our calculation agree with this. In mode 1, the voltages at the two nodes oscillate with the same amplitude and phase, while in mode 2 they have the same amplitude but are out of phase by π .

Using these symmetry arguments, it would have again been possible to calculate the vacuum amplitudes rather easily even without eq. (C.3). In the symmetric mode, the voltage drop across the coupling capacitor is zero and therefore the two LC circuits oscillate independently with their uncoupled frequencies $1/\sqrt{LC}$. The vacuum energy is distributed among them, hence the voltage amplitude is lower than for a single LC oscillator by a factor of $\sqrt{2}$. In the antisymmetric mode, the single coupling capacitor can be replaced by two connected in series, each with capacitance $2C_c$. The node between them is then at zero potential and can be connected to ground without changing the behaviour of the circuit. The system is therefore equivalent to two uncoupled LC circuits with capacitance $C + 2C_c$ oscillating out of phase by π .

C.3 Derived quantities

Eq. (C.2) allows us to evaluate some useful quantities such as the correlation function $\langle \hat{V}^{(i)}(t)\hat{V}^{(j)}(0) \rangle$ or propagators of the voltages in the circuit. Using eq. (C.1), we can express the correlation function in the Heisenberg picture as

$$\begin{aligned}
\langle \hat{V}^{(i)}(t)\hat{V}^{(j)}(0) \rangle &= \sum_{k,l} \langle (V_k^{(i)*} e^{-i\omega_k t} \hat{a}_k + V_k^{(i)} e^{i\omega_k t} \hat{a}_k^\dagger) (V_l^{(j)*} \hat{a}_l + V_l^{(j)} \hat{a}_l^\dagger) \rangle \\
&= \sum_{k,l} \langle V_k^{(i)*} V_l^{(j)} e^{-i\omega_k t} \hat{a}_k \hat{a}_l^\dagger + V_k^{(i)} V_l^{(j)*} e^{i\omega_k t} \hat{a}_k^\dagger \hat{a}_l \rangle \\
&= \sum_k V_k^{(i)*} V_k^{(j)} e^{-i\omega_k t} (n_k + 1) + V_k^{(i)} V_k^{(j)*} e^{i\omega_k t} n_k,
\end{aligned}$$

where $n_k = \langle \hat{a}_k^\dagger \hat{a}_k \rangle$ is the expected number of photons in mode k . We will assume that the system is in a thermal state at a temperature T , i.e. $n_k = 1/(\exp(\hbar\omega_k/k_B T) - 1)$.

The correlation function can then be written with the help of eq. (C.2) as

$$\langle \hat{V}^{(i)}(t)\hat{V}^{(j)}(0) \rangle = \int \frac{\hbar\omega}{2\pi} \frac{Z_{ji}(\omega) + Z_{ij}^*(\omega)}{1 - e^{-\hbar\omega/k_B T}} e^{-i\omega t} d\omega.$$

The voltage spectral density, which is defined as (Clerk *et al.*, 2010) $S_{VV}^{(i)}(\omega) = \int \langle \hat{V}^{(i)}(t)\hat{V}^{(i)}(0) \rangle e^{i\omega t} dt$, can therefore be written as

$$S_{VV}^{(i)}(\omega) = \frac{2\hbar\omega \operatorname{Re} Z_{ii}(\omega)}{1 - e^{-\hbar\omega/k_B T}}. \quad (\text{C.4})$$

Other useful quantities are the advanced and retarded propagators $G_{\text{adv}}^{(ij)}(t)$, $G_{\text{ret}}^{(ij)}(t)$ and the Feynman propagator $G_F^{(ij)}(t)$, defined as

$$\begin{aligned} G_{\text{adv}}^{(ij)}(t) &= \int \frac{d\omega}{2\pi} G_{\text{adv}}^{(ij)}(\omega) e^{-i\omega t} = -i \langle 0 | [\hat{V}^{(i)}(t)\hat{V}^{(j)}(0)] | 0 \rangle \Theta(-t) \\ G_{\text{ret}}^{(ij)}(t) &= \int \frac{d\omega}{2\pi} G_{\text{ret}}^{(ij)}(\omega) e^{-i\omega t} = i \langle 0 | [\hat{V}^{(i)}(t)\hat{V}^{(j)}(0)] | 0 \rangle \Theta(t) \\ G_F^{(ij)}(t) &= \int \frac{d\omega}{2\pi} G_F^{(ij)}(\omega) e^{-i\omega t} = i \langle 0 | \mathcal{T} \hat{V}^{(i)}(t)\hat{V}^{(j)}(0) | 0 \rangle, \end{aligned}$$

where \mathcal{T} denotes time-ordering. In a similar manner as for the correlation function, we can calculate the expectation values in the definitions of these propagators in terms of the vacuum voltage amplitudes and then express them using eq. (C.2). Fourier transforming the result then yields these expressions for the propagators in frequency space:

$$\left. \begin{aligned} G_{\text{adv}}^{(ij)}(\omega) \\ G_{\text{ret}}^{(ij)}(\omega) \end{aligned} \right\} = \int \frac{d\omega'}{2\pi} \frac{\hbar\omega' (Z_{ji}(\omega') + Z_{ij}^*(\omega'))}{\omega' - \omega \pm i\epsilon},$$

$$G_F^{(ij)}(\omega) = \int \frac{d\omega'}{2\pi} \frac{\hbar\omega' (Z_{ji}(\omega') + Z_{ij}^*(\omega'))}{\omega' - \omega(1 + i\epsilon)}.$$

Appendix D

Optimizing a second order transition

In this appendix, I present two methods for optimizing a pulse driving a higher order transition between two specific states in a quantum system. The first technique, which we have previously used to study the $|f0\rangle \rightarrow |g1\rangle$ transition in a transmon-resonator system (Zeytinoglu *et al.*, 2015), aims to achieve a good fidelity of the final state. The derivation given here closely follows the appendix of the paper, except in a slightly more general context. The second technique may be more useful in situations where not only the initial and final state matter but the fidelity of the intermediate state is also of importance. This is the case for example in photon shaping processes.

D.1 Method 1: Optimizing final state fidelity

Let us consider a quantum system with a Hamiltonian \hat{H}_0 . We wish to drive a transition between its two eigenstates $|\Phi_1\rangle$ and $|\Phi_2\rangle$. To do this, we apply a drive signal at a frequency close to the energy difference between the two states. We can tune the drive amplitude, its frequency and potentially also other parameters of the system. How do we need to vary these quantities to achieve for instance a swap operation between $|\Phi_1\rangle$ and $|\Phi_2\rangle$? While the answer to this question is trivial in the simple case of a two-level system, the presence of a coupling to other states complicates the situation. Driving of these off-resonant transitions induces Stark shifts of the energy levels which need to be compensated for.

We will denote the Hamiltonian of the driven system in a reference frame rotating at the drive frequency by $\hat{H}(\lambda)$, where λ stands for the variation in the parameters of the system. For $\lambda = 0$, the Hamiltonian reduces to \hat{H}_0 up to the rotating frame transformation. In the rotating frame, the states $|\Phi_1\rangle$ and $|\Phi_2\rangle$ are nearly degenerate with an energy separation $\Delta\varepsilon$. We will further assume that other eigenstates are separated from them by an energy gap ΔE much larger than $\Delta\varepsilon$. In addition, we consider that the Hamiltonian varies slowly compared with ΔE , that is, the process is adiabatic with respect to all transitions out of the subspace spanned by $|\Phi_1\rangle$ and $|\Phi_2\rangle$.

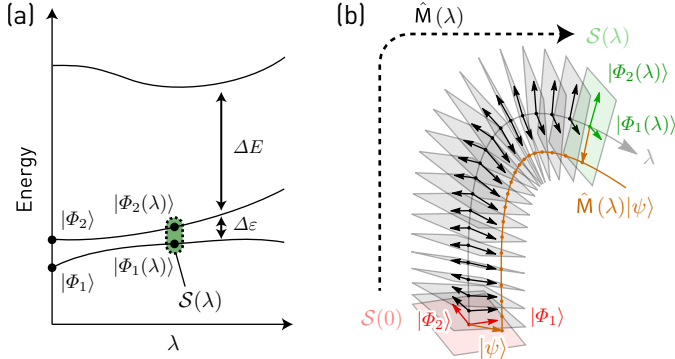


Figure D.1: (a) Energy level diagram illustrating the separation of the subspace \mathcal{S} spanned by the eigenstates $|\Phi_1\rangle$ and $|\Phi_2\rangle$ from other eigenstates. (b) Parallel transport connecting the subspaces $\mathcal{S}(\lambda)$ for different λ . The transported vector $|\psi\rangle$ (orange) is being repeatedly projected onto the successive subspaces. This results in a linear mapping $\hat{M}(\lambda)$ from $\mathcal{S}(0)$ to $\mathcal{S}(\lambda)$.

Finally, we also require that the separation of the energy scales and the adiabaticity condition are preserved as the system parameters are tuned around.

According to the adiabatic theorem (Born & Fock, 1928), if the system was initially prepared in a superposition of $|\Phi_1\rangle$ and $|\Phi_2\rangle$, it will at all times remain in the subspace $\mathcal{S}(\lambda)$ spanned by the eigenstates $|\Phi_1(\lambda)\rangle$ and $|\Phi_2(\lambda)\rangle$ of $\hat{H}(\lambda)$ corresponding to $|\Phi_1\rangle$ and $|\Phi_2\rangle$. To find out how the state of the system $|\Psi(t)\rangle$ evolves in the changing subspace $\mathcal{S}(\lambda)$, we will first parametrize it by a state $|\psi(t)\rangle$ in the initial subspace $\mathcal{S}(0)$ as $|\Psi(t)\rangle = \hat{M}(\lambda(t))|\psi(t)\rangle$, where $\hat{M}(\lambda)$ is some linear mapping from $\mathcal{S}(0)$ to $\mathcal{S}(\lambda)$. This reduces the problem of finding the evolution of $|\Psi(t)\rangle$ in the full Hilbert space to that of finding the evolution of $|\psi(t)\rangle$ in a fixed two-dimensional subspace. How do we choose the map $\hat{M}(\lambda)$? A natural candidate for a process mapping between subspaces continuously evolving along a curve $\mathcal{S}(\lambda)$ is a parallel transport defined in the following way:

$$\hat{M}(\lambda) = \lim_{\Delta\lambda \rightarrow 0} \hat{P}(\lambda)\hat{P}(\lambda - \Delta\lambda) \dots \hat{P}(2\Delta\lambda)\hat{P}(\Delta\lambda)\hat{P}(0), \quad (\text{D.1})$$

where $\hat{P}(\lambda) = \sum_{i=1,2} |\Phi_i(\lambda)\rangle\langle\Phi_i(\lambda)|$ is a projector onto $\mathcal{S}(\lambda)$. This map represents a continuous series of projections onto the subspaces $\mathcal{S}(x)$ for x varying from 0 to λ .

Since $|\Psi(t+dt)\rangle$ lies in $\mathcal{S}(\lambda(t+dt))$, it can be expressed as

$$\begin{aligned} |\Psi(t+dt)\rangle &= \hat{P}(\lambda(t+dt))|\Psi(t+dt)\rangle \\ &= \hat{P}(\lambda(t+dt)) \exp(-i\hat{H}(\lambda(t))dt)|\Psi(t)\rangle, \end{aligned}$$

resulting in the following evolution equation for $|\psi(t)\rangle$:

$$\begin{aligned} \hat{M}(\lambda(t+dt))|\psi(t+dt)\rangle = \\ \hat{P}(\lambda(t+dt))\exp(-i\hat{H}(\lambda(t))dt)\hat{M}(\lambda(t))|\psi(t)\rangle \end{aligned} \quad (\text{D.2})$$

Under the reasonable assumption that the subspace $\mathcal{S}(\lambda)$ changes smoothly with λ , it can be shown that $\hat{M}(\lambda)$ preserves vector norms in $\mathcal{S}(\lambda)$. It follows that $M(\lambda)^\dagger$, which is an infinite product of projectors analogous to $M(\lambda)$ but in the reverse order, is the inverse of $M(\lambda)$. Hence, after dropping the projector $\hat{P}(\lambda(t+dt))$ from the right-hand side of eq. (D.2) as well as from the product form of $\hat{M}(\lambda(t+dt))$ (cf. eq. (D.1)) on its left-hand side, we multiply the equation by $\hat{M}(\lambda(t))^\dagger$ to obtain

$$|\psi(t+dt)\rangle = \hat{M}(\lambda(t))^\dagger \exp(-i\hat{H}(\lambda(t))dt)\hat{M}(\lambda(t))|\psi(t)\rangle$$

which we transform into the differential form

$$\frac{d}{dt}|\psi(t)\rangle = -i\hat{M}(\lambda(t))^\dagger \hat{H}(\lambda(t))\hat{M}(\lambda(t))|\psi(t)\rangle.$$

The evolution of the vector $|\psi(t)\rangle$ is therefore governed by an effective Hamiltonian

$$\hat{H}_{\text{eff}}(\lambda) = \hat{M}(\lambda)^\dagger \hat{H}(\lambda)\hat{M}(\lambda) \quad (\text{D.3})$$

acting on $\mathcal{S}(0)$, resulting in the effective evolution operator $\hat{U}_{\text{eff}}(t_f, t_i) = \mathcal{T} \exp \int_{t_i}^{t_f} (-i\hat{H}_{\text{eff}}(\lambda(t))) dt$. If we assume that $\lambda(t_i) = \lambda(t_f) = 0$, we have $|\psi(t_i)\rangle = |\Psi(t_i)\rangle$ and $|\psi(t_f)\rangle = |\Psi(t_f)\rangle$. Then we can directly write down the evolution from $|\Psi(t_i)\rangle$ to $|\Psi(t_f)\rangle$:

$$|\Psi(t_f)\rangle = \hat{U}_{\text{eff}}(t_f, t_i)|\Psi(t_i)\rangle.$$

This result allows us to determine the variation of λ with time necessary to realize a perfect swap operation between $|\Phi_1\rangle$ and $|\Phi_2\rangle$. For this, the effective Hamiltonian has to have the form

$$\hat{H}_{\text{eff}}(t) = E_{\text{offset}}(t)\mathbb{1} + g(t)(|\Phi_1\rangle\langle\Phi_2| + \text{H.c.}), \quad (\text{D.4})$$

where the overall energy shift $E_{\text{offset}}(t)$ leading only to an overall phase shift is omitted since it is physically irrelevant. This equation is equivalent to the requirement that the equal superposition states $|\Phi_\pm\rangle = (|\Phi_1\rangle \pm |\Phi_2\rangle)/\sqrt{2}$ are eigenstates of $\hat{H}_{\text{eff}}(t)$ and therefore, by virtue of eq. (D.3), that $\hat{M}_{\lambda(t)}|\Phi_\pm\rangle$ are eigenstates of $\hat{H}(t)$ which we have previously denoted by $|\Phi_{1,2}(\lambda(t))\rangle$. In other words,

$$\{|\Phi_1(\lambda)\rangle, |\Phi_2(\lambda)\rangle\} = \{\hat{M}_\lambda|\Phi_+\rangle, \hat{M}_\lambda|\Phi_-\rangle\}. \quad (\text{D.5})$$

This equation can be solved for \hat{M}_λ . However, since our goal is to obtain a condition for λ , we need an equation for the Hamiltonian instead. To get it, we transform eq. (D.5) into a differential form. By substituting $\lambda \rightarrow \lambda + d\lambda$, we find the following relation between $|\Phi_i(\lambda + d\lambda)\rangle$ and $|\Phi_i(\lambda)\rangle$:

$$|\Phi_i(\lambda + d\lambda)\rangle = \hat{P}(\lambda + d\lambda)|\Phi_i(\lambda)\rangle,$$

which, after multiplication by $\langle \Phi_j(\lambda + d\lambda) |$, we write in the form

$$\langle \Phi_i(\lambda) | \frac{d}{d\lambda} | \Phi_j(\lambda) \rangle = 0.$$

The associated initial condition follows from taking the limit $\lambda \rightarrow 0$ in eq. (D.5), giving $\{ \lim_{\lambda \rightarrow 0} | \Phi_1(\lambda) \rangle, | \lim_{\lambda \rightarrow 0} \Phi_2(\lambda) \rangle \} = \{ | \Phi_+ \rangle, | \Phi_- \rangle \}$. Since the vectors on the left-hand side are eigenstates of the non-driven Hamiltonian, so have to be $| \Phi_+ \rangle$ and $| \Phi_- \rangle$. This is by definition also true for $| \Phi_1 \rangle$ and $| \Phi_2 \rangle$. The only way the two distinct pairs of vectors can be eigenstates at the same time is if the subspace they are spanning is degenerate. This can be achieved by choosing the correct frequency of the rotating frame, giving us a condition for the drive frequency at $\lambda = 0$.

For $i = j$, the differential equation above can be satisfied simply by choosing the correct phase of the eigenstates $| \Phi_{1,2}(\lambda) \rangle$. After expressing the derivative of the eigenstate in terms of the derivative of the Hamiltonian, the remaining equations for $i \neq j$ are equivalent to

$$\langle \Phi_1(\lambda) | \frac{d\hat{H}(\lambda)}{d\lambda} | \Phi_2(\lambda) \rangle = 0. \quad (\text{D.6})$$

This equation expresses a condition for the curve parametrized by λ that the Hamiltonian has to take in the parameter space. If it holds, the resulting operation in the subspace $\mathcal{S}(0)$ will have the desired form $\exp(-i\theta(| \Phi_1 \rangle \langle \Phi_2 | + \text{H.c.})/2)$ and can realize a perfect swap between $| \Phi_1 \rangle$ and $| \Phi_2 \rangle$. In general, if we have at our disposal at least one tunable parameter of the Hamiltonian in addition to the drive amplitude Ω , we can satisfy eq. (D.6) in the following way.

Let us consider for example that the additional parameter we can control is the drive frequency ω_d and let us fix the parametrization of Ω as $\Omega = \lambda$. ω_d is then an unknown function of Ω which we wish to choose such that eq. (D.6) is satisfied. We will expand the derivative $d\hat{H}(\lambda)/d\lambda$ using chain rule and get

$$\begin{aligned} & \langle \Phi_1(\Omega, \omega_d) | \frac{\partial \hat{H}(\Omega, \omega_d)}{\partial \Omega} | \Phi_2(\Omega, \omega_d) \rangle + \\ & \frac{d\omega_d(\Omega)}{d\Omega} \langle \Phi_1(\Omega, \omega_d) | \frac{\partial \hat{H}(\Omega, \omega_d)}{\partial \omega_d} | \Phi_2(\Omega, \omega_d) \rangle = 0. \end{aligned} \quad (\text{D.7})$$

We can solve this differential equation for $\omega_d(\Omega)$ numerically to find the desired amplitude dependence of the drive frequency. A simple procedure for finding the solution is summarized here:

1. Start with $\Omega = 0$. Find ω_d by requiring $| \Phi_1 \rangle$ and $| \Phi_2 \rangle$ to be degenerate in the rotating frame.
2. Find the eigenstates $| \Phi_{1,2}(\Omega, \omega_d) \rangle$ of the Hamiltonian $\hat{H}(\Omega, \omega_d)$. For the first step when $\Omega = 0$ and the eigenstates are degenerate, choose $| \Phi_{1,2}(\Omega, \omega_d) \rangle = (| \Phi_1 \rangle \pm | \Phi_2 \rangle) / \sqrt{2}$.
3. Use eq. (D.7) to calculate $d\omega_d(\Omega)/d\Omega$

4. Set $\omega_d \rightarrow \omega_d + \frac{d\omega_d(\Omega)}{d\Omega} \Delta\Omega$ and $\Omega \rightarrow \Omega + \Delta\Omega$.

5. Go to step 2.

Once the solution is known, the effective coupling $g(\Omega)$ between $|\Phi_1\rangle$ and $|\Phi_2\rangle$ can be calculated from the eigenenergies $E_{1,2}(\Omega, \omega_d)$ of the two eigenstates $|\Phi_{1,2}(\Omega, \omega_d)\rangle$. Inspection of eq. (D.4) shows that these eigenenergies are equal to $E_{\text{offset}} \pm g$ and therefore

$$g(\Omega) = \frac{E_1(\Omega, \omega_d) - E_2(\Omega, \omega_d)}{2}.$$

D.2 Method 2: Optimizing time-averaged fidelity

Let us now consider a scenario where we have a pair of states $|\psi_1\rangle, |\psi_2\rangle$ and would ideally like to drive Rabi oscillations between them, given by the unitary $\hat{U}_{\text{ideal}}(t)$:

$$\begin{aligned}\hat{U}_{\text{ideal}}(t)|\psi_1\rangle &= e^{-i\omega t} \cos \frac{\Omega t}{2} |\psi_1\rangle + e^{-i(\omega t - \phi)} \sin \frac{\Omega t}{2} |\psi_2\rangle, \\ \hat{U}_{\text{ideal}}(t)|\psi_2\rangle &= -e^{-i(\omega t + \phi)} \sin \frac{\Omega t}{2} |\psi_1\rangle + e^{-i\omega t} \cos \frac{\Omega t}{2} |\psi_2\rangle.\end{aligned}$$

The Hamiltonian \hat{H} at our disposal is time-independent, allows some degree of tuning but not such that we can implement the unitary operation above perfectly. How do we choose our Hamiltonian to get as close as possible to the given evolution? To answer this question, we first need to define a figure of merit which we aim to optimize. For us, this will be the time- and state-averaged distance

$$\Delta \equiv \sum_{j=1,2} \lim_{T \rightarrow \infty} \frac{1}{2T} \int_0^T \|\hat{U}(t)|\psi_j\rangle - \hat{U}_{\text{ideal}}(t)|\psi_j\rangle\|^2 dt.$$

We can rewrite the right-hand side expression to

$$\Delta = 2 - \lim_{T \rightarrow \infty} \frac{1}{T} \int_0^T \text{Re Tr } \hat{U}_{\text{ideal}}^\dagger(t) \hat{U}(t) \hat{P} dt,$$

where \hat{P} is a projector onto the subspace spanned by $|\psi_1\rangle$ and $|\psi_2\rangle$.

We can easily verify that the states

$$|\psi_\pm\rangle \equiv |\psi_1\rangle \pm i e^{i\phi} |\psi_2\rangle$$

are eigenstates of $\hat{U}_{\text{ideal}}(t)$ with eigenvalues $e^{-i(\omega \pm \Omega/2)t}$. If we furthermore denote the eigenstates of \hat{H} as $|\varphi_j\rangle$ and their respective eigenvalues as $\hbar\omega_j$, we can rewrite the trace in the expression for Δ as

$$\sum_j e^{-i(\omega_j - \omega - \Omega/2)t} \langle \psi_+ | \varphi_j \rangle \langle \varphi_j | \psi_+ \rangle + e^{-i(\omega_j - \omega + \Omega/2)t} \langle \psi_- | \varphi_j \rangle \langle \varphi_j | \psi_- \rangle,$$

finally leading to

$$\Delta = 2 - \sum_j \delta_{\omega_j - \omega - \Omega/2} |\langle \varphi_j | \psi_+ \rangle|^2 + \delta_{\omega_j - \omega + \Omega/2} |\langle \varphi_j | \psi_- \rangle|^2,$$

where δ is the Kronecker delta symbol. If we consider ω and Ω to be free parameters, the minimal value of Δ is achieved by picking two eigenstates $|\varphi_a\rangle$ and $|\varphi_b\rangle$ which maximize $|\langle \varphi_a | \psi_+ \rangle|^2 + |\langle \varphi_b | \psi_- \rangle|^2$ and then requiring $\omega_a = \omega + \Omega/2$ and $\omega_b = \omega - \Omega/2$. In other words, the minimal value of Δ is given by

$$\Delta = \min_{a \neq b} (2 - |\langle \varphi_a | \psi_+ \rangle|^2 - |\langle \varphi_b | \psi_- \rangle|^2). \quad (\text{D.8})$$

The error parameter Δ given by this equation quantifies how well a given Hamiltonian reproduces the desired Rabi oscillations (the lower the value of Δ , the better). It provides us with another operational definition of the ac Stark shift - as a shift of the drive frequency which minimizes Δ .

As an example, we will consider driving of the $|f0\rangle \leftrightarrow |g1\rangle$ transition in a transmon-resonator system. In this case, we have a rotating-frame Hamiltonian of the form

$$\hat{H} = \hat{H}_0 + \frac{1}{2} \varepsilon (\hat{b}^\dagger e^{i\theta} + \hat{b} e^{-i\theta}) - \delta_d \hat{N},$$

where \hat{H}_0 is the non-driven Jaynes-Cummings Hamiltonian, $\varepsilon(\hat{b}^\dagger e^{i\theta} + \hat{b} e^{-i\theta})/2$ is the drive term, \hat{N} is the excitation number operator and δ_d is a detuning of the drive signal from a fixed reference frequency. We will choose this reference such that for $\delta_d = 0$ and $\varepsilon = 0$, the dressed states $|f0\rangle$ and $|g1\rangle$ are degenerate.

Then, for a given drive strength ε , we find the values of θ and δ_d for which the error Δ given by eq. (D.8) is minimal. The transition rate Ω is then given by the difference $\omega_a - \omega_b$ of the eigenvalues corresponding to the eigenvectors $|\varphi_a\rangle$ and $|\varphi_b\rangle$ which optimize Δ .

Appendix E

Photon shaping and reabsorption theory

E.1 Photon shaping

A diagram of a generic system which may be used to emit single shaped photons is shown in Fig. 4.1. The unitary evolution happens within the subspace \mathcal{M} while the photon emission process from the state $|\varphi_e\rangle$ traps the system in the ground state $|G\rangle$.

The evolution of such a system can be conveniently described within the framework of quantum trajectories. The state vector evolves according to the non-unitary Schrödinger equation

$$\frac{d}{dt}|\psi(t)\rangle = -i \left(\hat{H}(t) - \frac{i\kappa}{2} |\varphi_e\rangle\langle\varphi_e| \right) |\psi(t)\rangle. \quad (\text{E.1})$$

The square of the norm of this vector represents the probability that the system has not emitted a photon before time t . Its time derivative is given by

$$\frac{d}{dt} \langle\psi(t)|\psi(t)\rangle = -\kappa |\langle\varphi_e|\psi(t)\rangle|^2. \quad (\text{E.2})$$

This implies that the normalized state vector $|\bar{\psi}(\tau)\rangle = |\psi(\tau)\rangle / \sqrt{\langle\psi(\tau)|\psi(\tau)\rangle}$ evolves according to

$$\frac{d}{dt}|\bar{\psi}(t)\rangle = -i \left(\hat{H}(t) - \frac{i\kappa}{2} |\varphi_e\rangle\langle\varphi_e| + \frac{i\kappa}{2} \langle\bar{\psi}(t)|\varphi_e\rangle\langle\varphi_e|\bar{\psi}(t)\rangle \right) |\bar{\psi}(t)\rangle. \quad (\text{E.3})$$

Consistently with eq. (E.2), the probability amplitude for emitting a photon in the time interval $(t, t + dt)$ is $\langle\varphi_e|\psi(t)\rangle\sqrt{\kappa}dt$. The state $|\Psi(t)\rangle$ of the combined system including the propagating field therefore is

$$|\Psi(t)\rangle = |\psi(t)\rangle \otimes |0\rangle + |G\rangle \otimes \int_{t_i}^t \sqrt{\kappa} \langle\varphi_e|\psi(\tau)\rangle a_{\text{out}}^\dagger(\tau) |0\rangle d\tau, \quad (\text{E.4})$$

where $\hat{a}_{\text{out}}^\dagger(\tau)$ is the creation operator for a propagating photon emitted in the time interval $(\tau, \tau + d\tau)$. It is normalized such that $[\hat{a}_{\text{out}}(\tau'), \hat{a}_{\text{out}}^\dagger(\tau)] = \delta(\tau' - \tau)$. Note

that this means a properly normalized state with a single photon localized at time τ is actually $\sqrt{d\tau} \hat{a}_{\text{out}}^\dagger(\tau)|0\rangle$, which together with the emission probability amplitude also proportional to $\sqrt{d\tau}$ gives the correct infinitesimal quantity $d\tau$ in the last integral.

The goal of photon shaping is to design the Hamiltonian $\hat{H}(t)$ to achieve a desired final state $|\Psi_f\rangle$ at $t = t_f$. We can write it in the general form

$$|\Psi_f\rangle = |\psi_f\rangle \otimes |0\rangle + |G\rangle \otimes \int_{t_i}^{t_f} f(\tau) \hat{a}_{\text{out}}^\dagger(\tau)|0\rangle d\tau. \quad (\text{E.5})$$

Here the function $f(\tau)$ represents the wavefunction of the photon. If we observe the output of the system with a photodetector, $|f(\tau)|^2 d\tau$ gives the probability of observing the photon being emitted in a time interval $(\tau, \tau + d\tau)$.

For simplicity, we will consider the state of the system at time $t_f \rightarrow \infty$ and assume that the photon was emitted with unit probability. In other words, $|\psi_f\rangle = 0$ and $\int_{t_i}^{\infty} |f(\tau)| d\tau = 1$. Comparison with eq. (E.4) then gives us an expression for the photon wavefunction $f(\tau)$ in terms of the probability amplitude $\langle \varphi_e | \psi(\tau) \rangle$:

$$\sqrt{\kappa} \langle \varphi_e | \psi(\tau) \rangle = f(\tau). \quad (\text{E.6})$$

This can be equivalently expressed in terms of the normalized state vector. Using eq. (E.2), we get $d\langle \psi(t) | \psi(t) \rangle / dt = -|f(\tau)|^2$ and therefore

$$\sqrt{\kappa} \langle \varphi_e | \bar{\psi}(\tau) \rangle = \frac{f(\tau)}{\sqrt{1 - \int_{t_i}^{\tau} |f(t)|^2 dt}}. \quad (\text{E.7})$$

In principle, this equation allows us to determine how the state $|\bar{\psi}(\tau)\rangle$ needs to vary with time to achieve a given photon wavefunction $f(\tau)$. Note, however, that the solution is physical only if $f(\tau)$ satisfies

$$|f(\tau)|^2 / \kappa \leq 1 - \int_{t_i}^{\tau} |f(t)|^2 dt.$$

This expresses the condition that the photon emission rate given by $|f(\tau)|^2$ cannot be higher than κ times the probability that the photon has not been emitted before time τ . It also means that the photon wavefunction cannot fall off faster than $\exp(-\kappa\tau/2)$. If we are looking for a photon pulse which is symmetric in time and falls off as sharply as possible but no faster than $\exp(-\kappa\tau/2)$, a natural candidate may be a function proportional to $1/\cosh(\kappa\tau/2)$. We will set the initial time t_i to $-\infty$ and normalize the photon wavefunction to satisfy $\int_{-\infty}^{+\infty} |f(\tau)|^2 d\tau = 1$. The resulting expression for $f(\tau)$ is

$$f(\tau) = \frac{\sqrt{\kappa}}{2 \cosh(\kappa\tau/2)}.$$

Using eq. (E.7), we then get

$$\langle \varphi_e | \bar{\psi}(\tau) \rangle = \frac{1}{\sqrt{1 + \exp(-\kappa\tau)}}. \quad (\text{E.8})$$

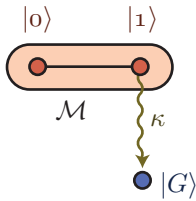


Figure E.1: Photon shaping scheme with a two-level system.

In general, finding a Hamiltonian resulting in a given evolution of the probability amplitude $\langle \varphi_e | \psi(\tau) \rangle$ is a very difficult task. However, it becomes more tractable in certain special cases – for example when the subspace \mathcal{M} is only two-dimensional, as illustrated in Fig. E.1. The emitting state $|\varphi_e\rangle$ in this particular example is $|1\rangle$.

We will assume that the two states $|0\rangle$ and $|1\rangle$ are resonant with each other. The non-Hermitian Hamiltonian describing this system is $\hat{H}(t) - i\kappa|1\rangle\langle 1|/2$, where

$$\hat{H}(t) = i\tilde{g}(t)(|0\rangle\langle 1| - |1\rangle\langle 0|).$$

If we parametrize the normalized state vector $|\bar{\psi}(t)\rangle$ as

$$|\bar{\psi}(t)\rangle = \cos\frac{\theta(t)}{2}|0\rangle + \sin\frac{\theta(t)}{2}|1\rangle$$

and substitute this form into the evolution equation eq. (E.3), we arrive at the following equation for $\theta(t)$:

$$\dot{\theta}(t) = 2\tilde{g}(t) - \frac{1}{2}\kappa\sin\theta(t). \quad (\text{E.9})$$

Using eq. (E.7), we can express $\sin(\theta(t)/2) = \langle 1 | \bar{\psi}(t) \rangle$ in terms of the desired photon wavefunction $f(t)$. This then allows us to solve eq. (E.9) for $\tilde{g}(t)$. Note that since we have fixed the phase of the drive signal, the probability amplitude $\langle 1 | \bar{\psi}(t) \rangle$ and therefore also $f(t)$ are restricted to be purely real. To obtain $f(t)$ whose phase is not constant in time, we would need to vary the phase of the drive signal.

For the particular form of $\langle 1 | \bar{\psi}(t) \rangle$ given by eq. (E.8) which results in the $1/\cosh$ photon wavefunction, we have

$$\theta(t) = 2 \arcsin\left(\frac{1}{\sqrt{1 + \exp(-\kappa t)}}\right).$$

Substituting this into eq. (E.9) yields a simple expression for $\tilde{g}(t)$:

$$\tilde{g}(t) = \frac{\kappa}{2 \cosh\frac{\kappa t}{2}}.$$

This result can be generalized for photon shapes of the form

$$f(t) = \frac{\sqrt{\kappa_{\text{eff}}}}{2 \cosh(\kappa_{\text{eff}} t/2)}$$

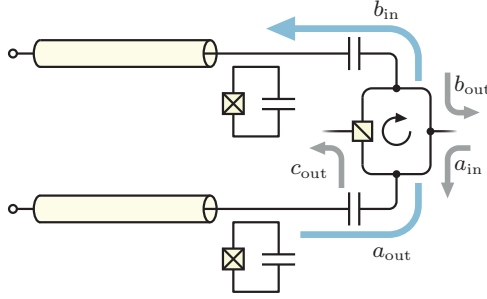


Figure E.2: Simplified diagram of the photon emission/reabsorption setup including losses in the connecting line, represented using a fictitious beamsplitter.

with $\kappa_{\text{eff}} \leq \kappa$. A derivation analogous to the one given above yields the form of the drive pulse

$$\tilde{g}(t) = \frac{\kappa_{\text{eff}}}{4 \cosh \frac{\kappa_{\text{eff}} t}{2}} \frac{1 - e^{\kappa_{\text{eff}} t} + (1 + e^{\kappa_{\text{eff}} t}) \kappa / \kappa_{\text{eff}}}{\sqrt{(1 + e^{\kappa_{\text{eff}} t}) \kappa / \kappa_{\text{eff}} - e^{\kappa_{\text{eff}} t}}}. \quad (\text{E.10})$$

E.2 Photon reabsorption

Here we consider a simple setup with two distant qubits as described in ch. 5 and illustrated in Fig. 5.1. We extend the diagram to explicitly model losses in the line connecting the two samples. This is done by including an beamsplitter which routes a small fraction $1 - \lambda^2$ of the signal power towards an imaginary port. The resulting diagram is shown in Fig. E.2. Based on this configuration, we will use input-output theory to eliminate the field propagating between the samples and derive an effective master equation of the cascaded system. A proposal to use a system of this type for quantum information transfer was presented in Cirac *et al.* (1997).

If we denote the fields incident on and reflected from the two subsystems as \hat{a}_{in} , \hat{b}_{in} , \hat{a}_{out} and \hat{b}_{out} and the resonator fields by \hat{a} and \hat{b} , the input-output relations become

$$\begin{aligned} \hat{a}_{\text{out}} &= \hat{a}_{\text{in}} + \sqrt{\kappa_a} \hat{a}, \\ \hat{b}_{\text{out}} &= \hat{b}_{\text{in}} + \sqrt{\kappa_b} \hat{b}, \end{aligned}$$

while the Heisenberg equations for \hat{a} and \hat{b} are

$$\begin{aligned} \frac{d}{dt} \hat{a} &= i[\hat{H}_a, \hat{a}] - \frac{\kappa_a}{2} \hat{a} - \sqrt{\kappa_a} \hat{a}_{\text{in}}, \\ \frac{d}{dt} \hat{b} &= i[\hat{H}_b, \hat{b}] - \frac{\kappa_b}{2} \hat{b} - \sqrt{\kappa_b} \hat{b}_{\text{in}}. \end{aligned}$$

In the cascaded system, the input of the second subsystem is directly given by the output of the first one. We only need to take into account the propagation delay Δt

and the losses represented by the transmission coefficient of the beamsplitter λ . The relation between \hat{b}_{in} and \hat{a}_{out} is then

$$\hat{b}_{\text{in}}(t) = \lambda \hat{a}_{\text{out}}(t - \Delta t).$$

Since the two subsystems are connected only by the propagating field, we can simply shift the time scale for the second system by Δt and effectively eliminate the propagation delay. In other words, we can effectively treat the system as if there were no propagation delay but in reality delay any drive pulses on the second system by Δt . With this convention and assuming the input at the first system is in the vacuum state, the Heisenberg equations become

$$\begin{aligned} \frac{d}{dt} \hat{a} &= i[\hat{H}_a, \hat{a}] - \frac{\kappa_a}{2} \hat{a}, \\ \frac{d}{dt} \hat{b} &= i[\hat{H}_b, \hat{b}] - \frac{\kappa_b}{2} \hat{b} - \lambda \sqrt{\kappa_a \kappa_b} \hat{a}. \end{aligned}$$

The real output of the cascaded system at the third port of the circulator is given by

$$\hat{b}_{\text{out}} = \lambda(\sqrt{\kappa_a} \hat{a} + \hat{a}_{\text{in}}) + \sqrt{1 - \lambda^2} \hat{h} + \sqrt{\kappa_b} \hat{b},$$

where \hat{h} is the vacuum port of the beamsplitter. The fictitious output representing the loss in the line is

$$\hat{c}_{\text{out}} = \sqrt{1 - \lambda^2}(\sqrt{\kappa_a} \hat{a} + \hat{a}_{\text{in}}) - \lambda \hat{h}.$$

We will now look for a master equation of the cascaded system in the form

$$\frac{d}{dt} \hat{\rho} = -i[\hat{H}_a + \hat{H}_b + \hat{H}_c, \hat{\rho}] + \mathcal{D}_{\hat{b}_{\text{out}}}[\hat{\rho}] + \mathcal{D}_{\hat{c}_{\text{out}}}[\hat{\rho}], \quad (\text{E.11})$$

where \hat{H}_c is an effective interaction term which we need to determine. This master equation results in the following evolution equations for the expectation values of \hat{a} and \hat{b} :

$$\begin{aligned} \frac{d}{dt} \langle \hat{a} \rangle &= \langle i[\hat{H}_a, \hat{a}] + i[\hat{H}_c, \hat{a}] - [\hat{a}, \hat{b}_{\text{out}}^\dagger] \hat{b}_{\text{out}}/2 - [\hat{a}, \hat{c}_{\text{out}}^\dagger] \hat{c}_{\text{out}}/2 \rangle \\ &= \langle i[\hat{H}_a, \hat{a}] + i[\hat{H}_c, \hat{a}] - \lambda^2 \kappa_a \hat{a}/2 - \lambda \sqrt{\kappa_a \kappa_b} \hat{b}/2 - (1 - \lambda^2) \kappa_a \hat{a}/2 \rangle, \\ \frac{d}{dt} \langle \hat{b} \rangle &= \langle i[\hat{H}_b, \hat{b}] + i[\hat{H}_c, \hat{b}] - [\hat{b}, \hat{b}_{\text{out}}^\dagger] \hat{b}_{\text{out}}/2 - [\hat{b}, \hat{c}_{\text{out}}^\dagger] \hat{c}_{\text{out}}/2 \rangle \\ &= \langle i[\hat{H}_b, \hat{b}] + i[\hat{H}_c, \hat{b}] - \lambda \sqrt{\kappa_a \kappa_b} \hat{a}/2 - \kappa_b \hat{b}/2 \rangle. \end{aligned}$$

Here we have again used the assumptions that the incoming field \hat{a}_{in} as well as the fourth port of the beamsplitter \hat{h} are in the vacuum state. If we require these equations to be equivalent to the Heisenberg equations derived above, the interaction Hamiltonian needs to satisfy

$$\begin{aligned} i[\hat{H}_c, \hat{a}] - \frac{1}{2} \lambda \sqrt{\kappa_a \kappa_b} \hat{b} &= 0, \\ i[\hat{H}_c, \hat{b}] + \frac{1}{2} \lambda \sqrt{\kappa_a \kappa_b} \hat{a} &= 0. \end{aligned}$$

These equations are solved by the exchange interaction term

$$\hat{H}_c = \frac{i}{2} \lambda \sqrt{\kappa_a \kappa_b} (\hat{a}^\dagger \hat{b} - \hat{b}^\dagger \hat{a}).$$

Using this term in eq. (E.11) gives us the master equation describing the cascaded system. From its form, we can immediately see that if the photon exchange process is to be ideal, the system needs to stay in a pure state at all times and this state $|\Psi\rangle$ needs to satisfy $\hat{b}_{\text{out}}|\Psi\rangle = 0$ and $\hat{c}_{\text{out}}|\Psi\rangle = 0$. The second condition can be satisfied if either $\lambda = 1$ or $\hat{a}|\Psi\rangle = 0$. The latter case, however, corresponds to a situation where the resonator of the first system is never excited and therefore no photon exchange can take place. The line between the samples therefore needs to be lossless, that is, $\lambda = 1$.

E.3 Photon reabsorption simulations

For my simulation, I take the following parameters as given: transmon transition frequency ω_q between the ground and first excited state, transmon anharmonicity α , resonator frequency ω_r , the Jaynes-Cummings coupling strength g between $|e0\rangle$ and $|g1\rangle$, the resonator relaxation rate κ .

The simulation proceeds as follows:

1. Calculate E_J and E_C of the transmon from the given transition frequency ω_q and anharmonicity α . Write the transmon Hamiltonian in a truncated charge basis $\{|n\rangle\}_{|n|\leq N}$ where N is sufficiently large (in my simulations $N = 20$). Diagonalize to get the eigenenergies ω_j of the transmon computational states and truncate the computational basis to the lowest d_q states. Express the charge operator \hat{n} in the computational basis, then rescale it by the matrix element $n_{eg} \equiv \langle e|\hat{n}|g\rangle$ and neglect non-nearest-neighbor couplings, keeping only the matrix elements of the form $|k\rangle\langle k+1|$. The result $\hat{b} \equiv \sum_k |k\rangle\langle k+1| \langle k|\hat{n}|k+1\rangle / n_{eg}$ is the transmon analogue of a ladder operator. Then $\tilde{g}(\hat{b} + \hat{b}^\dagger)/2$ is the drive term and \tilde{g} the angular frequency of resonantly driven Rabi oscillations between $|g\rangle$ and $|e\rangle$.
2. Form the Jaynes-Cummings Hamiltonian \hat{H}_0 of the composite transmon-resonator system, given as a combination of the bare energy terms $\sum_j \omega_j |j\rangle\langle j| \otimes \mathbb{1}$, $\omega_r \mathbb{1} \otimes \hat{a}^\dagger \hat{a}$ and the coupling term $g(\hat{b} \otimes \hat{a}^\dagger + \hat{b}^\dagger \otimes \hat{a})$. Here \hat{a} is the annihilation operator of the resonator. Diagonalize it and identify dressed eigenstates $|ij\rangle$ corresponding to the bare eigenstates $|i\rangle \otimes |j\rangle$ of the uncoupled Hamiltonian. This is done simply by finding the dressed eigenstate with the maximum overlap with a given bare eigenstate.
3. Find the eigenenergy difference between $|f0\rangle$ and $|g1\rangle$. This is the drive frequency ω_d for the second-order $|f0\rangle \leftrightarrow |g1\rangle$ transition in the weak drive limit. Form the excitation number operator $\hat{N} \equiv \sum_j j |j\rangle\langle j| \otimes \mathbb{1} + \mathbb{1} \otimes \hat{a}^\dagger \hat{a}$ and subtract the term $\omega_d \hat{N}$ from the Hamiltonian to transform it into the rotating frame.

4. Define a driven Hamiltonian $\hat{H} \equiv \hat{H}_0 - \delta_d \hat{N} + \tilde{g}(\hat{b} + \hat{b}^\dagger) \otimes \mathbb{1}/2$, where δ_d is the detuning of the drive signal from the low-power transition frequency. Sample \tilde{g} in an interval $(0, \tilde{g}_{\max})$ in small steps $\Delta\tilde{g}$ and for each value find the detuning $\delta_d(\tilde{g})$ which yields the optimal time-averaged fidelity of Rabi oscillations between $|f0\rangle$ and $|g1\rangle$. As described in sec. D.2, this is done by evaluating

$$\operatorname{argmax}_{\delta_d} \max_{|\varphi_{i,j}\rangle \in S} (|\langle \varphi_i | \psi_+ \rangle|^2 + |\langle \varphi_j | \psi_- \rangle|^2),$$

where $|\psi_\pm\rangle = (|f0\rangle \pm |g1\rangle)/\sqrt{2}$ and S is the set of eigenvectors of \hat{H} . In each step also calculate the difference between the eigenenergies of the two eigenvectors which maximize $|\langle \varphi_i | \psi_+ \rangle|^2 + |\langle \varphi_j | \psi_- \rangle|^2$. This yields the transition rate $\tilde{g}(\tilde{g})$ between $|f0\rangle$ and $|g1\rangle$. Fit appropriate polynomials to the obtained discrete data points to get an analytical approximation of the functions $\delta_d(\tilde{g})$, $\tilde{g}(\tilde{g})$ and their inverse functions.

5. Define the resonator relaxation operator \hat{c} by selecting those matrix elements of \hat{a} in the dressed basis which do not change the dressed qubit state, that is,

$$\hat{c} \equiv \sum_{i,j} |ij\rangle \langle i, j+1| \frac{\langle ij | \hat{a} | i, j+1 \rangle}{\langle g0 | \hat{a} | g1 \rangle}.$$

In this step, we assume that the system is connected to the environment (the transmission line) by a suitable Purcell filter which suppresses relaxation at all frequencies except very close to the resonator. This is why matrix elements such as $|e0\rangle \langle f0|$ are not present even though $\langle e0 | \hat{a} | f0 \rangle \neq 0$. The suppression of these relaxation channels is important to achieve high fidelities of the photon emission/reabsorption process.

6. Construct the Liouvillian of the cascaded system. Its Hamiltonian part is given by

$$\hat{H}_1 \otimes \mathbb{1} + \mathbb{1} \otimes \hat{H}_2 - i\kappa(\hat{c} \otimes \hat{c}^\dagger - \hat{c}^\dagger \otimes \hat{c}),$$

where $\hat{H}_{1,2}$ are the transmon-resonator Hamiltonians of the individual systems. The dissipator is $\mathcal{D}_{\hat{c}}$, where

$$\hat{C} \equiv \sqrt{\kappa}(\mathbb{1} \otimes \hat{c} + \hat{c} \otimes \mathbb{1}).$$

7. Choose a finite time range $(0, t_{\max})$ and a drive pulse identical for both systems with an amplitude

$$\tilde{g}(t) = \frac{\kappa}{\cosh(\kappa(t - t_0)/2)},$$

where the center of the pulse t_0 is set to the center of the interval, i.e. $t_0 = t_{\max}/2$. Calculate the corresponding drive amplitude $\tilde{g}(\tilde{g}(t))$ and Stark shift $\delta_d(\tilde{g}(t))$ using the results obtained above. Solve the master equation of the composite system with the initial state $|f0g0\rangle$. Evaluate the population of the desired target state $|g0f0\rangle$ at $t = t_{\max}$ to estimate the efficiency of the emission/reabsorption process.

Appendix F

Derivation of CPW properties

F.1 Propagating modes

As mentioned in sec. 1.1, a coplanar waveguide supports a propagating TEM mode if the medium on both sides of the CPW plane has the same dielectric constant. If the dielectrics in the two regions are different, the TEM mode is only an approximation of the actual fields which becomes exact in the limit of zero frequency.

To see why this is the case and how the generic situation with two different dielectrics and non-zero frequency deviates from the TEM mode, we will find an approximate solution of Maxwell's equations for the fields \mathbf{E} and \mathbf{B} oscillating at a frequency ω . There are no free charges except at the interface between the two regions, hence both \mathbf{E} and \mathbf{B} are divergence-less in the interior of each region and can therefore be written as curls of certain vector potentials \mathbf{F} and \mathbf{A} . To simplify the form of the resulting wave equations, we use a trick (Harrington, 2001) where instead of simply defining $\mathbf{E} = \nabla \times \mathbf{F}$ and $\mathbf{B} = \nabla \times \mathbf{A}$, we mix the two vector potentials in the following way:

$$\mathbf{E} = \nabla \times \left(\mathbf{F} + \frac{ic^2}{\omega} \nabla \times \mathbf{A} \right), \quad (\text{F.1})$$

$$\mathbf{B} = \nabla \times \left(\mathbf{A} - \frac{i}{\omega} \nabla \times \mathbf{F} \right). \quad (\text{F.2})$$

The Maxwell's equations $\nabla \cdot \mathbf{E} = 0$ and $\nabla \cdot \mathbf{B} = 0$ are now satisfied identically. After substituting into the remaining two Maxwell's equations $\nabla \times \mathbf{E} = i\omega\mathbf{B}$ and $\nabla \times \mathbf{B} = -i\omega\mathbf{E}/c^2$ and simplifying the expressions with the help of the identity $\nabla \times (\nabla \times \mathbf{X}) = \nabla(\nabla \cdot \mathbf{X}) - \nabla^2\mathbf{X}$, we find that \mathbf{E} and \mathbf{B} defined above in terms of \mathbf{F} and \mathbf{A} satisfy all four Maxwell's equations if

$$\begin{aligned} \left(\nabla^2 + \frac{\omega^2}{c^2} \right) \mathbf{F} &= 0, \\ \left(\nabla^2 + \frac{\omega^2}{c^2} \right) \mathbf{A} &= 0. \end{aligned}$$

Therefore, both vector potentials are solutions of the Helmholtz equation. Note that the double curl terms in eq. (F.1) and eq. (F.2) serve to eliminate the terms $\nabla(\nabla \cdot \mathbf{F})$ and $\nabla(\nabla \cdot \mathbf{A})$ from the Helmholtz equations where they would otherwise be present with the simple parametrization $\mathbf{E} = \nabla \times \mathbf{F}$ and $\mathbf{B} = \nabla \times \mathbf{A}$.

It can be shown (Harrington, 2001) that the solution to this problem can be written as a linear combination of a TE mode with an electric field perpendicular to the direction of propagation and a TM mode with a perpendicular magnetic field. These two modes result from choosing specific forms for \mathbf{F} and \mathbf{A} , namely $\mathbf{F} = \Psi \mathbf{e}_z$, $\mathbf{A} = 0$ for the TE mode and $\mathbf{F} = 0$, $\mathbf{A} = \Phi \mathbf{e}_z / c$ for the TM mode. Here \mathbf{e}_z is a unit vector along the z axis which we set to point in the direction of the CPW.

Thanks to the invariance of the problem under translations along z , we can write the potentials in the form $\Psi \exp(ikz)$ and $\Phi \exp(ikz)$, where we now take Ψ and Φ to be functions of only x and y . The resulting two-dimensional Helmholtz equations are

$$\begin{aligned} \left(\nabla^2 + \frac{\omega^2}{c^2} - k^2 \right) \Psi &= 0, \\ \left(\nabla^2 + \frac{\omega^2}{c^2} - k^2 \right) \Phi &= 0. \end{aligned}$$

Furthermore, the expressions for \mathbf{E} and \mathbf{B} (again, omitting the trivial dependence on z) now become

$$\mathbf{E} = (\nabla \times \mathbf{e}_z) \Psi - \frac{kc}{\omega} \nabla \Phi + \frac{ic}{\omega} \left(\frac{\omega^2}{c^2} - k^2 \right) \Phi \mathbf{e}_z, \quad (\text{F.3})$$

$$c\mathbf{B} = (\nabla \times \mathbf{e}_z) \Phi + \frac{kc}{\omega} \nabla \Psi - \frac{ic}{\omega} \left(\frac{\omega^2}{c^2} - k^2 \right) \Psi \mathbf{e}_z. \quad (\text{F.4})$$

So far, we have not made any approximations and these equations therefore describe the problem exactly. Let us now look at the special case mentioned above before proceeding with the general case.

CPW in a homogeneous dielectric

If the dielectric permittivity ε is the same in both regions then the propagation speed $c = 1/\sqrt{\varepsilon\mu}$ is constant in the whole space and the solution can be found in a greatly simplified form when $\omega^2/c^2 - k^2 = 0$ and $\Psi = 0$. In this case, the non-zero potential Φ has to satisfy the Laplace equation $\nabla^2 \Phi = 0$ and for $k > 0$ the fields are given by $\mathbf{E} = -\nabla \Phi$ and $c\mathbf{B} = \mathbf{e}_z \times \mathbf{E}$.

The fields are both perpendicular to the direction of propagation and to each other and they satisfy planar electro- and magnetostatic Maxwell's equations. A coplanar waveguide in a homogeneous dielectric therefore supports a propagating TEM mode with a linear dispersion relation $k = \pm\omega/c$.

CPW between two different dielectrics – static limit

If the dielectric constants on the two sides of the CPW plane are different then the wave number k , which needs to be the same in both regions, can no longer be chosen

to satisfy $\omega^2/c^2 - k^2$ everywhere. Consequently, the CPW does not support a TEM mode anymore and the problem becomes significantly more complicated. We will start our analysis of this more general situation by considering the static limit $\omega, k \rightarrow 0$. In this case, the Helmholtz equation again reduces to the Laplace equation.

In principle, we need to solve it in both regions separately and then impose boundary conditions at the interface. These require both components of \mathbf{B} , the in-plane component of \mathbf{E} and the normal component of $\mathbf{D} = \epsilon\mathbf{E}$ to be continuous across the interface of the dielectrics. At the surface of the conductors, the in-plane component of \mathbf{E} and the normal component of \mathbf{B} have to vanish. However, thanks to the symmetry of the geometry we are dealing with, the solution we got for the full space in the case of identical dielectric constants satisfies these boundary conditions automatically. Indeed, the mirror symmetry with respect to the plane $z = 0$ ensures that the normal component of \mathbf{E} vanishes at the interface. This takes care of the condition for \mathbf{D} . The other conditions are also satisfied because the fields \mathbf{E} and \mathbf{B} are continuous in the dielectric and fulfil the appropriate boundary conditions at the surface of the conductor.

Thus we see that even in the case of different dielectric constants in both regions, the fields in the zero frequency limit are the same as for the TEM propagating mode in a CPW with equal dielectric constants – they are given by $\mathbf{E} = -\nabla\Phi$ and $c\mathbf{B} = \mathbf{e}_z \times \mathbf{E}$. The last equation should make a cautious reader wary. What does c mean here? There are two different values of the propagation speed in the two dielectrics, c_1 and c_2 . Which one belongs in the expression for \mathbf{B} ?

To answer this question, let us denote the unknown proportionality constant between \mathbf{B} and $\mathbf{e}_z \times \mathbf{E}$ by c_{eff} . We will first determine how the potentials $\Psi_{1,2}$ and $\Phi_{1,2}$ in the two regions need to be chosen to get the fields $\mathbf{E} = -\nabla\Phi$ and $c_{\text{eff}}\mathbf{B} = \mathbf{e}_z \times \mathbf{E}$. Even though it may seem tempting to choose them to be $\Phi_1 = \Phi_2 = \Phi$ and $\Psi_1 = \Psi_2 = 0$, a single look at eq. (F.3) and eq. (F.4) shows us that this would result in discontinuous \mathbf{E} and \mathbf{B} . In fact, the correct way is to set $\Phi_1 = \Phi_2 = 0$ and leave $\Psi_{1,2}$ non-zero because then the expressions for the fields resulting from eq. (F.3) and eq. (F.4) in the limit $\omega, k \rightarrow 0$ do not include the propagation speeds $c_{1,2}$.

The fields in the two regions are then given by

$$\mathbf{E}_{1,2} = (\nabla \times \mathbf{e}_z)\Psi_{1,2}, \quad (\text{F.5})$$

$$c_{\text{eff}}\mathbf{B}_{1,2} = \nabla\Psi_{1,2}, \quad (\text{F.6})$$

where c_{eff} is the limit of ω/k for $\omega \rightarrow 0$. To determine $\Psi_{1,2}$, we express the magnetic field in one of the regions as $\mathbf{B}_1 = -\mathbf{e}_z \times \nabla\Phi/c_{\text{eff}}$ and calculate Ψ_1 by integrating eq. (F.5):

$$\Psi_1(x, y) = \int_{C(x,y)} (\mathbf{e}_z \times \nabla\Phi) \cdot d\mathbf{r}, \quad (\text{F.7})$$

where $C(x, y)$ is a curve from infinity to the point (x, y) . The choice of Ψ_2 is then determined by the symmetry of the fields under rotation by π around the origin, namely $\mathbf{B}_2(x, y) = -\mathbf{B}_1(-x, -y)$. This is satisfied if we define

$$\Psi_2(x, y) = \Psi_1(-x, -y). \quad (\text{F.8})$$

Note that Ψ cannot be defined globally because unlike each of the two half-planes, the full space is not simply-connected and therefore the integral of eq. (F.5) will in general depend on the chosen integration path.

As seen from eq. (F.5) and eq. (F.6), the fields are related by $c_{\text{eff}}\mathbf{B} = \mathbf{e}_z \times \mathbf{E}$. While in the case of the propagating TEM mode, the proportionality constant relating \mathbf{B} to \mathbf{E} was simply the propagation speed c , the constant c_{eff} in our current solution seems to be arbitrary. This is a direct consequence of the limit $\omega \rightarrow 0$. In the static case, the electric and the magnetic field are independent of each other. We can have a purely electrostatic field without any currents to induce a magnetic field and vice versa. In our derivation, this is reflected by the fact that we satisfied the condition $\omega^2/c^2 - k^2 = 0$ by taking the limit $\omega, k \rightarrow 0$ rather than by imposing a relation between ω and k and therefore the limit $c_{\text{eff}} = \lim_{\omega \rightarrow 0} \omega/k$ can be chosen arbitrarily.

CPW between two different dielectrics – non-zero frequency

The electric and the magnetic field are truly independent only if the frequency is exactly zero. For any non-zero frequency, the fields will propagate along the waveguide with a well-defined phase velocity $\omega/k = c_{\text{eff}}$, which we will now calculate in the limit of low frequency.

Let us start by clarifying what exactly we mean by saying that the frequency is low. If we choose a length-scale a which characterizes the transverse dimensions of the CPW (imagine a to be for example the width of the center conductor), we can express the frequency, the wave number and the nabla operator in terms of their dimensionless counterparts $\bar{\omega}$ and $\bar{\nabla}$ defined as $\omega = \bar{\omega}c_{\text{eff}}/a$, $k = \bar{\omega}/a$ and $\nabla = \bar{\nabla}/a$. The Helmholtz equations then become

$$\begin{aligned}\bar{\nabla}^2\Psi + \bar{\omega}^2\left(\frac{c_{\text{eff}}^2}{c^2} - 1\right)\Psi &= 0, \\ \bar{\nabla}^2\Phi + \bar{\omega}^2\left(\frac{c_{\text{eff}}^2}{c^2} - 1\right)\Phi &= 0\end{aligned}$$

and the fields can be expressed as

$$a\mathbf{E} = (\bar{\nabla} \times \mathbf{e}_z)\Psi - \frac{c}{c_{\text{eff}}}\bar{\nabla}\Phi + i\bar{\omega}\frac{c}{c_{\text{eff}}}\left(\frac{c_{\text{eff}}^2}{c^2} - 1\right)\Phi\mathbf{e}_z, \quad (\text{F.9})$$

$$ac\mathbf{B} = (\bar{\nabla} \times \mathbf{e}_z)\Phi + \frac{c}{c_{\text{eff}}}\bar{\nabla}\Psi - i\bar{\omega}\frac{c}{c_{\text{eff}}}\left(\frac{c_{\text{eff}}^2}{c^2} - 1\right)\Psi\mathbf{e}_z. \quad (\text{F.10})$$

This form of the equations lends itself to an expansion of the fields as a Taylor series in a small parameter $\bar{\omega}$. This expansion will be a good approximation of the full solution if $\bar{\omega} \ll 1$. Looking back at the definition of $\bar{\omega}$, this is equivalent to $a \ll c_{\text{eff}}/\omega$, that is, the wavelength of the propagating wave needs to be much larger than the transverse dimensions of the CPW. This condition is satisfied in our systems because the wavelength at the used microwave frequencies is of the order of 10 mm while the width of the waveguides is only 20 μm .

To get the static limit, we truncated the Taylor series at zeroth order. Now we need to go one order further. The $\bar{\omega}^2$ term in the Helmholtz equations tells us that corrections to the Laplace equation solutions for the potentials which we got in the static case will be of second order in $\bar{\omega}$. Therefore, to get a first-order expansion of the fields, we can substitute the static potentials Ψ and Φ into eq. (F.9) and eq. (F.10).

As we have already established, the resulting x - and y -components of \mathbf{E} and \mathbf{B} satisfy the boundary conditions. We only need to make sure that the z -components do as well. Since $\Phi = 0$, the electric field boundary condition is fulfilled identically. The one remaining condition is for the z -component of the \mathbf{B} field to be continuous across the boundary, that is,

$$-i\bar{\omega} \frac{1}{ac_{\text{eff}}} \left(\frac{c_{\text{eff}}^2}{c_1^2} - 1 \right) \Psi_1 = -i\bar{\omega} \frac{1}{ac_{\text{eff}}} \left(\frac{c_{\text{eff}}^2}{c_2^2} - 1 \right) \Psi_2.$$

Thanks to the mirror symmetry with respect to the plane $x = 0$, the potential Φ for the homogeneous dielectric case satisfies $\Phi(x, y) = \Phi(-x, y)$ and therefore, according to the definition of Ψ_1 in eq. (F.7), $\Psi_1(x, y) = -\Psi_1(-x, y)$. Since Ψ_1 and Ψ_2 are related by eq. (F.8), we get

$$\Psi_1(x, y) = -\Psi_2(x, -y).$$

Hence, at the interface $y = 0$ the potentials Ψ_1 and Ψ_2 satisfy $\Psi_1 = -\Psi_2$. Using this relation, the boundary condition then gives us an equation relating the propagation speed $c_{1,2}$ in the two dielectrics to the propagation speed c_{eff} of a wave traveling along the waveguide:

$$\frac{1}{c_{\text{eff}}^2} = \frac{1}{2} \left(\frac{1}{c_1^2} + \frac{1}{c_2^2} \right).$$

If we define an effective permittivity ε_{eff} for the space around the CPW using the standard expression for propagation speed of electromagnetic waves $c_{\text{eff}} = 1/\sqrt{\varepsilon_{\text{eff}}\mu}$, it will be related to the permittivities $\varepsilon_{1,2}$ of the two dielectric media by

$$\varepsilon_{\text{eff}} = \frac{\varepsilon_1 + \varepsilon_2}{2}. \quad (\text{F.11})$$

The small z -component of the \mathbf{B} field is

$$B_{z1,2} = \pm \frac{i\omega}{2} \frac{c_1^2 - c_2^2}{c_1^2 c_2^2} \Psi_{1,2}.$$

F.2 Capacitance, inductance, impedance

We will now proceed to calculate the field distribution and several quantities characterizing the waveguide – its capacitance and inductance per unit length and its characteristic impedance. To do this, we first need to get the potential Φ for the case of the homogeneous dielectric by solving the two-dimensional Laplace equation $\nabla^2\Phi = 0$. The potential of the ground plane and the center conductor will be fixed to zero and Φ_0 , respectively. The solution domain Ω as well as the boundary conditions and the dimensions of the waveguide are illustrated in Fig. F.1(a).

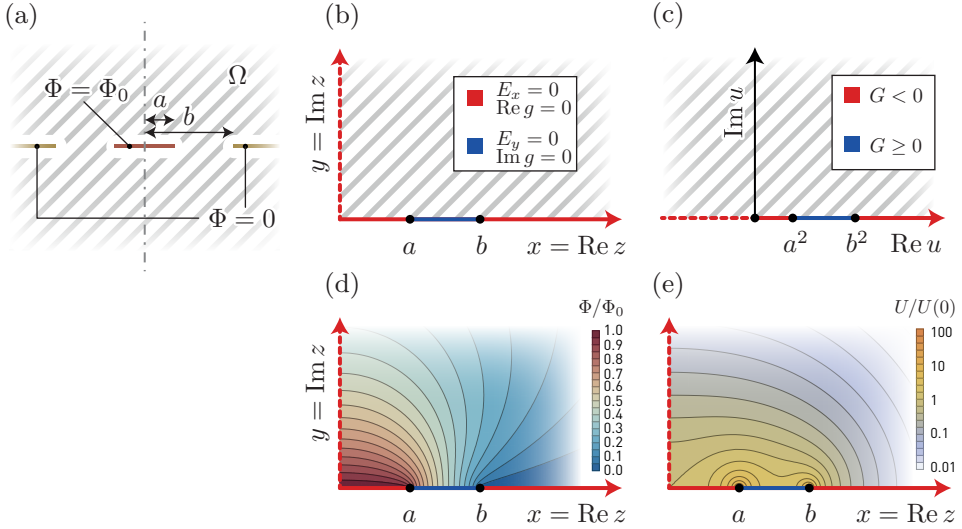


Figure F.1: (a) Solution domain Ω for the Laplace equation around a coplanar waveguide together with the boundary conditions: fixed potential $\Phi = 0$ on the ground plane marked in yellow and $\Phi = \Phi_0$ on the center conductor marked in red. The half-width of the center conductor is a and the distance between its center and the edge of the ground plane is b . (b) Boundary conditions for the electric field and its corresponding analytical function $g : \mathbb{C} \rightarrow \mathbb{C}$ in one quadrant of the full solution domain. (c) Boundary conditions for the function $G(u)$ defined as $g(z) = \sqrt{G(u)}$, where $u = z^2$. The positive imaginary axis in the z -plane, marked by the dashed line in (b), becomes the negative real axis in the u -plane, as indicated by the dashed line in (c). The original quadrant $\text{Re } z > 0, \text{Im } z > 0$ is mapped onto the half-plane $\text{Im } u > 0$. (d) Resulting potential Φ normalized to the center conductor potential Φ_0 for the specific choice of $b = 2a$ and (e) the corresponding electrostatic energy density $U \propto E_x^2 + E_y^2$ normalized to the value U_0 near the mid-point of the center conductor.

To find functions satisfying the Laplace equation in a two-dimensional space, one can use a very handy correspondence between them and analytical functions of a complex variable. Suppose we are given a function $f : \mathbb{C} \rightarrow \mathbb{C}$ which is analytical on a certain set $\Omega \subseteq \mathbb{C}$. Then its real part defines a scalar function $\Phi : \mathbb{R}^2 \rightarrow \mathbb{R}$ as

$$\Phi(x, y) = \operatorname{Re} f(x + iy).$$

Simple use of the chain rules then shows that the derivatives of Φ satisfy $\partial\Phi/\partial x = \operatorname{Re} f'$ and $\partial\Phi/\partial y = -\operatorname{Im} f'$. The second derivatives are $\partial^2\Phi/\partial x^2 = \operatorname{Re} f''$ and $\partial^2\Phi/\partial y^2 = -\operatorname{Re} f''$, hence the function Φ defined above automatically satisfies the Laplace equation.

If Φ is an electrostatic potential, the components of the corresponding electric field $\mathbf{E} = -\nabla\Phi$ are given in terms of the (likewise analytical) function $g(z) = f'(z)$.

$$E_x(x, y) = -\operatorname{Re} g(x + iy), \quad (\text{F.12})$$

$$E_y(x, y) = \operatorname{Im} g(x + iy). \quad (\text{F.13})$$

$$(\text{F.14})$$

We will make an educated guess about the form of the function g based on the boundary conditions and asymptotic behaviour of the electric field. To simplify the problem, we make use of the reflection symmetries with respect to the x - and y -axis and search for a solution only in a single quadrant of the full space Ω . The same symmetries also dictate that $E_x = 0$ on the y -axis and $E_y = 0$ on the section of the x -axis between the conductors. In addition, E_x also needs to vanish at the surface of the conductors. These boundary conditions and the corresponding conditions for the function g are shown in Fig. F.1(b).

A function satisfying these requirements could be found in the form $g = \sqrt{G}$ if the function G is analytical and real on the boundary of the quadrant. The conditions $\operatorname{Re} g = 0$ and $\operatorname{Im} g = 0$ on the sets marked in Fig. F.1(b) in red and blue will be fulfilled if G is negative or positive, respectively. Moreover, as the square root is not a holonomic function but has a cut (which we will define to be along the negative real axis), G should not take negative real values inside the quadrant.

The problem can be further simplified if we map the quadrant onto the upper complex half-plane by making a substitution $u = z^2$ and considering G as a function of u . The positive real and the positive imaginary axis in the z -plane become the positive real and the negative real axis, respectively, in the u -plane. The boundary conditions which need to be satisfied by $G(u)$ are shown in Fig. F.1(c). The function has to be real on the real axis. Specifically, it needs to be negative everywhere except in the interval $[a^2, b^2]$.

A very simple example of such a function would be for instance the polynomial $G(u) = (u - a^2)(b^2 - u)$. We can be slightly more general and take any odd power of this polynomial, that is, $G(u) = (u - a^2)^k(b^2 - u)^k$. All of these functions satisfy the boundary conditions. However, we also need to impose the condition that G is not negative real in the interior of the half-plane. Let us consider the behaviour of G in the vicinity of the point a^2 . We can parametrize u as $u = a^2 + \epsilon \exp(i\phi)$ where ϵ is small and ϕ takes values from 0 to π . We then approximate $G(u) \approx (b^2 - a^2)^k \epsilon^k \exp(i\phi k)$.

From here it immediately follows that if $|k| > 1$, we can always choose ϕ to make $G(u)$ negative real. The only exponents k for which $g = \sqrt{G}$ might not have a cut are $k = \pm 1$.

Since the electric field has to vanish far from the transmission line, we also need to exclude the option $k = 1$ which results in $|g|$ growing with increasing $|z|$. The remaining value of $k = -1$ yields a function $G(u)$ which correctly vanishes in the limit $|u| \rightarrow \infty$. Moreover, $G(u)$ can then be written as $(w^2 - (u - v)^2)^{-1}$, where $v = (a^2 + b^2)/2$ and $w = (b^2 - a^2)/2$. This means that $G(u)$ is real only if $u - v$ is real or purely imaginary. The first case is not possible for u in the upper half-plane and the second case gives $G(u) > 0$. This shows that the function $G(u) = 1/(u - a^2)(b^2 - u)$ satisfies all the required boundary conditions and its square root is an analytical function for $\text{Im } u > 0$. Going back to the original function g of z and taking into account that we can rescale the solution by an arbitrary constant A , we get

$$g(z) = \frac{A}{\sqrt{(z^2 - a^2)(b^2 - z^2)}}. \quad (\text{F.15})$$

This solution already allows us to calculate the electric field up to a scaling factor. If we want to proceed further and determine the potential or the capacitance of the CPW, we need to integrate $g(z)$ and obtain its primitive function $\phi(z)$ whose real part is the potential Φ . The integral can be expressed in terms of the *incomplete elliptic integral of the first kind* – a special function defined as the analytical continuation of (Abramowitz & Stegun, 1972)

$$F(\varphi|m) \equiv \int_0^{\sin \varphi} \frac{dt}{\sqrt{(1-t^2)(1-mt^2)}}.$$

The potential Φ is given by

$$\Phi(x, y) = \frac{A}{b} \text{Im } F \left(\arcsin \frac{x + iy}{a} \left| \frac{a^2}{b^2} \right. \right) + B. \quad (\text{F.16})$$

The integration constant B and the scaling factor A can be determined from the conditions that $\Phi = 0$ at infinity and $\Phi = \Phi_0$ on the center conductor. Substituting $x = y = 0$ into eq. (F.16) gives $\Phi(0, 0) = B$ and therefore $B = \Phi_0$. The condition $\lim_{y \rightarrow \infty} \Phi(0, y) = 0$ then results in the equation $A \lim_{t \rightarrow \infty} \text{Im } F(it|a^2/b^2) = -\Phi_0 b$. Using the identity $F(i\varphi|m) = iF(\arctan \sinh \varphi|1-m)$, we can express A in terms of the *complete elliptic integral of the first kind*

$$K(m) \equiv F(\pi/2|m)$$

as $A = -\Phi_0 b / K(1 - a^2/b^2)$. The resulting form of eq. (F.16) is then

$$\frac{\Phi(x, y)}{\Phi_0} = 1 - \frac{1}{K(1 - a^2/b^2)} \text{Im } F \left(\arcsin \frac{x + iy}{a} \left| \frac{a^2}{b^2} \right. \right). \quad (\text{F.17})$$

The shape of this potential is illustrated in Fig. F.1(d) for the specific case $b = 2a$.

Now that we have determined how the scaling factor A in eq. (F.15) depends on the potential of the center conductor Φ_0 , we can use eq. (F.12) and eq. (F.13) to evaluate other quantities of interest. For instance, the energy density of the electric field $U = \varepsilon|\mathbf{E}|^2/2$ can be readily expressed as $U(x, y) = \varepsilon|g(x + iy)|^2/2$, that is,

$$U(x, y) = \frac{\varepsilon\Phi_0^2 b^2}{2K^2(1 - a^2/b^2)} \frac{1}{|(x + iy)^2 - a^2| |(x + iy)^2 - b^2|}.$$

The shape of this energy distribution, again evaluated for the special case $b = 2a$, is displayed in Fig. F.1(e). It is interesting to note that this expression clearly diverges at the edges of the center conductor and the ground plane, for $y = 0$ and $x = \pm a, \pm b$. This indicates that the charges tend to accumulate at the edge, giving rise to a singular behaviour of the charge distribution.

We can easily calculate the surface charge density σ on the planar conductors using Gauss's law which relates it to the discontinuity in the normal component of the electrical displacement field \mathbf{D} :

$$\sigma(x) = \lim_{y \rightarrow 0^+} D_y(x, y) - \lim_{y \rightarrow 0^-} D_y(x, y).$$

Note that this expression involves \mathbf{D} instead of \mathbf{E} because we wish to calculate the density of the free charges residing on the conductors. If we replace \mathbf{D} in the previous formula by \mathbf{E} , we get the total charge density, including the polarization charges induced on the interface between the conductor and the dielectric. The displacement field can be expressed as $\mathbf{D} = \varepsilon\mathbf{E}$. Moreover, thanks to the symmetry of the problem, we have $E_y(x, -y) = -E_y(x, y)$. Therefore $\sigma(x) = (\varepsilon_1 + \varepsilon_2) \lim_{y \rightarrow 0^+} E_y(x, y)$, where ε_1 and ε_2 are the dielectric constants in the regions $y > 0$ and $y < 0$, respectively. Using eq. (F.13) and eq. (F.15), we get

$$\sigma(x) = -\frac{(\varepsilon_1 + \varepsilon_2)\Phi_0 b}{K(1 - a^2/b^2)} \text{Im} \lim_{y \rightarrow 0^+} \frac{1}{\sqrt{((x + iy)^2 - a^2)(b^2 - (x + iy)^2)}}.$$

For points between the center conductor and the ground plane, the limit is real and the charge density zero as expected. We will therefore further consider only the case of negative $(x^2 - a^2)(b^2 - x^2)$, corresponding to points lying at the conducting surface. To evaluate the limit, we expand the expression under the square root to first order in y which transforms it into the form $-\alpha + iy\beta$. Here $\alpha = (a^2 - x^2)(b^2 - x^2)$ is positive and since we are working in the quadrant $x, y > 0$, $\beta = 2x(a^2 + b^2 - 2x^2)$ is positive for $x < a$ and negative for $x > b$. The limit is therefore given by $\mp 1/\sqrt{\alpha}$ with a negative sign for points at the center conductor ($x < a$) and a positive sign for points at the ground plane ($x > b$). The resulting form of $\sigma(x)$ is

$$\sigma(x) = \frac{(\varepsilon_1 + \varepsilon_2)\Phi_0 b}{K(1 - a^2/b^2)} \frac{\text{sgn}(a + b - 2x)}{\sqrt{(a^2 - x^2)(b^2 - x^2)}}.$$

We will now calculate the charge per unit length dQ/dl on the center conductor by integrating the charge density. The result can be written in terms of the complete

elliptic integral of the first kind:

$$\frac{dQ}{dl} = 2 \int_0^a \sigma(x) dx = 4\varepsilon_{\text{eff}}\Phi_0 \frac{K(a^2/b^2)}{K(1-a^2/b^2)}.$$

Here we have used eq. (F.11) to replace the sum $\varepsilon_1 + \varepsilon_2$ by twice the effective dielectric constant ε_{eff} .

We can now write an expression for the capacitance of the CPW¹. It is defined as $C \equiv Q/V$, where V is the voltage between the center conductor and the ground plane – in this case equal to Φ_0 . The capacitance per unit length is then given by

$$\frac{dC}{dl} = 4\varepsilon_{\text{eff}} \frac{K(a^2/b^2)}{K(1-a^2/b^2)}. \quad (\text{F.18})$$

The solution we have obtained here also allows us to find the transverse components of the magnetic field using the relation $c_{\text{eff}}\mathbf{B} = \mathbf{e}_z \times \mathbf{E}$. It implies that the magnetic flux per unit length $d\phi/dl$ circulating around the center conductor is given by

$$\frac{d\phi}{dl} = \int_a^b B_y(x, 0) dx = \frac{1}{c_{\text{eff}}} \int_a^b E_x(x, 0) dx = \frac{1}{c_{\text{eff}}}\Phi_0.$$

Similarly, the current flowing in the center conductor is given by a curve integral of \mathbf{B} along a curve which encircles it. We can choose this curve to run at an infinitesimal distance ϵ along the surface of the center conductor, in which case the integral takes the form $\int_{-a}^a B_x(x, -\epsilon) dx + \int_a^{-a} B_x(x, +\epsilon) dx$.

Thanks to symmetry, we can write this as $-4 \int_0^a B_x(x, +\epsilon) dx$. Then, using the relations $B_x = -E_y/c_{\text{eff}}$ and $E_y(x, +\epsilon) = \sigma(x)/(\varepsilon_1 + \varepsilon_2)$, we find that the calculation of the current leads to the same type of integral as dQ/dl , yielding the final result

$$I = \frac{1}{\mu} \oint \mathbf{B} \cdot d\mathbf{r} = c_{\text{eff}} \frac{dQ}{dl}.$$

The inductance of the CPW is defined as $L \equiv \phi/I$ and its value per unit length is therefore

$$\frac{dL}{dl} = \frac{1}{c_{\text{eff}}^2} \left(\frac{dC}{dl} \right)^{-1}. \quad (\text{F.19})$$

¹It is worth pointing out that a completely analogous procedure can be carried out to find the field around an interdigital capacitor in the limit of infinite finger length and infinite number of fingers. The function $g(z)$ which provides this solution is $A/\sqrt{\cos(2\pi z/D) - \cos(\pi d/D)}$, where d is the width of the interdigital gap and D the distance between the centers of neighbouring fingers. It can be easily verified that this function satisfies the appropriate boundary conditions in each of the regions $B_k \equiv \{z \in \mathbb{C} | 0 \leq \text{Re } z - 2\pi k < 2\pi \wedge \text{Im } z \geq 0\}$ if the square root is defined to have a cut along the positive real axis. Flipping the sign of $g(z)$ in all odd-numbered B_k then provides the correct stitching across the region boundaries. Integration of the electric field components yields the potential difference and the charge, resulting in the expression for capacitance per finger per length $C/lN = \varepsilon_{\text{eff}}K(\cos^2(\pi d/2D))/K(\sin^2(\pi d/2D))$, equivalent to the expression given in Bahl (2003).

We can now also easily calculate the characteristic impedance of the CPW defined as $Z_0 \equiv V/I$. Substituting the relation $I = c_{\text{eff}}dQ/dl$ into this definition results in the equation

$$Z_0 = \frac{1}{c_{\text{eff}}} \left(\frac{dC}{dl} \right)^{-1}. \quad (\text{F.20})$$

These relations for the parameters of the CPW as well as for other waveguide geometries such as striplines can be found in a number of microwave engineering publications, for instance (Simons, 2001).

Anisotropic dielectric

The results derived in the previous section describe a waveguide between two isotropic dielectrics. However, the substrate commonly used to fabricate samples in the Qudev lab is sapphire – a crystalline form of aluminium oxide whose dielectric constant is anisotropic. The used sapphire wafers are cut perpendicularly to the principal axis which in our coordinate system is the y -axis. The corresponding component of the relative permittivity tensor is $\varepsilon_{ry} = 11.1$ while the in-plane components are $\varepsilon_{rx} = \varepsilon_{rz} = 8.9$.

The anisotropic Maxwell's equations are significantly more complicated but can still be solved in the zero frequency limit. The two-dimensional Laplace equation $\nabla^2\Phi = 0$ originating from Gauss's law $\nabla \cdot \varepsilon\mathbf{E}$ under the assumption of scalar ε now becomes

$$\varepsilon_x \frac{\partial^2 \Phi}{\partial x^2} + \varepsilon_y \frac{\partial^2 \Phi}{\partial y^2} = 0.$$

We can find its solution using simple coordinate transformation. We will keep the dimensions in the x directions unchanged to preserve the boundary conditions but rescale the y -coordinate by a factor of $\sqrt{\varepsilon_x/\varepsilon_y}$, defining

$$\tilde{\Phi}(x, y) = \Phi(x, y\sqrt{\varepsilon_x/\varepsilon_y}),$$

where Φ is the solution of the isotropic Laplace equation we found earlier. It is rather easy to show that the potential $\tilde{\Phi}$ defined in this way satisfies the anisotropic equation. The y -component of the electric field is rescaled as $\tilde{E}_y = E_y\sqrt{\varepsilon_x/\varepsilon_y}$ while the x -component remains unchanged. The boundary conditions at the dielectric interface and at the surface of the conductor are therefore still satisfied.

The normal component of the displacement field $\tilde{\mathbf{D}}$ is given by $D_y = \sqrt{\varepsilon_x\varepsilon_y}E_y$. Hence, the surface charge density at the conductor is the same as if the dielectric were homogeneous with a dielectric constant $\sqrt{\varepsilon_x\varepsilon_y}$ (equal to approximately $9.94\varepsilon_0$ for sapphire). Consequently, eq. (F.18) for the capacitance of the CPW remains valid if we modify eq. (F.11) defining the effective dielectric constant to

$$\varepsilon_{\text{eff}} = \frac{\sqrt{\varepsilon_{1x}\varepsilon_{1y}} + \sqrt{\varepsilon_{2x}\varepsilon_{2y}}}{2}.$$

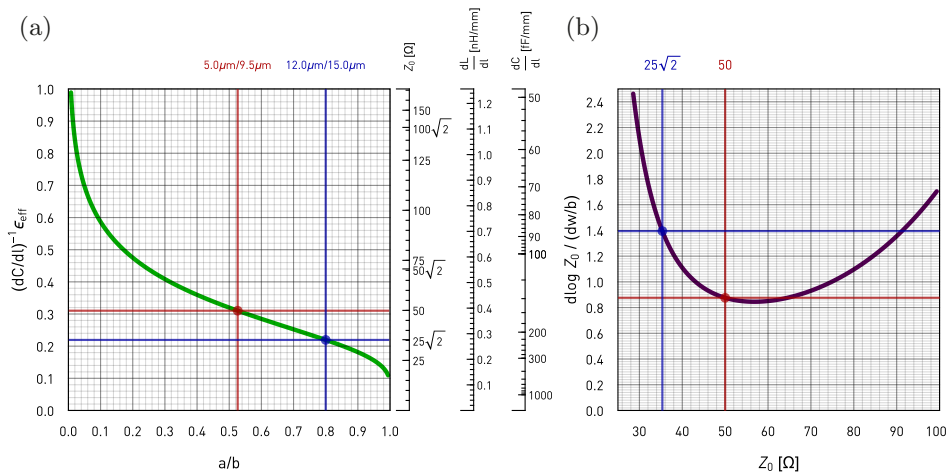


Figure F.2: (a) Dependence of the CPW parameters on the ratio of the dimensions a/b . The y -axis on the left shows the dimensionless quantity $(dC/dl)^{-1}\epsilon_{\text{eff}}$ which is independent of the used dielectrics. The axes on the right show the characteristic impedance, the inductance and the capacitance per unit length specifically for a CPW on sapphire ($\epsilon_{r,\text{eff}} \approx 5.47$). The points corresponding to the $50\ \Omega$ and the $25\sqrt{2}\ \Omega$ waveguide used in our samples are indicated in red and blue, respectively. (b) ...

Practical considerations

For our standard samples where the two media surrounding the waveguide are sapphire and vacuum, the effective dielectric constant is given by $\epsilon_{r,\text{eff}} = \epsilon_{\text{eff}}/\epsilon_0 \approx 5.47$.

The characteristic impedance of the waveguides is chosen to be $Z_0 = 50\ \Omega$ for compatibility with commercially available RF cables and components. The dependence of Z_0 on the ratio a/b is plotted in Fig. F.2(a). The impedance of $50\ \Omega$ is obtained for $a/b \approx 0.526$. In the actual chip designs, the two dimensions are chosen as $a = 5.0\ \mu\text{m}$ and $b = 9.5\ \mu\text{m}$, giving the correct ratio to three decimal places. To construct on-chip $\pi/2$ -hybrid couplers, we also use CPWs with a nominal characteristic impedance of $Z_0 = 25\sqrt{2}\ \Omega \approx 35.4\ \Omega$ as the design of the coupler requires two types of waveguides whose characteristic impedances are in a ratio $\sqrt{2} : 1$. The corresponding ratio of the waveguide dimensions is then $a/b \approx 0.800$. Specifically, in our designs we use $a = 12.0\ \mu\text{m}$ and $b = 15.0\ \mu\text{m}$, again resulting in the correct value to three decimal places. To avoid confusion, we will further refer to the stated dimensions of the $50\ \Omega$ and the $25\sqrt{2}\ \Omega$ waveguide as a_1, b_1 and a_2, b_2 , respectively.

Finally, let us point out that the choice of $a_1 = 5.0\ \mu\text{m}$, $b_1 = 9.5\ \mu\text{m}$, $a_2 = 12.0\ \mu\text{m}$ and $b_2 = 15.0\ \mu\text{m}$ is not entirely arbitrary. Obviously, the ratios a_1/b_1 and a_2/b_2 are fixed by the given characteristic impedances of $50\ \Omega$ and $50/\sqrt{2}\ \Omega$. Apart from this, however, the dimensions a_1, b_1 could be in principle chosen independently from a_2, b_2 .

In practice, when fabricating the waveguides by photolithography, imperfections in the exposure or etching process can lead to the amount of removed metal being slightly more or less than desired. This means that the width of the gap between the center conductor and the ground plane can differ by a small amount dw from the designed value. Assuming that this over- or underetching is symmetric, the dimensions b and a of the waveguide will change by $+dw/2$ and $-dw/2$, respectively. A simple calculation then tells us that the parameter a^2/b^2 which appears in eq. (F.18) changes by $-(a/b + 1)(a/b)dw/b$.

Using eq. (F.20), we can then express the relative change in the characteristic impedance $d \log Z_0$ as

$$\frac{d \log Z_0}{dw/b} = \frac{a}{b} \left(\frac{a}{b} + 1 \right) \left(\frac{K'(1 - a^2/b^2)}{K(1 - a^2/b^2)} + \frac{K'(a^2/b^2)}{K(a^2/b^2)} \right).$$

The expression on the right-hand side is plotted in Fig. F.2(b) as a function of the characteristic impedance Z_0 (again assuming the effective dielectric constant for a sapphire substrate $\varepsilon_{r,\text{eff}} = 5.47$). What does it tell us? For the two characteristic impedances of interest – 50Ω and $25\sqrt{2} \Omega$ – the plotted value is 0.876 and 1.395, respectively. Therefore, if the gap between the center conductor and the ground plane is symmetrically overetched by an amount dw , the relative change of the characteristic impedance dZ_0/Z_0 will be $0.876 \times dw/b_1$ for the 50Ω line and $1.395 \times dw/b_2$ for the $25\sqrt{2} \Omega$ line. Therefore, if the dimensions b_1 and b_2 are chosen in a ratio $0.876 : 1.395 \approx 0.628$, the relative changes of the two characteristic impedances will be identical to first order in dw , making the ratio $\sqrt{2} : 1$ between them significantly less sensitive to small imperfections in the etching process. The ratio between the chosen dimensions $b_1 = 9.5 \mu\text{m}$ and $b_2 = 15.0 \mu\text{m}$ is approximately 0.633 – rather close to the value of 0.628 which offers improved resilience against over- or underetching.

Appendix G

Qubit spectroscopy with a weak probe

In this appendix, I will show how to derive an analytical form for the measured signal in the continuous qubit spectroscopy measurement in two important limits – weak resonator drive and weak qubit drive. The measurement results can obviously be obtained numerically by solving for the steady state of the corresponding master equation. However, a suitable approximation of the measured spectrum by an analytical expression is useful for fitting the parameters of the system and gives a better insight into the influence of the different parameters on the measurement.

Let us start by considering a system governed by the master equation

$$\frac{d}{dt}\hat{\rho}(t) = \mathcal{L}[\hat{\rho}(t)],$$

where the Liouvillian superoperator \mathcal{L} generates the time evolution of the density matrix $\hat{\rho}(t)$. Suppose that \mathcal{L} can be split into a “free” part \mathcal{L}_0 and a small perturbation $\delta\mathcal{L}$. In our case, this perturbation will be the Hamiltonian term describing the weak drive of the resonator or the qubit. We will write the steady-state density matrix $\hat{\rho}$ of the system as a series of the form

$$\hat{\rho} = \hat{\rho}_0 + \hat{\rho}_1 + \hat{\rho}_2 + \dots,$$

where the terms on the right-hand side are of increasingly higher orders in the perturbation $\delta\mathcal{L}$. If $\hat{\rho}$ is to be constant in time, it has to satisfy the equation $\mathcal{L}[\hat{\rho}] = 0$. By expressing \mathcal{L} as $\mathcal{L}_0 + \delta\mathcal{L}$ and requiring this equation to hold order-by-order, we obtain the recurrence relations

$$\mathcal{L}_0\hat{\rho}_{i+1} + \delta\mathcal{L}\hat{\rho}_i = 0, \tag{G.1}$$

$$\mathcal{L}_0\hat{\rho}_0 = 0. \tag{G.2}$$

In other words, the zeroth order approximation $\hat{\rho}_0$ to the density matrix is simply the density matrix of the unperturbed system and the successive higher orders can be

formally expressed as $\hat{\rho}_{i+1} = -\mathcal{L}_0^{-1} \delta \mathcal{L}[\hat{\rho}_i]$. A more rigorous treatment of perturbation theory for open systems is given for example in Li *et al.* (2014). Of course, the most difficult step in a calculation of the perturbation series is finding the inverse \mathcal{L}_0^{-1} of the superoperator \mathcal{L}_0 .

The Liouvillian of a qubit coupled to a resonator in the dispersive limit, as discussed in sec. 1.6, is of the form

$$\begin{aligned} \mathcal{L} &= \mathcal{L}_r \otimes \text{Id} + \text{Id} \otimes \mathcal{L}_q + \mathcal{L}_{\text{int}}, \text{ where} \\ \mathcal{L}_r[\hat{\rho}] &= -i[\delta_r \hat{a}^\dagger \hat{a} + \varepsilon(\hat{a}^\dagger + \hat{a})/2, \hat{\rho}] + \kappa \mathcal{D}_{\hat{a}}[\hat{\rho}], \\ \mathcal{L}_q[\hat{\rho}] &= -i[\delta_q \hat{\sigma}_{ee} + \Omega \hat{\sigma}_x/2, \hat{\rho}] + \Gamma \mathcal{D}_{\hat{\sigma}_-}[\hat{\rho}] + \frac{\gamma}{2} \mathcal{D}_{\hat{\sigma}_z}[\hat{\rho}], \\ \mathcal{L}_{\text{int}}[\hat{\rho}] &= -i[2\chi \hat{a}^\dagger \hat{a} \otimes \hat{\sigma}_{ee}, \hat{\rho}]. \end{aligned}$$

Here the superoperators \mathcal{L}_r and \mathcal{L}_q describe the independent evolution of the resonator and the qubit, respectively, while \mathcal{L}_{int} represents their coupling. Since we are working in a reference frame rotating at the drive frequency, the coefficients of the free terms in the Hamiltonians are the detunings δ_r and δ_q of the resonator and the qubit from their respective drives. The drive strengths are given by the parameters ε and Ω . We assume that the coupling between the qubit and the resonator is dispersive where each additional photon in the resonator shifts the qubit transition frequency by an amount 2χ . The non-unitary terms generate energy relaxation in the resonator with a rate κ and in the qubit with a rate Γ . The qubit can in addition be subject to pure dephasing with a rate γ .

G.1 Weak resonator drive

In the limit of weak resonator drive, we can choose the drive term in \mathcal{L}_r proportional to ε to be $\delta \mathcal{L}$ and the rest of the Liouvillian to be \mathcal{L}_0 .

Since the resonator drive is absent from \mathcal{L}_0 , its corresponding steady-state density matrix will be of the form

$$\hat{\rho}_0 = |0\rangle\langle 0| \otimes \hat{\rho}_q, \quad (\text{G.3})$$

where, since the resonator is in its ground state, the qubit steady state is simply given by

$$\mathcal{L}_q[\hat{\rho}_q] = 0. \quad (\text{G.4})$$

To calculate the first order correction, we need to solve eq. (G.1). The second summand on its left-hand side is

$$\delta \mathcal{L}[\hat{\rho}_0] = -i\varepsilon[(\hat{a} + \hat{a}^\dagger) \otimes \mathbb{1}, |0\rangle\langle 0| \otimes \hat{\rho}_q]/2 = -i\varepsilon(|1\rangle\langle 0| - |0\rangle\langle 1|) \otimes \hat{\rho}_q/2$$

It can be shown that the result of the free Liouvillian \mathcal{L}_0 acting on an operator of the form $|1\rangle\langle 0| \otimes \dots$ is again an operator of the same form. The same of course holds for operators $|0\rangle\langle 1| \otimes \dots$. We can therefore expect the solution $\hat{\rho}_1$ to eq. (G.1) in the form

$$\hat{\rho}_1 = |1\rangle\langle 0| \otimes \delta \hat{\rho}_q + |0\rangle\langle 1| \otimes \delta \hat{\rho}_q^\dagger \quad (\text{G.5})$$

for some yet to be determined operator $\delta\hat{\rho}_q$. Substituting this Ansatz into eq. (G.1) then yields the following condition for $\delta\hat{\rho}_q$:

$$\mathcal{L}_q[\delta\hat{\rho}_q] - \left(i\delta_r + \frac{\kappa}{2}\right)\delta\hat{\rho}_q - 2i\chi\hat{\sigma}_{ee}\delta\hat{\rho}_q - i\varepsilon\hat{\rho}_q/2 = 0. \quad (\text{G.6})$$

The operators $\delta\hat{\rho}_q$ and $\hat{\rho}_q$ are elements of a 4-dimensional linear space whose basis can be chosen for example as $\{\mathbb{1}, \hat{\sigma}_x, \hat{\sigma}_y, \hat{\sigma}_z\}$. In this basis, we can represent $\delta\hat{\rho}_q$ and $\hat{\rho}_q$ in terms of \mathbb{R}^4 vectors $\delta\mathbf{v}$ and \mathbf{v} as

$$\begin{aligned} \delta\hat{\rho}_q &= \delta v_1 \mathbb{1} + \delta v_2 \hat{\sigma}_x + \delta v_3 \hat{\sigma}_y + \delta v_4 \hat{\sigma}_z, \\ \hat{\rho}_q &= v_1 \mathbb{1} + v_2 \hat{\sigma}_x + v_3 \hat{\sigma}_y + v_4 \hat{\sigma}_z. \end{aligned}$$

In this representation, the action of the superoperator \mathcal{L}_q is described by the matrix

$$\mathbf{L} \equiv \begin{pmatrix} 0 & 0 & 0 & 0 \\ 0 & -\Gamma/2 - \gamma & -\delta_q & 0 \\ 0 & \delta_q & -\Gamma/2 - \gamma & -\Omega \\ -\Gamma & 0 & \Omega & -\Gamma \end{pmatrix}.$$

Similarly, the left multiplication by $2\hat{\sigma}_{ee}$ which also appears in eq. (G.6) corresponds to the matrix

$$\mathbf{M} \equiv \begin{pmatrix} 1 & 0 & 0 & 1 \\ 0 & 1 & -i & 0 \\ 0 & i & 1 & 0 \\ 1 & 0 & 0 & 1 \end{pmatrix}.$$

We can therefore write eq. (G.6) in the matrix form as

$$\delta\mathbf{v} = \frac{i\varepsilon}{2} \left(\mathbf{L} - i\chi\mathbf{M} - i\delta_r - \frac{\kappa}{2} \right)^{-1} \cdot \mathbf{v}. \quad (\text{G.7})$$

The vector \mathbf{v} representing $\hat{\rho}_q$ is given by the matrix form of eq. (G.4), which is simply

$$\mathbf{M} \cdot \mathbf{v} = 0. \quad (\text{G.8})$$

The solution to this homogeneous equation is determined uniquely by the additional normalization condition $\text{Tr} \hat{\rho}_q = 1$, that is, $v_1 = 1/2$.

Now we have found the first-order correction to the steady-state density matrix which is given by the vector $\delta\mathbf{v}$. But how does it relate to the quantity that we actually want to calculate – the signal transmitted through the resonator? In the linear detection scheme used in most microwave setups including those in our lab, the measured voltage is proportional to the expectation value of the output field operator \hat{a}_{out} and therefore also to $\langle \hat{a} \rangle$. From eq. (G.5) we see that to first order, this expectation value is simply given by $\text{Tr} \delta\hat{\rho}_q$. In the vector representation, this trace is equal to $2\delta v_1$.

The exact expression for $\langle a \rangle$ is rather complicated and since it can be derived from eq. (G.8) and eq. (G.7) in a straightforward way, we will not show it explicitly. The

asymptotic forms it takes when some of the system's parameters are very large or very small become more tractable

In the absence of the dispersive shift, that is for $\chi = 0$, the qubit and the resonator are decoupled and the expectation value $\langle a \rangle$ reduces to

$$\langle a \rangle = -\frac{\varepsilon}{2\delta_r - i\kappa}.$$

However, this case is not very interesting because the presence of the qubit has no effect on the response of the resonator which behaves as a purely linear system.

Another instance in which $\langle a \rangle$ takes a particularly simple form is if the qubit is driven very strongly such that the drive amplitude Ω is much larger than all other energy scales such as Γ , κ , χ and so on. In this limit $\Omega \rightarrow \infty$ we obtain

$$\langle a \rangle = -\frac{\varepsilon}{2(\delta_r + \chi) - i\kappa}.$$

We see that the response function of the resonator has again a Lorentzian shape but its center is shifted by χ . This behavior can be understood as a result of averaging between the two states of the qubit. When the qubit is in the ground state, the resonance frequency of the resonator is ω_r whereas for the qubit in the excited state, it gets shifted to $\omega_r + 2\chi$. If the qubit drive is very strong, we can imagine the qubit quickly alternating between the ground and the excited state. Since the speed of this flipping is much higher than the response time of the resonator, it behaves effectively as a system with the mean resonance frequency $\omega_r + \chi$.

In the opposite limit of weak qubit drive and under the simplifying assumption that the pure dephasing rate of the qubit γ is zero, we get the following expression for $\langle a \rangle$:

$$\langle a \rangle = -\frac{\varepsilon}{2\delta_r - i\kappa} \left(1 - \frac{4(\Gamma + \kappa + i(\delta_q + \delta_r))\chi\Omega^2}{(2\delta_r - i\kappa)(\Gamma^2 + 4\delta_q^2)(\Gamma + \kappa + 2i(\delta_q + \delta_r + 2\chi))} \right)$$

Again, for $\chi = 0$ or $\Omega = 0$, we recover the simple Lorentzian response of the decoupled resonator. The same is true for large qubit-drive detunings δ_q . In a typical qubit spectroscopy measurement, we sweep the qubit-drive frequency ω_{qd} , or equivalently the detuning $\delta_q = \omega_q - \omega_{qd}$, while keeping all other parameters of the system fixed. In particular, the resonator is most often driven resonantly, that is, with $\delta_r = 0$. In this case, the measured signal relative to its asymptotic value $\langle a \rangle_\infty$ for $\delta_q \rightarrow \infty$ is given by

$$\frac{\langle a \rangle}{\langle a \rangle_\infty} = 1 - \frac{2\chi\Omega^2}{\kappa} \frac{\Gamma + \kappa + i\delta_q}{(4\delta_q^2 + \Gamma^2)(\delta_q + 2\chi - i(\Gamma + \kappa)/2)}. \quad (\text{G.9})$$

We can see that if χ is large compared with κ and Γ , the amplitude of the signal as a function of δ_q will have two dips. One at $\delta_q = 0$ with a width of approximately Γ , the other at $\delta_q = -2\chi$ with a width of the order $\Gamma + \kappa$. For smaller values of χ , the two dips merge into one. These different regimes are illustrated in Fig. G.1. This figure also shows that eq. (G.9) is no longer valid when the drive strength Ω is comparable with one of the other rates in the system, here specifically with Γ . In this

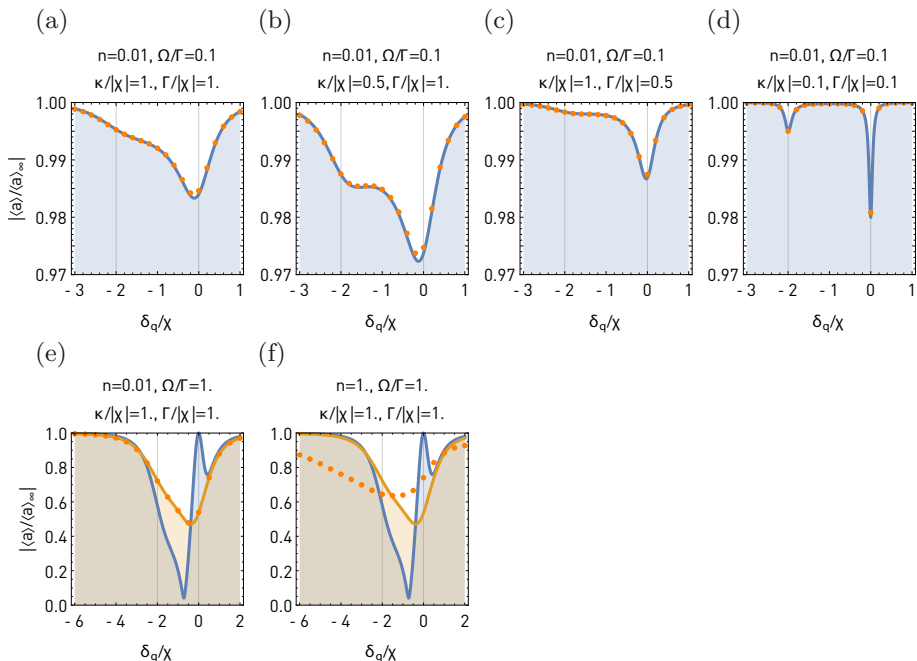


Figure G.1: Comparison of the results obtained using eq. (G.9) (blue lines) with numerical simulations (orange points) of the master equation including five Fock states of the resonator. The vertical lines indicate the positions of the zero-photon qubit resonance at $\delta_q = 0$ and the one-photon resonance at $\delta_q = -2\chi$. (a) Example of relatively high dissipation rates $\kappa/|\chi| = \Gamma/|\chi| = 1$, (b) lower resonator relaxation rate $\kappa/|\chi| = 0.5$, (c) lower qubit decay rate $\Gamma/|\chi| = 0.5$ and (d) $\kappa/|\chi| = \Gamma/|\chi| = 0.1$. (e) Breakdown of the low Ω approximation used to derive eq. (G.9). Eq. (G.7) (orange line) still matches the simulated resonator response but it fails (f) when the mean number of photons is increased, violating the low ε approximation.

case, we need to use the full result obtained directly from eq. (G.7). However, when the resonator drive strength ε is increased and the mean number of photons n rises, this approximation also fails.

G.2 Weak qubit drive

Let us now consider the limit of weak qubit drive. This case turns out to be slightly more complicated than the approximation of small ε analyzed above. As we have seen in eq. (G.9), the lowest-order correction in Ω is quadratic. This suggests that we will need to evaluate the perturbative series given by eq. (G.1) to second order. We will also see that inverting the free Liouvillian \mathcal{L}_0 is not as straightforward as in the small ε expansion because the Hilbert space of the resonator is infinite-dimensional.

We will choose as the perturbation $\delta\mathcal{L}$ the drive term in \mathcal{L}_r proportional to Ω . Again, the rest of the Liouvillian will be \mathcal{L}_0 . This superoperator acts on the qubit in a rather simple way. If we separate it into

$$\begin{aligned}\mathcal{L}_0 &= \tilde{\mathcal{L}}_0 + \text{Id} \otimes \tilde{\mathcal{D}}_{\hat{\sigma}_-}, \text{ where} \\ \tilde{\mathcal{D}}_{\hat{\sigma}_-}[\hat{X}] &= \Gamma\hat{\sigma}_-\hat{X}\hat{\sigma}_+, \end{aligned}$$

then the operator $\tilde{\mathcal{L}}_0[\hat{\rho}]$ is diagonal in the qubit basis $\{|g\rangle, |e\rangle\}$. That is, it acts as $\tilde{\mathcal{L}}_0[\hat{X} \otimes |i\rangle\langle j|] = \mathcal{L}_{ij}[\hat{X}] \otimes |i\rangle\langle j|$, where $i, j \in \{g, e\}$ and

$$\begin{aligned}\mathcal{L}_{gg}[\hat{X}] &= \mathcal{L}_r[\hat{X}], \\ \mathcal{L}_{ee}[\hat{X}] &= \mathcal{L}_r[\hat{X}] - 2i\chi[\hat{a}^\dagger\hat{a}, \hat{X}] - \Gamma\hat{X}, \\ \mathcal{L}_{eg}[\hat{X}] &= \mathcal{L}_r[\hat{X}] - (i\delta_q + \Gamma/2 + \gamma)\hat{X} - 2i\chi\hat{a}^\dagger\hat{a}\hat{X}, \\ \mathcal{L}_{ge}[\hat{X}] &= \mathcal{L}_r[\hat{X}] + (i\delta_q - \Gamma/2 - \gamma)\hat{X} + 2i\chi\hat{X}\hat{a}^\dagger\hat{a}. \end{aligned}$$

Moreover, note that $\tilde{\mathcal{L}}_0$ commutes with $\text{Id} \otimes \tilde{\mathcal{D}}_{\hat{\sigma}_-}$ and $\tilde{\mathcal{D}}_{\hat{\sigma}_-}^2 = 0$. Therefore, if we expand the inverse of \mathcal{L}_0 into a series

$$\mathcal{L}_0^{-1} = \tilde{\mathcal{L}}_0^{-1} - \tilde{\mathcal{L}}_0^{-1}(\text{Id} \otimes \tilde{\mathcal{D}}_{\hat{\sigma}_-})\tilde{\mathcal{L}}_0^{-1} + \tilde{\mathcal{L}}_0^{-1}(\text{Id} \otimes \tilde{\mathcal{D}}_{\hat{\sigma}_-})\tilde{\mathcal{L}}_0^{-1}(\text{Id} \otimes \tilde{\mathcal{D}}_{\hat{\sigma}_-})\tilde{\mathcal{L}}_0^{-1} + \dots,$$

then only the first two terms are non-zero. In addition, $\tilde{\mathcal{D}}_{\hat{\sigma}_-}$ only gives a non-zero result when acting on $|e\rangle\langle e|$. Hence, the inverse of \mathcal{L}_0 acts as

$$\begin{aligned}\mathcal{L}_0^{-1}[\hat{X} \otimes |i\rangle\langle j|] &= \mathcal{L}_{ij}^{-1}[\hat{X}] \otimes |i\rangle\langle j| \text{ for } |i\rangle\langle j| \neq |e\rangle\langle e| \text{ and} \\ \mathcal{L}_0^{-1}[\hat{X} \otimes |e\rangle\langle e|] &= \mathcal{L}_{ee}^{-1}[\hat{X}] \otimes |e\rangle\langle e| - \Gamma\mathcal{L}_{gg}^{-1}\mathcal{L}_{ee}^{-1}[\hat{X}] \otimes |g\rangle\langle g|. \end{aligned}$$

With these identities, we are now ready to start evaluating the perturbative series for the steady state $\hat{\rho}$. We are again using eq. (G.1) where $\hat{\rho}_0$ is the steady state of the system with $\Omega = 0$, which is a solution to $\mathcal{L}_0[\hat{\rho}_0] = 0$. When the qubit is not driven, the steady state is simply

$$\hat{\rho}_0 = |\alpha_0\rangle\langle\alpha_0| \otimes |g\rangle\langle g|,$$

where $|\alpha_0\rangle$ is a coherent state with a displacement $\alpha_0 = -\varepsilon/(2\delta_r - i\kappa)$ that can be found by solving the equation $\mathcal{L}_r[|\alpha_0\rangle\langle\alpha_0|] = 0$. Acting with the perturbation superoperator $\delta\mathcal{L}$ gives us $\delta\mathcal{L}[\hat{\rho}_0] = -i\Omega|\alpha_0\rangle\langle\alpha_0| \otimes (|e\rangle\langle g| - |g\rangle\langle e|)/2$ and therefore

$$\hat{\rho}_1 = -\mathcal{L}_0^{-1}\delta\mathcal{L}[\hat{\rho}_0] = \frac{i\Omega}{2}(\mathcal{L}_{eg}^{-1}[|\alpha_0\rangle\langle\alpha_0|] \otimes |e\rangle\langle g| - \mathcal{L}_{ge}^{-1}[|\alpha_0\rangle\langle\alpha_0|] \otimes |g\rangle\langle e|).$$

Now we can see why it is necessary to go to second order in Ω . The first order correction to the measured signal $\text{Tr} \hat{\rho}_1$ is zero because $\hat{\rho}_1$ only contains off-diagonal elements in the qubit Hilbert space.

Applying $\delta\mathcal{L}$ again yields

$$\delta\mathcal{L}[\hat{\rho}_1] = \frac{\Omega^2}{4}(\mathcal{L}_{eg}^{-1} + \mathcal{L}_{ge}^{-1})[|\alpha_0\rangle\langle\alpha_0|] \otimes (|g\rangle\langle g| - |e\rangle\langle e|)$$

and the second order correction is

$$\begin{aligned}\hat{\rho}_2 &= -\mathcal{L}_0^{-1}\delta\mathcal{L}[\hat{\rho}_1] = -\frac{\Omega^2}{4}\mathcal{L}_{gg}^{-1}(\text{Id} + \Gamma\mathcal{L}_{ee}^{-1})(\mathcal{L}_{eg}^{-1} + \mathcal{L}_{ge}^{-1})[|\alpha_0\rangle\langle\alpha_0|] \otimes |g\rangle\langle g| \\ &\quad + \frac{\Omega^2}{4}\mathcal{L}_{ee}^{-1}(\mathcal{L}_{eg}^{-1} + \mathcal{L}_{ge}^{-1})[|\alpha_0\rangle\langle\alpha_0|] \otimes |e\rangle\langle e|.\end{aligned}$$

The corresponding correction to the expectation value of \hat{a} is therefore

$$\text{Tr}\hat{a}\hat{\rho}_2 = \frac{\Omega^2}{4}\text{Tr}\hat{a}(\mathcal{L}_{ee}^{-1} - \mathcal{L}_{gg}^{-1}(\text{Id} + \Gamma\mathcal{L}_{ee}^{-1}))(\mathcal{L}_{eg}^{-1} + \mathcal{L}_{ge}^{-1})[|\alpha_0\rangle\langle\alpha_0|]. \quad (\text{G.10})$$

To simplify this expression further, we use a convenient property of the superoperators \mathcal{L}_{gg} and \mathcal{L}_{ee} , namely that $\text{Tr}\hat{a}\mathcal{L}_{ii}[\hat{X}]$ can be expressed as a function of $\text{Tr}\hat{a}\hat{X}$ and $\text{Tr}\hat{X}$. A simple calculation shows that indeed,

$$\begin{aligned}\text{Tr}\hat{a}\mathcal{L}_{gg}[\hat{X}] &= -(i\delta_r + \kappa/2)\text{Tr}\hat{a}\hat{X} - i\varepsilon\text{Tr}\hat{X}/2, \\ \text{Tr}\hat{a}\mathcal{L}_{ee}[\hat{X}] &= -(i(\delta_r + 2\chi) + \kappa/2 + \Gamma)\text{Tr}\hat{a}\hat{X} - i\varepsilon\text{Tr}\hat{X}/2.\end{aligned}$$

For clarity, we will now denote the expression $(\mathcal{L}_{eg}^{-1} + \mathcal{L}_{ge}^{-1})[|\alpha_0\rangle\langle\alpha_0|]$ by \hat{Y} and $(\text{Id} + \Gamma\mathcal{L}_{ee}^{-1})[\hat{Y}]$ by \hat{Z} . Substituting $\hat{X} = \mathcal{L}_{gg}^{-1}[\hat{Z}]$ into the expression for $\text{Tr}\hat{a}\mathcal{L}_{gg}[\hat{X}]$ and $\hat{X} = \mathcal{L}_{ee}^{-1}[\hat{Y}]$ into the expression for $\text{Tr}\hat{a}\mathcal{L}_{ee}[\hat{X}]$ gives

$$\text{Tr}\hat{a}\hat{Z} = -(i\delta_r + \kappa/2)\text{Tr}\hat{a}\mathcal{L}_{gg}^{-1}[\hat{Z}] - i\varepsilon\text{Tr}\mathcal{L}_{gg}^{-1}[\hat{Z}]/2, \quad (\text{G.11})$$

$$\text{Tr}\hat{a}\hat{Y} = -(i(\delta_r + 2\chi) + \kappa/2 + \Gamma)\text{Tr}\hat{a}\mathcal{L}_{ee}^{-1}[\hat{Y}] - i\varepsilon\text{Tr}\mathcal{L}_{ee}^{-1}[\hat{Y}]/2. \quad (\text{G.12})$$

We need to note at this point that since $\mathcal{L}_{gg}[|\alpha_0\rangle\langle\alpha_0|] = 0$, the superoperator \mathcal{L}_{gg} is singular and the value of $\text{Tr}\mathcal{L}_{gg}^{-1}[\hat{Z}]$ in eq. (G.11) is therefore not uniquely defined. However, the normalization condition $\text{Tr}\hat{\rho} = 0$ implies that all the corrections $\hat{\rho}_i$ for $i > 0$ need to be traceless which for $\hat{\rho}_2$ means

$$\text{Tr}(\mathcal{L}_{gg}^{-1}[\hat{Z}] - \mathcal{L}_{ee}^{-1}[\hat{Y}]) = 0.$$

Moreover, it follows directly from the definition of \mathcal{L}_{ee} that $\text{Tr}\mathcal{L}_{ee}[\hat{X}] = -\Gamma\text{Tr}\hat{X}$, hence $\text{Tr}\mathcal{L}_{ee}^{-1}[\hat{Y}] = -\text{Tr}\hat{Y}/\Gamma$. Eq. (G.11) and eq. (G.12) can then be written as

$$\text{Tr}\hat{a}\mathcal{L}_{gg}^{-1}[\hat{Z}] = -\frac{\text{Tr}\hat{a}\hat{Z} - i\varepsilon\text{Tr}\hat{Y}/2\Gamma}{i\delta_r + \kappa/2}, \quad (\text{G.13})$$

$$\text{Tr}\hat{a}\mathcal{L}_{ee}^{-1}[\hat{Y}] = -\frac{\text{Tr}\hat{a}\hat{Y} - i\varepsilon\text{Tr}\hat{Y}/2\Gamma}{i(\delta_r + 2\chi) + \kappa/2 + \Gamma}. \quad (\text{G.14})$$

To express the right-hand side of eq. (G.13) in terms of \hat{Y} , we substitute $\hat{Y} + \Gamma\mathcal{L}_{ee}^{-1}[\hat{Y}]$ for \hat{Z} and use eq. (G.14) to evaluate the resulting term $\text{Tr}\hat{a}\mathcal{L}_{ee}^{-1}[\hat{Y}]$. Then we

can calculate the trace on the right-hand side of eq. (G.10), which is equal to $\text{Tr} \hat{a}(\mathcal{L}_{ee}^{-1}[\hat{Y}] - \mathcal{L}_{gg}^{-1}[\hat{Z}])$, and obtain

$$\text{Tr} \hat{a} \hat{\rho}_2 = -\frac{\Omega^2}{4} \frac{2i\chi}{(\delta_r - i\kappa/2)(\delta_r + 2\chi - i\kappa/2 - i\Gamma)} \left(\text{Tr} \hat{a} \hat{Y} - \frac{i\varepsilon}{2\Gamma} \text{Tr} \hat{Y} \right). \quad (\text{G.15})$$

Compared with eq. (G.10), this expression for the second-order correction contains only first powers of the inverse operators \mathcal{L}_{ge}^{-1} and \mathcal{L}_{eg}^{-1} . The traces $\text{Tr} \hat{a} \hat{Y}$ and $\text{Tr} \hat{Y}$ cannot be calculated using a trick of the type we used to derive eq. (G.13) and eq. (G.14). The reason are the terms $\hat{a}^\dagger \hat{a} \hat{X}$ and $\hat{X} \hat{a}^\dagger \hat{a}$ in $\mathcal{L}_{eg}[\hat{X}]$ and $\mathcal{L}_{ge}[\hat{X}]$. Because of them, the traces $\text{Tr} \hat{a} \mathcal{L}_{ge}[\hat{X}]$ and $\text{Tr} \hat{a} \mathcal{L}_{eg}[\hat{X}]$ cannot be expressed solely in terms of $\text{Tr} \hat{a} \hat{X}$ and $\text{Tr} \hat{X}$.

Now we need to calculate $\hat{Y} = (\mathcal{L}_{ge}^{-1} + \mathcal{L}_{eg}^{-1})[|\alpha_0\rangle\langle\alpha_0|]$. How do we invert \mathcal{L}_{ge} and \mathcal{L}_{eg} ? Suppose we have a superoperator \mathcal{S} and an operator \hat{A} which satisfy $\lim_{t \rightarrow \infty} \exp(t\mathcal{S})[\hat{A}] = 0$. If the integral $-\int_0^\infty \exp(t\mathcal{S})[\hat{A}] dt$ exists and its value is \hat{B} then $\mathcal{S}[\hat{B}] = \hat{A}$. This identity can be very simply proven by applying \mathcal{S} to the integral and noting that $\mathcal{S} \exp(t\mathcal{S})[\hat{A}] = d \exp(t\mathcal{S})[\hat{A}] / dt$. If the assumptions about the asymptotic behaviour of $\exp(t\mathcal{S})[\hat{A}]$ and its integrability hold, we have

$$\mathcal{S}^{-1}[\hat{A}] = -\int_0^\infty \exp(t\mathcal{S})[\hat{A}] dt. \quad (\text{G.16})$$

The first step towards using this identity for calculating $\mathcal{L}_{ge}^{-1}[|\alpha_0\rangle\langle\alpha_0|]$ and $\mathcal{L}_{eg}^{-1}[|\alpha_0\rangle\langle\alpha_0|]$ is to calculate their exponentials acting on $|\alpha_0\rangle\langle\alpha_0|$. Let us define $\hat{\rho}_{ij}(t) \equiv \exp(t\mathcal{L}_{ij})[|\alpha_0\rangle\langle\alpha_0|]$. The superoperators \mathcal{L}_{ij} have the property that $(\mathcal{L}_{ij}[\hat{X}])^\dagger = \mathcal{L}_{ji}[\hat{X}^\dagger]$ which implies that $\hat{\rho}_{ij}(t) = (\hat{\rho}_{ji}(t))^\dagger$ and therefore we only need to calculate one of the operators $\hat{\rho}_{ge}$, $\hat{\rho}_{eg}$. It can be found by solving the differential equation

$$\frac{d}{dt} \hat{\rho}_{eg}(t) = \mathcal{L}_{eg}[\hat{\rho}_{eg}(t)] \quad \text{with} \quad (\text{G.17})$$

$$\hat{\rho}_{eg}(0) = |\alpha_0\rangle\langle\alpha_0|. \quad (\text{G.18})$$

Thanks to the special form of the superoperator \mathcal{L}_{eg} , the solution can be found using the Ansatz

$$\hat{\rho}_{eg}(t) = N(t) ||\alpha_L(t)\rangle\langle\alpha_R(t)||,$$

where $N(t)$, $\alpha_{L,R}(t)$ are functions to be found and $||\alpha\rangle$ is a rescaled coherent state defined as $||\alpha\rangle = \exp(|\alpha|^2/2)|\alpha\rangle = \sum_k \alpha^k |k\rangle / \sqrt{k!}$. Using this form rather than the normalized coherent state $|\alpha\rangle$ makes the expression for the time derivative of $\hat{\rho}_{eg}(t)$ particularly simple. It is easy to show that $d||\alpha\rangle = \hat{a}^\dagger ||\alpha\rangle d\alpha$ and therefore

$$\frac{d}{dt} \hat{\rho}_{eg}(t) = \frac{1}{N(t)} \frac{dN(t)}{dt} \hat{\rho}_{eg}(t) + \frac{d\alpha_L(t)}{dt} \hat{a}^\dagger \hat{\rho}_{eg}(t) + \left(\frac{d\alpha_R(t)}{dt} \right)^* \hat{\rho}_{eg}(t) \hat{a}.$$

Applying \mathcal{L}_{eg} to $\hat{\rho}_{eg}$ yields

$$\begin{aligned}\mathcal{L}_{eg}[\hat{\rho}_{eg}] = & (-i\varepsilon(\alpha_L - \alpha_R^*)/2 - i\delta_q - \Gamma/2 - \gamma + \kappa\alpha_L\alpha_R^*)\hat{\rho}_{eg} \\ & + (-i(\delta_r + 2\chi) + \kappa/2)\alpha_L - i\varepsilon/2)\hat{a}^\dagger\hat{\rho}_{eg} \\ & + ((i\delta_r - \kappa/2)\alpha_R^* + i\varepsilon/2)\hat{\rho}_{eg}\hat{a}.\end{aligned}$$

Equating the terms $\hat{\rho}_{eg}$, $\hat{a}^\dagger\hat{\rho}_{eg}$ and $\hat{\rho}_{eg}\hat{a}$ on both sides of eq. (G.17) separately then gives the following differential equations for $\alpha_{L,R}$:

$$\begin{aligned}\frac{d\alpha_L}{dt} &= -i(\delta_r + 2\chi) + \kappa/2)\alpha_L - i\varepsilon/2, \\ \frac{d\alpha_R}{dt} &= -i(\delta_r + \kappa/2)\alpha_R - i\varepsilon/2\end{aligned}$$

and for N :

$$\frac{1}{N(t)} \frac{dN(t)}{dt} = -i\varepsilon(\alpha_L - \alpha_R^*)/2 - i\delta_q - \Gamma/2 - \gamma + \kappa\alpha_L\alpha_R^*.$$

We can see that the displacement α_R satisfies the equation of motion of a decoupled resonator whose steady state is α_0 . Since it is equal to α_0 at $t = 0$, it does not vary with time. The equation for the remaining displacement α_L has the solution

$$\begin{aligned}\alpha_L &= \Delta_0 \exp(-\eta t) + \beta_0, \text{ where} & (G.19) \\ \beta_0 &= -\frac{\varepsilon}{2(\delta_r + 2\chi) - i\kappa}, \\ \Delta_0 &= \alpha_0 - \beta_0 \text{ and} \\ \eta &= i(\delta_r + 2\chi) + \kappa/2.\end{aligned}$$

Solving for N and simplifying the resulting expression then gives us

$$N(t) = \exp\left(2i\chi\alpha_0^*\beta_0(1 - \exp(-\eta t))/\eta - (i\delta_q + \Gamma/2 + \gamma + 2i\chi\alpha_0^*\beta_0)t - |\alpha_0|^2\right). \quad (G.20)$$

It is easy to verify that $\text{Re } 2i\chi\beta_0\alpha_0^* \geq 0$, hence $N(t)$ exponentially decays to zero for large t . In other words, we have verified that $\exp(t\mathcal{L}_{eg})[|\alpha_0\rangle\langle\alpha_0|]$ vanishes in the limit of $t \rightarrow \infty$ and is integrable. We can therefore use eq. (G.16) to calculate $\mathcal{L}_{eg}^{-1}[|\alpha_0\rangle\langle\alpha_0|]$ and $\mathcal{L}_{ge}^{-1}[|\alpha_0\rangle\langle\alpha_0|]$, getting

$$\begin{aligned}\mathcal{L}_{eg}^{-1}[|\alpha_0\rangle\langle\alpha_0|] &= -\int_0^\infty N(t)|\alpha_L(t)\rangle\langle\alpha_0| dt, \\ \mathcal{L}_{ge}^{-1}[|\alpha_0\rangle\langle\alpha_0|] &= -\int_0^\infty N^*(t)|\alpha_0\rangle\langle\alpha_L(t)| dt.\end{aligned}$$

However, we will not evaluate these operators explicitly because we only need to get the traces $\text{Tr } \hat{a}\hat{Y}$ and $\text{Tr } \hat{Y}$, not \hat{Y} itself. This will considerably simplify the calculation.

As a trace of the type $\text{Tr} ||x\rangle\langle y||$ is equal to $\exp(xy^*)$ and $\text{Tr} \hat{a} ||x\rangle\langle y||$ to $x \exp(xy^*)$, we can express $\text{Tr} \hat{a} \hat{Y}$ and $\text{Tr} \hat{Y}$ as

$$\begin{aligned}\text{Tr} \hat{a} \hat{Y} &= -(\beta_0 F(0) + \alpha_0 F^*(0) + \Delta_0 F(\eta)), \\ \text{Tr} \hat{Y} &= -2\text{Re} F(0), \text{ where} \\ F(u) &\equiv \int_0^\infty N(t) \exp(\alpha_0^* \alpha_L(t) - ut) dt.\end{aligned}$$

After substituting the explicit form of $\alpha_L(t)$ and $N(t)$ from eq. (G.19) and eq. (G.20), we write the integral $F(u)$ as

$$\begin{aligned}F(u) &= e^A \int_0^\infty \exp(-A \exp(-\eta t) - (B + u)t) dt, \text{ where} \\ A &= 4\chi^2 |\alpha_0|^2 / \eta^2, \\ B &= i\delta_q + \Gamma/2 + \gamma + 2i\chi\alpha_0^* \beta_0.\end{aligned}$$

Using a substitution $v = A \exp(-\eta t)$, this integral can be expressed in terms of the lower incomplete Gamma function G defined as

$$G(s, x) \equiv \int_0^x t^{s-1} e^{-t} dt.$$

The result is

$$F(u) = \frac{e^A}{\eta A^{(B+u)/\eta}} G((B+u)/\eta, A).$$

The Gamma function satisfies the recurrence relation $G(s+1, x) = sG(s, x) - x^s e^{-x}$ which allows us to express $F(\eta)$ in terms of $F(0)$. Furthermore, the Gamma function can be expressed as a series

$$G(s, x) = \sum_{k=0}^{\infty} \frac{(-1)^k}{k!} \frac{x^{s+k}}{s+k}.$$

This allows us to write the final form of the second-order correction to $\text{Tr} \hat{a} \hat{\rho}$ from eq. (G.15) as

$$\begin{aligned}\text{Tr} \hat{a} \hat{\rho}_2 &= \frac{\Omega^2}{4} \frac{1}{(\delta_r - i\kappa/2)(\delta_r + 2\chi - i\kappa/2 - i\Gamma)} \\ &\times \left[\left(-\frac{i\delta_q + \Gamma/2 + \gamma}{\alpha_0^*} + \frac{\chi\varepsilon}{\Gamma} \right) F(0) + \left(2i\chi\alpha_0 + \frac{\chi\varepsilon}{\Gamma} \right) F^*(0) + \frac{1}{\alpha_0^*} \right], \text{ where} \\ F(0) &= e^A \sum_{k=0}^{\infty} \frac{(-1)^k}{k!} \frac{A^k}{B + k\eta}.\end{aligned}\tag{G.21}$$

This rather complicated expression in principle allows us to calculate the signal to second order in Ω . However, it does not provide a lot of insight into the shape of the

resulting spectrum. We will further analyze its asymptotic form in the limit $\Gamma, \gamma \rightarrow 0$ and for the resonator drive frequency matching the resonance with the qubit in the ground state, that is, $\delta_r = 0$. In the limit of $\Gamma \rightarrow 0$, the only non-negligible terms in the previous expression will be those proportional to $\chi\varepsilon/\Gamma$.

$$\frac{\text{Tr } \hat{\alpha}\hat{\rho}_2}{\alpha_0} = -\frac{\Omega^2\chi}{\Gamma} \frac{1}{2\chi - i\kappa/2} \sum_{k=0}^{\infty} \frac{1}{k!} \text{Re} \frac{e^A(-A)^k}{i(\delta_q + 2k\chi + 2\chi|\beta_0|^2) + 8\chi^2|\beta_0|^2/\kappa + k\kappa/2}.$$

In typical qubit spectroscopy measurements, we analyze the amplitude of the signal which is proportional to $|\text{Tr } \hat{\alpha}\hat{\rho}|$ as a function of the qubit detuning δ_d . This can be approximated as

$$\frac{|\text{Tr } \hat{\alpha}\hat{\rho}|}{|\alpha_0|} = 1 - \frac{8\Omega^2\chi^2}{\Gamma(16\chi^2 + \kappa^2)} \sum_{k=0}^{\infty} \frac{1}{k!} \text{Re} \frac{e^A(-A)^k}{i(\delta_q + 2k\chi + 2\chi|\beta_0|^2) + 8\chi^2|\beta_0|^2/\kappa + k\kappa/2}. \quad (\text{G.22})$$

We will first note that in the limit $\chi \gg \kappa$ when the imaginary part of A can be neglected and we can approximate $A \approx -|\alpha_0|^2$, this further reduces to the simpler form

$$\frac{|\text{Tr } \hat{\alpha}\hat{\rho}|}{|\alpha_0|} = 1 - \frac{16\Omega^2}{2\Gamma} \sum_{k=0}^{\infty} \frac{e^{-\bar{n}}\bar{n}^{2k}}{k!} \frac{(k + \bar{n})\kappa}{4(\delta_q + 2k\chi + \kappa^2\bar{n}/8\chi)^2 + (k + \bar{n})^2\kappa^2}, \quad (\text{G.23})$$

where $\bar{n} = |\alpha_0|^2$ is the mean number of photons in the steady state if the qubit is in the ground state. Considered as a function of the qubit detuning δ_q , the signal approaches the steady state value α_0 for large δ_q . Its amplitude drops when δ_q is close to one of the frequencies $-2k\chi - \kappa^2\bar{n}/8\chi$.

These dips in the signal amplitude have a Lorentzian shape with widths (FWHM) of $(k + \bar{n})\kappa$ and amplitudes proportional to $p_k/(k + \bar{n})$, where $p_k = \exp(-\bar{n})\bar{n}^k/k!$ is the probability of finding k photons in the coherent state $|\alpha_0\rangle$. This phenomenon where the measured spectroscopy signal consists of multiple peaks is known as ‘‘number splitting’’. It arises from the dispersive shift of the qubit frequency which is proportional to the number of photons and takes values which are integer multiples of 2χ .

This kind of measurement is often used to calibrate the magnitude of the drive strength ε since the observed shape of the spectrum provides information about the photon number distribution and therefore, in turn, about α_0 and ε . For this, a sum of Lorentzian functions is fitted to the measured signal.

Note that, contrary to what one might naively expect, the amplitudes of the signal dips are not proportional directly to the photon number probabilities p_k but to the expressions $p_k/(k + \bar{n})$. To extract the photon number distribution, we should rather use the integrated areas of the fitted Lorentzian functions which are proportional to p_k . When using this approach, we need to beware – the simple correspondence between p_k and the dip areas is only valid in this special limit we have analyzed here. It is correct only when the qubit drive strength Ω is weak, qubit decoherence rates can be neglected and the dispersive shift χ is much larger than the resonator linewidth κ .

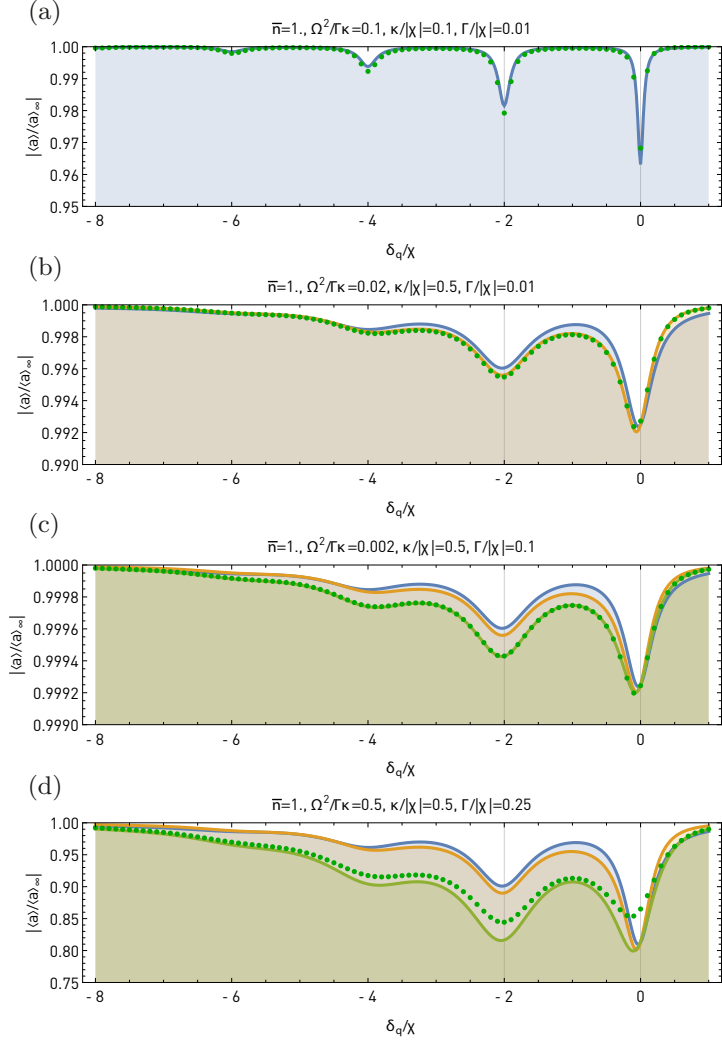


Figure G.2: Qubit spectroscopy curves obtained by numerical calculation of the steady state of the Liouvillian (green dots) compared with the various approximations derived in sec. G.2 – the low κ/χ approximation given by eq. (G.23) (blue line), the low Γ limit in eq. (G.22) (orange line) and the full second-order perturbative expansion in Ω given by eq. (G.21) (green line). Subplot (a) shows a regime in which even the crudest of the three approximations matches the numerical simulation. (b), (c) and (d) show regimes in which these approximations successively fail.

Appendix H

Theoretical considerations on dispersive read-out

H.1 Extraction of state populations from time traces

The following section presents an analysis of the procedure to obtain transmon state populations from averaged voltage traces measured in a pulsed dispersive read-out. It also shows how noise performance of the population estimation depends on filtering of the measured voltage traces.

The dependence of the averaged time trace on the state populations is given by

$$v(t) = a_g(t)p_g + a_e(t)p_e + \dots \quad (\text{H.1})$$

This equation is analogous to eq. (2.2) except v and a_g, a_e, a_f, \dots are now functions of time. We can also look at these functions as infinite-dimensional vectors. But even though the vector space Ω of all possible time traces is infinite-dimensional, if we assume that only a finite number n of transmon energy levels are occupied, the measured voltages $v(t)$ cannot be just any vectors. They are restricted to an $(n - 1)$ -dimensional plane P spanned by the eigenstate responses $a_g(t), a_e(t), \dots$ belonging to the occupied states. For example, if the only occupied states are $|g\rangle, |e\rangle$ and $|f\rangle$, all possible measurement outcomes $v(t)$ lie in the two-dimensional plane containing $a_g(t), a_e(t)$ and $a_f(t)$. Provided that the eigenstate responses a_g, a_e, \dots are known, finding the populations p_g, p_e, \dots is equivalent to a simple decomposition of a given vector v into a linear combination of n other vectors.

In practice, implementation of this seemingly simple prescription has its caveats. If the observed voltage trace $v(t)$ lies exactly in the plane, everything is simple. But in real life, measured voltage traces contain noise and $v(t)$ therefore does not have to lie exactly in P .

The decomposition of v into a linear combination of a_g, a_e, \dots is guaranteed to exist by definition for ideal measurement outcomes but we need to define a procedure to estimate the populations even for noisy voltage traces. For this, we need to map the whole space Ω onto P where the decomposition exists. We will look for a linear

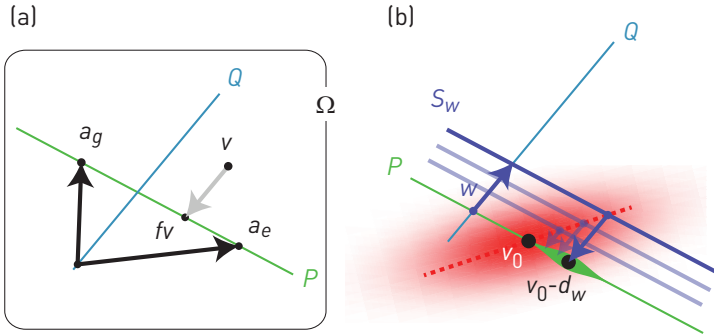


Figure H.1: (a) Simple illustration of the mapping from the space of voltage traces Ω to the $(n - 1)$ -dimensional plane P (shown in green; $n = 2$ in this particular example) spanned by the eigenstate traces a_g, a_e . The voltage trace, seen as a vector $v \in \Omega$, is displaced by a vector from the null space Q (in blue) chosen to bring it to P . (b) Mapping of a noisy signal $v = v_0 + \eta$ where v_0 is an ideal voltage trace from P and η is a Gaussian random vector. The probability density of v is indicated by the density plot in red. The purple lines represent the infinitesimal slices S_w of Ω obtained by shifting P by a vector w from the null space Q . The dashed red line indicates positions of the means of the probability distributions of v conditioned on $v \in S_w$. For one particular slice S_w , shown by the dark purple line, the resulting probability distribution of the projection $fv \in P$ is indicated by the varying thickness of the green line representing P . The mean of this distribution is given by $v_0 - d_w$ where d_w depends on w , resulting in an increased variance of the overall distribution of fv unless the red dashed locus of the conditional means is parallel to the null space Q , in which case $d_w = 0$ for all w .

map f from Ω to P which leaves P itself invariant. Note that any vector v can be decomposed into a sum of fv and $v - fv$ where the vector fv lies in P and $v - fv$ lies in the null space Q of f since $fv - f(v - fv) = 0$. Therefore, the direct sum $P \oplus Q$ covers the whole space Ω and the action of f on Ω is uniquely determined by specifying the null space. Indeed, for any vector $v \in \Omega$, we can find a unique decomposition into $v = u + w$ where $u \in P$ and $w \in Q$. Then $fv = fu + fw = u$. This means that we can view the action of f on Ω as an operation where a vector v from Ω is translated by some vector from the null space Q which brings it to P . This process is illustrated in Fig. H.1(a).

To see how the choice of the null space Q affects the noise properties of the estimated populations, let us start by assuming that the measured voltage trace v can be written as a sum $v_0 + \eta$ where v_0 is an ideal trace lying in P and η is the added noise which is a random vector in Ω . We will consider this noise to be Gaussian-distributed with a zero expectation value. The probability density Π of the random

variable $v = v_0 + \eta$ is then given by

$$\Pi(v) \propto \exp(-A(v - v_0, v - v_0)),$$

where A is a quadratic form characterizing the Gaussian distribution. An example of such a distribution is shown in Fig. H.1(b). To find the probability density for the projected vector fv , consider a decomposition of the full space Ω into infinitesimal slices parallel to the plane P , indicated in Fig. H.1(b) by the purple lines. One of these slices – let us call it S_0 – will contain the plane P itself and each other slice can be described as its image under translation by some vector w from the null space Q . We will call this shifted slice S_w . If the random vector v happens to lie in S_w , we have $v = fv + w$. The probability density of fv is therefore

$$\Pi(fv = v')|_{v \in S_w} \propto \exp(-A(v' + w - v_0, v' + w - v_0)).$$

This is again a Gaussian distribution. As the exponent has the same quadratic term $-A(v', v')$ for any w , this distribution has the same shape for all the slices but its center may be shifted depending on w , as illustrated graphically in Fig. H.1(b). Up to an additive constant, we can rewrite the term $A(v' + w - v_0, v' + w - v_0)$ in the exponential as $A(v' + d_w - v_0, v' + d_w - v_0)$, where d_w is a vector tangential to P chosen such that $A(x - y, d_w - w) = 0$ for any $x, y \in P$. The rewritten conditional probability density

$$\Pi(fv = v')|_{v \in S_w} \propto \exp(-A(v' + d_w - v_0, v' + d_w - v_0)).$$

can be interpreted as follows: If the random vector v lies in the slice S_w then it will be projected onto $v' = fv$ which is Gaussian-distributed with a mean $v_0 - d_w$. To get the final probability density of fv , we would need to integrate this conditional distribution over all the slices S_w . We will not carry out this calculation as the actual result is not of much interest to us. We would rather like to find the conditions under which the noise in the resulting fv is minimized. Since the probability distribution of fv is given by a weighted sum of Gaussian distributions with identical covariance matrices, it will always have variances at least as large as each of the constituent distributions. In fact, the optimal case is realized when the individual conditional probability distributions $\Pi(fv = v')|_{v \in S_w}$ all have the same mean. In the context of Fig. H.1(b), this would happen if the red dashed line, formed by the means of the conditional distributions, were parallel to the null space Q . This is satisfied if and only if $d_w = 0$ for every $w \in Q$. From the definition of d_w we see that this is equivalent to the requirement that $A(x - y, w) = 0$ for every $w \in Q$ and $x, y \in P$. In other words, if we define a scalar product as $x \cdot y = A(x, y)$, the optimal noise performance is achieved when the null space Q is perpendicular to P with respect to this scalar product. The projection operation T then becomes simply the orthogonal projection onto P .

To put this abstract result into perspective, let us investigate an example: Consider a stationary noise with a power spectral density $S(\omega)$. This means that its Fourier transform

$$h(\omega) = \frac{1}{\sqrt{2\pi}} \int e^{i\omega t} \eta(t) dt$$

satisfies $\langle h(\omega)h^*(\omega') \rangle = \delta(\omega - \omega')S(\omega)$. The corresponding probability density is therefore

$$\Pi(h) \propto \exp\left(-\int \frac{|h(\omega)|^2}{S(\omega)} d\omega\right)$$

and the associated scalar product is defined as $x \cdot y \equiv \int \tilde{x}^*(\omega)\tilde{y}(\omega)/S(\omega) d\omega$, where \tilde{x}, \tilde{y} are Fourier transforms of x, y . To project a voltage trace v onto P , one starts with a basis of the tangent space of P , for example $a_e - a_g, a_f - a_g, \dots$, and orthogonalizes it to find an orthonormal basis b_1, b_2, \dots . Then the projection fv is given by

$$fv = a_g + \sum_j b_j(b_j \cdot (v - a_g)).$$

In particular, if the plane P is only one-dimensional, as it is in the case when only two states of the transmon are populated, the sum contains only a single term and the equation becomes

$$fv = a_g + \frac{(a_e - a_g)((a_e - a_g) \cdot (v - a_g))}{(a_e - a_g) \cdot (a_e - a_g)}.$$

The populations are easily extracted in this case by comparison with the relation $v = p_g a_g + p_e a_e$:

$$p_e = \frac{(a_e - a_g) \cdot (v - a_g)}{(a_e - a_g) \cdot (a_e - a_g)}.$$

H.2 Resonator response in dispersive readout

In this section we show how an analytical expression can be derived for the time-dependent coherent response of a resonator during a pulsed dispersive readout.

In general, there is no simple analytical solution of the dynamics of a dispersively coupled system if both the qubit and the resonator are driven at the same time. Approximate solutions can be found in the steady state to lowest order in the qubit or resonator drive strengths, as we have seen in app. G. The dynamics can be also solved approximately using the so-called optical Bloch equations derived by Bianchetti *et al.* (2009).

As we will show in the following, if the qubit is not driven, the evolution of the system can be solved exactly. The dispersive coupling between the resonator and the transmon is described by eq. (1.17) and the Hamiltonian in question is given by

$$\hat{H} = \sum_i \delta_i \hat{P}_i \hat{a}^\dagger \hat{a} + \frac{1}{2} \varepsilon (\hat{a} + \hat{a}^\dagger),$$

where \hat{P}_i are projectors onto the qubit computational states and δ_i the corresponding detunings of the resonator frequency from its drive. Note that we have eliminated the qubit energy term by going into the interaction picture with respect to it. If the qubit is in one of the computational states, the evolution described by this Hamiltonian can

be found very easily. The qubit stays in the same state and the resonator evolves as if it were decoupled and driven with a detuning δ_i .

After adding resonator dissipation into the picture by including the Liouvillian term $\kappa\hat{a}\hat{\rho}\hat{a}^\dagger - \kappa\{\hat{a}^\dagger\hat{a}, \hat{\rho}\}$, we can still treat the resonator effectively as a decoupled dissipative linear oscillator with a qubit-state-dependent detuning.

To account for qubit relaxation, we will add a term \mathcal{L}_J to the Liouvillian which describes random jumps between the computational states. Its form is

$$\mathcal{L}_J[\hat{\rho}] = \sum_{i,j} \Gamma_{ij} \left(\hat{J}_{ij} \hat{\rho} \hat{J}_{ij}^\dagger - \frac{1}{2} \{ \hat{J}_{ij}^\dagger \hat{J}_{ij}, \hat{\rho} \} \right),$$

where $\hat{J}_{ij} = |i\rangle\langle j|$ describes a jump from the qubit computational state $|j\rangle$ to $|i\rangle$ and Γ_{ij} its corresponding transition rate. With the qubit transitioning between different computational states at random times and thus effectively changing the resonator detuning, solving the resonator state evolution becomes more complicated.

To find the solution, one can use for example the quantum trajectory approach (Gardiner & Zoller, 1991). Each of the individual realizations of the qubit's stochastic evolution gives a resonator detuning which is piecewise constant in time and therefore permits an analytical solution for the resonator state. One then needs to average over the different qubit state trajectories to obtain the expectation value of the resonator response. However, this method, when implemented in the naive way outlined here, turns out to be relatively cumbersome.

We will use a slightly different but ultimately equivalent approach. Let us consider the evolution equations for the expectation values $\langle \hat{P}_i \hat{a} \rangle$ and $\langle \hat{P}_i \rangle$. The latter is particularly easy to derive from the master equation and takes the form a classical rate equation described by the rates Γ_{ij} :

$$\frac{d}{dt} \langle \hat{P}_i \rangle = \sum_j \Gamma_{ij} \langle \hat{P}_j \rangle - \Gamma_{ji} \langle \hat{P}_i \rangle.$$

This result is not entirely unexpected since the relaxation of the qubit is not affected by its dispersive coupling to the resonator.

The derivation of $d\langle \hat{P}_i \hat{a} \rangle / dt$ is only marginally more complicated. As the projectors \hat{P}_i commute with \hat{a} , we will get rate equation terms analogous to those above but in addition, the Hamiltonian and the resonator dissipator from the master equation will result in terms corresponding to the evolution of $\langle \hat{a} \rangle$ for the particular computational qubit state $|i\rangle$:

$$\frac{d}{dt} \langle \hat{P}_i \hat{a} \rangle = - \left(i\delta_i + \frac{\kappa}{2} \right) \langle \hat{P}_i \hat{a} \rangle - \frac{i\varepsilon}{2} \langle \hat{P}_i \rangle + \sum_j \Gamma_{ij} \langle \hat{P}_j \hat{a} \rangle - \Gamma_{ji} \langle \hat{P}_i \hat{a} \rangle.$$

We now see that the differential equations for $\langle \hat{P}_i \hat{a} \rangle$ and $\langle \hat{P}_i \rangle$ form a closed system. This would not be the case in the presence of qubit drive and it is exactly this property which will allow us to write the solution in a simple closed form.

We will express all the relevant expectation values in the form of a single vector

$$\mathbf{v} = \begin{pmatrix} \langle \hat{P}_1 \hat{a} \rangle \\ \langle \hat{P}_2 \hat{a} \rangle \\ \vdots \\ \langle \hat{P}_1 \rangle \\ \langle \hat{P}_2 \rangle \\ \vdots \end{pmatrix}.$$

The matrix \mathbf{M} relating $d\mathbf{v}/dt$ to \mathbf{v} then has a block form

$$\mathbf{M} = \begin{pmatrix} \mathbf{D} + \mathbf{T} & -\frac{i\varepsilon}{2} \mathbb{1} \\ 0 & \mathbf{T} \end{pmatrix}, \text{ where}$$

$$\mathbf{D} = \text{diag}(-i\delta_1 + \kappa/2, -i\delta_2 + \kappa/2, \dots),$$

$$T_{ij} = \Gamma_{ij} - \delta_{ij} \sum_k \Gamma_{ki}.$$

To solve the equation $d\mathbf{v}/dt = \mathbf{M} \cdot \mathbf{v}$, we need to find the exponential of $t\mathbf{M}$. We first notice that the powers of \mathbf{M} can be written as

$$\mathbf{M}^n = \begin{pmatrix} (\mathbf{D} + \mathbf{T})^n & -\frac{i\varepsilon}{2} \sum_{j=0}^{n-1} (\mathbf{D} + \mathbf{T})^j \mathbf{T}^{n-1-j} \\ 0 & \mathbf{T}^n \end{pmatrix}.$$

This identity can be simply proven by induction. The expression for the right upper block can be evaluated by diagonalizing the matrices \mathbf{T} and $\mathbf{D} + \mathbf{T}$ as

$$\mathbf{T} = \sum_i \tau_i \mathbf{U} \mathbf{P}_i \mathbf{U}^{-1},$$

$$\mathbf{D} + \mathbf{T} = \sum_i \tilde{\tau}_i \tilde{\mathbf{U}} \tilde{\mathbf{P}}_i \tilde{\mathbf{U}}^{-1},$$

where τ_i and $\tilde{\tau}_i$ are the eigenvalues of \mathbf{T} and $\mathbf{D} + \mathbf{T}$, respectively, and \mathbf{P}_i are diagonal matrices with zeros everywhere except for a one in the i -th diagonal element. The term $(\mathbf{D} + \mathbf{T})^j \mathbf{T}^{n-1-j}$ can now be written as $\sum_{k,l} \tau_k^{n-1-j} \tilde{\tau}_l^j \tilde{\mathbf{U}} \tilde{\mathbf{P}}_l \tilde{\mathbf{U}}^{-1} \mathbf{U} \mathbf{P}_k \mathbf{U}^{-1}$. The summation over j in the expression for \mathbf{M}^n can then be performed analytically to obtain

$$\sum_{j=0}^{n-1} \tau_k^{n-1-j} \tilde{\tau}_l^j = \frac{\tilde{\tau}_l^n - \tau_k^n}{\tilde{\tau}_l - \tau_k}.$$

The exponential $\exp t\mathbf{M}$ then takes the form

$$\exp t\mathbf{M} = \begin{pmatrix} \exp t(\mathbf{D} + \mathbf{T}) & -\frac{i\varepsilon}{2} \sum_{k,l} \frac{e^{t\tilde{\tau}_l} - e^{t\tau_k}}{\tilde{\tau}_l - \tau_k} \tilde{\mathbf{U}} \tilde{\mathbf{P}}_l \tilde{\mathbf{U}}^{-1} \mathbf{U} \mathbf{P}_k \mathbf{U}^{-1} \\ 0 & \exp t\mathbf{T} \end{pmatrix}.$$

We will now assume that the resonator was in its vacuum state at time $t = 0$ and the qubit in state $|j\rangle$, or in other words that $\langle \hat{a} \hat{P}_k \rangle = 0$ and $\langle \hat{P}_k \rangle = \delta_{jk}$. Furthermore, to

emphasize the dependence on the initial qubit state j , we will denote the expectation value of \hat{a} by $\langle \hat{a} \rangle_j$. Its time-dependence is then given by

$$\langle \hat{a} \rangle_j = \sum_i \langle \hat{a} \hat{P}_i \rangle = -\frac{i\varepsilon}{2} \sum_{i,l,k} \frac{e^{t\tilde{\tau}_i} - e^{t\tau_k}}{\tilde{\tau}_i - \tau_k} C_{lk,j}, \text{ where} \quad (\text{H.2})$$

$$C_{lk,j} \equiv (\tilde{\mathbf{U}}\mathbf{P}_l\tilde{\mathbf{U}}^{-1}\mathbf{U}\mathbf{P}_k\mathbf{U}^{-1})_{ij}. \quad (\text{H.3})$$

Single qubit case

To apply this formula, we will have a look at the simple case of a single two-level system. The relaxation of this qubit is governed by the rate equations $d\langle \hat{P}_g \rangle / dt = \Gamma \langle \hat{P}_e \rangle$ and $d\langle \hat{P}_e \rangle / dt = -\Gamma \langle \hat{P}_e \rangle$. The matrix \mathbf{T} therefore has the form

$$\mathbf{T} = \begin{pmatrix} 0 & \Gamma \\ 0 & -\Gamma \end{pmatrix}.$$

If we denote the resonator frequencies corresponding to the two qubit states by δ_g and δ_e , the matrix \mathbf{D} will be given by

$$\mathbf{D} = \begin{pmatrix} -i\delta_g - \kappa/2 & 0 \\ 0 & -i\delta_e - \kappa/2 \end{pmatrix}.$$

By diagonalizing \mathbf{T} and $\mathbf{D} + \mathbf{T}$, we find the eigenvalues

$$\begin{aligned} \tau_1 &= -\Gamma, \\ \tau_2 &= 0, \\ \tilde{\tau}_1 &= -i\delta_e - \kappa/2 - \Gamma, \\ \tilde{\tau}_2 &= -i\delta_g - \kappa/2 \end{aligned}$$

and the transformation matrices

$$\begin{aligned} \mathbf{U} &= \begin{pmatrix} -1 & 1 \\ 1 & 0 \end{pmatrix}, \\ \tilde{\mathbf{U}} &= \begin{pmatrix} -\frac{\Gamma}{\Gamma + i(\delta_e - \delta_g)} & 1 \\ 1 & 0 \end{pmatrix}. \end{aligned}$$

The terms $C_{lk,j} \equiv (\tilde{\mathbf{U}}\mathbf{P}_l\tilde{\mathbf{U}}^{-1}\mathbf{U}\mathbf{P}_k\mathbf{U}^{-1})_{ij}$ can then be easily calculated as

$$\begin{aligned} C_{11,g} &= C_{12,g} = C_{21,g} = C_{12,e} = 0, \\ C_{22,g} &= C_{22,e} = 1, \\ C_{11,e} &= -C_{21,e} = \frac{2i\chi}{\Gamma + 2i\chi}, \end{aligned}$$

where χ is the resonator dispersive shift, defined as $2\chi \equiv \delta_e - \delta_g$. This leads to the following expressions for $\langle \hat{a} \rangle_g$, $\langle \hat{a} \rangle_e$:

$$\begin{aligned}\langle \hat{a} \rangle_g &= \frac{i\varepsilon}{2} \frac{e^{-(i\delta_g + \kappa/2)t} - 1}{i\delta_g + \kappa/2}, \\ \langle \hat{a} \rangle_e &= \frac{i\varepsilon}{2} \left(\frac{e^{-(i\delta_g + \kappa/2)t} - 1}{i\delta_g + \kappa/2} + \right. \\ &\quad \left. + \frac{2i\chi}{\Gamma + 2i\chi} \left(\frac{e^{-(\Gamma + i\delta_e + \kappa/2)t} - e^{-\Gamma t}}{i\delta_e + \kappa/2} - \frac{e^{-(i\delta_g + \kappa/2)t} - e^{-\Gamma t}}{i\delta_g + \kappa/2 - \Gamma} \right) \right).\end{aligned}$$

Two qubit case

The same procedure can be used to determine the resonator response for a system of multiple dispersively coupled qubits. Without showing the intermediate steps which are analogous to the previous case, we will show the result for the two qubit case. Here the eigenvalues are

$$\begin{aligned}\tau_1 &= 0, \\ \tau_2 &= -\Gamma_1, \\ \tau_3 &= -\Gamma_2, \\ \tau_4 &= -\Gamma_1 - \Gamma_2, \\ \tilde{\tau}_1 &= -i\delta_{gg} - \kappa/2, \\ \tilde{\tau}_2 &= -i\delta_{eg} - \kappa/2 - \Gamma_1, \\ \tilde{\tau}_3 &= -i\delta_{ge} - \kappa/2 - \Gamma_2, \\ \tilde{\tau}_4 &= -i\delta_{ee} - \kappa/2 - \Gamma_1 - \Gamma_2\end{aligned}$$

and the transformation matrices

$$\begin{aligned}\mathbf{U} &= \begin{pmatrix} 1 & -1 & -1 & 1 \\ 0 & 1 & 0 & -1 \\ 0 & 0 & 1 & -1 \\ 0 & 0 & 0 & 1 \end{pmatrix}, \\ \tilde{\mathbf{U}} &= \begin{pmatrix} 1 & -\frac{\Gamma_1}{\Gamma_1 + 2i\chi_1} & -\frac{\Gamma_2}{\Gamma_2 + 2i\chi_2} & \frac{\Gamma_1\Gamma_2}{(\Gamma_1 + 2i\chi_1)(\Gamma_2 + 2i\chi_2)} \\ 0 & 1 & 0 & -\frac{\Gamma_2}{\Gamma_2 + 2i\chi_2} \\ 0 & 0 & 1 & -\frac{\Gamma_1}{\Gamma_1 + 2i\chi_1} \\ 0 & 0 & 0 & 1 \end{pmatrix}.\end{aligned}$$

The dispersive shifts $\chi_{1,2}$ are defined as $2\chi_1 = \delta_{eg} - \delta_{gg}$ and $2\chi_2 = \delta_{ge} - \delta_{gg}$. Note that we assume $\delta_{ee} = \delta_{gg} + 2\chi_1 + 2\chi_2$ and do not allow δ_{ee} to be independent of δ_{gg} , δ_{eg} and δ_{ge} .

The response of the resonator for qubit states $|gg\rangle$, $|eg\rangle$ and $|ge\rangle$ can be obtained from the single qubit calculation since the unexcited qubit can be considered simply

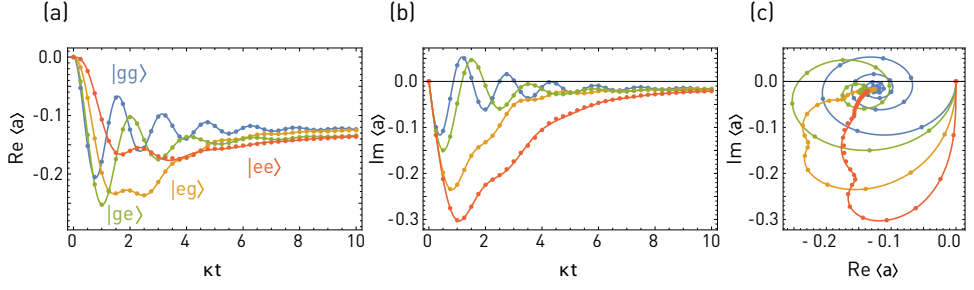


Figure H.2: Examples of the resonator response $\langle \hat{a} \rangle$ for the two-qubit states $|gg\rangle$ (blue), $|eg\rangle$ (yellow), $|ge\rangle$ (green) and $|ee\rangle$ (red). The parameters chosen here are $\delta_{gg}/\kappa = 4$, $2\chi_1/\kappa = -3$, $2\chi_2/\kappa = -1$, $\Gamma_1/\kappa = 1/2$, $\Gamma_2/\kappa = 1/8$. The real and the imaginary part of $\langle \hat{a} \rangle$ are plotted as a function of time in (a) and (b), respectively, while the path traced by $\langle \hat{a} \rangle$ in the complex plane is shown in (c). The solid lines represent results of the expression derived here while the points show results of quantum trajectory simulations with 1000 individual realizations.

as a spectator with no influence on the dynamics of the other qubit and the resonator. The case which is new in the system with two qubits is the $|ee\rangle$ state. We will therefore be interested only in the expectation value $\langle \hat{a} \rangle_{ee}$. To calculate it, we need to evaluate $C_{lk,ee} \equiv \sum_i (\tilde{\mathbf{U}}\mathbf{P}_l\tilde{\mathbf{U}}^{-1}\mathbf{U}\mathbf{P}_k\mathbf{U}^{-1})_{i,ee}$. These coefficients are given by

$$\begin{aligned}
C_{11,ee} &= 1, \\
C_{21,ee} &= C_{31,ee} = C_{41,ee} = \\
&= C_{32,ee} = C_{42,ee} = C_{23,ee} = C_{43,ee} = 0, \\
C_{22,ee} &= -C_{12,ee} = \frac{2i\chi_1}{\Gamma_1 + 2i\chi_1}, \\
C_{33,ee} &= -C_{13,ee} = \frac{2i\chi_2}{\Gamma_2 + 2i\chi_2}, \\
C_{24,ee} &= C_{34,ee} = -C_{14,ee} = -C_{44,ee} = \frac{4\chi_1\chi_2}{(\Gamma_1 + 2i\chi_1)(\Gamma_2 + 2i\chi_2)}.
\end{aligned}$$

Using eq. (H.2) then yields the final expression.

An example of resonator response curves calculated using the formulas derived in this appendix is shown in Fig. H.2. As also illustrated in the figure, these results match those obtained using quantum trajectory simulations.

Appendix I

Switch controlled by a single impedance: a no-go statement

In this appendix we consider a general RF network which contains one or more lumped element components acting as controls. The S -matrix of the network can be tuned by changing the impedances Z_{c1}, Z_{c2}, \dots of the control elements and it is our objective here to determine how \mathbf{S} depends on Z_{c1}, Z_{c2}, \dots and what types of tuning can be achieved in this scenario.

In particular, we will show that a non-reflective microwave switch cannot be implemented with a single control element and therefore using at least two tunable inductors as in our on-chip-switch device cannot be avoided. Similarly, we will see that a bi-directional tunable phase shifter also requires at least two control elements.

I.1 Dependence of S -matrix on lumped control impedances

The system in question is an arbitrary network with $N + 2k$ external nodes, as shown in Fig. I.1. Out of these, N are connected to external ports with characteristic impedances Z_0 while the remaining $2k$ are pairwise connected by the control elements with impedances $Z_{c1}, Z_{c2}, \dots, Z_{ck}$. In the following, we will for clarity denote the indices of these nodes by a_1, a_2, \dots, a_k and b_1, b_2, \dots, b_k instead of $N + 1, N + 2, \dots, N + 2k$.

If the admittance matrix of the network *excluding* the control elements is \mathbf{Y}_n , then the admittance matrix of the system *including* the controls is

$$\mathbf{Y} = (\mathbf{Y}_n + \mathbf{Y}_{c1} + \dots + \mathbf{Y}_{ck})^{-1},$$

where \mathbf{Y}_{cj} are the admittance matrices of the control elements. They each have only four non-zero elements: $(\mathbf{Y}_{cj})_{a_j a_j} = (\mathbf{Y}_{cj})_{b_j b_j} = Y_{cj}$ and $(\mathbf{Y}_{cj})_{a_j b_j} = (\mathbf{Y}_{cj})_{b_j a_j} = -Y_{cj}$, where $Y_{cj} = 1/Z_{cj}$. To emphasize this special matrix structure, we will write them as $\mathbf{Y}_{cj} = Y_{cj} \mathbf{v}_j \mathbf{v}_j^T$. Here \mathbf{v}_j are vectors with the only non-zero elements being $(\mathbf{v}_j)_{a_j} = 1$ and $(\mathbf{v}_j)_{b_j} = -1$.

The corresponding impedance matrix is $\mathbf{Z} = \mathbf{Y}^{-1}$. If we treat the nodes a_1, \dots, a_k and b_1, \dots, b_k as internal, the impedance matrix $\tilde{\mathbf{Z}}$ with respect to the remaining N

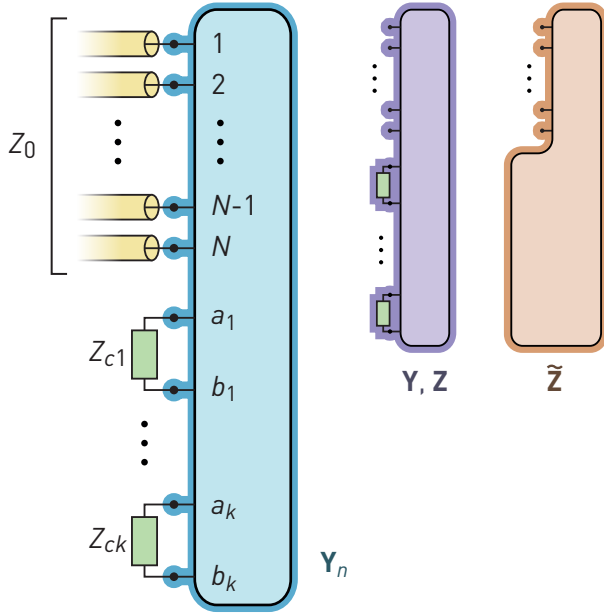


Figure I.1: Structure of the generic network with N external ports and k control impedances considered in this appendix. The schematic on the left represents the admittance matrix \mathbf{Y}_n of the network without the control elements as shown by the blue outline. The middle figure shows the $(N + 2k) \times (N + 2k)$ impedance matrix $\mathbf{Z} = \mathbf{Y}^{-1}$ including the controls where their nodes are still considered as external. The figure on the right then represents the restricted impedance matrix $\tilde{\mathbf{Z}} = [\mathbf{Z}]$, where only the N nodes connected to the ports are considered as external.

external nodes is obtained from \mathbf{Z} simply by dropping the last $2k$ rows and columns corresponding to a_1, \dots, a_k and b_1, \dots, b_k . We will denote this restriction operation by $[\cdot]$, that is, $\tilde{\mathbf{Z}} = [\mathbf{Z}]$. The S -matrix is related to $\tilde{\mathbf{Z}}$ by the usual relation

$$\mathbf{S} = (\tilde{\mathbf{Z}} - Z_0)(\tilde{\mathbf{Z}} + Z_0)^{-1} = 1 - 2Z_0(\tilde{\mathbf{Z}} + Z_0)^{-1}.$$

We will further rewrite this expression using the following identity holding for any matrix \mathbf{M} (for which the inverses exist):

$$[\mathbf{M}]^{-1} = [(\mathbf{P}\mathbf{M} + \bar{\mathbf{P}})^{-1}],$$

where \mathbf{P} is a diagonal matrix with the only non-zero elements being ones in positions $1, 2, \dots, N$ and $\bar{\mathbf{P}} = 1 - \mathbf{P}$. This identity says that taking the inverse of the upper left $N \times N$ block of \mathbf{M} is equivalent to replacing the last $2k$ rows of \mathbf{M} by zeros everywhere except for $2k$ ones on the diagonal, calculating the inverse and then taking

the upper $N \times N$ block of the result. This statement is easily proven by noting that the determinants of $[\mathbf{M}]$ and $\mathbf{P}\mathbf{M} + \bar{\mathbf{P}}$ are equal and so are their (i, j) minors for all $i, j \leq N$. Applying the identity to $\mathbf{M} = \mathbf{Z}/Z_0 + 1$ results in $(\bar{\mathbf{Z}} + Z_0)^{-1} = [(\mathbf{P}\mathbf{Z} + Z_0)^{-1}]$ which then leads to

$$\begin{aligned} \mathbf{S} &= [1 - 2Z_0(\mathbf{P}\mathbf{Z} + Z_0)^{-1}] = [(\mathbf{P}\mathbf{Z} - Z_0)(\mathbf{P}\mathbf{Z} + Z_0)^{-1}] \\ &= [(Y_0\mathbf{P} - \mathbf{Y})(Y_0\mathbf{P} + \mathbf{Y})^{-1}] \\ &= -1 + 2Y_0[(\mathbf{Y} + Y_0\mathbf{P})^{-1}], \end{aligned} \tag{I.1}$$

where $Y_0 = 1/Z_0$.

Let us now assume that the S -matrix is equal to $\mathbf{S}^{(1)}$ for a certain combination of control admittances $Y_{c1}^{(1)}, \dots, Y_{ck}^{(1)}$ and can be tuned to $\mathbf{S}^{(2)}$ by changing the admittances to $Y_{c1}^{(2)}, \dots, Y_{ck}^{(2)}$. Then it follows from eq. (I.1) that

$$\mathbf{S}^{(1)} - \mathbf{S}^{(2)} = 2Y_0[(\mathbf{Y}^{(1)} + Y_0\mathbf{P})^{-1} - (\mathbf{Y}^{(2)} + Y_0\mathbf{P})^{-1}], \text{ where}$$

$$\mathbf{Y}^{(m)} = \mathbf{Y}_n + \sum_{j=1}^k Y_{cj}^{(k)} \mathbf{v}_j \mathbf{v}_j^T.$$

Using the matrix identity $\mathbf{A}^{-1} - \mathbf{B}^{-1} = \mathbf{A}^{-1}(\mathbf{B} - \mathbf{A})\mathbf{B}^{-1}$, we can rewrite this relation as

$$\mathbf{S}^{(1)} - \mathbf{S}^{(2)} = 2Y_0 \sum_{j=1}^k \Delta Y_{cj} [(\mathbf{Y}^{(1)} + Y_0\mathbf{P})^{-1} \mathbf{v}_j \mathbf{v}_j^T (\mathbf{Y}^{(2)} + Y_0\mathbf{P})^{-1}],$$

where $\Delta Y_{cj} \equiv Y_{cj}^{(2)} - Y_{cj}^{(1)}$ are the control admittance changes. We will further denote the vectors $[(\mathbf{Y}^{(1)} + Y_0\mathbf{P})^{-1} \mathbf{v}_j]$ and $[\mathbf{v}_j^T (\mathbf{Y}^{(2)} + Y_0\mathbf{P})^{-1}]$ by \mathbf{u}_j and \mathbf{w}_j^T which allows us to write the expression for $\mathbf{S}^{(1)} - \mathbf{S}^{(2)}$ in the compact form

$$\mathbf{S}^{(1)} - \mathbf{S}^{(2)} = 2Y_0 \sum_{j=1}^k \Delta Y_{cj} \mathbf{u}_j \mathbf{w}_j^T.$$

Since the rank of any matrix of the form $\mathbf{u}\mathbf{w}^T$ is one and rank is a subadditive property¹, we get the following inequality for the rank of $\mathbf{S}^{(1)} - \mathbf{S}^{(2)}$:

$$\text{rank}(\mathbf{S}^{(1)} - \mathbf{S}^{(2)}) \leq k. \tag{I.2}$$

In other words, the rank of $\mathbf{S}^{(1)} - \mathbf{S}^{(2)}$ provides a lower bound for the number of lumped element controls necessary to achieve tuning of the S -matrix between $\mathbf{S}^{(1)}$ and $\mathbf{S}^{(2)}$.

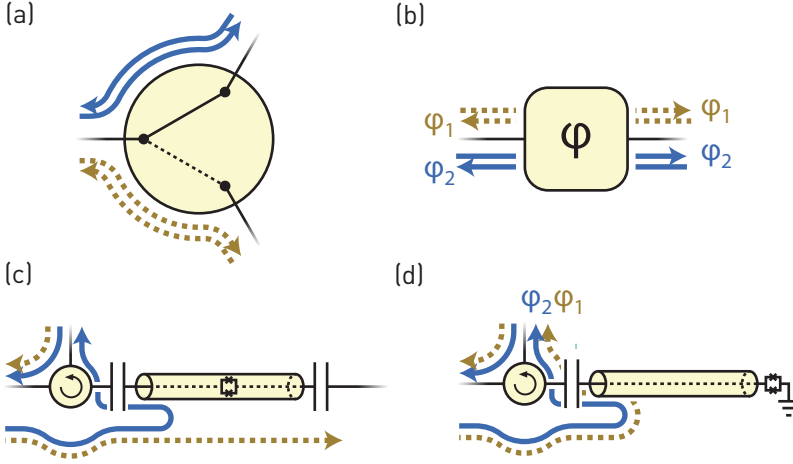


Figure I.2: (a) Schematic diagram of the switch discussed in this appendix. The two colors represent the two states of the switch. (b) A representation of an ideal bi-directional phase-shifter. (c,d) The non-reciprocal realizations of the two devices from (a,b) using circulators and a single control element.

I.2 Impossibility of switching with a single control element

The S -matrix of an ideal bi-directional switch as illustrated in Fig. I.2(a) has the form

$$\mathbf{S}^{(1)} = \begin{pmatrix} 0 & t_1 & 0 \\ t_1 & 0 & 0 \\ 0 & 0 & r_1 \end{pmatrix} \text{ in one state of the switch and}$$

$$\mathbf{S}^{(2)} = \begin{pmatrix} 0 & 0 & t_2 \\ 0 & r_2 & 0 \\ t_2 & 0 & 0 \end{pmatrix} \text{ in the other.}$$

Here t_1 and t_2 are the transmission coefficients between ports 1,2 and 1,3 in the two states of the switch. For a lossless switch, we would require $|t_1| = |t_2| = 1$. We will not place any restrictions on the reflection coefficients r_1 and r_2 of the port which is disconnected from port 1.

The rank of a matrix is equal to the size of its largest submatrix with non-zero determinant. Since the matrix $\mathbf{S}^{(1)} - \mathbf{S}^{(2)}$ is non-zero, its rank is at least one. The determinants of its size-2 submatrices are $-t_1^2$, $-t_2^2$, $t_1 t_2$, $-r_1 r_2$, $r_1 t_1$, $-r_2 t_2$. At least

¹That is, $\text{rank}(\mathbf{A} + \mathbf{B}) \leq \text{rank} \mathbf{A} + \text{rank} \mathbf{B}$.

the first three of these are non-zero, therefore the rank is larger or equal to 2. The determinant of $\mathbf{S}^{(1)} - \mathbf{S}^{(2)}$ itself is equal to $r_2 t_2^2 - r_1 t_1^2$. Hence, the rank is

$$\begin{aligned}\text{rank}(\mathbf{S}^{(1)} - \mathbf{S}^{(2)}) &= 2 \text{ if } r_2 t_2^2 - r_1 t_1^2 = 0, \\ \text{rank}(\mathbf{S}^{(1)} - \mathbf{S}^{(2)}) &= 3 \text{ if } r_2 t_2^2 - r_1 t_1^2 \neq 0.\end{aligned}$$

It now follows from eq. (I.2) that to realize such a switch, we need at least two lumped control elements. In addition, to be able to do this, the transmission and reflection coefficients need to satisfy $r_2 t_2^2 - r_1 t_1^2 = 0$.

Another interesting implication of eq. (I.2) is that a reciprocal tunable phase shifter as shown in Fig. I.2(b) also cannot be realized with a single control element. Its S -matrix is

$$\begin{aligned}\mathbf{S}^{(1)} &= \begin{pmatrix} 0 & e^{i\varphi_1} \\ e^{i\varphi_1} & 0 \end{pmatrix} \text{ in one state of the phase-shifter and} \\ \mathbf{S}^{(2)} &= \begin{pmatrix} 0 & e^{i\varphi_2} \\ e^{i\varphi_2} & 0 \end{pmatrix} \text{ in the other.}\end{aligned}$$

The matrix $\mathbf{S}^{(1)} - \mathbf{S}^{(2)}$ is clearly regular, or in other words has rank 2, unless $\varphi_1 = \varphi_2$ in which case the phase is not really tunable. Therefore, at least two control elements are needed to build such a device.

We should emphasize that these statements only hold for a reciprocal switch and a reciprocal phase shifter. If we allow the device to work only in one direction, we can implement it using a single control element. An example of a non-reciprocal switch based on a transmission line resonator tuned by a SQUID loop (the control element) and a circulator is shown in Fig. I.2(c). A similar device acting as a uni-directional tunable phase shifter is illustrated in Fig. I.2(d). To see that the existence of these devices does not contradict eq. (I.2), let us have a look at their S -matrices. For the non-reciprocal switch, we have

$$\begin{aligned}\mathbf{S}^{(1)} &= \begin{pmatrix} 0 & 0 & 1 \\ -1 & 0 & 0 \\ 0 & -1 & 0 \end{pmatrix} \text{ in one state of the switch and} \\ \mathbf{S}^{(2)} &= \begin{pmatrix} 0 & 0 & 1 \\ 0 & 1 & 0 \\ 1 & 0 & 0 \end{pmatrix} \text{ in the other.}\end{aligned}$$

Since the first two columns of $\mathbf{S}^{(1)} - \mathbf{S}^{(2)}$ are identical and the third one is zero, its rank is 1 and eq. (I.2) does not exclude that such a device could be realized with one

control element. Similarly for the phase shifter we have

$$\mathbf{S}^{(1)} = \begin{pmatrix} 0 & 1 \\ e^{i\varphi_1} & 0 \end{pmatrix} \text{ in one state of the phase-shifter and}$$
$$\mathbf{S}^{(2)} = \begin{pmatrix} 0 & 1 \\ e^{i\varphi_2} & 0 \end{pmatrix} \text{ in the other.}$$

Again, one of the columns of $\mathbf{S}^{(1)} - \mathbf{S}^{(2)}$ is zero and its rank is therefore 1.

Appendix J

Microwave $\pi/2$ hybrid

The S -parameter matrix of the on-chip $\pi/2$ -hybrid shown schematically in Fig. J.1(a) can be expressed in terms of its admittance matrix \mathbf{Y} as $\mathbf{S} = (1 - Z_0 \mathbf{Y})(1 + Z_0 \mathbf{Y})^{-1}$, where $Z_0 = 50 \Omega$ is the characteristic impedance of the input/output lines. The admittance matrix is given by the sum of the four constituent transmission line seg-

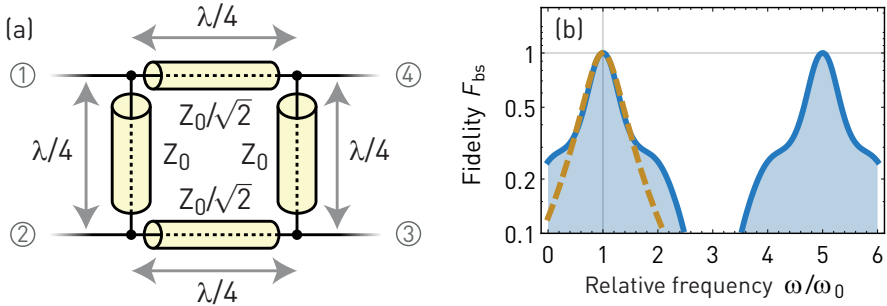


Figure J.1: (a) Circuit diagram of the on-chip $\pi/2$ -hybrid with the input/output ports numbered. (b) The fidelity of the hybrid S -parameter matrix as a function of signal frequency ω (blue solid line) and the Lorentzian approximation given by eq. (J.1) (yellow dashed line).

ments:

$$Z_0 \mathbf{Y} = \begin{pmatrix} \alpha & \beta & 0 & 0 \\ \beta & \alpha & 0 & 0 \\ 0 & 0 & 0 & 0 \\ 0 & 0 & 0 & 0 \end{pmatrix} + \begin{pmatrix} 0 & 0 & 0 & 0 \\ 0 & 0 & 0 & 0 \\ 0 & 0 & \alpha & \beta \\ 0 & 0 & \beta & \alpha \end{pmatrix} + \\ \sqrt{2} \begin{pmatrix} \alpha & 0 & 0 & \beta \\ 0 & 0 & 0 & 0 \\ 0 & 0 & 0 & 0 \\ \beta & 0 & 0 & \alpha \end{pmatrix} + \sqrt{2} \begin{pmatrix} 0 & 0 & 0 & 0 \\ 0 & \alpha & \beta & 0 \\ 0 & \beta & \alpha & 0 \\ 0 & 0 & 0 & 0 \end{pmatrix},$$

where $\alpha = -i \cot(\pi\omega/2\omega_0)$ and $\beta = i \csc(\pi\omega/2\omega_0)$. Here ω_0 is the operating frequency for which the hybrid is designed. For $\omega = \omega_0$ the S -parameter matrix becomes

$$\mathbf{S}_{\text{bs}} = -\frac{1}{\sqrt{2}} \begin{pmatrix} 0 & 0 & 1 & i \\ 0 & 0 & i & 1 \\ 1 & i & 0 & 0 \\ i & 1 & 0 & 0 \end{pmatrix}.$$

To quantify how \mathbf{S} deviates from this ideal value when the frequency differs from ω_0 , we can define the fidelity $F_{\text{bs}} = |\text{Tr} \mathbf{S}_{\text{bs}}^\dagger \mathbf{S}/4|^2$. It is given by a rather complicated function of frequency which can be approximated in the vicinity of the operating frequency ω_0 as

$$F_{\text{bs}} = \left(1 - \frac{(3 + 2\sqrt{2})\pi^2}{8} \left(\frac{\omega - \omega_0}{\omega_0}\right)^2\right)^{-1} + \mathcal{O}\left(\left(\frac{\omega - \omega_0}{\omega_0}\right)^4\right). \quad (\text{J.1})$$

The exact dependence of the fidelity on frequency as well as the Lorentzian approximation above are shown in Fig. J.1(b). The detunings from the operating frequency corresponding to a few selected values of F are given in the following table:

$ \omega - \omega_0 /\omega_0$	F_{bs}
0.0373	0.99
0.0840	0.95
0.1754	0.8
0.3431	0.5

If we define the bandwidth of the hybrid δ_{bs} as the width of the frequency range in which $F_{\text{bs}} > 1/2$, we get $\delta_{\text{bs}} \approx 2\omega_0/3$.

Appendix K

Modification of a RADIALL switch for cryogenic operation

To make future experiments with multi-port devices more flexible, it would be beneficial to install a microwave switch inside the cryostat. Other experimental groups have successfully used the R573423600 switch from RADIALL at cryogenic temperatures. The heat dissipated in the solenoids of a mechanical switch such as this one contributes significantly to the total heat-load in a typical dilution fridge setup. As reported by Ranzani *et al.* (2013), it can take up to 15 minutes for the base temperature of the cryostat to stabilize after the switch is pulsed. It is therefore clearly desirable to reduce this power dissipation as much as possible.

A modification of the RADIALL switch leading to a reduction of the power required for switching by a factor of 2 has been proposed and tested by the group of John Martinis at UCSB. I have followed the steps outlined on the group's freely accessible website¹ to modify one of our switches.

The switch is a single pole, six throw. That is, it allows to connect one input to one of six different outputs. The connections are made mechanically using six solenoids. Each of these solenoids has two windings with opposite orientations which are used for turning the given switch channel on and off. The windings are connected to the control pins of the switch via two stacked PCBs whose pictures are shown in Fig. K.1(a). The diagram of this circuit is displayed in Fig. K.1(b).

As we can see in the diagram, the channels are turned on by passing current from individual set inputs S_1, S_2, \dots, S_6 to the common ground C . On the other hand, switching the channels off is done with all solenoids simultaneously, by passing current from the reset input R to the common ground. This method is presumably employed to keep the number of control inputs low but it increases the current needed for switching the channels off sixfold. To deal with this problem, the circuit can be modified by cutting certain PCB connections as illustrated by the photos in Fig. K.1(c,d) and by the diagram in Fig. K.1(e). The structure of the modified circuit is shown in Fig. K.1(f).

¹<http://web.physics.ucsb.edu/~martinisgroup/electronics.shtml>

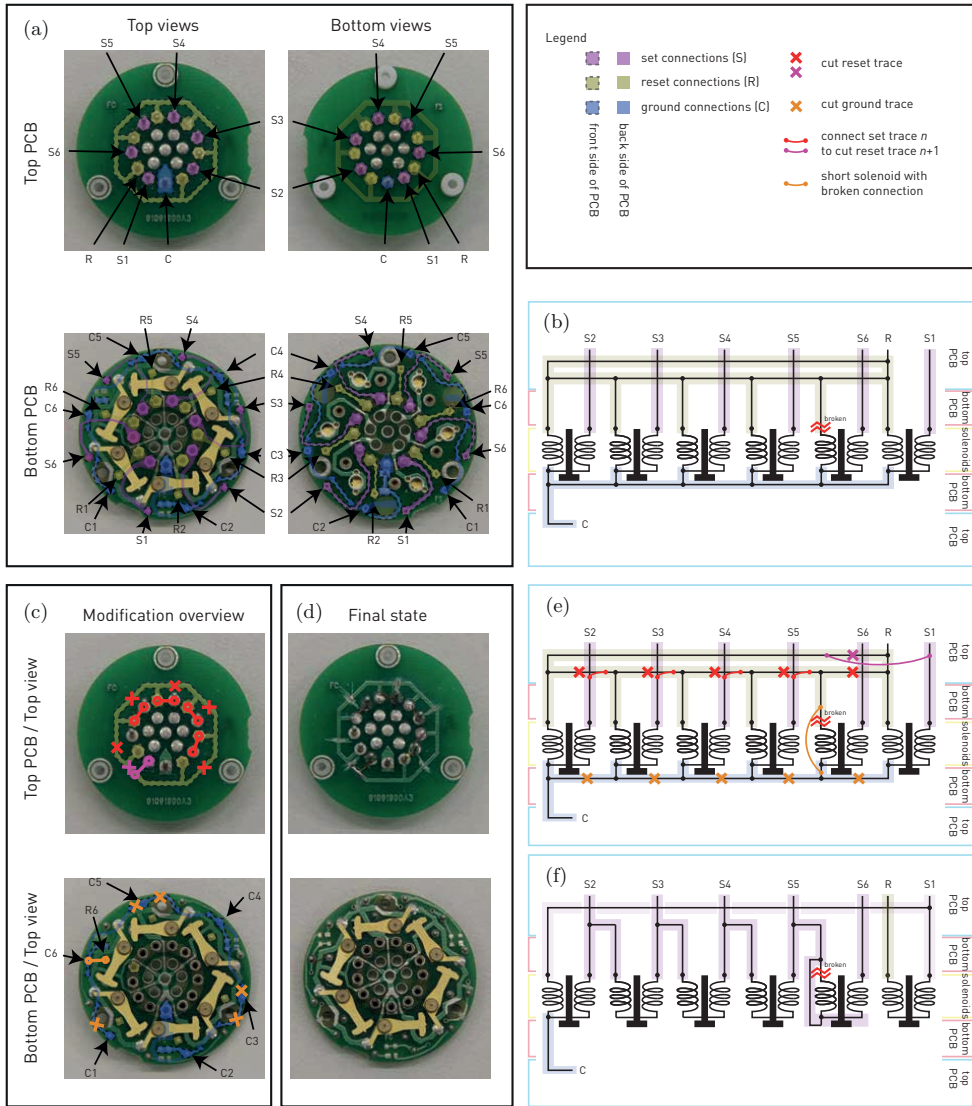


Figure K.1: (a) Top and bottom views of the two PCBs connecting the solenoids of the switch with the control pins. The different set, reset and ground traces are highlighted in color. (b) Schematic diagram of the switch. (c) Overview of the modifications made to the switch – cuts and added wire connections. (d) The PCBs of the switch after the modifications. (e,f) Schematic representations of (c,d).

The common ground is no longer used in the modified switch. Instead, the set and reset winding of each channel are connected in series, reducing the current required for switching by a factor of 2. Each two neighbouring solenoids n and $n + 1$ now have a common set input S_n . To turn channel n of the switch on, current must be passed from pin n to $n - 1$ (where pin 0 is the original reset pin). To turn it off, the direction of the current has to be reversed.

During disassembly of the switch, despite trying to exercise caution, I broke one of the pins connecting the solenoids to the bottom PCB. These pins are not fixed to the body of the switch very rigidly and the fine wire of the solenoids breaks rather easily. To prevent this happening again, I reinforced them later with a bit of Stycast 1266 epoxy. In the future, this should perhaps be done before removing the PCBs. The winding of solenoid 6 originally connected to the broken pin cannot be used anymore. I shorted it to preserve some functionality of the solenoid. This way, it can still be used but requires twice as much current for switching on and off compared with solenoids 1-5.

Since the modified switch requires a bi-directional current source, I have designed and made a new constant current source, partially inspired by the original design in Bianchetti (2010). The source is controlled via a USB/UART bridge which, when connected to the USB port of a PC, appears as a virtual serial port.

The schematic diagram of the source is shown in Fig. K.2. To keep the switch galvanically isolated from the digital control electronics, the circuit consists of two parts separated by optoisolators OK1-OK4. The analog part of the circuit shown in the upper half of the schematic operates at ground GND2 which is disconnected from the digital ground GND used by the digital part in the lower half of the diagram.

Power is provided to the analog part from a 30 V voltage source. The power transistor T15 acts as a simple constant current source whose output current is set by the Zener diode D15 and the resistor R10. The parameters of these components are chosen to result in an output current of approximately 75 mA.

Each of the seven outputs of the device is connected to the current source and to ground by two PNP transistors. If the base of the upper transistor is pulled to ground, the corresponding output will be connected to the collector of T15 and will therefore act as a current source. Pulling the base of the lower transistor to ground makes the output a current sink. The diodes D1-14 connected in parallel with the transistors act to protect these from switching transients.

Each of the transistor bases is connected to an optoisolator which will pull it to ground if current is passed through the diode at the galvanically isolated input side. These diodes are controlled by the outputs of two 1-of-8 demultiplexers. Depending on the state of the three digital inputs, one of the outputs Y0, . . . , Y7 of the demultiplexer will be low while the rest is high. If output Y0 is selected, all diodes are reverse-biased and none of the optoisolators will be activated. Each of the other outputs Y1, . . . , Y7 switches one of the optoisolators.

The output of the device to be used as the current source is therefore determined by the 3-bit combination of the demultiplexer inputs VCCI0, VCCI1 and VCCI2. The current sink output is similarly determined by GNDI0, GNDI1 and GNDI2. The outputs of the demultiplexers are enabled only if their inputs G2A are pulled low. Therefore,

after selecting the current source and sink, the current needs to be switched on by pulsing the line \sim EN.

The seven control lines V_{CCIO-2} , G_{NDIO-2} and \sim EN are controlled by an Atmel AT-TINY84 microcontroller. Note that the lines G_{NDIO} , G_{NDI1} and V_{CCI2} double as SPI serial interface lines $MISO$, $MOSI$ and SCK used for programming the microcontroller.

Communication with the PC is handled on the microcontroller side by a software-emulated serial port connected to a PC via a USB/UART bridge at 1200 baud. The bridge appears to the PC as a virtual COM port. After sending the 4-byte command $PUL[B]$ (bytes $0x50$, $0x55$, $0x4C$ and an additional arbitrary byte B containing the parameter of the command) to the source, it generates a current pulse whose length in milliseconds is approximately given by 7.5 times the value of B . The command $SET[B]$ (bytes $0x53$, $0x45$, $0x54$ and a parameter byte B) sets outputs (numbered $1, \dots, 7$) of the device as current sources and sinks. The output whose number is given by the three least significant bits $[b2] [b1] [b0]$ of $[B]$ will be the source and the output with the number given by the next three bits $[b5] [b4] [b3]$ will be the sink. The controller responds to a successfully received command by sending an acknowledgement 3-byte message ACK (bytes $0x41$, $0x43$ and $0x4B$).

This is achieved by the following simple code run by the microcontroller which monitors the serial port input and if it receives one of the commands SET or PUL, it sets the levels at the multiplexer data inputs or pulses the multiplexer enable input according to the parameter byte sent along with the command. The code was written and uploaded using the popular Arduino IDE.

```
#include <SoftwareSerial.h>

SoftwareSerial mySerial(0,1);    // initialize port (TxD = pin 0, RxD = pin 1)

byte b1 = 0; byte b2 = 0; byte b3 = 0; byte b4 = 0;    // make buffer for data in

void setup()
{
  // set the data rate for the SoftwareSerial port
  // * note that the SoftwareSerial library was written for the ATMEGA family of
  // * microcontrollers; due to the different clock used by the ATTINY, initializing
  // * the port with 9600 baud actually results in a speed of 1200 baud.
  mySerial.begin(9600);
  // initialize pin modes and levels
  pinMode(2,OUTPUT); pinMode(3,OUTPUT); pinMode(4,OUTPUT);
  pinMode(5,OUTPUT); pinMode(6,OUTPUT);
  pinMode(7,OUTPUT); pinMode(8,OUTPUT);
  digitalWrite(2,LOW); digitalWrite(3,LOW); digitalWrite(4,LOW);
  digitalWrite(5,LOW); digitalWrite(6,LOW);
  digitalWrite(7,LOW); digitalWrite(8,HIGH);
}

void loop()
{
  if (mySerial.available()) {    // if byte received, shift into the 4-byte buffer
    b4 = b3; b3 = b2; b2 = b1;    // (b1 is the newest byte in the buffer)
    b1 = mySerial.read();
  }

  // SET command:
  // if buffer starts with "SET"
  if ((b2 == 84) && (b3 == 69) && (b4 == 83)) {    // (ASCII 83,69,84)
    mySerial.write("ACK");    // write "ACK" message
    digitalWrite(2, b1 % 2); b1 = b1 >> 1;    // set outputs 2-7 to values
    digitalWrite(3, b1 % 2); b1 = b1 >> 1;    // given by bits of the
    digitalWrite(4, b1 % 2); b1 = b1 >> 1;    // parameter byte b1
    digitalWrite(5, b1 % 2); b1 = b1 >> 1;
    digitalWrite(6, b1 % 2); b1 = b1 >> 1;
    digitalWrite(7, b1 % 2);
    b1 = 0; b2 = 0; b3 = 0; b4 = 0;    // empty buffer
  }

  // PUL command:
  // if buffer starts with "PUL"
  if ((b2 == 76) && (b3 == 85) && (b4 == 80)) {    // (ASCII 80,85,76)
    mySerial.write("ACK");    // write "ACK" message
    digitalWrite(8, LOW);    // set output 8 LOW
    delay(b1);    // wait
    digitalWrite(8, HIGH);    // set output 8 HIGH
    b1 = 0; b2 = 0; b3 = 0; b4 = 0;    // empty buffer
  }
}
}
```

As an example, assuming that the reset pin of the switch is connected to output 1 of the source, pin 1 to output 2, and so on, the following Python code describes the procedure to set a switch channel on and off:

```

import serial
import time

ser = serial.Serial('COM4',1200,timeout=2) # open serial port
ser.flush()
time.sleep(1) # wait for port to be ready

def set_source_and_sink(source,sink):
    ser.write("SET"+chr(8*sink+source)) # write command SET + parameter
    resp = ser.read(3) # read ACK message
    return (resp == "ACK") # return success flag

def make_pulse(t):
    send("PUL"+chr(t)) # write command PUL + parameter
    resp = ser.read(3) # read ACK message
    return (resp == "ACK") # return success flag

def set_switch_channel(ch,state,t):
    if state:
        succ1 = set_source_and_sink(ch+1,ch) # on: source=ch+1, sink=ch
    else:
        succ1 = set_source_and_sink(ch,ch+1) # off: source=ch, sink=ch+1
    time.sleep(0.1)
    succ2 = make_pulse(t) # make switching pulse
    time.sleep(0.1)
    succ3 = set_source_and_sink(0,0) # disconnect source and sink
    return (succ1 and succ2 and succ3) # return success flag

set_switch_channel(4,True,1) # set switch channel 4 on (7.5ms pulse)
... # do whatever you want
set_switch_channel(4,False,1) # set switch channel 4 off

```


Part	Component type	Value
C1	capacitor	1m
C2-C4	capacitor	100n
D1-D14	diode	1N4005
D15	Zener diode	1N4728
IC1-IC2	1-of-8 demux	74AC138N
JP1	2x3 pin header	
OK1-OK4	optoisolator	ILQ30
R1-R7	resistor	4k7
R8-R9	resistor	1k
R10	resistor	22R
R11	resistor	2k2
R12-R18	resistor	47R
T1-T14	transistor	2N5401
T15	transistor	BD900A
U1	microcontroller	ATTINY84

Other parts

CP2101- or FTDI232-based USB to UART converter
project enclosure
9-pin D-SUB female connector
2-pin LEMO female connector

Table K.1: List of components for the RADIALL switch current source

The current source easily fits onto a $100 \times 160 \text{ mm}^2$ PCB. A mask for its fabrication is presented in Fig. K.3(a). A photo of the assembled first version of the source is shown in Fig. K.3(b). The PCB used here was slightly different as the microcontroller was kept on a board separate from the rest of the circuit for easier testing. A list of used components is given in Tab. K.1.

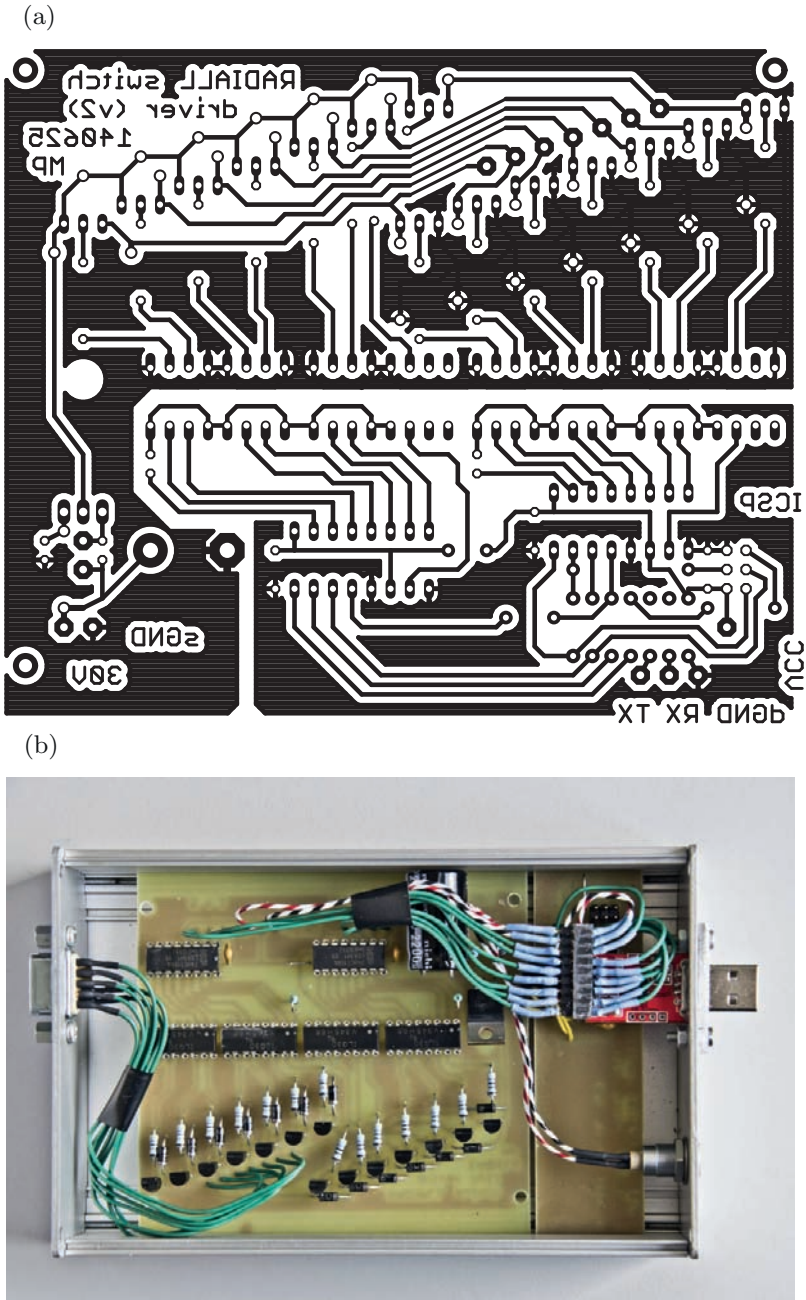


Figure K.3: (a) PCB mask for the switch current source and (b) photo of the completed device. In this prototype version, the controller was placed on a separate board from the rest of the circuit. The USB-to-serial converter is visible as the small red board on the right.

Bibliography

- Abadal, A. R. 2014 (08). *Calibration of an IQ mixer for continuous and pulsed modulation*. M.Phil. thesis, ETHZ.
- Abramowitz, M., & Stegun, I. (eds). 1972. *Handbook of Mathematical Functions*. United States Department of Commerce.
- Aharonov, Y., & Anandan, J. 1987. Phase-Change During A Cyclic Quantum Evolution. *Phys. Rev. Lett.*, **58**(16), 1593–1596.
- Al-Khalili, J. 2015. In retrospect: Book of Optics. *Nature*, **518**, 164–165.
- Andersen, U. L. 2013. Quantum optics: Squeezing more out of LIGO. *Nature Photonics*, **7**, 589–590.
- Bahl, I. J. 2003. *Lumped Elements for RF and Microwave Circuits*. Artech House.
- Barends, R., Wenner, J., Lenander, M., Chen, Y., Bialczak, R. C., Kelly, J., Lucero, E., O’Malley, P., Mariantoni, M., Sank, D., Wang, H., White, T. C., Yin, Y., Zhao, J., Cleland, A. N., Martinis, J. M., & Baselmans, J. J. A. 2011. Minimizing quasi-particle generation from stray infrared light in superconducting quantum circuits. *Appl. Phys. Lett.*, **99**(11), 113507.
- Barends, R., Kelly, J., Megrant, A., Sank, D., Jeffrey, E., Chen, Y., Yin, Y., Chiaro, B., Mutus, J., Neill, C., OMalley, P., Roushan, P., Wenner, J., White, T. C., Cleland, A. N., & Martinis, J. M. 2013. Coherent Josephson Qubit Suitable for Scalable Quantum Integrated Circuits. *Phys. Rev. Lett.*, **111**(8), 080502–.
- Barends, R., Lamata, L., Kelly, J., García-Álvarez, L., Fowler, A. G., Megrant, A., Jeffrey, E., White, T. C., Sank, D., Mutus, J. Y., Campbell, B., Chen, Y., Chen, Z., Chiaro, B., Dunsworth, A., Hoi, I.-C., Neill, C., O’Malley, P. J. J., Quintana, C., Roushan, P., Vainsencher, A., Wenner, J., Solano, E., & Martinis, J. M. 2015. Digital quantum simulation of fermionic models with a superconducting circuit. *arXiv:1501.07703*.
- Baur, M. 2012 (03). *Realizing quantum gates and algorithms with three superconducting qubits*. Ph.D. thesis, ETH Zurich.
- Bennett, C. H., & Brassard, G. 1984. Quantum cryptography: public key distribution and coin tossing. *Int. Conf. on Computers, Systems and Signal Processing*, 175.

- Berger, S., Pechal, M., Abdumalikov Jr., A. A., Eichler, C., Steffen, L., Fedorov, A., Wallraff, A., & Filipp, S. 2013. Exploring the effect of noise on the Berry phase. *Phys. Rev. A*, **87**, 060303(R).
- Berger, S. 2015. *Geometric phases and noise in circuit QED*. Ph.D. thesis, ETH Zurich.
- Bernstein, E., & Vazirani, U. 1997. Quantum Complexity Theory. *SIAM J. Comput.*, **26**(5), 1411–1473.
- Berry, M. V. 1984. Quantal Phase-Factors Accompanying Adiabatic Changes. *Proceedings Of The Royal Society Of London Series A-Mathematical Physical And Engineering Sciences*, **392**(1802), 45–57.
- Bialczak, R. C., Ansmann, M., Hofheinz, M., Lucero, E., Neeley, M., O’Connell, A. D., Sank, D., Wang, H., Wenner, J., Steffen, M., Cleland, A. N., & Martinis, J. M. 2010. Quantum process tomography of a universal entangling gate implemented with Josephson phase qubits. *Nat. Phys.*, **6**(6), 409–413.
- Bianchetti, R., Filipp, S., Baur, M., Fink, J. M., Göppl, M., Leek, P. J., Steffen, L., Blais, A., & Wallraff, A. 2009. Dynamics of dispersive single-qubit readout in circuit quantum electrodynamics. *Phys. Rev. A*, **80**(4), 043840–7.
- Bianchetti, R., Filipp, S., Baur, M., Fink, J. M., Lang, C., Steffen, L., Boissonneault, M., Blais, A., & Wallraff, A. 2010. Control and Tomography of a Three Level Superconducting Artificial Atom. *Phys. Rev. Lett.*, **105**(Nov), 223601.
- Bianchetti, R. 2010 (08). *Control and readout of a superconducting artificial atom*. Ph.D. thesis, ETH Zurich.
- Birnbaum, K. M., Boca, A., Miller, R., Boozer, A. D., Northup, T. E., & Kimble, H. J. 2005. Photon blockade in an optical cavity with one trapped atom. *Nature*, **436**(7047), 87–90.
- Blais, A., Huang, R.-S., Wallraff, A., Girvin, S. M., & Schoelkopf, R. J. 2004. Cavity quantum electrodynamics for superconducting electrical circuits: An architecture for quantum computation. *Phys. Rev. A*, **69**(6), 062320–14.
- Born, M., & Fock, V. 1928. Beweis des Adiabatenatzes. *Z. Phys.*, **51**, 165–180.
- Bozyigit, D., Lang, C., Steffen, L., Fink, J. M., Eichler, C., Baur, M., Bianchetti, R., Leek, P. J., Filipp, S., da Silva, M. P., Blais, A., & Wallraff, A. 2011. Antibunching of microwave-frequency photons observed in correlation measurements using linear detectors. *Nat. Phys.*, **7**(2), 154–158.
- Bozyigit, D. 2008 (12). *Design and Development of a High Performance Signal Processing Platform for Qubit Readout*. M.Phil. thesis, ETH Zurich.
- Breuer, H. 2012. Foundations and Measures of Quantum Non-Markovianity. *arXiv:1206.5346v1*.

- Brooks, P., Kitaev, A., & Preskill, J. 2013. Protected gates for superconducting qubits. *Phys. Rev. A*, **87**(5).
- Brune, M., Schmidt-Kaler, F., Maali, A., Dreyer, J., Hagley, E., Raimond, J. M., & Haroche, S. 1996. Quantum Rabi Oscillation: A Direct Test of Field Quantization in a Cavity. *Phys. Rev. Lett.*, **76**(11), 1800–1803.
- Businger, M. 2015. *Further developments on the Conversion Box*. M.Phil. thesis, ETH Zürich.
- Cahill, K. E., & Glauber, R. J. 1969. Density Operators and Quasiprobability Distributions. *Phys. Rev.*, **177**(Jan), 1882–1902.
- Castellanos-Beltran, M. A., & Lehnert, K. W. 2007. Widely tunable parametric amplifier based on a superconducting quantum interference device array resonator. *Appl. Phys. Lett.*, **91**(8), 083509–3.
- Chang, J. B., Vissers, M. R., Corcoles, A. D., Sandberg, M., Gao, J., Abraham, D. W., Chow, J. M., Gambetta, J. M., Rothwell, M. B., Keefe, G. A., Steffen, M., & Pappas, D. P. 2013. Improved superconducting qubit coherence using titanium nitride. *Appl. Phys. Lett.*, **103**(1), 012602.
- Chapman, B. J., Moores, B. A., Rosenthal, E. I., Kerckhoff, J., & Lehnert, K. W. 2016. General purpose multiplexing device for cryogenic microwave systems. *arXiv:1603.02716*.
- Childs, A. M., Chuang, I. L., & Leung, D. W. 2001. Realization of quantum process tomography in NMR. *Phys. Rev. A*, **64**(1), 012314–.
- Choi, M.-D. 1975. Completely positive linear maps on complex matrices. *Linear Algebra Appl.*, **10**(3), 285 – 290.
- Christandl, M., & Renner, R. 2012. Reliable Quantum State Tomography. *Phys. Rev. Lett.*, **109**, 120403.
- Chuang, I. L., & Nielsen, M. A. 1997. Prescription for experimental determination of the dynamics of a quantum black box. *J. Mod. Opt.*, **44**(11), 2455–2467.
- Cirac, J. I., Zoller, P., Kimble, H. J., & Mabuchi, H. 1997. Quantum State Transfer and Entanglement Distribution among Distant Nodes in a Quantum Network. *Phys. Rev. Lett.*, **78**(16), 3221–3224.
- Clarke, J., & Wilhelm, F. K. 2008. Superconducting quantum bits. *Nature*, **453**(7198), 1031–1042.
- Clerk, A. A., Devoret, M. H., Girvin, S. M., Marquardt, F., & Schoelkopf, R. J. 2010. Introduction to quantum noise, measurement, and amplification. *Rev. Mod. Phys.*, **82**(2), 1155–1208.

- Compton, A. H. 1923. A Quantum Theory of the Scattering of X-rays by Light Elements. *Phys. Rev.*, **21**, 483.
- Córcoles, A. D., Chow, J. M., Gambetta, J. M., Rigetti, C., Rozen, J. R., Keefe, G. A., Rothwell, M. B., Ketchen, M. B., & Steffen, M. 2011. Protecting superconducting qubits from radiation. *Appl. Phys. Lett.*, **99**(18), 181906.
- da Silva, M. P., Bozyigit, D., Wallraff, A., & Blais, A. 2010. Schemes for the observation of photon correlation functions in circuit QED with linear detectors. *Phys. Rev. A*, **82**(4), 043804–12.
- d’Enterria, D., & da Silveira, G. G. 2013. Observing Light-by-Light Scattering at the Large Hadron Collider. *Phys. Rev. Lett.*, **111**, 080405.
- Deutsch, D. 1985. Quantum Theory, the Church-Turing Principle and the Universal Quantum Computer. *Proceedings of the Royal Society of London. Series A, Mathematical and Physical Sciences*, **400**(1818), 97–117.
- DiCarlo, L., Chow, J. M., Gambetta, J. M., Bishop, L. S., Johnson, B. R., Schuster, D. I., Majer, J., Blais, A., Frunzio, L., Girvin, S. M., & Schoelkopf, R. J. 2009. Demonstration of two-qubit algorithms with a superconducting quantum processor. *Nature*, **460**(7252), 240–244.
- Dyson, F. J. 1949. The Radiation Theories of Tomonaga, Schwinger, and Feynman. *Phys. Rev.*, **75**(Feb), 486–502.
- Eichler, C., Bozyigit, D., Lang, C., Baur, M., Steffen, L., Fink, J. M., Filipp, S., & Wallraff, A. 2011. Observation of Two-Mode Squeezing in the Microwave Frequency Domain. *Phys. Rev. Lett.*, **107**(Sep), 113601.
- Eichler, C., Bozyigit, D., & Wallraff, A. 2012a. Characterizing quantum microwave radiation and its entanglement with superconducting qubits using linear detectors. *Phys. Rev. A*, **86**(Sep), 032106.
- Eichler, C., Lang, C., Fink, J. M., Govenius, J., Filipp, S., & Wallraff, A. 2012b. Observation of Entanglement between Itinerant Microwave Photons and a Superconducting Qubit. *Phys. Rev. Lett.*, **109**(Dec), 240501–5.
- Eichler, C. 2013 (01). *Experimental Characterization of Quantum Microwave Radiation and its Entanglement with a Superconducting Qubit*. Ph.D. thesis, ETH Zurich.
- Eichler, C., & Wallraff, A. 2014. Controlling the dynamic range of a Josephson parametric amplifier. *EPJ Quantum Technology*, **1**(1), 2.
- Einstein, A. 1905. Über einen die Erzeugung und Verwandlung des Lichtes betreffenden heuristischen Gesichtspunkt. *Ann. Phys.*, **322**(6), 132–148.
- Emerson, J., Silva, M., Moussa, O., Ryan, C., Laforest, M., Baugh, J., Cory, D. G., & Laflamme, R. 2007. Symmetrized Characterization of Noisy Quantum Processes. *Science*, **317**, 1893.

- Faist, P., & Renner, R. 2016. Practical and Reliable Error Bars in Quantum Tomography. *Physical Review Letters*, **117**(1), 010404.
- Fedorov, A., Steffen, L., Baur, M., da Silva, M. P., & Wallraff, A. 2012. Implementation of a Toffoli gate with superconducting circuits. *Nature*, **481**(7380), 170–172.
- Feynman, R. P. 1982. Simulating physics with computers. *Int. J. Theor. Phys.*, **21**(6), 467–488.
- Filipp, S., Maurer, P., Leek, P. J., Baur, M., Bianchetti, R., Fink, J. M., Göppl, M., Steffen, L., Gambetta, J. M., Blais, A., & Wallraff, A. 2009. Two-Qubit State Tomography Using a Joint Dispersive Readout. *Phys. Rev. Lett.*, **102**(20), 200402.
- Fink, J. M., Göppl, M., Baur, M., Bianchetti, R., Leek, P. J., Blais, A., & Wallraff, A. 2008. Climbing the Jaynes-Cummings ladder and observing its nonlinearity in a cavity QED system. *Nature*, **454**(7202), 315–318.
- Gao, J., Vale, L. R., Mates, J. A. B., Schmidt, D. R., Hilton, G. C., Irwin, K. D., Mallet, F., Castellanos-Beltran, M. A., Lehnert, K. W., Zmuidzinas, J., & Leduc, H. G. 2011. Strongly quadrature-dependent noise in superconducting microresonators measured at the vacuum-noise limit. *Appl. Phys. Lett.*, **98**(23), 232508.
- Gao, J., Daal, M., Vayonakis, A., Kumar, S., Zmuidzinas, J., Sadoulet, B., Mazin, B. A., Day, P. K., & Leduc, H. G. 2008a. Experimental evidence for a surface distribution of two-level systems in superconducting lithographed microwave resonators. *Appl. Phys. Lett.*, **92**(15), 152505.
- Gao, J., Daal, M., Martinis, J. M., Vayonakis, A., Zmuidzinas, J., Sadoulet, B., Mazin, B. A., Day, P. K., & Leduc, H. G. 2008b. A semiempirical model for two-level system noise in superconducting microresonators. *Appl. Phys. Lett.*, **92**(21), 212504.
- Gardiner, C. W., & Zoller, P. 1991. *Quantum Noise*. Springer.
- Gasparinetti, S., Berger, S., Abdumalikov, A. A., Pechal, M., Filipp, S., & Wallraff, A. J. 2016. Measurement of a vacuum-induced geometric phase. *Science Advances*, **2**(5), e1501732.
- Geerlings, K., Leghtas, Z., Pop, I. M., Shankar, S., Frunzio, L., Schoelkopf, R. J., Mirrahimi, M., & Devoret, M. H. 2013. Demonstrating a Driven Reset Protocol for a Superconducting Qubit. *Phys. Rev. Lett.*, **110**(Mar), 120501.
- Göppl, M., Fagner, A., Baur, M., Bianchetti, R., Filipp, S., Fink, J. M., Leek, P. J., Puebla, G., Steffen, L., & Wallraff, A. 2008. Coplanar Waveguide Resonators for Circuit Quantum Electrodynamics. *J. Appl. Phys.*, **104**(6), 113904.
- Hagley, E., Maitra, X., Nogues, G., Wunderlich, C., Brune, M., Raimond, J. M., & Haroche, S. 1997. Generation of Einstein-Podolsky-Rosen Pairs of Atoms. *Phys. Rev. Lett.*, **79**, 1.

- Haroche, S., & Kleppner, D. 1989. Cavity Quantum Electrodynamics. *Physics Today*, **42**, 24–30.
- Harrington, R. F. 2001. *Time-Harmonic Electromagnetic Fields*. IEEE Press.
- Harrow, A. W., Hassidim, A., & Lloyd, S. 2009. Quantum Algorithm for Linear Systems of Equations. *Phys. Rev. Lett.*, **103**(Oct), 150502.
- Heisenberg, W., & Euler, H. 1936. Folgerungen aus der Diracschen Theorie des Positrons. *Z. Phys.*, **98**, 714.
- Hofheinz, M., Wang, H., Ansmann, M., Bialczak, R. C., Lucero, E., Neeley, M., O’Connell, A. D., Sank, D., Wenner, J., Martinis, J. M., & Cleland, A. N. 2009. Synthesizing arbitrary quantum states in a superconducting resonator. *Nature*, **459**, 546–549.
- Hong, C. K., Ou, Z. Y., & Mandel, L. 1987. Measurement of Subpicosecond Time Intervals between Two Photons by Interference. *Phys. Rev. Lett.*, **59**(18), 2044–2046.
- Isham, C. J. 1999. *Modern Differential Geometry for Physicists (2nd Edition)*. World Scientific Publishing Co. Pte. Ltd.
- Isserlis, L. 1918. On a Formula for the Product-Moment Coefficient of any Order of a Normal Frequency Distribution in any Number of Variables. *Biometrika*, **12**, 134.
- James, D. F. V., Kwiat, P. G., Munro, W. J., & White, A. G. 2001. Measurement of qubits. *Phys. Rev. A*, **64**, 052312.
- Jaynes, E., & Cummings, F. 1963. Comparison of quantum and semiclassical radiation theories with application to the beam maser. *Proceedings of the IEEE*, **51**(1), 89–109.
- Josephson, B. D. 1974. The discovery of tunnelling supercurrents. *Rev. Mod. Phys.*, **46**(Apr), 251–254.
- Kalb, N., Reiserer, A., Ritter, S., & Rempe, G. 2015. Heralded Storage of a Photonic Quantum Bit in a Single Atom. *Phys. Rev. Lett.*, **114**, 220501.
- Keller, M., Lange, B., Hayasaka, K., Lange, W., & Walther, H. 2004. Continuous generation of single photons with controlled waveform in an ion-trap cavity system. *Nature*, **431**, 1075.
- Kelly, J., Barends, R., Fowler, A. G., Megrant, A., Jeffrey, E., White, T. C., Sank, D., Mutus, J. Y., Campbell, B., Chen, Y., Chen, Z., Chiaro, B., Dunsworth, A., Hoi, I.-C., Neill, C., O’Malley, P. J. J., Quintana, C., Roushan, P., Vainsencher, A., Wenner, J., Cleland, A. N., & Martinis, J. M. 2015. State preservation by repetitive error detection in a superconducting quantum circuit. *Nature*, **519**, 66.
- Kimble, H. J. 2008. The quantum internet. *Nature*, **453**(7198), 1023–1030.

- Knill, E., Laflamme, R., & Milburn, G. J. 2001. A scheme for efficient quantum computation with linear optics. *Nature*, **409**(6816), 46–52.
- Knill, E., Leibfried, D., Reichle, R., Britton, J., Blakestad, R. B., Jost, J. D., Langer, C., Ozeri, R., Seidelin, S., & Wineland, D. J. 2008. Randomized benchmarking of quantum gates. *Phys. Rev. A*, **77**(Jan), 012307.
- Koch, J., Yu, T. M., Gambetta, J., Houck, A. A., Schuster, D. I., Majer, J., Blais, A., Devoret, M. H., Girvin, S. M., & Schoelkopf, R. J. 2007. Charge-insensitive qubit design derived from the Cooper pair box. *Phys. Rev. A*, **76**(4), 042319.
- Kuhn, A., Hennrich, M., & Rempe, G. 2002. Deterministic Single-Photon Source for Distributed Quantum Networking. *Phys. Rev. Lett.*, **89**(6), 067901.
- Lang, C., Bozyigit, D., Eichler, C., Steffen, L., Fink, J. M., Abdumalikov Jr., A. A., Baur, M., Philipp, S., da Silva, M. P., Blais, A., & Wallraff, A. 2011. Observation of Resonant Photon Blockade at Microwave Frequencies Using Correlation Function Measurements. *Phys. Rev. Lett.*, **106**(24), 243601–4.
- Lang, C., Eichler, C., Steffen, L., Fink, J. M., Woolley, M. J., Blais, A., & Wallraff, A. 2013. Correlations, indistinguishability and entanglement in Hong-Ou-Mandel experiments at microwave frequencies. *Nat. Phys.*, **9**(6), 345–348.
- Lang, C. 2014 (02). *Quantum Microwave Radiation and its Interference Characterized by Correlation Function Measurements in Circuit Quantum Electrodynamics*. Ph.D. thesis, ETH Zurich.
- Leibfried, D., DeMarco, B., Meyer, V., Lucas, D., Barrett, M., Britton, J., Itano, W. M., Jelenkovic, B., Langer, C., Rosenband, T., & Wineland, D. J. 2003. Experimental demonstration of a robust, high-fidelity geometric two ion-qubit phase gate. *Nature*, **422**(6930), 412–415.
- Li, A. C. Y., Petruccione, F., & Koch, J. 2014. Perturbative approach to Markovian open quantum systems. *Sci. Rep.*, **4**(May), –.
- Liu, Y., & Houck, A. A. 2016. Quantum electrodynamics near a photonic band-gap. *arXiv:1603.02998 [quant-ph]*, Mar. arXiv: 1603.02998.
- Mabuchi, H., & Doherty, A. C. 2002. Cavity Quantum Electrodynamics: Coherence in Context. *Science*, **298**(5597), 1372–1377.
- Magesan, E., Gambetta, J. M., Johnson, B. R., Ryan, C. A., Chow, J. M., Merkel, S. T., da Silva, M. P., Keefe, G. A., Rothwell, M. B., Ohki, T. A., Ketchen, M. B., & Steffen, M. 2012. Efficient Measurement of Quantum Gate Error by Interleaved Randomized Benchmarking. *Phys. Rev. Lett.*, **109**(Aug), 080505.
- Majer, J., Chow, J. M., Gambetta, J. M., Koch, J., Johnson, B. R., Schreier, J. A., Frunzio, L., Schuster, D. I., Houck, A. A., Wallraff, A., Blais, A., Devoret, M. H., Girvin, S. M., & Schoelkopf, R. J. 2007. Coupling superconducting qubits via a cavity bus. *Nature*, **449**(7161), 443–447.

- Manucharyan, V. E., Koch, J., Glazman, L. I., & Devoret, M. H. 2009. Fluxonium: Single Cooper-Pair Circuit Free of Charge Offsets. *Science*, **326**(5949), 113–116.
- Manzoni, M. T., Reiter, F., Taylor, J. M., & Sørensen, A. S. 2014. Single-photon transistor based on superconducting systems. *Phys. Rev. B*, **89**(18), 180502–.
- Mariantoni, M., Wang, H., Yamamoto, T., Neeley, M., Bialczak, R. C., Chen, Y., Lenander, M., Lucero, E., O’Connell, A. D., Sank, D., Weides, M., Wenner, J., Yin, Y., Zhao, J., Korotkov, A. N., Cleland, A. N., & Martinis, J. M. 2011a. Implementing the Quantum von Neumann Architecture with Superconducting Circuits. *Science*, **334**(6052), 61–65.
- Mariantoni, M., Wang, H., Bialczak, R. C., Lenander, M., Lucero, E., Neeley, M., O’Connell, A. D., Sank, D., Weides, M., Wenner, J., Yamamoto, T., Yin, Y., Zhao, J., Martinis, J. M., & Cleland, A. N. 2011b. Photon shell game in three-resonator circuit quantum electrodynamics. *Nat. Phys.*, **7**(4), 287–293.
- Martinis, J. M., Nam, S., Aumentado, J., & Urbina, C. 2002. Rabi oscillations in a large Josephson-junction qubit. *Phys. Rev. Lett.*, **89**(11), 117901.
- Maxfield, B. W., & McLean, W. L. 1965. Superconducting Penetration Depth of Niobium. *Phys. Rev.*, **139**, 1515.
- Maxwell, J. C. 1865. A dynamical theory of the electromagnetic field. *Phil. Trans. R. Soc. Lond.*, **155**, 459–512.
- Menzel, E. P., Deppe, F., Mariantoni, M., Araque Caballero, M. A., Baust, A., Niemczyk, T., Hoffmann, E., Marx, A., Solano, E., & Gross, R. 2010. Dual-Path State Reconstruction Scheme for Propagating Quantum Microwaves and Detector Noise Tomography. *Phys. Rev. Lett.*, **105**(10), 100401.
- Motzoi, F., Gambetta, J. M., Rebentrost, P., & Wilhelm, F. K. 2009. Simple Pulses for Elimination of Leakage in Weakly Nonlinear Qubits. *Phys. Rev. Lett.*, **103**(11), 110501.
- Naaman, O., Abutaleb, M. O., Kirby, C., & Rennie, M. 2016. On-chip Josephson junction microwave switch. *Appl. Phys. Lett.*, **108**(11), 112601.
- Nakamura, Y., Pashkin, Y. A., & Tsai, J. S. 1999. Coherent control of macroscopic quantum states in a single-Cooper-pair box. *Nature*, **398**(6730), 786–788.
- Newton, I. 1730. *Opticks: Or, a treatise of the reflexions, refractions, inflexions and colours of light*. London.
- Nigg, S. E., Paik, H., Vlastakis, B., Kirchmair, G., Shankar, S., Frunzio, L., Devoret, M. H., Schoelkopf, R. J., & Girvin, S. M. 2012. Black-Box Superconducting Circuit Quantization. *Phys. Rev. Lett.*, **108**(Jun), 240502.
- Nisbet-Jones, P. B. R., Dille, J., Ljunggren, D., & Kuhn, A. 2011. Highly efficient source for indistinguishable single photons of controlled shape. *New J. Phys.*, **13**(10), 103036–.

- O'Connell, A. D., Ansmann, M., Bialczak, R. C., Hofheinz, M., Katz, N., Lucero, E., McKenney, C., Neeley, M., Wang, H., Weig, E. M., Cleland, A. N., & Martinis, J. M. 2008. Microwave dielectric loss at single photon energies and millikelvin temperatures. *Appl. Phys. Lett.*, **92**(11), 112903–3.
- Oh, S., Cicak, K., Kline, J. S., Sillanpää, M. A., Osborn, K. D., Whittaker, J. D., Simmonds, R. W., & Pappas, D. P. 2006. Elimination of two level fluctuators in superconducting quantum bits by an epitaxial tunnel barrier. *Phys. Rev. B*, **74**, 100502(R).
- Paik, H., Schuster, D. I., Bishop, L. S., Kirchmair, G., Catelani, G., Sears, A. P., Johnson, B. R., Reagor, M. J., Frunzio, L., Glazman, L. I., Girvin, S. M., Devoret, M. H., & Schoelkopf, R. J. 2011. Observation of High Coherence in Josephson Junction Qubits Measured in a Three-Dimensional Circuit QED Architecture. *Phys. Rev. Lett.*, **107**(Dec), 240501.
- Pancharatnam, S. 1956. Generalized theory of interference and its applications. *Proc. Indian Acad. Sci.*, **A44**, 247–262.
- Pechal, M., Berger, S., Abdumalikov Jr., A. A., Fink, J. M., Mlynek, J. A., Steffen, L., Wallraff, A., & Filipp, S. 2012. Geometric Phase and Nonadiabatic Effects in an Electronic Harmonic Oscillator. *Phys. Rev. Lett.*, **108**, 170401.
- Pechal, M., Huthmacher, L., Eichler, C., Zeytinoglu, S., Abdumalikov Jr., A., Berger, S., Wallraff, A., & Filipp, S. 2014. Microwave-Controlled Generation of Shaped Single Photons in Circuit Quantum Electrodynamics. *Phys. Rev. X*, **4**, 041010.
- Pechal, M. 2011 (03). *Geometric phase of a harmonic oscillator in circuit QED*. M.Phil. thesis, ETH Zurich.
- Peng, Z. H., Tsai, J. S., & Astafiev, O. V. 2015. Tuneable on-demand single-photon source. *arXiv:1505.05614*.
- Peters, A., Chung, K. Y., & Chu, S. 2001. High-precision gravity measurements using atom interferometry. *Metrologia*, **38**, 25–61.
- Planck, M. 1901. Über das Gesetz der Energieverteilung im Normalspectrum. *Ann. Phys.*, **309**(3), 553–563.
- Pobell, F. 2006. *Matter and Methods at Low Temperatures*. Springer, 3rd edition,.
- Pospieszalski, M. W., Weinreb, S., Norrod, R. D., & Harris, R. 1988. FET's and HEMT's at Cryogenic Temperatures - Their Properties and Use in Low-Noise Amplifiers. *IEEE Trans. Microwave Theory Tech.*, **36**, 552.
- Pozar, D. M. 2011. *Microwave Engineering*. 4th ed. edn. John Wiley & Sons, Inc.

- Quintana, C. M., Megrant, A., Chen, Z., Dunsworth, A., Chiaro, B., Barends, R., Campbell, B., Chen, Y., Hoi, I.-C., Jeffrey, E., Kelly, J., Mutus, J. Y., O'Malley, P. J. J., Neill, C., Roushan, P., Sank, D., Vainsencher, A., Wenner, J., White, T. C., Cleland, A. N., & Martinis, J. M. 2014. Characterization and reduction of microfabrication-induced decoherence in superconducting quantum circuits. *Applied Physics Letters*, **105**(6), 062601.
- Ranzani, L., Spietz, L., Popovic, Z., & Aumentado, J. 2013. Two-port microwave calibration at millikelvin temperatures. *Rev. Sci. Instrum.*, **84**(3), 034704–9.
- Reed, M. D., Johnson, B. R., Houck, A. A., DiCarlo, L., Chow, J. M., Schuster, D. I., Frunzio, L., & Schoelkopf, R. J. 2010. Fast reset and suppressing spontaneous emission of a superconducting qubit. *Appl. Phys. Lett.*, **96**(20), 203110.
- Reiserer, A., Ritter, S., & Rempe, G. 2013. Nondestructive Detection of an Optical Photon. *Science*, Nov., –.
- Ritter, S., Nolleke, C., Hahn, C., Reiserer, A., Neuzner, A., Uphoff, M., Mucke, M., Figueroa, E., Bochmann, J., & Rempe, G. 2012. An elementary quantum network of single atoms in optical cavities. *Nature*, **484**(7393), 195–200.
- Sakurai, J. J., & Napolitano, J. J. 2010. *Modern quantum mechanics*. 2 edn. Addison-Wesley.
- Salathé, Y., Mondal, M., Oppliger, M., Heinsoo, J., Kurpiers, P., Potočnik, A., Mezzacapo, A., Las Heras, U., Lamata, L., Solano, E., Filipp, S., & Wallraff, A. 2015. Digital Quantum Simulation of Spin Models with Circuit Quantum Electrodynamics. *Phys. Rev. X*, **5**(06), 021027.
- Salathé, Y. 2011 (10). *Towards Gigahertz Bandwidth Digital Signal Processing in Circuit Quantum Electrodynamics*. M.Phil. thesis, ETH Zurich.
- Sete, E. A., Martinis, J. M., & Korotkov, A. N. 2015. Quantum theory of a bandpass Purcell filter for qubit readout. *Phys. Rev. A*, **92**(Jul), 012325.
- Shor, P. W. 1994. Algorithms for Quantum Computation: Discrete Logarithms and Factoring. *Page 124 of: Proceedings, 35th Annual Symposium on Foundations of Computer Science, Santa Fe*. IEEE Computer Society Press.
- Shore, B. W., & Knight, P. L. 1993. The Jaynes-Cummings Model. *J. Mod. Opt.*, **40**, 1195–1238.
- Simons, R. N. 2001. *Coplanar waveguide circuits, components and systems*. Wiley Series in Microwave and Optical Engineering. Wiley Inter-Science.
- Smolin, J. A., Gambetta, J. M., & Smith, G. 2012. Efficient Method for Computing the Maximum-Likelihood Quantum State from Measurements with Additive Gaussian Noise. *Phys. Rev. Lett.*, **108**(Feb), 070502.

- Srinivasan, S. J., Hoffman, A. J., Gambetta, J. M., & Houck, A. A. 2011. Tunable Coupling in Circuit Quantum Electrodynamics Using a Superconducting Charge Qubit with a V-Shaped Energy Level Diagram. *Phys. Rev. Lett.*, **106**(8), 083601.
- Srinivasan, S. J., Sundaresan, N. M., Sadri, D., Liu, Y., Gambetta, J. M., Yu, T., Girvin, S. M., & Houck, A. A. 2014. Time-reversal symmetrization of spontaneous emission for quantum state transfer. *Phys. Rev. A*, **89**(Mar), 033857.
- Steffen, L., Salathe, Y., Oppliger, M., Kurpiers, P., Baur, M., Lang, C., Eichler, C., Puebla-Hellmann, G., Fedorov, A., & Wallraff, A. 2013. Deterministic quantum teleportation with feed-forward in a solid state system. *Nature*, **500**, 319–322.
- Thompson, R. J., Rempe, G., & Kimble, H. J. 1992. Observation of normal-mode splitting for an atom in an optical cavity. *Phys. Rev. Lett.*, **68**(8), 1132–1135.
- Tinkham, M. 1996. *Introduction to Superconductivity*. McGraw-Hill International Editions.
- van Loo, A., Fedorov, A., Lalumière, K., Sanders, B., Blais, A., & Wallraff, A. 2013. Photon-Mediated Interactions Between Distant Artificial Atoms. *Science*, **342**(6165), 1494–1496.
- van Loo, A. F. 2014 (07). *Interactions in waveguide quantum electrodynamics*. Ph.D. thesis, ETH Zurich.
- Vandenberghe, L., & Boyd, S. 1996. Semidefinite Programming. *SIAM Review*, **38**(1), 49–95.
- Vion, D., Aassime, A., Cottet, A., Joyez, P., Pothier, H., Urbina, C., Esteve, D., & Devoret, M. H. 2002. Manipulating the quantum state of an electrical circuit. *Science*, **296**, 886–889.
- Wallraff, A., Schuster, D. I., Blais, A., Frunzio, L., Huang, R.-S., Majer, J., Kumar, S., Girvin, S. M., & Schoelkopf, R. J. 2004. Strong coupling of a single photon to a superconducting qubit using circuit quantum electrodynamics. *Nature*, **431**, 162–167.
- Walls, D. F., & Milburn, G. J. 2008. *Quantum Optics*. 2 edn. Berlin: Springer Verlag.
- Wang, C., Thummes, G., & Heiden, C. 1997. A two-stage pulse tube cooler operating below 4 K. *Cryogenics*, **37**(3), 159 – 164.
- Wick, G. C. 1950. The Evaluation of the Collision Matrix. *Phys. Rev.*, **80**, 268.
- Wiseman, H., & Milburn, G. 2010. *Quantum Measurement and Control*. Cambridge University Press.
- Wootters, W. K., & Zurek, W. H. 1982. A single quantum cannot be cloned. *Nature*, **299**, 802–803.

- Yamamoto, Y., & İmamođlu, A. 1999. *Mesoscopic Quantum Optics*. Wiley.
- Yin, Y., Chen, Y., Sank, D., O'Malley, P. J. J., White, T. C., Barends, R., Kelly, J., Lucero, E., Mariantoni, M., Megrant, A., Neill, C., Vainsencher, A., Wenner, J., Korotkov, A. N., Cleland, A. N., & Martinis, J. M. 2013. Catch and Release of Microwave Photon States. *Phys. Rev. Lett.*, **110**(Mar), 107001.
- Young, T. 1804. The Bakerian Lecture: Experiments and Calculations Relative to Physical Optics. *Phil. Trans. R. Soc. Lond.*, **94**, 1–16.
- Yurke, B., & Buks, E. 2006. Performance of Cavity-Parametric Amplifiers, Employing Kerr Nonlinearites, in the Presence of Two-Photon Loss. *J. Lightwave Technol.*, **24**(12), 5054–5066.
- Zeytinoglu, S., Pechal, M., Berger, S., Abdumalikov Jr., A. A., Wallraff, A., & Filipp, S. 2015. Microwave-induced amplitude- and phase-tunable qubit-resonator coupling in circuit quantum electrodynamics. *Phys. Rev. A*, **91**, 043846.

List of publications

- 1.* *M. Pechal*, S. Berger, A. A. Abdumalikov, J. M. Fink, J. A. Mlynek, A. Wallraff and S. Filipp. ‘Geometric phase and non-adiabatic effects in an electronic harmonic oscillator’, *Phys. Rev. Lett.* **108**, 170401 (2012)
- 2.* *M. Pechal*, L. Huthmacher, C. Eichler, S. Zeytinoglu, A. A. Abdumalikov, S. Berger, A. Wallraff and S. Filipp. ‘Microwave-controlled generation of shaped single photons in circuit quantum electrodynamics’. *Phys. Rev. X* **4**, 041010 (2014)
- 3.* S. Zeytinoglu, *M. Pechal*, S. Berger, A. A. Abdumalikov, A. Wallraff and S. Filipp. ‘Microwave-induced amplitude and phase tunable qubit-resonator coupling in circuit quantum electrodynamics’. *Phys. Rev. A* **91**, 043846 (2015)
- 4.* *M. Pechal*, J.-C. Besse, M. Mondal, M. Oppliger, S. Gasparinetti, and A. Wallraff. ‘Superconducting Switch for Fast On-Chip Routing of Quantum Microwave Fields’. *Phys. Rev. Applied* **6**, 024009 (2016)
5. A. A. Abdumalikov, J. M. Fink, K. Juliusson, *M. Pechal*, S. Berger, A. Wallraff and S. Filipp. ‘Experimental realization of non-Abelian non-adiabatic geometric gates’. *Nature* **496**, 482 (2013)
6. S. Berger, *M. Pechal*, P. Kurpiers, A. A. Abdumalikov, C. Eichler, J. A. Mlynek, A. Shnirman, Y. Gefen, S. Filipp and A. Wallraff. ‘Measurement of geometric dephasing using a superconducting qubit’. *Nature Communications* **6**, 8757 (2015)
7. S. Berger, *M. Pechal*, A. A. Abdumalikov, C. Eichler, L. Steffen, A. Fedorov, A. Wallraff and S. Filipp. ‘Exploring the effect of noise on the Berry phase’. *Phys. Rev. A* **87**, 060303(R) (2013)
8. S. Berger, *M. Pechal*, S. Pugnetti, A. A. Abdumalikov, L. Steffen, A. Fedorov, A. Wallraff and S. Filipp. ‘Geometric phases in superconducting qubits beyond the two-level approximation’. *Phys. Rev. B* **85**, 220502(R) (2012)
9. S. Gasparinetti, S. Berger, A. A. Abdumalikov, *M. Pechal*, S. Filipp and A. Wallraff. ‘Measurement of a vacuum-induced geometric phase’. *Science Advances* **2**, e1501732 (2016)

*First and co-first author papers.

Curriculum vitae

Name Marek Pechal
Date of birth 16/04/1987
Citizenship Czech Republic

Professional experience

03/2011 – 07/2016 Research assistant (with Prof. A. Wallraff) and teaching assistant, Department of Physics, ETH Zürich
08/2008 Teaching assistant at a summer school, Faculty of Mathematics and Physics, Charles University in Prague

Education

03/2011 – 07/2016 PhD studies, Department of Physics, ETH Zürich, “*Microwave photonics in superconducting circuits*”
09/2009 – 06/2011 MSc Physics, ETH Zürich.
09/2006 – 06/2009 BSc Physics, Charles University in Prague
Czech Republic
09/1998 – 05/2006 Secondary education:
Gymnázium Zlín - Lesní čtvrť
Zlín, Czech Republic

Zurich, September 2016

Acknowledgements

Pluralis modestiae – the author’s “we”, so abundant in scientific literature, seems especially appropriate when used in a PhD thesis. Replacing it with “I”, which it is commonly understood to substitute, would be extremely immodest here. As they say, even though a PhD thesis is written by a single author, the underlying work is rarely undertaken by a single individual without a healthy amount of external help. For this reason, it is necessary to dispense many thanks all around:

To Andreas, for providing the chance, inspiration and equipment to try my hands on research in an exciting field of physics. To Jonathan Home and Konrad Lehnert for finding the time to be on my PhD committee. To Stefan and Simon for providing a lot of advice during my early days in the lab. To Arjan for being an awesome office- and flat-mate and for all the coffee-break distractions and motorbike trips. To Anna for the relaxing running breaks. To Lukas for making my duties as his master thesis supervisor very easy and especially for his heroic accomplishment in single-handedly re-cabling the Vericold measurement setups. To Stephan for the valuable contributions during his semester thesis work. To Jean-Claude for all the help with the on-chip switch measurements. To Simone for many insightful discussions about both experiments and theory. To all the members of the awesome D17 office – Arjan, Simon, Lars, Anna, Yves, Philipp and others – for making it a very special workplace. And to all the Qudev members for being great co-workers and friends.

Special thanks should also go to my family and friends for their love and support.



Declaration of originality

The signed declaration of originality is a component of every semester paper, Bachelor's thesis, Master's thesis and any other degree paper undertaken during the course of studies, including the respective electronic versions.

Lecturers may also require a declaration of originality for other written papers compiled for their courses.

I hereby confirm that I am the sole author of the written work here enclosed and that I have compiled it in my own words. Parts excepted are corrections of form and content by the supervisor.

Title of work (in block letters):

Microwave photonics in superconducting circuits

Authored by (in block letters):

For papers written by groups the names of all authors are required.

Name(s):

Pechal

First name(s):

Marek

With my signature I confirm that

- I have committed none of the forms of plagiarism described in the '[Citation etiquette](#)' information sheet.
- I have documented all methods, data and processes truthfully.
- I have not manipulated any data.
- I have mentioned all persons who were significant facilitators of the work.

I am aware that the work may be screened electronically for plagiarism.

Place, date

Vizovice, 12.09.2016

Signature(s)

Marek Pechal

For papers written by groups the names of all authors are required. Their signatures collectively guarantee the entire content of the written paper.